Available online at www.sciencedirect.com

SciVerse ScienceDirect

Procedia Engineering 00 (2012) 000–000

Procedia Engineering

www.elsevier.com/locate/procedia

5th BSME International Conference on Thermal Engineering

Analytical Solution of Free Convection for Porous Material of Quadratic Heat Generation in a Circular Cavity

Kamyar Mansour*

Department Of Aerospace Engineering,Amirkabir University of Technology Tehran, Iran, 15875-4413

and

Flow Research and Engineering 788 Maplewood Avenue, Palo Alto, CA 94303†

Abstract

We consider the two-dimensional problem of steady natural convection in a circular cavity with quadratic volumetric generation filled with porous material. We use Darcy's law for this cavity filled with porous material. The solution is governed by dimensionless parameter Darcy-Rayleigh number. The solution is expanded for low Darcy-Rayleigh number as was done by [1] and extended to 18 terms by computer. Analysis of these expansions allows the exact computation for arbitrarily accuracy up to 50000 figures. Although the range of the radius of convergence is small but Pade approximation leads our results to be good even for higher value of the similarity parameter.

Keywords: Free convection flow, Nonlinear equations, Symbolic calculations .

Nomenclature

g	Gravity
$K = \varepsilon^2 Ra$	Similarity parameter
$Rq = \frac{g\beta\Delta T_q (KK) R_l}{\nu\alpha}$	Rayleigh number
T	Temperature
C	further nomenclature continues down the page inside the text box
Greek symbols	
α	Thermal diffusivity
β	The coefficient of thermal expansion
ν	Kinematic viscosity
k	Effective thermal conductivity
KK	Thermal diffusivity
ψ	Stream function
ΔT_q	Imposed temperature difference
Subscripts	
r	value at reference temperature

* Corresponding author. Tel.: +982164543216; fax: +982166959020.
E-mail address: Mansour@aut.ac.ir

1. Introduction

We consider the two-dimensional problem of steady natural convection in a circular cavity with linear volumetric heat flux filled with porous material. We use Darcy's law for this cavity filled with porous material. The solution is governed by dimensionless parameter Darcy-Rayleigh number. The solution is expanded for low Darcy-Rayleigh number as was done by [1], [2],[3] and extended to 18 terms by computer. Analysis of these expansions allows the exact computation for arbitrarily accuracy up to 50000 figures. Although the range of the radius of convergence is small but Pade approximation leads our result to be good even for higher value of the similarity parameter. This investigation is in a porous circular cavity driven by heating in the horizontal direction is our interest. We use Darcy's law for this cavity filled with porous material. The solution is governed by dimensionless parameter Darcy-Rayleigh number. The solution is expanded up to 18 terms by computer in powers of Darcy-Rayleigh number. Analysis of these expansions allows the exact computation for arbitrarily accuracy up to 50000 figures. Although the range of the radius of convergence is small but Pade approximation leads our result to be good even for higher value of the similarity parameter. The analysis yields a solution for all values of Rayleigh number from zero to finite value in a continuous fashion. The natural convection in a cavities filled with porous medium has received much attention because of the theoretical interest of [4], [5], [6], [7] for isothermal surfaces and [8] for isothermal inner and sinusoidal outer boundaries. As far as the numerical works for the case of isothermal surfaces a parameter study of diameter-ratio effects on the heat transfer coefficient was performed by [4] and angle of heating by [8] and other related problem of Natural Convection Non-Darcy effect by [9] and finally experimental work of [4]. The question of Hydrodynamic instability induces steady or oscillatory flows have been subject of many studies for example [4] and [10]. I hope the present exact solution of steady flow will help to answer such question more clearly. We recently have done the same present approach of symbolic calculation for laminar flow through heated horizontal pipe [3] and similar work done for concentrically spheres [11]. The similar approach was done for rectangular cavity by [12] and they found boundary limit solution from their regular perturbation for small Darcy-Rayleigh number.

2. Statement of problem

The governing equations for porous materials with Darcy's law can be written in dimensionless form as:

$$\nabla \dot{V} = 0 \qquad (1)$$

$$\dot{V} = -\frac{K}{\mu}(\nabla \dot{P} - \dot{\rho} g J) \qquad (2)$$

$$q''' + \dot{\rho} c (V.\dot{V}) \dot{T} = k \nabla^2 \dot{T} \qquad (3)$$

$$\dot{\rho} = \rho_r (1 - \beta (T - T_r))$$

Where $\dot{V}$ is the velocity vector, $\dot{\rho}$ density, T temperature, μ viscosity, $\dot{P}$ pressure, J=(cosθ,-sinθ) is a unit vector in the direction of gravity and $\lambda = \frac{g\beta\Delta T_q a}{\nu\alpha}$ is the Rayleigh number. The equations (1),(2) and (3) have been non-dimensional zed by using the radius of cavity (R) as the length scale, for velocity $\frac{\kappa}{R(\rho c)_r}$, and for temperature ΔT_q. ΔT_q is calculated from coefficient of heat generation q''', $\Delta T_q \approx \frac{q''' R^3}{\alpha}$ is somehow certain gradient of temperature across the cavity, K is the permeability of the media , β is the coefficient of volumetric expansion of the fluid and g the acceleration due to gravity. Introducing the stream function in order to satisfy Eq. (1), eliminating the pressure from Eq. (2) and writing the resulting equation in cylindrical polar coordinates , the continuity equation can be satisfied by introducing a Stokes stream function ψ for the cross flow. We mainly follow Mansour's notation [1993]. Then the velocity component U, V, W in the fluid are functions of r and θ only. The governing equations for porous materials with Darcy'law can be written in dimensionless form as:

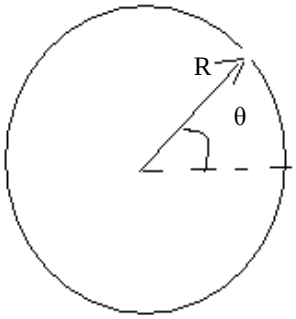

Fig.1 Geometry of the Problem

We mainly follow Mansour's notation [1]. Then the velocity component U, V, W in the fluid are functions of r and θ only. The continuity equation can be satisfied by introducing a Stokes stream function ψ for the cross flow The governing equations for porous materials with Darcy'law can be written in dimensionless form as:

$$\nabla^2\psi = -\lambda \left(\sin\theta\frac{\partial T}{\partial r}+\frac{\cos\theta}{r}\frac{\partial T}{\partial\theta}\right) \quad (4)$$

$$\nabla^2 T = \frac{1}{r}\left(-\frac{\partial\psi}{\partial\theta}\frac{\partial T}{\partial r}+\frac{\partial\psi}{\partial r}\frac{\partial T}{\partial\theta}\right)+16r^2 \quad (5)$$

$$\nabla^2 = \frac{\partial^2}{\partial \boldsymbol{r}^2}+\frac{1}{\boldsymbol{r}}\left(\frac{\partial}{\partial \boldsymbol{r}}\right)+\frac{1}{\boldsymbol{r}^2}\left(\frac{\partial^2}{\partial \boldsymbol{\theta}^2}\right) \quad (6)$$

The corresponding boundary conditions expressing the impermeability of the wall, the no-slip conditions, and imposed temperature distribution are respectively:

$$\begin{cases}\psi = 0, T = 0 \ on \ \ r = 0\\ \psi = 0, T = 1 \ on \ r = 1,\end{cases}$$

$\lambda = \frac{g\beta\Delta T_q (KK) R_i}{\nu\alpha}$ is is the Rayleigh number. Coordinates are non-dimensional zed by using the radius of cavity as the length scale. Here ΔT_q is imposed temperature difference (ν is kinematics viscosity, β the coefficient of volumetric expansion

2.1. Series Derivation and Computer Extension

In this work we delegated the mounting algebra to the computer and, for our boundary condition (9) one can systematically improve on this approximation).

$$\begin{cases} T = T_0 + (\frac{\lambda}{32})\, T_1 + (\frac{\lambda}{32})^2 T_2 + (\frac{\lambda}{32})^3 T_3 + ... \\ \psi = (\frac{\lambda}{32})\, \psi_1 + (\frac{\lambda}{32})^2 \psi_2 + (\frac{\lambda}{32})^3 \psi_3 + ... \end{cases} \quad (7)$$

We substitute the expansions (7) into our simplified equations (4) and (5) then equating like powers of K Gives for T_0 the equation: $\frac{\partial^2 T_0}{\partial r^2}+\frac{1}{r}\frac{\partial T_0}{\partial r}=16r^2$

Subject to boundary condition, It is easy to show that $T_0 = (r)^4$ and $\psi_0 = 0$. Therefore, the basic solution is the state of simple conduction. Substituting and equating like powers of λ yields this sequence of successive linear equations, together with boundary conditions

$$\psi_1 = \frac{16}{3}(-1+r^4)\ (r\cos(\theta))$$

$$\psi_2 = -\frac{16}{45}r^2(4-5r^4+r^8)Sin(2\theta)$$

$$\psi_3 = \frac{1}{42525}(32(3r(1517\text{-}1995r^2\ + 665r^6\ \text{-}217r^{10}\ +\ 30r^{14})Cos(\theta) - 35r^3\ (-19+27r^2-9r^8+r^{12})Cos(3\theta)))$$

$$\psi_4 = \text{-}\frac{1}{7016625}(16(2r^2\ (\text{-}706043\ +800560r^2\ + 250305r^4\ \text{-}457380\ r^6\ +139920r^{10} \text{-}30030\ r^{14}\ +2668r^{18})Sin(2\theta)+ 5\ r^4\ (14495\ \text{-}23100r^4\ + 10593r^8\ \text{-}2156r^{12}\ +\ 168r^{16})Sin(4\theta)))$$

$$T_1 = (\text{-}(\frac{4}{45}))r(7\text{-}\ 10r^3+3r^8\ )Sin(\theta)$$

$$T_2 = (\frac{1}{14175})(4(4(368\ \text{-}\ 735r^2+595r^6\ \text{-}273r^{10}+45r^{14})\ \text{-} 105\ r^2(\text{-}3+r^4)^2\ (\text{-}1+r^4)\ Cos(2\theta)))$$

$$T_3 = \ \text{-}\frac{1}{7016625}(8\ (33r(\text{-}31227+44730r^2\ +15170r^4\ \text{-}\ 43400r^6\ +\ 19334r^{10}\ \text{-}\ 5145r^{14}+538r^{18})Sin(\theta)\ \text{-}\ 10r^3\ (9175\ \text{-}\ 17325r^4\ +\ 10593r^8\ \text{-}\ 2695r^{12}\ +\ 252r^{16})\ Sin(3\theta)))$$

$$T_4 = (\text{-}\frac{1}{316063873125})(4(10r^2\ (7377934765\ \text{-}\ 8889961080\ r^2\ \text{-}\ 6272840574r^4\ +\ 10723280568\ r^6\ +\ 1052332281r^8\ \text{-}5412390984r^{10}\ + 1711184904r^{14}\ \text{-}313196884\ r^{18}\ + 23657004r^{22}\ )\ Cos(2\theta)\text{-}\ 3003(22(\text{-}1+\ r^2)^3\ (826973\ \text{-}29841r^2\ +\ 696192r^4\ +59260r^6\ +\ 380115r^8\ +\ 29721r^{10}\ \text{-}\ 105442r^{12}\ \text{-}25374r^{14}+10995r^{16}+3665r^{18})+ 5r^4(\text{-}196994+418780r^4\text{-}317295r^8+113916r^{12}\ \text{-}19775r^{16}+1368r^{20})Cos(4\theta)\ +$$

It is possible to introduce the quantity average of temperature defined as:

$$T_{ave} = \frac{12}{\pi}\int_{r=0}^{1}\int_{0}^{2\pi} Trdrd\theta$$

$$4+\frac{40}{27}(\frac{\lambda}{32})^2\ \text{-}(\frac{178784224}{91216125}(\frac{\lambda}{32})^4)\ +\ (\frac{33127587128816}{9050920003125}*(\frac{\lambda}{32})^6)\ \text{-}\ (\frac{4152464766691835964920 32}{5242142733674448164062 5}*(\frac{\lambda}{32})^8)\ \text{-}\ +\ (\frac{13856116561981926942506797974752}{74381680623085138028311523437 5}*(\frac{\lambda}{32})^{10})\ (\frac{18360411242377420007743478835544798407926452027757656370467070344568}{27084969239485182768891654658157775438773066067407790891723632812 5}*(\frac{\lambda}{32})^{12})\ +\ldots$$

Of course for lack of space we omit showing the calculation further than this order if any reader interested to have more calculation please contacts the author

2.2. Pade Approximation

Pade approximants has been used in original forms to enable us to increase the range of applicability of the series as has been used in the works of Mansour [2] and Mansour [3]. This method does not necessarily require any information about the radius of convergence. The Pade approximants provide an approximation that is invariant under an Euler transformation of the independent variables. The theory of Pade approximants has been used extensively in Mansour [1]. Briefly stated, the Pade approximant is the ratio P (λ)/Q (λ) of polynomials P and Q of degree m and n, respectively, that, when expanded, agrees with the given series through terms of degree m+n, and normalized by P (Q) =1. Such rational fractions are known to have remarkable properties of analytic continuation. The coefficients of the power series must be known to degree m+n. By equating like power of g(λ) and P(λ)/Q(λ), the linear system of m+n+1 equation must be solved to obtain the coefficients in the functional form P(λ)/Q(λ) Pade approximation of orders [1/2], [2/3] and [3/4] for T_{ave} series are respectively:

pade[1/2]:

$$\frac{4}{\left(1-\frac{10\left(\frac{\lambda}{32}\right)^2}{27}\right)}$$

pade[2/3]:

$$\frac{4+\left(\frac{114417112\left(\frac{\lambda}{32}\right)^2}{16891875}\right)}{1+\left(\frac{22348028\left(\frac{\lambda}{32}\right)^2}{16891875}\right)}$$

pade[3/4]:

$$\frac{\left(4+\frac{12026891273204\left(\frac{\lambda}{32}\right)^2}{1419129742275}\right)}{\left(1+\frac{2481119210051\left(\frac{\lambda}{32}\right)^2}{1419129742275}-\frac{4315769032925186\left(\frac{\lambda}{32}\right)^4}{27396299674618875}\right)}$$

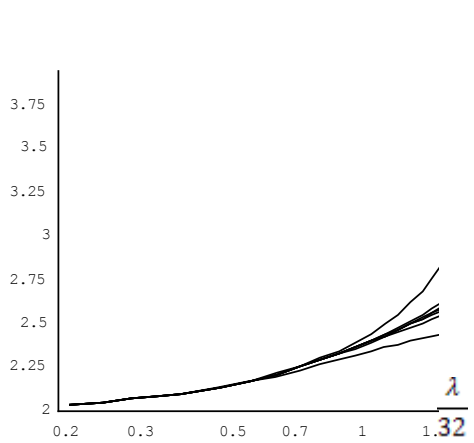

Fig.2. Plots of [8/9], [7/8],[6/7],[5/6],[4/5], [3/4]and [2/3] of the Pade approximants for T_{ave} versus $\frac{\lambda}{32}$

When we form the ratios [8/9], [7/8], [6/7],[5/6], [4/5], [3/4]and [2/3] of the Pade approximants, It can be shown, they agreed up to the value$\frac{\lambda}{32}$=.7. This conclusion is confirmed as is plotted in Figure 2.

3. Conclusion

This is problem of the two-dimensional problem of steady natural convection in a horizontal cylinder filled with porous medium due to quadratic volumetric generation. The solution is expanded for low Darcy-Rayleigh number and the series extended by means of symbolic calculation up to 18 terms. Analysis of these expansions allows the exact computation for

arbitrarily accuracy up to 50000 figures. Although the range of the radius of convergence is small but Pade approximation leads our result to be good even for much higher value of the similarity parameter we have found extending terms exactly by means of symbolic calculation up to 18th order. Then we tried to make analytic continuation by using Pade approximation. In other words, we have solved the nonlinear partial differential equation exactly by means of computer and that is a real success. Finally we mention recent work of [14] with viscous fluid for micro gap which shows our analytical approach more attractive and successful.

References

[1] Mansour, K. 1993 "Using Stokes Expansion For NaturalConvectio inside a two-dimensional cavity". Fluid Dynamics Research, 1-33
[2] Mansour, K. 1985 "Laminar flow through a slowly rotating straight pipe". Journal of Fluid Mech. 150, 1-24.

[3] Mansour, K 2004 "Using Symbolic Calculation For Solving laminar Flow Through Heated Horizontal Pipe" *Proceeding of 2nd BSME – ASME International conference on Thermal Enginnering*, 2-4 January 2004 Dhaka, Bangladesh.

[4] Caltagirone, J.P. 1976 "Thermo convective instabilities in a porous medium bounded by two concentric horizontal cylinders" Journal of Fluid Mech. 76, part 2, 1-24.

[5] Bau, H. H. 1984"Thermal Convection in a Horizontal, eccentric Annulus containing a Saturated Porous Medium—an extended perturbation expansion" Int. J. Heat Mass Transfer, Vol. 27, No. 12, pp. 2277-2287.
[6] Bau, H. H. 1984 "Low Rayleigh Number Thermal Convection in a Saturated Porous Medium bounded by two horizontal, eccentric cylinders" Trans. ASME Vol. 106, pp. 166-175.

[7] Bau, H. H. 1984 "Low Rayleigh Number Thermal Convection in a Saturated Porous Medium bounded by two horizontal, eccentric cylinders" Trans. ASME Vol. 106, pp. 166-175.

[8]. Prudhomme, M., Robillard, L., Vasseur, P., 1986 " Free convection in a two Dimensional Porous Loop" Journal of Heat Transfer, Vol. 108, pp. 277-283.

[9] Muralidhar, K. ,Kulacki, F.A. 1988 "Non- Darcy Natural Convection in a Saturated Horizontal Porous Annulus" Journal of Heat Transfer, Vol. 110, pp. 133-139.

[10]. Fant,D.B.,Prusa,J.,Rothmayer, A. P. 1990 "Unsteady Multi cellular Natural Convection in a narrow Horizontal Cylindrical annulus" Journal of Heat Transfer, Vol. 112, pp. 379-385.

[11] TeBeest, K. G., Trogdon, S. A., Douglass, R. W., 1993 " Natural Convection Within Spherical Annuli by Symbolic Algebra" Journal of Heat Transfer, Vol. 115, pp. 807-809.

[12] Walker, Ken L., Homsy, George M.," Convection in a porous Cavity," Journal of Fluid Mech., 87,449, 1978.

[13.]Vasseur, P, Nguyen, T.H., Robillard, L, Tong Thi,V.K., Natural Convection Between Horizontal Concentric Cylinders Filled with a Porous Layer With Internal Heat Generation, Int. J. Heat Mass Transfer, Vol. 27, No. 12, pp.337-349, 1984.

[14] Kamyar Mansour, The Analytical Solution of Natural Convection in a Micro Size Horizontal Cylindrical Annulus with Periodic Volumetric Heat Flux, Heat Transfer Asian Research , Vol. 40, pp.26-40 Wiley, 2011.

Available online at www.sciencedirect.com

SciVerse ScienceDirect

Procedia Engineering 00 (2012) 000–000

Procedia Engineering

www.elsevier.com/locate/procedia

5th BSME International Conference on Thermal Engineering

Heat conduction through eccentric hollow prismatic cylinders

Manoj Kumar Moharana*

Department of Mechanical Engineering, National Institute of Technology Rourkela, Rourkela 769008, India

Abstract

Heat conduction through eccentric hollow prismatic cylinders has been analyzed using a semi-analytical two-dimensional boundary collocation technique. This problem has been solved with the prior assumption of isothermal inner and outer walls. The methodology consists in using the exact solution of the governing differential equation of the problem and satisfying the given boundary conditions only at finite number of discrete points. Based on the outcome of this method conduction shape factor of such geometries are calculated. The position of the eccentric hole in any prismatic cylinder can lead to different orientations. Two orientations are discussed. A comparison with existing one dimensional solution to this problem is carried out and found that the present technique can predict more accurately than the existing one dimensional approach.

Keywords: Heat conduction; Boundary collocation method; Conduction shape factor; Eccentric hollow prismatic cylinder

Nomenclature

A, B, C, D, A_k, B_k, C_k, D_k, λ_k	unknown constants in Eq. (3)
$\overline{D}$	ratio of r_o and r_i
e	eccentricity
$\overline{E}$	ratio of e and r_i
K_t	thermal conductivity
M	number of collocation points
N	number of regular sides of prismatic cylinder
Q	heat transfer
r	radial coordinate, radius
r_i	radius of the inner circular surface
r_o	radius of the inscribed circle of the outer regular polygonal surface
r_s	radius to the outer surface
R	ratio of r and r_i
$\overline{R}$	ratio of r_s and r_i
S	conduction shape factor
T	temperature
Y_k	unknowns

* Corresponding author. Tel.: +91-661-246-2533; fax: +91-661-247-2926.
E-mail address: moharanam@nitrkl.ac.in

Greek symbols	
θ	angular coordinate
Θ	dimensionless temperature
Γ	angular direction
Subscripts	
i	inner
o	outer

1. Introduction

Conduction of heat between two isothermal boundaries of any two-dimensional annular region can be calculated using $Q = K_t \cdot S \cdot dT$ if the conduction shape factor S is known for such geometries. Here K_t is the thermal conductivity of the solid, and dT is the difference in temperature of the two isothermal surfaces. The conduction shape factor depends only on the geometrical shape of the body and the position of both isothermal surfaces. In literature the conduction shape factor of a variety of geometries are calculated. The shape factor of some commonly used geometry can be found in standard heat transfer books [1-2].

Different hollow prismatic cylinders are widely used in industrial applications. A square cylinder with a concentric circular hole is frequently used. Smith et al. [3] used measurement of electrical resistance to calculate the shape factor of different hollow cylinders including a square cylinder with a concentric circular hole. Later on Shih [4] used method of point matching and calculated shape factor. Dugan [5] used a boundary residual technique to calculate the shape factor more accurately. Nickolay et al. [6] used finite element and finite difference for this purpose.

Regular prismatic cylinders having a circular hole is also used in different engineering applications. Balcerzak and Raynor [7] calculated conduction shape factor of regular polygonal cylinder with a concentric circular hole using method of conformal mapping. Laura and Susemihl [8] used conformal mapping without a point matching approach. Simeza and Yovanovich [9] used parallel flux tube heat flux model and derived approximate analytical expression for evaluating the conduction shape factor. Kolodziej et al. [10] used boundary collocation method to find shape factor of regular polygonal cylinder with concentric circular hole. Teertstra et al. [11] developed an analytical conduction shape factor model based on the equivalent circular annulus with a modified independent parameter.

Some applications may require an eccentric circular hole in a regular polygonal cylinder (see Fig. 1) rather than a concentric circular hole. Secondly, sometimes during the manufacturing process the eccentricity arises. In this work a two-dimensional boundary collocation method is used to study heat conduction through regular polygonal tubes with eccentric circular hole. Recently Moharana and Das [12] used an approximate one dimensional approach to predict heat transfer/conduction shape factor of regular polygonal cylinder having an eccentric circular hole. The accuracy of the one dimensional approach proposed by Moharana and Das [12] decreases with increase in the value of eccentricity. The present two-dimensional solution is more accurate compared to that of Moharana and Das [12]. Secondly, the level of accuracy is not affected even at higher value of eccentricity. Based on the temperature profile predicted by the present method, the conduction shape factor of different eccentric hollow prismatic cylinders is calculated.

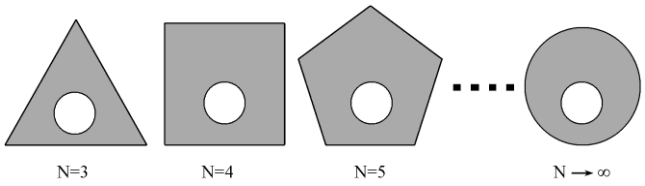

Fig. 1. schematic of regular polygonal tubes with eccentric circular hole.

2. Boundary collocation method

Two dimensional semi-analytical boundary collocation method which belongs to the family of boundary procedures has been used for two dimensional heat conduction analysis of the domain of this problem. The boundary collocation method can be summarized as the method that consists in using the exact solution to the governing differential equation of the problem and satisfying the given boundary conditions at a finite number of discrete points along the boundary. An extensive review of use of boundary collocation method in linear continuous mechanics is available in Kolodziej [13]. While many applications in the field of continuous mechanics of solid structures have evolved [14], limited applications in solving fluid flow [13, 15] as well as heat transfer problems [10, 12, 16, 17] are also available.

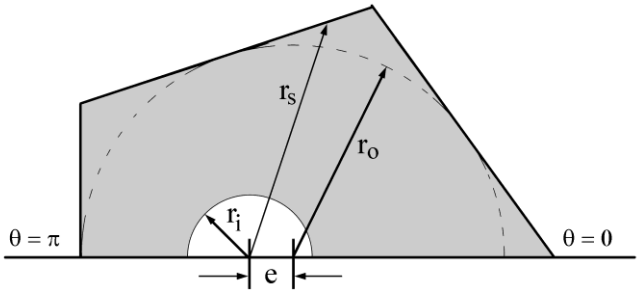

Fig. 2. schematic of the symmetrical module of a regular pentagonal tube with an eccentric circular hole.

The problem has been solved with the following prior assumptions (a) steady state heat transfer through the tube (b) no heat generation in the tube material (c) thermal conductivity of the tube material is constant (d) heat transfer takes place in the radial direction only (e) temperature is constant but different over the inner and the outer surface of the tube. . Considering symmetry only one half of any polygonal tube between $\theta = 0$, and $\theta = \pi$ in anti-clockwise direction is considered in the analysis (See Fig. 2). The non dimensional parameters used are

$$\Theta = (T - T_o)/(T_i - T_o), \qquad R = r/r_i, \qquad \overline{R} = r_s(\theta)/r_i, \qquad \overline{D} = r_o/r_i, \qquad \overline{E} = e/r_i \tag{1}$$

where r_o is the radius of the inscribed circle of the regular polygon. The governing equation in non dimensional form is

$$\frac{\partial^2\Theta}{\partial R^2} + \frac{1}{R}\frac{\partial\Theta}{\partial R} + \frac{1}{R^2}\frac{\partial^2\Theta}{\partial\theta^2} = 0 \tag{2}$$

Taking the queue from Kolodziej and Strek [10], the generalized variation of temperature in r-θ co-ordinate can be expressed as

$$\Theta(R,\theta) = A + B\ln R + C\theta + D\theta\ln R + \sum_{k=1}^{\infty}(A_k R^{\lambda_k} + B_k R^{-\lambda_k})\cos(\lambda_k\theta) + \sum_{k=1}^{\infty}(C_k R^{\lambda_k} + D_k R^{-\lambda_k})\sin(\lambda_k\theta) \tag{3}$$

where A, B, C, D, A_k, B_k, C_k, D_k, λ_k are unknown constants. The boundary conditions in non-dimensional form are

$$\partial\Theta/\partial\theta = 0 \quad \text{for} \quad \theta = 0 \tag{4a}$$

$$\partial\Theta/\partial\theta = 0 \quad \text{for} \quad \theta = \pi \tag{4b}$$

$$\Theta = 1 \quad \text{for} \quad R = 1 \tag{4c}$$

$$\Theta = 0 \quad \text{for} \quad R = \overline{R} \tag{4d}$$

Equation (4a) will be fulfilled if $C = D = C_k = D_k = 0$ for $k = 1, 2, 3\ldots$Now, application of Eq. (4b) gives $\lambda_k = k$. Substituting values of C, D, C_k, D_k, and λ_k in Eq. (3)

$$\Theta(R,\theta) = A + B\ln R + \sum_{k=1}^{\infty}(A_k R^k + B_k R^{-k})\cos(k\theta) \tag{5}$$

From Eq. (4c) and Eq. (5), $A = 1$, and $B_k = -A_k$. Now using value of A, and B_k in Eq. (5)

$$\Theta(R,\theta) = 1 + B\ln R + \sum_{k=1}^{\infty}A_k(R^k - R^{-k})\cos(k\theta) \tag{6}$$

Introducing new symbols $Y_1 = B$, $Y_2 = A_1$, $Y_3 = A_2$ and so on in Eq. (6)

$$\Theta(R,\theta) = 1 + Y_1\ln R + \sum_{k=2}^{\infty}Y_k(R^{(k-1)} - R^{-(k-1)})\cos[(k-1)\theta] \tag{7}$$

This is the temperature profile in the domain of the problem with Y_1, Y_2, $Y_3\ldots$ as the unknowns. Finally, the boundary condition in Eq. (4d) is applied in Eq. (7) to get

$$Y_1 \ln \bar{R} + \sum_{k=2}^{\infty} Y_k (\bar{R}^{(k-1)} - \bar{R}^{-(k-1)}) \cos[(k-1)\theta] = -1 \tag{8}$$

The expression given in Eq. (8) can not be evaluated explicitly due to the geometry of the outer periphery of the eccentric hollow prismatic cylinders with respect to the centre of the inner surface. So at this point, boundary collocation method is applied by truncation the infinite series in Eq. (8) to first M terms, and taking M number of collocation points on the boundary (outer surface) of the prismatic cylinders. This forms a system of M number of linear equations having M number of unknowns, given by

$$Y_1 \ln \bar{R} + \sum_{k=2}^{M} Y_k (\bar{R}^{(k-1)} - \bar{R}^{-(k-1)}) \cos[(k-1)\theta] = -1 \tag{9}$$

Eq. (9) on solving gives values of unknown constants Y_k. Now the non dimensional temperature profile of the eccentric hollow prismatic cylinders can be found from Eq. (7) using calculated values of Y_k. It may be noted that though some approximation is involved in this technique, the accuracy of prediction can be increased by increasing the number of the collocation points. This gives the temperature profile as

$$\Theta(R,\theta) = 1 + Y_1 \ln R + \sum_{k=2}^{N} Y_k (R^{(k-1)} - R^{-(k-1)}) \cos[(k-1)\theta] \tag{10}$$

3. Results and discussion

The expression for the temperature profile given in Eq. (10) is applicable to eccentric hollow prismatic cylinders with any number of sides N > 2. The value of $\bar{R}$ which is function of angle θ will vary with value of N for any angular position. So it is required to express $\bar{R}$ as function of angle θ for individual prismatic cylinder. Equation (10) can be used to find the shape factor of individual prismatic cylinder. The general form of the shape factor is given by:

$$S = \int_{\Gamma} (\partial\Theta / \partial n)\, d\Gamma = -2 \int_{0}^{\pi} (\partial\Theta / \partial R)\, R\, d\theta \tag{11}$$

For the present analysis from Eq. (10) and Eq. (11), the value of the conduction shape factor will be $S = -2\pi Y_1$. Thus, only the logarithmic term in Eq. (10) i.e. the coefficient Y_1 is only responsible for the magnitude of the conduction shape factor. The coefficients Y_k can be obtained from Eq. (9).

Eccentric annulus is a special case of eccentric hollow prismatic cylinders when the number of regular sides of the outer surface tends to infinity i.e. N →∞ (see Fig. 3 (a)). Carslaw and Jaeger [18] proposed an expression to predict the conduction shape factor of an eccentric annulus with isothermal boundaries, given by

$$S = \frac{2\pi}{\cosh^{-1}\left(\left(r_o^2 + r_i^2 - e^2\right) / 2 r_i r_o\right)} \tag{12}$$

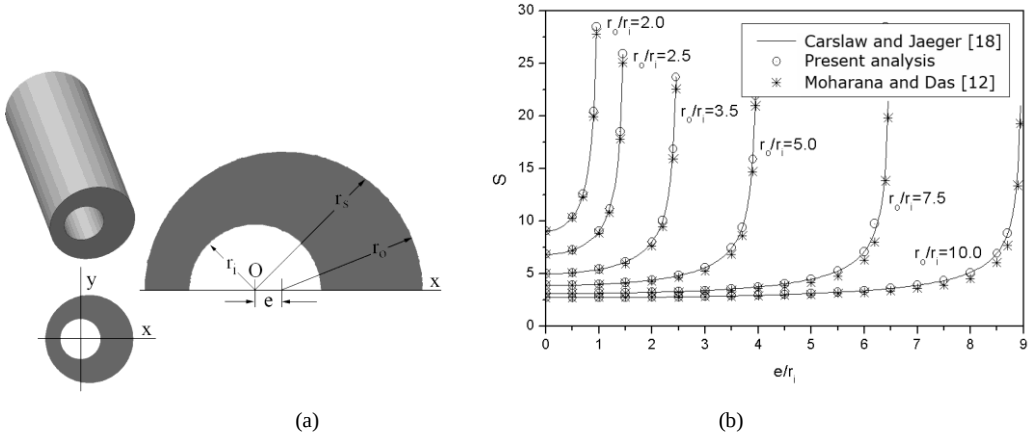

(a) (b)

Fig. 3. (a) schematic of an eccentric tube with eccentricity; (b) conduction shape factor in an eccentric circular cross-section.

where r_i, r_o, and e are inner radius, outer radius, and eccentricity between the centre of the inner and the outer surface respectively (see Fig. 3 (a)). The present analysis is validated by comparison with Eq. (12), which is presented in Fig. 3 (b). Moharana and Das [12] used a one dimensional approximate solution to predict the shape factor of an eccentric annulus, is also presented in Fig. 3 (b) for comparison. Figure 3 (b) presents the variation of conduction shape factor of an eccentric annulus as a function of e/r_i and r_o/r_i. For any value of r_o/r_i the conduction shape factor is increasing with increasing value of e/r_i, beyond a certain value of e/r_i the value of S increases sharply. Secondly, the value of S decreases with increase in value of r_o/r_i. It can be observed in Fig. 2 (b) that the prediction of S from the present analysis is in perfect agreement with that of Carslaw and Jaeger [18]. It can also be observed that the predictions by Moharana and Das [12] also give a close agreement with the existing analysis but only at lower value of e/r_i or higher value of r_o/r_i. As the value of e/r_i increasing or the value of r_o/r_i decreasing, the prediction by Moharana and Das [12] deviates from the value of present analysis. This is because the work by Moharana and Das [12] was based on one dimensional approximate analysis.

In all geometrical configurations discussed in this work, r_i is the radius of the inner circular surface, and r_o is the radius of the inscribed circle of the outer regular polygonal surface. A square cylinder with a concentric circular hole is a widely used geometry (see Fig. 4 (a)). Figure 4 (b) depicts a comparison of shape factor calculated using present investigation and the previous studies as discussed earlier. The predictions from the present analysis give a very close agreement with previous studies.

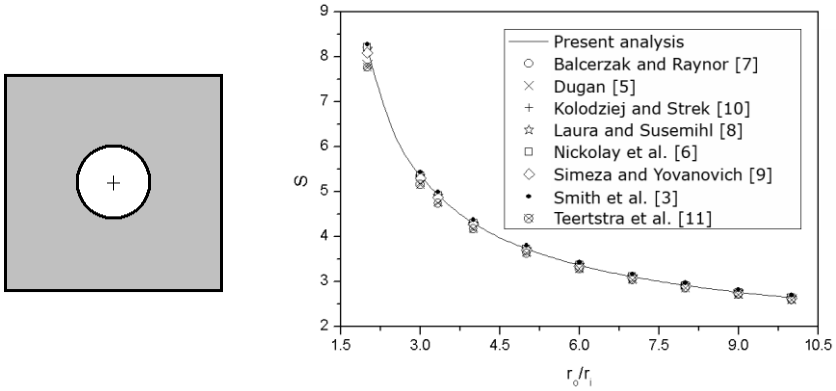

(a) (b)

Fig. 4. (a) square cylinder with a concentric circular hole; (b) its conduction shape factor as a function of r_i and r_o.

The position of the eccentric circular hole in any prismatic cylinder can lead to different orientations. In the present work only two orientations as shown in Fig. 5 are discussed for each prismatic cylinder. Figure 6 shows the temperature contour in a square cylinder where the inner circular hole is placed eccentrically in two geometric orientations as discussed in Fig. 5.

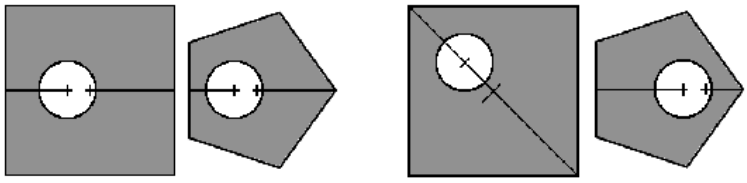

(a) (b)

Fig. 5. schematic of regular prismatic cylinders (square and pentagon) with an eccentric circular hole (a) Orientation-I; (b) Orientation-II.

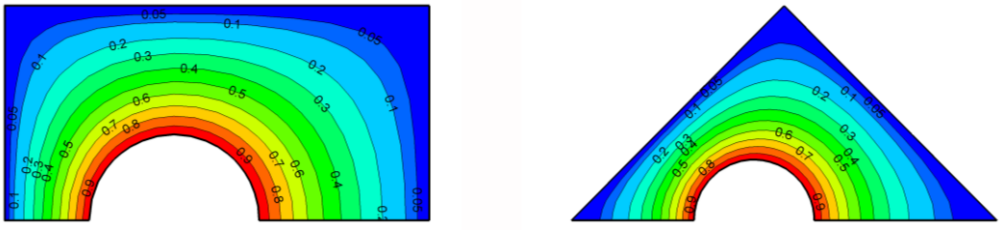

(a) (b)

Fig. 6. temperature contour of an eccentric square cylinder having $r_o/r_i = 2.5$, $e/r_i = 0.5$ (a) Orientation-I; (b) Orientation-II.

The predicted shape factor as a function of eccentricity ratio (e/r_i) and radius ratio (r_o/r_i) is given in Figs. 7 (a) and 7 (b) for an eccentric hollow regular pentagonal and hexagonal cylinder, respectively. The shape factor decreases with increasing radius ratio (r_o/r_i) and increases with increasing eccentricity ratio (e/r_i) of the circular hole. When e/r_i increases, the thermal resistance on one side of the duct decreases but on the opposite side it increases. The net thermal resistance decreases with increasing eccentricity. When the radius ratio increases always it leads to increase in thermal resistance; thus always the shape factor decreases. For every possible geometric configuration the shape factor for two orientation of the circular hole (i.e. orientation-I and II; see Fig. 5 for orientations) are depicted in Fig. 7. The shape factor for orientation-I and II remain almost equal up to certain value of eccentricity. With increasing eccentricity the shape factor for orientation-I increases more rapidly than for orientation-II for same value of eccentricity. For orientation-I the shape factor will approach towards infinity at $\overline{E} = \overline{D} - 1$. This is because when $\overline{E} = \overline{D} - 1$, the eccentric hole will tear off at one point, thus making thermal resistance equal to zero. For orientation-II, this situation will arise at a value of $\overline{E}$ higher than $\overline{D} - 1$. So for equal value of eccentricity the shape factor for orientation-II will be either always almost equal or less than the value for orientation-I depending on the value of eccentricity while the radius ratio is
constant. For any other orientation other than orientation-I and II the shape factor value will lie between the values for orientation-I and II. This is because the tear off distance for any orientation will lie between the tear off distance for orientation-I, and II.

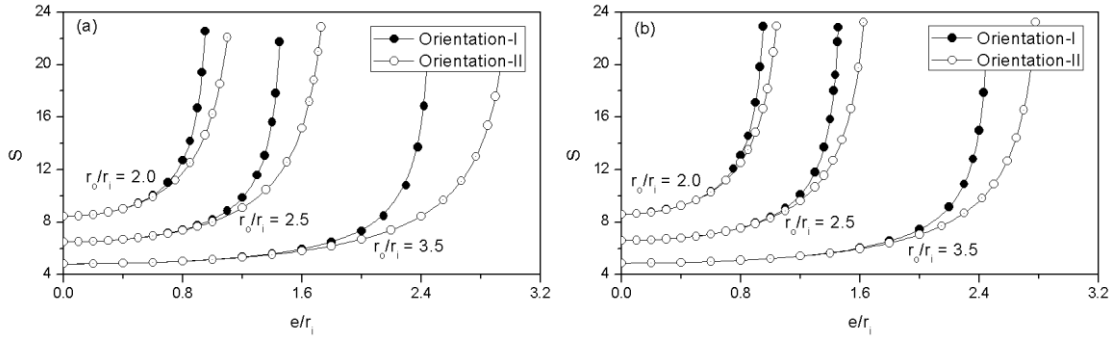

Fig. 7. conduction shape factor of regular polygonal cylinder with an eccentric circular hole (a) pentagonal; (b) hexagonal cylinder.

4. Summary and conclusion

In this work a two dimensional semi-analytical boundary collocation technique is used to predict the heat transfer in eccentric hollow prismatic cylinders. The temperature contour in the domain of the problem is predicted and the heat conduction is calculated. Based on the outcome of this method conduction shape factor of such geometries are calculated. The position of the eccentric hole in any prismatic cylinder can lead to different orientations. Two orientations are discussed. A comparison with existing one dimensional solution to this problem is carried out and found that the present technique can predict more accurately than the existing one dimensional approach.

References

[1] Holman, J.P., 1989. Heat Transfer, McGraw-Hill, New York.
[2] Incropera, F.P., DeWitt D.P., 2004. Fundamentals of Heat and Mass Transfer, 5th ed., Wiley & Sons, New York.
[3] Smith, J.C., Lind, J.E., Lermond, D.S., 1958. Shape Factors for Conductive Heat Flow, AIChE Journal 4, p. 330.
[4] Shih, F.S., 1970. On the Temperature Field of a Square Column Embedding a Heating Cylinder, AIChE Journal 16, p. 134.
[5] Dugan, J.P., 1972. On the Shape Factor for a Hollow, Square Cylinder, AIChE Journal 18, p. 1082.
[6] Nickolay, M., Fischer, L., Martin, H., 1998. Shape Factors for Conductive Heat Flow in Circular and Quadratic Cross-sections, International Journal of Heat and Mass Transfer 41, p. 1437.
[7] Balcerzak, M.J., Raynor, S., 1961. Steady State Temperature Distribution and Heat Flow in Prismatic Bars with Isothermal Boundary Conditions, International Journal of Heat and Mass Transfer 41, p. 1437.
[8] Laura, P.A., Susemihl, E.A., 1973. Determination of Heat Flow Shape Factors for Hollow, Regular Polygonal Prisms, Nuclear Engineering and Design 25, p. 409.
[9] Simeza, L.M., Yovanovich, M.M., 1987. Shape Factors for Hollow Prismatic Cylinders Bounded by Isothermal Inner Circles and Outer Regular Polygons, International Journal of Heat and Mass Transfer 30, p. 812.
[10] Kolodziej, J.A., Strek, T., 2001. Analytical Approximations of the Shape Factors for Conductive Heat Flow in Circular and Regular Polygonal Cross-sections, International Journal of Heat and Mass Transfer 44, p. 999.
[11] Teertstra, P.M., Yovanovich, M.M., Culham, J.R., 2009. Conduction Shape Factor Models for Hollow Cylinders with Nonuniform Gap Spacing, Journal of Thermophysics and Heat Transfer 23, p. 28.

[12] Moharana, M.K., Das, P.K., 2011. Heat Conduction Through Ecentric Polygonal Tubes: Solution by One Dimensional Approach, Proc 10th ISHMT-ASME Heat and Mass Transfer Conference, Dec 27-30, IIT Madras, India.
[13] Kolodziej, J.A., 1987. Review of Application of Boundary Collocation Method in Mechanics of Continuous Media, Solid Mechanics Archives 12, P. 187.
[14] Kolodziej, J.A., Zielinski A.P., 2009. Boundary Collocation Techniques and Their Application in Engineering, WIT press, Boston.
[15] Kucaba-Pietal, A., 2000. Application of Boundary Collocation Method in Fluid Mechanics, Second conference on Numerical analysis and applications. University of Rousse, Rousse, Bulgaria.
[16] Abou-Dina, M.S., 2002. Implementation of Trefftz Method for the Solution of Some Elliptic Boundary Value Problems, Applied Mathematics and Computation 127, P. 125.
[17] Moharana, M.K, Das, P.K. 2008. Heat Conduction Through Heat Exchanger Tubes of Noncircular Cross Section, Journal of Heat Transfer 130, p. 1.
[18] Carslaw, H.S., Jaeger, J.C., 1954. Conduction of Heat in Solids. Oxford Science Publication.

Available online at www.sciencedirect.com

SciVerse ScienceDirect

Procedia Engineering 00 (2012) 000–000

Procedia Engineering

www.elsevier.com/locate/procedia

5th BSME International Conference on Thermal Engineering

Effect of Prandtl Number on Free Convection in a Solar Collector Filled with Nanofluid

Rehena Nasrin*, Salma Parvin and M. A. Alim

Department of Mathematics, Bangladesh University of Engineering & Technology,Dhaka-1000, Bangladesh

Abstract

Numerical study of the influence of Prandtl number on free convection flow phenomena in a solar collector having glass cover plate and sinusoidal absorber is done. The working fluid is water-Al_2O_3 nanofluid. The cover plate has initially constant temperature T_h, while bottom absorber is at temperature T_c, with $T_h > T_c$. The remaining walls are considered adiabatic. By Penalty Finite Element Method the governing differential equations with boundary conditions are solved. The effect of the Prandtl number on the flow pattern and heat transfer has been depicted. Comprehensive average Nusselt number, average temperature and mean velocity inside the collector are presented as a function of the governing parameter mentioned above. The highest *Pr* causes the greatest heat transfer. The enhancing performance of heat transfer rate is more effective for the water-Al_2O_3 nanofluid than the base fluid.

Keywords: Water-Al_2O_3 nanofluid; solar collector; Prandtl number; finite element method.

1. Introduction

Because of the desirable environmental and safety aspects it is widely believed that solar energy should be utilized instead of other alternative energy forms, even when the costs involved are slightly higher. The flat-plate solar collector is commonly used today for the collection of low temperature solar thermal energy. Solar collectors are key elements in many applications, such as building heating systems, solar drying devices, etc. Solar energy has the greatest potential of all the sources of renewable energy especially when other sources in the country have depleted. The fluids with solid-sized nanoparticles suspended in them are called "nanofluids." The natural convection in enclosures continues to be a very active area of research during the past few decades. Applications of nanoparticles in thermal field are to **e**nhance heat transfer from solar collectors to storage tanks, to improve efficiency of coolants in transformers.

Conventional analysis and design of solar collector is based on a one-dimensional conduction equation formulation [1]. The analysis has been substantially assisted by the derivation of plate-fin efficiency factors. The factors relate the design and operating conditions of the collector in a systematic manner that facilitates prediction of heat collection rates at the design stage. The one-dimensional analysis offers a desired accuracy required in a routine analysis even though a two-dimensional temperature distribution exists over the absorber plate of the collector. Therefore, for more accurate analysis at low mass flow rates, a two-dimensional temperature distribution must be considered. Various investigators have used two dimensional conduction equations in their analysis with different boundary conditions.

* Corresponding author. Tel: +8801913583407
E-mail address: rehena@math.buet.ac.bd

Nag et al. [2] used the two-dimensional model proposed by Lund, but with convection boundary condition at the upper and lower edge of the absorber plate. They solved the governing equations using finite element method. They concluded that the isotherms deviated from a one-dimensional pattern for a high flow rate to a predominantly two-dimensional distribution for a low mass flow rate. Stasiek [3] made experimental studies of heat transfer and fluid flow across corrugated and undulated heat exchanger surfaces. Piao et al. [4] investigated experimentally natural, forced and mixed convective heat transfer in a cross-corrugated channel solar air heater. Detailed experimental and numerical studies on the performance of the solar air heater were made by Gao [5].

There are so many methods introduced to increase the efficiency of the solar water heater [6–9]. But the novel approach is to introduce the nanofluids in solar water heater instead of conventional heat transfer fluids (like water). The poor heat transfer properties of these conventional fluids compared to most solids are the primary obstacle to the high compactness and effectiveness of the system. The essential initiative is to seek the solid particles having thermal conductivity of several hundred times higher than those of conventional fluids. These early studies, however, used suspensions of millimeter- or micrometer-sized particles, which, although showed some enhancement, experienced problems such as poor suspension stability and hence channel clogging, which are particularly serious for systems using mini sized and micro sized particles. The suspended metallic or nonmetallic nanoparticles change the transport properties and heat transfer characteristics of the base fluid. Stability and thermal conductivity characteristics of nanofluids was performed by Hwang et al. [10]. In this study, they concluded that the thermal conductivity of ethylene glycol was increased by 30%.

The absorptance of the collector surface for shortwave solar radiation depends on the nature and colour of the coating and on the incident angle. Usually black colour is used. Various colour coatings had been proposed in [11–13] mainly for aesthetic reasons. A low-cost mechanically manufactured selective solar absorber surface method had been proposed by Konttinen et al. [14]. These are usually low-cost units which can offer cost effective solar thermal energy in applications such as water preheating for domestic or industrial use, heating of swimming pools, space heating and air heating for industrial or agricultural applications. The principal requirement of the solar collector is a large contact area between the absorbing surface and the air.

In this paper, we investigate numerically the natural convection inside the solar collector having the flat-plate cover and wavelike absorber. The objective of this paper is to present flow and heat transfer used to harness solar energy.

Nomenclature

A_m	Dimensionless amplitude of wave
C_p	Specific heat at constant pressure (kJ kg^{-1} K^{-1})
g	Gravitational acceleration (m s^{-2})
h	Local heat transfer coefficient (W m^{-2} K^{-1})
k	Thermal conductivity (W m^{-1} K^{-1})
L	Length of the solar collector (m)
Nu	Nusselt number, $Nu = hL/k_f$
Pr	Prandtl number
Ra	Rayleigh number
T	Dimensional temperature (^{o}K)
T_i	Initial temperature of nanofluid (^{o}K)
u, v	Dimensional x and y components of velocity (m s^{-1})
U, V	Dimensionless velocities
X, Y	Dimensionless coordinates
x, y	Dimensional coordinates (m)

Greek Symbols

α	Fluid thermal diffusivity (m^2 s^{-1})
β	Thermal expansion coefficient (K^{-1})
ε	Emissivity
ϕ	Nanoparticles volume fraction
ν	Kinematic viscosity (m^2 s^{-1})
θ	Dimensionless temperature
ρ	Density (kg m^{-3})
λ	Number of wave
μ	Dynamic viscosity (N s m^{-2})

σ Stefan Boltzmann constant

ω Dimensionless velocity field

Subscripts

av average
c cold
f fluid
h hot
nf nanofluid
s solid particle
w top wall

2. Problem Formulation

Fig. 1 shows a schematic diagram of a solar collector. The fluid in the collector is water-based nanofluid containing Al_2O_3 nanoparticles. The nanofluid is assumed incompressible and the flow is considered to be laminar. It is taken that water and nanoparticles are in thermal equilibrium and no slip occurs between them. The solar collector is a metal box with a cover on top and a dark colored wavelike absorber plate on the bottom. The top horizontal wall has initially constant temperature T_h, while bottom sinusoidal wall is at temperature T_c, with $T_h > T_c$. The two vertical walls are considered adiabatic. The thermophysical properties of the nanofluid are taken from Lin and Violi [15] and given in Table 1. The density of the nanofluid is approximated by the Boussinesq model. Only steady state case is considered.

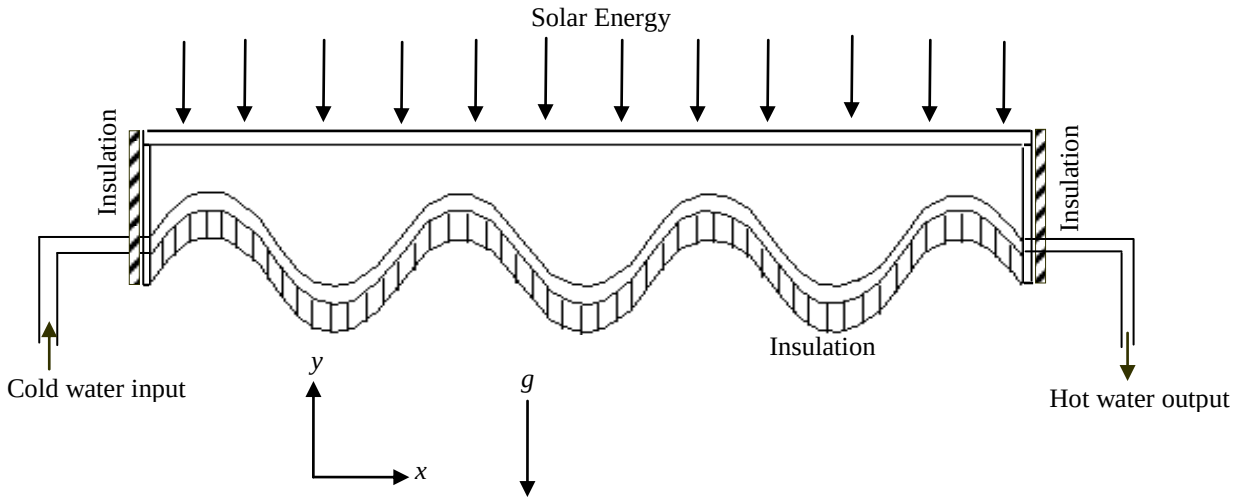

Fig.1. Schematic diagram of the Solar Collector

The governing equations for laminar natural convection in a solar collector filled with water-alumina nanofluid in terms of the Navier-Stokes and energy equation (dimensional form) are given as:
Continuity equation:

$$\frac{\partial u}{\partial x}+\frac{\partial v}{\partial y}=0 \qquad (1)$$

x-momentum equation:

$$\rho_{nf}\left(u\frac{\partial u}{\partial x}+v\frac{\partial u}{\partial y}\right)=-\frac{\partial p}{\partial x}+\mu_{nf}\left(\frac{\partial^2 u}{\partial x^2}+\frac{\partial^2 u}{\partial y^2}\right) \qquad (2)$$

y-momentum equation:

$$\rho_{nf}\left(u\frac{\partial v}{\partial x}+v\frac{\partial v}{\partial y}\right)=-\frac{\partial p}{\partial y}+\mu_{nf}\left(\frac{\partial^2 v}{\partial x^2}+\frac{\partial^2 v}{\partial y^2}\right)+g\rho_{nf}\beta_{nf}(T-T_c) \quad (3)$$

Energy equation:

$$u\frac{\partial T}{\partial x}+v\frac{\partial T}{\partial y}=\alpha_{nf}\left(\frac{\partial^2 T}{\partial x^2}+\frac{\partial^2 T}{\partial y^2}\right) \quad (4)$$

where, $\rho_{nf}=(1-\phi)\rho_f+\phi\rho_s$ is the density,

$(\rho C_p)_{nf}=(1-\phi)(\rho C_p)_f+\phi(\rho C_p)_s$ is the heat capacitance,

$\beta_{nf}=(1-\phi)\beta_f+\phi\beta_s$ is the thermal expansion coefficient,

$\alpha_{nf}=k_{nf}/(\rho C_p)_{nf}$ is the thermal diffusivity,

the dynamic viscosity of Brinkman model [16] is $\mu_{nf}=\mu_f(1-\phi)^{-2.5}$

and the thermal conductivity of Maxwell Garnett (MG) model [17] is $k_{nf}=k_f\dfrac{k_s+2k_f-2\phi(k_f-k_s)}{k_s+2k_f+\phi(k_f-k_s)}$.

Radiation heat transfer by the top glass cover surface must account for thermal radiation which can be absorbed, reflected, or transmitted. This decomposition can be expressed by,

$$q_{net}=q_{absorbed}+q_{transmitted}+q_{reflected}$$

Outside the boundary layer, the amount of energy $q_{reflected}$ is neglected.

Thus total energy of the glass cover plate becomes $q_{net}=q_{absorbed}+q_{transmitted}$

Now the amount of transmitted energy is radiated from the cover plate to the bottom wavy absorber without any medium as:

$$q_{transmitted}=q_r=\varepsilon\sigma A\left(T_w{}^4-T_c^4\right)$$

Here ε is emissivity of the glass cover plate, σ is Stefan Boltzmann constant 5.670400 x 10^{-8} $Js^{-1}m^{-2}K^{-4}$ and T_w is the variable temperature of the top wall. Again, the amount of absorbed energy is transferred from cover plate to bottom absorber by natural convection where medium is nanofluid as:

$$q_{absorbed}=q_c=hA(T_w-T_i)$$

So total energy gained or loosed by the cover plate is $q_{net}=hA(T_w-T_i)+\varepsilon\sigma A\left(T_w{}^4-T_c^4\right)$

The boundary conditions are:

at all solid boundaries $u = v = 0$

at the top cover plate $q=hA(T_w-T_i)+\varepsilon\sigma A\left(T_w{}^4-T_c^4\right)$

at the vertical walls $\dfrac{\partial T}{\partial x}=0$

at the bottom wavy absorber $T = T_c$

The above equations are non-dimensionalized by using the following dimensionless dependent and independent variables:

$$X=\frac{x}{L},\quad Y=\frac{y}{L},\quad U=\frac{uL}{\nu_f},\quad V=\frac{vL}{\nu_f},\quad P=\frac{pL^2}{\rho_f\nu_f{}^2},\theta=\frac{T-T_c}{T_h-T_c}$$

Then the non-dimensional governing equations are

$$\frac{\partial U}{\partial X}+\frac{\partial V}{\partial Y}=0 \quad (5)$$

$$U\frac{\partial U}{\partial X}+V\frac{\partial U}{\partial Y}=-\frac{\rho_f}{\rho_{nf}}\frac{\partial P}{\partial X}+Pr\frac{\nu_{nf}}{\nu_f}\left(\frac{\partial^2 U}{\partial X^2}+\frac{\partial^2 U}{\partial Y^2}\right) \quad (6)$$

$$U\frac{\partial V}{\partial X}+V\frac{\partial V}{\partial Y}=-\frac{\rho_f}{\rho_{nf}}\frac{\partial P}{\partial Y}+Pr\frac{\nu_{nf}}{\nu_f}\left(\frac{\partial^2 V}{\partial X^2}+\frac{\partial^2 V}{\partial Y^2}\right)+Ra\,Pr\frac{(1-\phi)\rho_f\beta_f+\phi\rho_s\beta_s}{\rho_{nf}\beta_f}\theta \quad (7)$$

$$U\frac{\partial \theta}{\partial X}+V\frac{\partial \theta}{\partial Y}=\frac{1}{Pr}\left(\frac{\partial^2 \theta}{\partial X^2}+\frac{\partial^2 \theta}{\partial Y^2}\right) \quad (8)$$

where $Pr=\frac{\nu_f}{\alpha_f}$ is the Prandtl number, $Ra=\frac{g\beta_f L^3(T_h-T_c)}{\nu_f^2}$ is the Rayleigh number.

The corresponding boundary conditions take the following form:
at all solid boundaries $U = V = 0$
at the vertical walls $\frac{\partial \theta}{\partial X}=0$
at the bottom wavy absorber $\theta = 0$

2.1. Average Nusselt number

The average Nusselt number (*Nu*) is expected to depend on a number of factors such as thermal conductivity, heat capacitance, viscosity, flow structure of nanofluids, volume fraction, dimensions and fractal distributions of nanoparticles.

The local variation of the convective Nusselt number of the fluid at the top cover plate is $\overline{Nu_c}=-\frac{k_{nf}}{k_f}\frac{\partial T}{\partial x}$.

The non-dimensional form of local convective heat transfer is $\overline{Nu_c}=-\frac{k_{nf}}{k_f}\frac{\partial \theta}{\partial X}$.

By integrating the local Nusselt number over the top heated surface, the average convective heat transfer along the heated wall of the collector is used by Saleh et al. [18] as $Nu_c=\int_0^1 \overline{Nu_c}\,dX$.

The radiated heat transfer rate is expressed as $Nu_r=\int_0^1 q_r\,dX$.

The average Nusselt number is $Nu = Nu_c + Nu_r$

The mean bulk temperature and average sub domain velocity of the fluid inside the collector may be written as $\theta_{av}=\int\theta\,d\bar{V}/\bar{V}$ and $\omega_{av}=\int\omega\,d\bar{V}/\bar{V}$, where $\bar{V}$ is the volume of the collector.

3. Numerical Implementation

The Galerkin finite element method [19, 20] is used to solve the non-dimensional governing equations along with boundary conditions for the considered problem. The equation of continuity has been used as a constraint due to mass conservation and this restriction may be used to find the pressure distribution. The finite element method is used to solve the Eqs. (6) - (8), where the pressure *P* is eliminated by a constraint. The continuity equation is automatically fulfilled for large values of this constraint. Then the velocity components (*U, V*) and temperature (θ) are expanded using a basis set. The Galerkin finite element technique yields the subsequent nonlinear residual equations. Three points Gaussian quadrature is used to evaluate the integrals in these equations. The non-linear residual equations are solved using Newton–Raphson method to determine the coefficients of the expansions. The convergence of solutions is assumed when the relative error for each variable between consecutive iterations is recorded below the convergence criterion such that $\left|\psi^{n+1}-\psi^{n}\right|\le 10^{-4}$, where *n* is the number of iteration and Ψ is a function of *U*, *V* and θ.

3.1. Mesh Generation

In the finite element method, the mesh generation is the technique to subdivide a domain into a set of sub-domains, called finite elements, control volume, etc. The discrete locations are defined by the numerical grid, at which the variables

are to be calculated. It is basically a discrete representation of the geometric domain on which the problem is to be solved. The computational domains with irregular geometries by a collection of finite elements make the method a valuable practical tool for the solution of boundary value problems arising in various fields of engineering. Fig. 2 displays the finite element mesh of the present physical domain.

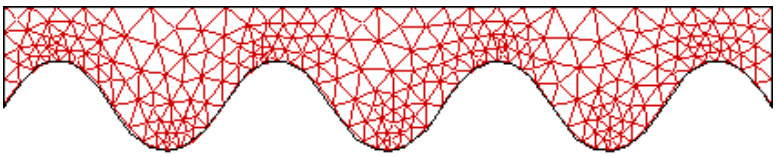

Fig. 2: Mesh generation of the collector

3.2. Grid Independent Test

An extensive mesh testing procedure is conducted to guarantee a grid-independent solution for $Ra = 10^4$and $Pr = 1.73$ in a solar collector. In the present work, we examine five different non-uniform grid systems with the following number of elements within the resolution field: 2969, 5130, 6916, 9057 and 11426. The numerical scheme is carried out for highly precise key in the average convective and radiated Nusselt numbers namely Nu_c and Nu_r for the aforesaid elements to develop an understanding of the grid fineness as shown in Table 2 and Fig. 3. The scale of the average Nusselt and Sherwood numbers for 9057 elements shows a little difference with the results obtained for the other elements. Hence, considering the non-uniform grid system of 9057 elements is preferred for the computation.

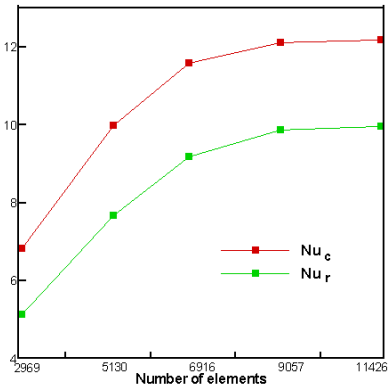

Fig. 3: Grid test for the geometry

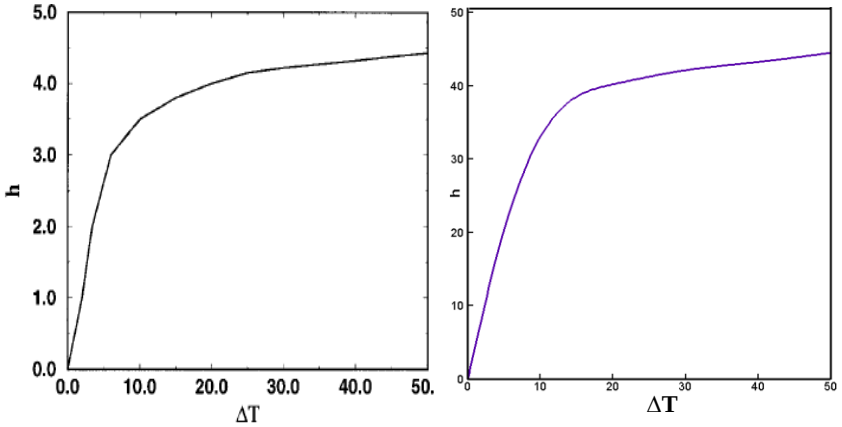

Gao et al. [21] Present Work

Fig. 4: Comparison of present code with Gao et al. [21] with $Pr = 0.73$ and $Ra = 10^4$

3.3. Code Validation

The present numerical solution is validated by comparing the current code results for heat transfer - temperature difference profile at Pr = 0.73, $Gr = 10^4$ with the graphical representation of Gao et al. [21] which was reported for heat transfer augmentation inside a channel between the flat-plate cover and sine-wave absorber of a cross-corrugated solar air heater. Fig. 4 demonstrates the above stated comparison. As shown in Fig. 4, the numerical solutions (present work and Gao et al. [21]) are in good agreement.

4. Results and Discussion

In this section, numerical results of streamlines and isotherms for various values of Prandtl number (Pr) with Al_2O_3 /water nanofluid in a solar collector are displayed. The considered values of Pr are Pr (= 1.73, 2.45, 3.77 and 6.62) while the Rayleigh number $Ra = 10^4$, the solid volume fraction ϕ = 5%, the emissivity ε = 0.9, the wave amplitude of bottom surface A_m = 0.075 and number of wave λ = 3.5. In addition, the values of the average Nusselt number both for convection and radiation as well as mean bulk temperature and average sub domain velocity profile are shown graphically.

Fig. 5 (a)–(b) exposes the heat transfer and fluid flow for various Prandtl number Pr (= 1.73-6.62). In this figure we observe that as the Prandtl number enhances from 1.73 to 6.62, the isothermal contours tend to get affected considerably. In addition, these lines corresponding to Pr = 6.62 become less bended whereas initially (Pr = 1.73) the lines take sinusoidal wavelike form. The isotherms cover the whole region of the solar collector due to comparatively higher temperature of the working water-Al_2O_3 nanofluid at the lowest Pr where the contour lines mimic the wall's (absorber) profile. Rising Prandtl number leads to deformation of the thermal boundary layer at the cold wavy absorber. However, the increase in the thermal gradients at the upper horizontal wall is much higher for the considered nanofluid than for the clear water. This means that higher heat transfer rate is predicted by the nanofluid than the base fluid (water). The fluid flow covers the entire collector at the lowest Pr forming few eddies. The streamlines have no significant change due to rising Pr except the core of the vortices becomes slightly smaller. This is expected because highly viscous fluid having larger Prandtl number does not move freely.

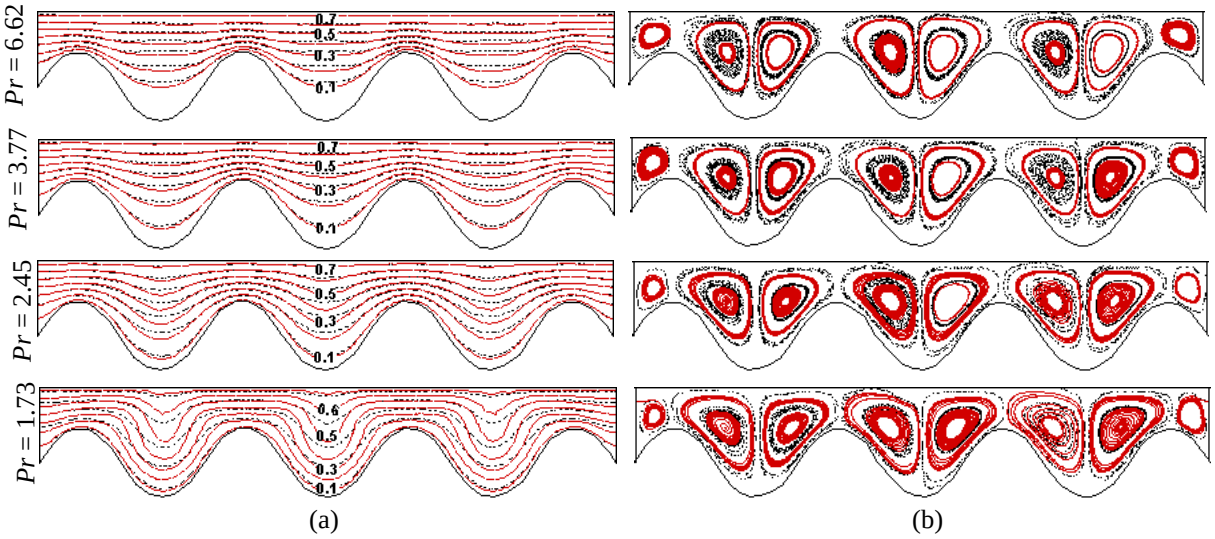

Fig. 5: Effect of Pr on (a) Isotherms and (b) Streamlines at $Ra = 10^4$ (solid lines for nanofluid and dashed lines for base fluid)

Fig. 6(i)-(iii) displays the Nu_c, Nu_r, θ_{av} and ω_{av} for the effect of Prandtl number Pr. Mounting Pr enhances average Nusselt number for both convection and radiation. From Fig. 6 (i), it is found that, rate of convective heat transfer enhances by 26% and 18% for nanofluid and base fluid respectively whereas this rate for radiation is 8% with the increasing values of Pr from 1.73 to 6.62. On the other hand, θ_{av} devalues due to the variation of Pr as temperature of fluid grows down with growing Pr. ω_{av} has notable changes with different values of Prandtl number.

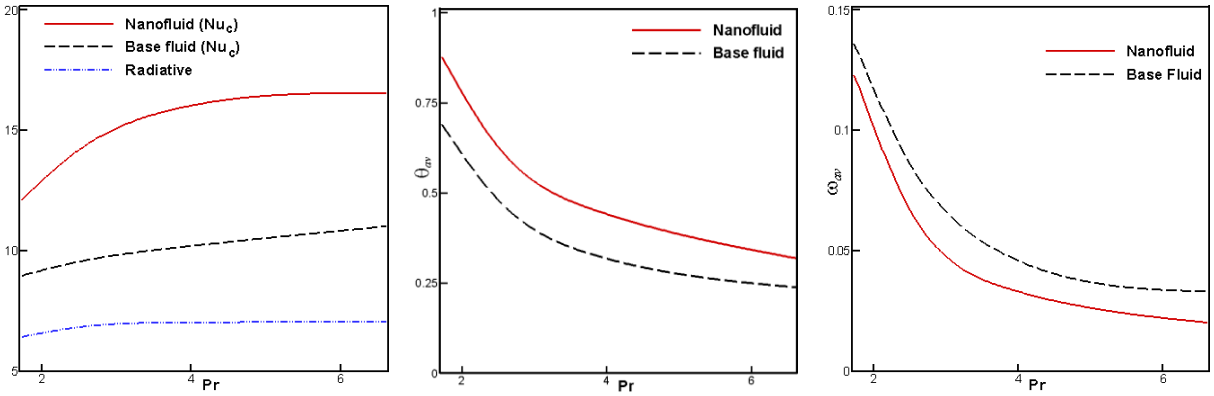

(i) (ii) (iii)

Fig. 6: Effect of *Pr* on (i) *Nu* (ii) θ_{av} and (iii) ω_{av} at $Ra = 10^4$

5. Conclusion

The influence of Prandtl number on natural convection boundary layer flow inside a solar collector with water-Al_2O_3 nanofluid is accounted. Various Prandtl number have been considered for the flow and temperature fields as well as the convective and radiated heat transfer rates, mean bulk temperature of the fluids and average velocity field in the collector while *Ra*, ϕ and ε are fixed at 10^4, 5% and 0.9 respectively. The results of the numerical analysis lead to the following conclusions:

- The structure of the fluid streamlines and isotherms within the solar collector is found to significantly depend upon the *Pr*.
- The Al_2O_3 nanoparticles with the highest *Pr* is established to be most effective in enhancing performance of heat transfer rate than base fluid.
- Average heat transfer is obtained higher for convection than radiation.
- Mean temperature diminishes for both fluids with rising mentioned parameter.
- Average velocity field increases due to falling *Pr*.

Overall the analysis also defines the operating range where water-Al_2O_3 nanofluid can be considered effectively in determining the level of heat transfer augmentation.

Acknowledgement

The work is supported by the department of Mathematics, Bangladesh University of Engineering & Technology.

References

[1] Sukhatme SP. Solar energy, principles of thermal collection and storage. New Delhi, Tata McGraw-Hill, 1991.

[2] Nag A, Misra D, De KE, Bhattacharya A, Saha SK. Parametric study of parallel flow flat plate solar collector using finite element method, In: Numerical Methods in Thermal Problems. Proceedings of the 6th International Conference, Swansea, UK, 1989.

[3] Stasiek JA. Experimental studies of heat transfer and fluid flow across corrugated-undulated heat exchanger surfaces. Int. J. Heat Mass Transfer 1998; 41: 899-914.

[4] Piao Y, Hauptmann EG, Iqbal M. Forced convective heat transfer in cross-corrugated solar air heaters. ASME Journal of Solar Energy Engineering 1994; 116: 212-214.

[5] Gao W. Analysis and performance of a solar air heater with cross corrugated absorber and back-plate. MS thesis, Yunnan Normal University, Kunming, 1996.

[6] Ho CD, Chen TC. The recycle effect on the collector efficiency improvement of double-pass sheet-and-tube solar water heaters with external recycle. Renewable Energy 2006; 31: 953–97.

[7] Hussain A. The performance of a cylindrical solar water heater. Renewable Energy 2006; 31: 1751–1763.

[8] Xiaowu W, Hua B. Energy analysis of domestic-scale solar water heaters. Renewable Sustainable Energy Rev. 2005; 9: 638–645.

[9] Xuesheng W, Ruzhu W, Jingyi W. Experimental investigation of a new-style double-tube heat exchanger for heating crude oil using solar hot water. Appllied Therm. Eng. 2005; 25: 1753–1763.

[10] Hwang Y, Lee JK, Lee CH, Jung YM, Cheong SI, Lee CG, Ku BC, Jang SP. Stability and thermal conductivity characteristics of nanofluids. Thermochimica Acta. 2007; 455: 70–74.

[11] Tripanagnostopoulos Y, Souliotis M, Nousia Th. Solar collectors with colored absorbers. Solar Energy. 2000; 68: 343–356.

[12] Wazwaz J, Salmi H, Hallak R. Solar thermal performance of a nickel-pigmented aluminium oxide selective absorber. Renewable Energy. 2002; 27: 277–292

[13] Orel ZC, Gunde MK, Hutchins MG. Spectrally selective solar absorbers in different non-black colours. Proceedings of WREC VII, Cologne on CD-ROM, 2002.

[14] Konttinen P, Lund PD, Kilpi RJ. Mechanically manufactured selective solar absorber surfaces. Solar Energy Mater Solar Cells. 2003; 79: 273–283.

[15] Lin, KC, Violi, A. Natural convection heat transfer of nanofluids in a vertical cavity: Effects of non-uniform particle diameter and temperature on thermal conductivity. International Journal of Heat and Fluid Flow. 2010; 31: 236–245.

[16] Brinkman, HC. The viscosity of concentrated suspensions and solution. J. Chem. Phys. 1952; 20: 571–581.

[17] Maxwell-Garnett, JC. Colours in metal glasses and in metallic films. Philos. Trans. Roy. Soc. A. 1904; 203: 385–420.

[18] Saleh, H., Roslan, R., Hashim, I. Natural convection heat transfer in a nanofluid-filled trapezoidal enclosure. International Journal of Heat and Mass Transfer. 2011; 54: 194–201.

[19] Taylor, C., Hood, P. A numerical solution of the Navier-Stokes equations using finite element technique. Computer and Fluids. 1973; 1: 73–89.

[20] Dechaumphai, P. Finite Element Method in Engineering, 2nd ed., Chulalongkorn University Press, Bangkok, 1999.

[21] Gao, W., Lin, W., Lu, E. Numerical study on natural convection inside the channel between the flat-plate cover and sine-wave absorber of a cross-corrugated solar air heater. Energy Conversion & Management. 2000; 41: 145-151.

Available online at www.sciencedirect.com

SciVerse ScienceDirect

Procedia Engineering 00 (2012) 000–000

Procedia Engineering

www.elsevier.com/locate/procedia

5th BSME International Conference on Thermal Engineering

Micro-scale Multi-effect Distillation System for Low Steam Inputs

P. V. Sen, Bhuwanesh K., Ashutosh K., Z. Engineer, S. Hegde, P.K. Sen*, R. Lal

Department of Applied Mechanics, Indian Institute of Technology Delhi, New Delhi 110016, India

Abstract

Distillation can remove all types of contaminants at any concentration level. In this phase change method the feed water is evaporated into steam using a heat source. The vapor formed leaves behind all contaminants in the feed water. The steam led to a condenser gives premium quality water with Total Dissolve Solids (TDS) less than 10 ppm. Generation of 1 kg of steam takes about 1kWh of energy making it energy and cost intensive. Recycling of latent heat of vaporization by Multi-Effect Distillation (MED) makes the process economical. The challenge is to develop small scale MED units for applications in rural areas. The paper describes a Micro Scale MED (MSMED) designed specifically for a low heat source where amount of steam generated is low as with small solar energy collectors. An earlier MED design by some of the present authors, comprising vertical tube evaporators, condenser and water reservoir was optimized for MSMED to work with about 3 kg input of steam at 1.5 bar, which can be generated by a solar concentrator of area 6 m^2. Using 3 effects and a condenser the MSMED was able to produce 11 to 12 liters of water per hour. The Gained Output Ratio (GOR) was 3.6 and the heat recovery at every effect was high. The TDS of the distilled water was reduced from an initial value of 748 to less than 10 ppm..

Keywords: Multi-effect distillation; recycling latent heat; total dissolved solids; drinking water preparation.

Nomenclature

A	area of cross section of heat transfer
D	water flow rate
H_{fg}	latent heat of vaporization
M_d	rate of condensation
U	overall heat transfer coefficient
ΔT	temperature difference

1. Introduction

High level of water pollution due to industrial activities, growth of population and increasing requirement of water for the agricultural sector has led to rampant pollution of water sources. In many areas natural salinity of water is the issue. Distillation can remove all types of contaminants at any concentration level. In this phase change method the feed water is evaporated into steam using a heat source. The vapors so formed leave behind all contaminants in the feed water. Condensation of these vapors gives premium quality water, with total dissolved solids (TDS) as low as 10 parts per million (ppm). Energy required for distillation is independent of concentration level of impurities in feed water. The major drawback with the distillation process is the high initial energy input. It takes about 1 kWh of energy to produce 1 kg of

* Corresponding Author. Tel: +91-11-26591179; Fax: +91-11-26581119
E-mail address: pksen@am.iitd.ernet.in

steam or equivalent amount of distilled water. Recycling of latent heat of vaporization several times, as in multi effect distillation, makes the process more economical. The efficiency of heat recycling in distillation is expressed in terms of the Gained Output Ratio (GOR).

In our earlier work a Small scale MED (SMED) was designed with vertical tube evaporators to handle 30 Kg/hr of steam generated by a boiler. If steam is produced using solar energy, expenditure on fuel can be saved. Considering that a Fresnel mirror collector of 6 m^2 can give about 3 kg/hr of steam, a Micro Scale MED (MSMED) was designed for working at this level of steam output. In this paper the fabrication and parametric studies on this system are presented.

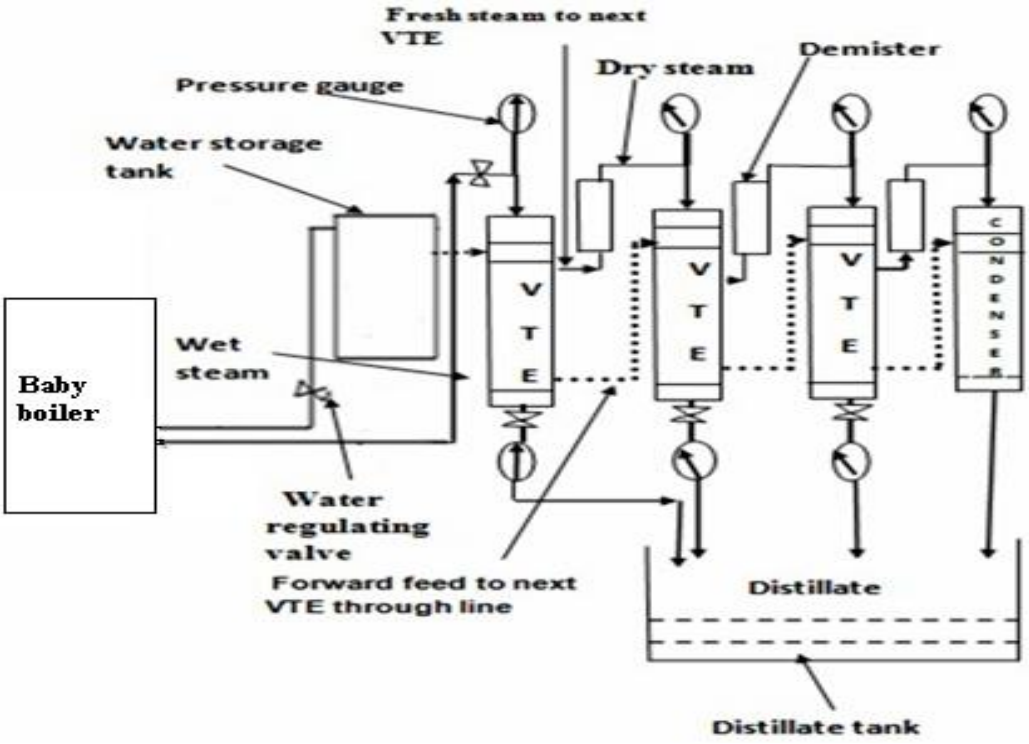

Fig. 1. Schematic diagram of Micro Scale MED

2. Design and Fabrication of MSMED system

The main components of the system as shown in Fig. 1, are vertical tube evaporators (VTEs), condenser, mist eliminators or feed entrainment separators, distillate withdrawal capillaries, forward feed and brine transferring capillaries, pump and other peripherals. The unit is insulated to minimize heat loss to the surroundings [1-2]. Primary steam from a baby boiler or a solar energy source is fed to the tube-side of the first VTE and this gets condensed by transferring its latent heat of condensation to the evaporating feed water on the shell-side. The fresh steam formed on the shell side of this VTE carries brine mist along with it. To remove the mist, it is passed through an inter-effect mist separator before being fed to the next effect and the process is repeated. Due to cyclonic effect heavier water particles settle down in the mist separator and steam moves upward due to lower density. The steam is further dewetted using de-mister screens. The steam generated in the last effect is condensed in a falling feed water film condenser. This liquid-film is actually the feed water (to be decontaminated) which is preheated in the process. The distillate and brine are withdrawn using capillaries, having diameters of 4.5 mm or less. The feed water progress is simplest if it passes from effect one to effect two, to effect three, and so on, as in these circumstances the feed will flow without pumping. This “forward feed” arrangement also helps in conservation of energy. Fresh brine from water storage tank is used for cooling the condenser and returned to the tank. In this way all vapours get condensed in the condenser. In our earlier work on a Small scale MED (SMED) each VTE had seven fluted aluminum tubes of calculated length and diameter designed for condensing ≈ 20 – 30 kg steam at 1.5 bar. Thus ≈ 3 – 5 kg steam condenses in each tube. Parametric studies were done for this system with 3 – 10 such VTE (effects) [3-5]. In the current study [6-7] on MSMED, only one fluted aluminum tube is used per VTE and three such effects are used with a condenser. As the dimension of the fluted tube was same as with SMED, in the VTE with one tube about 3 kg of steam can be condensed. In Fig. (2-4) the photographs of various fabricated components and assembly of MSMED are shown.

Fig.2. Unassembled parts of MED

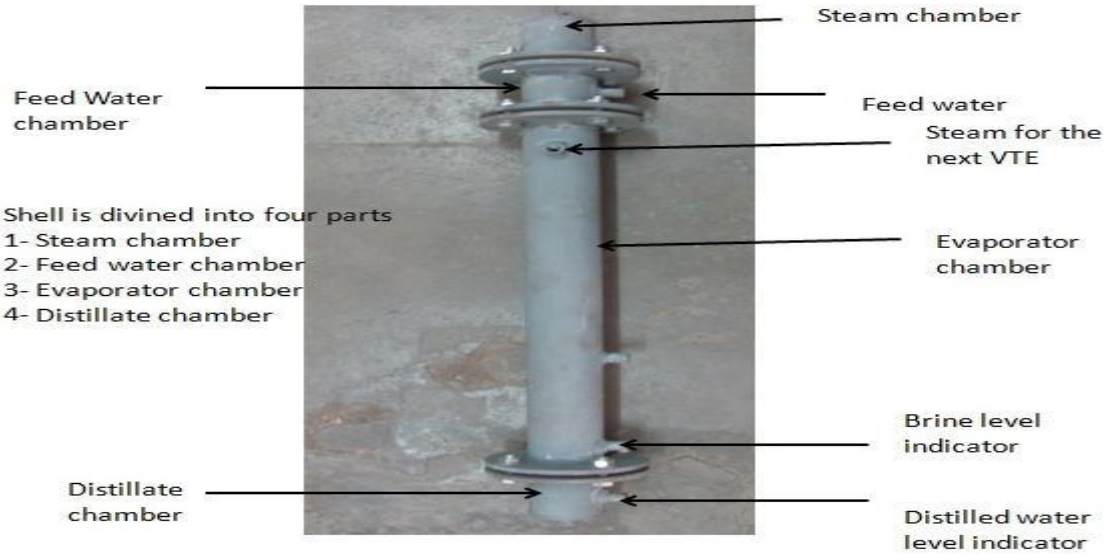

Fig. 3. Vertical Tube Evaporator

(a)  (b) 

Fig.4. Micro Scale Multi Effect Distillation (MSMED) Unit (a) before insulation (b) after Insulation.

3. Calculations for Operating Conditions

3.1 Heat transfer area

The distillation process requires a large heat transfer area. The overall heat transfer coefficient U can be as high as 14,000 W/m^2/K for a thin film vertical tube evaporator (VTE) using single fluted tubes. However, U=10,000 W/m^2-K was assumed in the present design, for readily available outside fluted 24 mm diameter aluminium tubes that are used in the construction of the VTEs. These tubes are commonly used as curtain rods. Further, considering the temperature difference, ΔT, across tube and shell sides of VTE as 5 °C (even though condensation of liquid for a heat transfer temperature difference of 2 °C has been reported), the heat transfer area is calculated using equation:

$M_d H_{fg} = UA\Delta T$

Assume H_{fg} = 2257 kJ/kg

U = 10000 W/M^2-K

ΔT = 5K

Here, M_d and H_{fg} are respectively the rate of condensation of steam, and latent heat of vaporization.

For a steam condensation rate (i.e., distillate flow rate) of 3 Kg/h, 0.0565 m^2 of heat transfer area is required for the values of ΔT and U assumed. Considering handling convenience and total height of VTE, a shell length of 0.75 m was needed to form the evaporator section of VTE. However, the actual tube length taken is 0.9 m; this account for projections outside tube plate and also the length of feed water jacket where feed water is sprayed. The value is close to that required for a temperature difference of 5 °C as assumed. There are 21 numbers of flutes in each tube, with flute depth of 0.50 mm, running along the length of the tubes. Fluting increases the actual area of heat transfer and also ensures very thin films at the ridges. This would allow for heat transfer for much smaller temperature differences between tube and shell side. For similarity in construction, the heat transfer area is kept identical in all VTEs, and also in the final condenser.

4. Experimental Results

Analysis and investigations were done with the MSMED, (3 effects + Condenser). The unit was operated with input primary steam pressure supplied by a baby boiler in the range of 1.2 bar gauge to 1.6 bar gauge with increment of input steam pressure of 0.2 bar. All the readings namely pressure, temperature and distillate production were measured and recorded at different locations for each input steam pressure. The sum of distilled water produced from each effect, or cumulative distillate production, at a given input steam pressure, is the indicator of plant performance. At each input pressure the whole set of readings were repeated four times and the average figures obtained.

In table 1 the amount of distillate, D1 – D3 in the three effects and D4 in the condenser, and total cumulative distillate D, are shown, for the insulated system. It is seen that inlet pressure of 1.4 bar gives optimal distillate output. Table 2 shows the recovery ratio at each effect for different steam input pressures. It was also seen that the heat transfer is high and optimal at 1.4 bar input pressures, and, the overall heat transfer coefficient (OHTC) was found to be in the range of 6000-7000 W/M^2-K. This is less than the figures obtained in Sen et al. [3-5], because the feed water was not pre-heated, and part of the evaporator tube length was used up in raising the feed water temperature to saturation.

Table 1. Distilled water flow rate at different inlet steam pressures

distilled water flow rate	D1(kg/h)	D2(kg/h)	D3(kg/h)	D4(kg/h)	D=$\sum_1^4 D_i$	GOR (D/D1)
inlet pressure 1.2 bar gauge	3	2.85	2.55	2.4	10.8	3.6
inlet pressure 1.4 bar gauge	3.1	2.96	2.72	2.69	11.47	3.7
inlet pressure 1.6 bar gauge	3.15	2.96	2.66	2.55	11.32	3.59

Table 2. Recovery ratio at different inlet steam pressures

Recovery ratio	D2/D1	D3/D2	D4/D3
inlet pressure 1.2 bar gauge	0.95	0.89	0.94
inlet pressure 1.4 bar gauge	0.995	0.92	0.98
inlet pressure 1.6 bar gauge	0.94	0.90	0.96

Conclusion

An efficient MSMED system for rural communities has been designed, fabricated and optimized. As for rural application, where decentralized production and supply of water is needed, the plant should be small, cost effective and easy to construct, operate and maintain. Overall features and conclusions drawn are summarized below:

1) The unit designed and fabricated is rugged and robust and can easily be installed and operated in rural circumstances by rural populations with a little training.
2) The unit is capable of producing 80 to 90 liters distilled water per day, for about 7 hrs of operation.
3) Very high overall heat transfer coefficients (OHTCs) were obtained i.e. in the range of 6,000 – 7000 W/m^2-K, due to simultaneous phase change on both sides of the heat exchanger tubes, viz. condensation of steam in the tube side, and evaporation of feed water in the shell side.
4) On increasing the input steam pressure, the quantity of distillated water increases and reaches a maximum value at the respective optimum pressure of 1.4 bar gauge for 3 effects + Condenser.
5) At the inlet steam pressure of 1.4 bar gauge the Gained Output Ratio is 3.7. This indicates effective utilization of energy.
6) The system has reduced TDS from initial value of 748 ppm to 7 ppm. The performance depends on quality of feed water and proper functioning of VTEs and demisters. From the output results obtained we can say that fabricated VTEs and demisters are working well as the quality of distilled water depends on the demister. The minimum recorded TDS value of distilled water was 7 ppm and maximum was 9 ppm.
7) If steam is raised using solar energy there will be considerable saving of energy, since the main energy input is for raising the primary steam in the baby boiler.

Acknowledgement

Authors are thankful for the financial support under RC-UK DST, India funded project (EP/G021937/1). We are also thankful to Mr. D. C. Sharma and Mr. Sitaram (senior technicians at IIT Delhi), for their help during the course of the project.
We are thankful to Mr. Cyrus Engineer, Industrial Boilers Pvt. Ltd. for helpful discussions.

References

[1] Vyas, S.K., 2003. Small scale Multi Effect Distillation (MED) system for rural drinking water supply, PhD Thesis, IIT Delhi.
[2] Mudgal, Anurag., 2009. Multi Effect Distillation (MED) of water as a Rural Micro Enterprise, PhD Thesis, IIT Delhi.
[3] Sen, P. K., Sen, P.V., Singh, S.N., Mudgal, A., 2011. A small scale Multi Effect Distillation unit for rural micro enterprises: Part I - Design and Fabrication, Desalination 279, pp. 15-27.
[4] Sen, P. K., Sen, P.V., Mugdal A., Singh, S.N., 2011. A small scale Multi Effect Distillation (MED) unit for rural micro enterprises: Part II - Parametric studies and performance analysis, Desalination 279, pp. 27-37
[5] Sen, P. K., Sen, P.V., Mugdal, A., Singh, S.N., 2011. A small scale Multi Effect Distillation (MED) unit for rural micro enterprises: Part III - Heat Transfer aspects, Desalination 279, pp. 37-46.
[6] Kumar, Bhuwanesh, 2012. Performance of Micro Scale Multi Effect Distillation system compatible with solar energy, M. Tech Thesis, Department of Applied Mechanics, IIT Delhi.
[7] Kumar, Ashutosh, 2012. Studies on steam generation using Linear Fresnel Mirror Solar Concentrator with Tracking, M. Tech Thesis, Department of Applied Mechanics, IIT Delhi.

Available online at www.sciencedirect.com

SciVerse ScienceDirect

Procedia Engineering 00 (2012) 000–000

Procedia Engineering

www.elsevier.com/locate/procedia

5th BSME International Conference on Thermal Engineering

MHD Free Convection flow with Temperature Dependent Thermal Conductivity in Presence of Heat Absorption along a Vertical Wavy Surface

Nazma Parveen * and Md. Abdul Alim

Department of Mathematics, Bangladesh University of Engineering and Technology, Dhaka-1000, Bangladesh, nazma@math.buet.ac.bd

Abstract

MHD (magnetohydrodynamic) free convection flow of viscous incompressible fluid with temperature dependent thermal conductivity in presence of heat absorption along a uniformly heated vertical wavy surface have been numerically solved and analyzed. Using suitable set of dimensionless variables the governing boundary layer equations are first transformed into a non-dimensional form. The resulting nonlinear system of partial differential equations are mapped into the domain of a vertical flat plate and then solved numerically employing the implicit finite difference method, known as the Keller-box scheme. . The numerical results of the skin friction coefficient, the rate of heat transfer in terms of local Nusselt number, the streamlines as well as the isotherms are presented graphically for different values of thermal conductivity parameter γ and heat absorption parameter Q for a fluid having Prandtl number equal to 1.

Keywords: Heat absorption; MHD; temperature dependent thermal conductivity; free convection; uniform surface temperature; Keller-box method; wavy surface.

Nomenclature

C_{fx}	local skin friction coefficient
C_p	specific heat at constant pressure (Jk/gK)
f	dimensionless stream function
g	acceleration due to gravity (m/s^2)
Nu_x	local Nusselt number
P	pressure of the fluid (N/m^2)
T	temperature of the fluid in the boundary layer (K)
T_w	temperature at the surface (K)
T_∞	temperature of the ambient fluid (K)
u, v	dimensionless velocity components along the (x, y) axes (m/s)
x, y	axis in the direction along and normal to the tangent of the surface
Greek symbols	
α	amplitude-to-length ratio of the wavy surface

* Corresponding author. Tel.: 88-017-11265349
E-mail address: nazma@math.buet.ac.bd

β	volumetric coefficient of thermal expansion (1/K)
β_0	applied magnetic field strength
θ	dimensionless temperature function
ψ	stream function (m^2/s)
μ	viscosity of the fluid (kg/ms)
ν	kinematic viscosity (m^2/s)
ρ	density of the fluid (kg/m^3)
σ_0	electrical conductivity
$\sigma(x)$	surface profile function defined in equation (1)

Subscripts

w	wall conditions
∞	ambient conditions

Superscripts

$'$	differentiation with respect to η

1. Introduction

The effect of Heat generation/absorption of the laminar free convection flow of an electrically conducting fluid and heat transfer problem has been presented by many investigators because of its considerable practical applications. It is also necessary to study the heat transfer from an irregular surface because irregular surfaces are often present in many applications, such as radiator, heat exchangers and heat transfer enhancement devices. Yao [1] first investigated the natural convection heat transfer from an isothermal vertical wavy surface and used an extended Prantdl's transposition theorem and a finite-difference scheme. Vajravelu and Hadjinolaou [2], studied the heat transfer characteristics in the laminar boundary layer of a viscous fluid over a stretching sheet with viscous dissipation or frictional heating and internal heat generation. In this study they considered that the volumetric rate of heat generation, q''' [W/m^3], should be $q^m = Q_0(T- T_\infty)$, for $T \geq T_\infty$ and equal to zero for $T < T_\infty$, where Q_0 is the heat generation constant. The above relation explained by Vajravelu and Hadjinolaou [2], is valid as an approximation of the state of some exothermic process and having T_∞ as the onset temperature. When the inlet temperature are not less than T_∞ they used $q^m = Q_0(T- T_\infty)$. Hossain and Munir [3] studied numerically natural convection flow of a viscous fluid about a truncated cone with temperature dependent viscosity and thermal conductivity. Molla et al. [4] considered natural convection flow along a vertical wavy surface with uniform surface temperature in presence of heat generation/absorption. Very recently, Parveen and Alim [5] investigated MHD free convection flow along a vertical wavy surface with temperature dependent thermal conductivity in presence of heat generation.

The above literatures survey it is found that MHD free convection flow of an electrically conducting fluid variation of thermal conductivity with temperature in presence of heat absorption along a vertical wavy surface has not been studied yet and the present work demonstrates the issue. In this paper, attention has been given to a study of the free convection flow of a viscous incompressible fluid and temperature dependent thermal conductivity along a heated vertical wavy surface in presence of heat absorption. The surface shear stress in terms of local skin friction coefficient and the rate of heat transfer in terms of local Nusselt number, the streamlines as well as the isotherms patterns are shown graphically for the effect of varying the heat absorption and the thermal conductivity parameter.

2. Formulation of the problem

The boundary layer analysis outlined below allows $\bar{\sigma}(X)$ being arbitrary, but our detailed numerical work assumed that the surface exhibits sinusoidal deformations. The wavy surface may be described by

$$Y_w = \bar{\sigma}(X) = \alpha \sin\left(\frac{n\pi X}{L}\right) \tag{1}$$

where L is the wave length associated with the wavy surface.

The geometry of the wavy surface and the two-dimensional cartesian coordinate system are shown in Fig. 1.

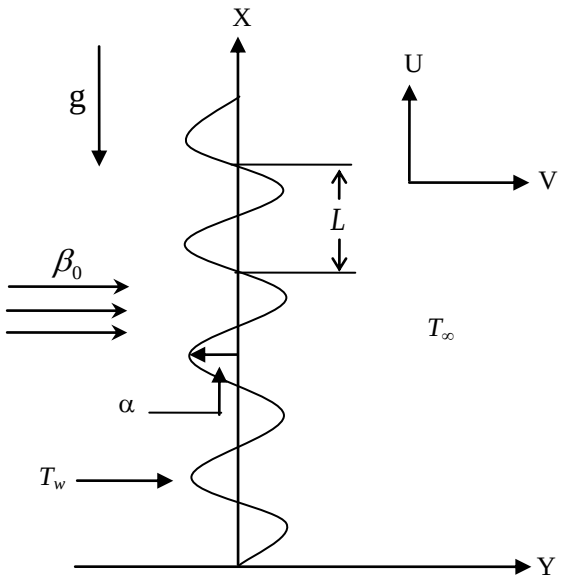

Fig. 1. Physical model and coordinate system

Under the usual Boussinesq approximation, the flow governed by the following dimensionless form of the governing

$$\frac{\partial u}{\partial x}+\frac{\partial v}{\partial y}=0 \tag{2}$$

$$u\frac{\partial u}{\partial x}+v\frac{\partial u}{\partial y}=-\frac{\partial p}{\partial x}+Gr^{1/4}\sigma_x\frac{\partial p}{\partial y}+\left(1+\sigma_x^2\right)\frac{\partial^2 u}{\partial y^2}-Mu+\theta \tag{3}$$

$$\sigma_x\left(u\frac{\partial u}{\partial x}+v\frac{\partial u}{\partial y}\right)=-Gr^{1/4}\frac{\partial p}{\partial y}+\sigma_x\left(1+\sigma_x^2\right)\frac{\partial^2 u}{\partial y^2}-\sigma_{xx}u^2 \tag{4}$$

$$u\frac{\partial \theta}{\partial x}+v\frac{\partial \theta}{\partial y}=\frac{1}{\Pr}\left(1+\sigma_x^2\right)\left(1+\gamma\theta\right)\frac{\partial^2 \theta}{\partial y^2}+\frac{1}{\Pr}\left(1+\sigma_x^2\right)\gamma\left(\frac{\partial \theta}{\partial y}\right)^2+Q\theta \tag{5}$$

In the above equations Pr, Q, γ and M are respectively known as the Prandtl number, heat absorption parameter, thermal conductivity variation parameter and magnetic parameter, which are defined as

$$\Pr=\frac{C_p\mu}{k_\infty},\ Q=\frac{Q_0L^2}{\mu CpGr^{1/2}},\ \gamma=\gamma^*(T_w-T_\infty)\ \text{and}\ M=\frac{\sigma_0\beta_0^2L^2}{\mu Gr^{1/2}} \tag{6}$$

The variable thermal conductivity chosen in this study which is used by Hossain and Munir [3] as follows:

$$k=k_\infty\left[1+\gamma^*\left(T-T_\infty\right)\right] \tag{7}$$

where k_∞ is the thermal conductivity of the ambient fluid and and $\gamma*$ is a constant.

Following Yao [1], here introduce the following non-dimensional variables

$$x=\frac{X}{L},\ y=\frac{Y-\overline{\sigma}}{L}Gr^{\frac{1}{4}},\ u=\frac{L}{\nu}Gr^{-1/2}U,\quad v=\frac{L}{\nu}Gr^{-1/4}(V-\sigma_xU) \tag{8}$$

$$\theta = \frac{T - T_\infty}{T_w - T_\infty}, \sigma_x = \frac{d\bar{\sigma}}{dX} = \frac{d\sigma}{dx}, Gr = \frac{g\beta(T_w - T_\infty)}{\nu^2} L^3 \ , \ p = \frac{L^2}{\rho \nu^2} Gr^{-1} P$$

Equation (4) indicates that the pressure gradient along the *y*-direction is $O(Gr^{-1/4})$, which implies that lowest order pressure gradient along *x*-direction can be determined from the inviscid flow solution. For the present problem this pressure gradient ($\partial p/\partial x = 0$) is zero. Equation (4) further shows that $Gr^{1/4}\partial p/\partial y$ is O(1) and is determined by the left-hand side of this equation. Thus, the elimination of $\partial p/\partial y$ from Equations (3) and (4) leads to

$$u\frac{\partial u}{\partial x} + v\frac{\partial u}{\partial y} = \left(1+\sigma_x^2\right)\frac{\partial^2 u}{\partial y^2} - \frac{\sigma_x \sigma_{xx}}{1+\sigma_x^2}u^2 - \frac{M}{1+\sigma_x^2}u + \frac{1}{1+\sigma_x^2}\theta \tag{9}$$

The corresponding boundary conditions for the present problem are

$$\left.\begin{aligned} &u = v = 0, \quad \theta = 1 \qquad at \quad y = 0 \\ &u = \theta = 0, \quad p = 0 \qquad as \quad y \to \infty \end{aligned}\right\} \tag{10}$$

Now we introduce the following transformations to reduce the governing equations to a convenient form:

$$\psi = x^{3/4} f(x,\eta), \quad \eta = y x^{-1/4}, \quad \theta = \theta(x,\eta) \tag{11}$$

where η is the pseudo similarity variable and ψ is the stream function.

Introducing the transformations given in Equation (11) into Equations (9) and (5) the momentum and energy equations are transformed the following forms,

$$\left(1+\sigma_x^2\right) f''' + \frac{3}{4} ff'' - \left(\frac{1}{2} + \frac{x\sigma_x\sigma_{xx}}{1+\sigma_x^2}\right) f'^2 + \frac{1}{1+\sigma_x^2}\theta - \frac{Mx^{1/2}}{1+\sigma_x^2} f' = x\left(f'\frac{\partial f'}{\partial x} - f''\frac{\partial f}{\partial x}\right) \tag{12}$$

$$\frac{1}{\Pr}\left(1+\sigma_x^2\right)\left(1+\gamma\theta\right)\theta'' + \frac{1}{\Pr}\left(1+\sigma_x^2\right)\gamma\theta'^2 + \frac{3}{4} f\theta' + x^{1/2} Q\theta = x\left(f'\frac{\partial \theta}{\partial x} - \theta'\frac{\partial f}{\partial x}\right) \tag{13}$$

The boundary condition (10) now take the following form:

$$\left.\begin{aligned} &f(x,o) = f'(x,o) = 0, \qquad \theta(x,o) = 1 \\ &f'(x,\infty) = 0, \qquad \theta(x,\infty) = 0 \end{aligned}\right\} \tag{14}$$

The rate of heat transfer in terms of the local Nusselt number, Nu_x and the local skin friction coefficient, C_{fx} take the following forms:

$$Nu_x (Gr/x)^{-1/4} = -\left(1+\gamma\right)\sqrt{1+\sigma_x^2}\,\theta'(x,o) \tag{15}$$

$$C_{fx}(Gr/x)^{1/4}/2 = \sqrt{1+\sigma_x^2}\, f''(x,o) \tag{16}$$

3. Method of Solution

This paper concerns the MHD free convection flow of viscous incompressible fluid along a uniformly heated vertical wavy surface in presence of heat absorption with temperature dependent thermal conductivity along a vertical wavy surface. The governing Equations (12) and (13) with the boundary conditions in Equation (14) are solved numerically using the very efficient implicit finite difference method known as Keller box scheme developed by Keller [6].

4. Result and Discussion

Numerical values of the shear stress in terms of the skin friction coefficients C_{fx}, the rate of heat transfer in terms of the Nusselt number Nu_x, the streamlines and the isotherms are presented graphically for different values of heat absorption

parameter Q = 0.0 to -0.6 and temperature dependent thermal conductivity parameter γ = 0.0 to 10.0 while magnetic parameter M = 0.5, Prandtl number Pr = 1.0 and the amplitude-to-length ratio of the wavy surface α = 0.3 are fixed.

The effect of heat absorption parameter Q the local skin friction coefficient C_{fx} and the rate of heat transfer in terms of the local Nusselt number Nu_x against x from the wavy surface while α = 0.3, M = 0.5, γ = 4.0 and Pr = 1.0 are displayed in Fig. 2(a) and 2(b) respectively. From Fig. 2, it is observed that for increasing values of Q, the skin friction coefficient decreases and the heat transfer rate increases along the upstream direction of the surface. The presence of heat absorption (Q < 0) creates a layer of cold fluid adjacent to the heated surface and therefore the rate of heat transfer in terms of the local Nusselt number from the surface increases.

The skin friction coefficient C_{fx} and local rate of heat transfer Nu_x for influence of γ are illustrated by Fig. 3 while α = 0.3, M = 0.5, Q = -0.2 and Pr = 1.0. It is noted that an increase in the values of γ, the skin friction coefficient and the heat transfer rates increase monotonically along the upstream direction of the surface.

Figs. 4 and 5 illustrate the effect of heat absorption parameter Q on the development of streamlines and isotherms profile which are plotted for α = 0.3, Pr = 1.0, γ = 4.0 and M = 0.5. The maximum values of ψ, that is, ψ_{max} are 9.01, 6.15, 4.31 and 3.27 for Q = 0.0, - 0.2, - 0.4 and - 0.6 respectively. It is observed that as the values of Q increase the velocity boundary layer becomes thinner gradually. The same result is observed on the isotherms profile due to increase value of Q. Finally it is concluded that for the effect of heat absorption parameter Q both the velocity of the fluid flow and temperature distribution within the boundary layer decrease.

The effects of γ equal to 0.0, 2.0, 6.0 and 10.0 on the streamlines and isotherms profile are depicted by the Figs. 6 and 7 respectively while Pr = 1.0, α = 0.3, Q = -0.2 and M = 0.5. Fig. 6 depicts that the maximum values of ψ increases steadily while the value of γ increases. The maximum values of ψ, that is, ψ_{max} is 2.88 for γ = 0.0, ψ_{max} is 4.75 for γ = 2.0, $\psi_{\max}$ is 7.24 for γ = 6.0 and ψ_{max} is 8.90 for γ = 10.0. From Fig. 7, it is noted that the temperature distribution also increases for increasing value of γ.

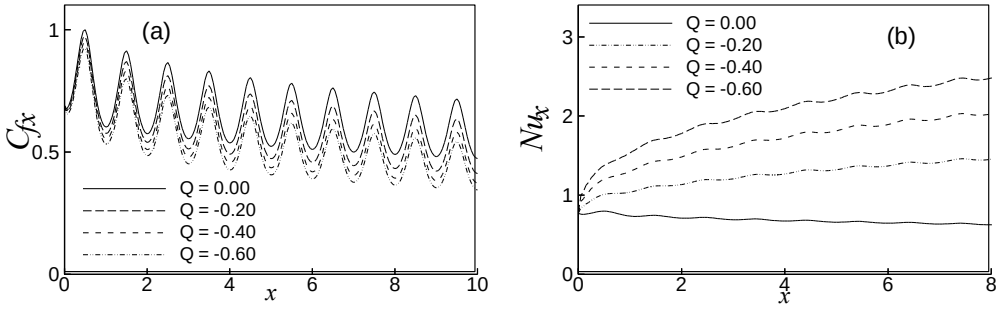

Fig. 2. Variation of (a) skin friction coefficient C_{fx} and (b) rate of heat transfer Nu_x against x for different values of heat absorption parameter Q while Pr = 1.0, α = 0.3, M = 0.5 and γ = 4.0.

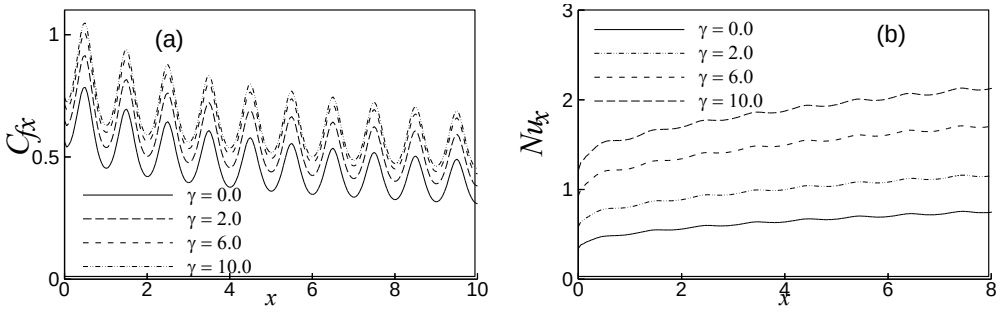

Fig. 3. Variation of (a) skin friction coefficient C_{fx} and (b) rate of heat transfer Nu_x against x for different values of thermal conductivity parameter γ with α = 0.3, M = 0.5, Q = - 0.2 and Pr = 1.0.

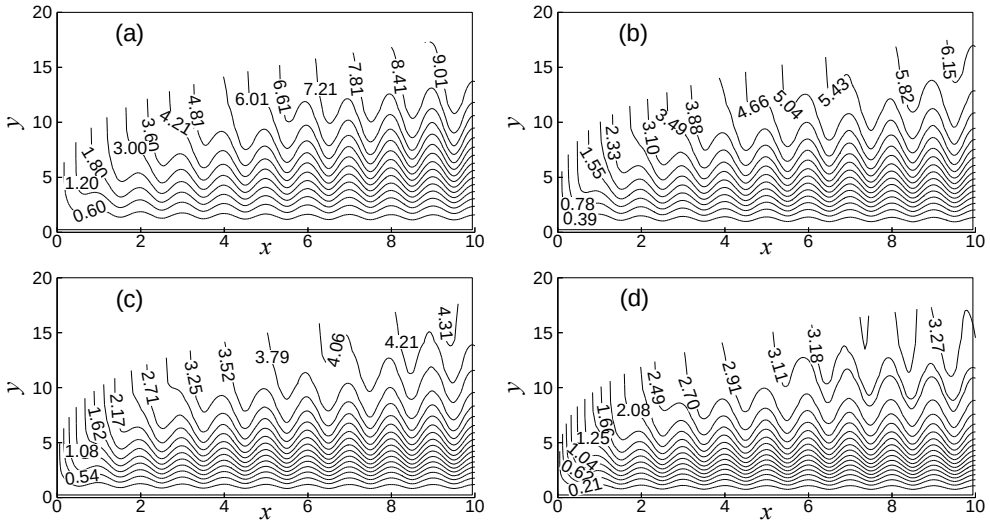

Fig. 4. Streamlines for (a) Q = 0.0 (b) Q = - 0.2 (c) Q = - 0.4 and (d) Q = - 0.6 while Pr = 1.0, M = 0.5, γ = 4.0 and α = 0.3.

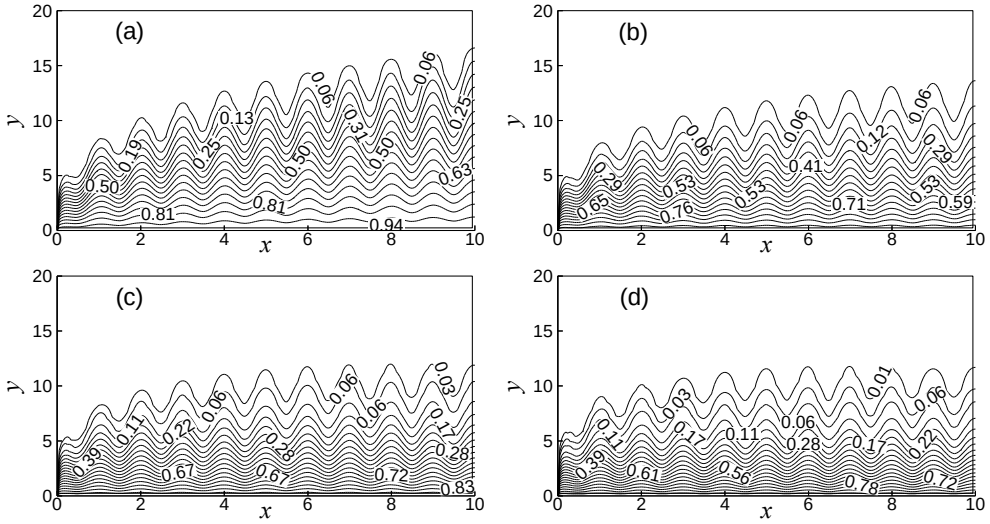

Fig. 5. Isotherms for (a) Q = 0.0 (b) Q = - 0.2 (c) Q = - 0.4 and (d) Q = - 0.6 while Pr = 1.0, M = 0.5, γ = 4.0 and α = 0.3.

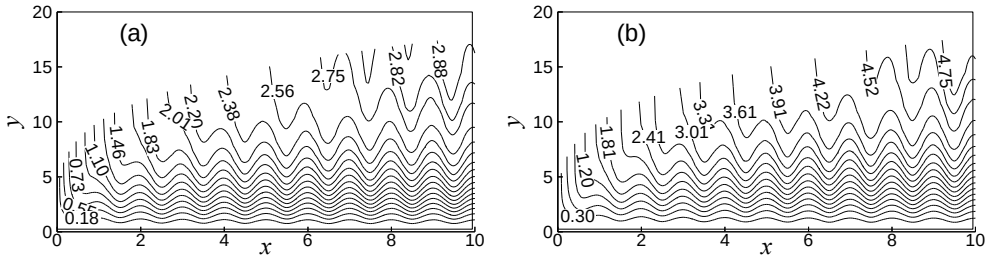

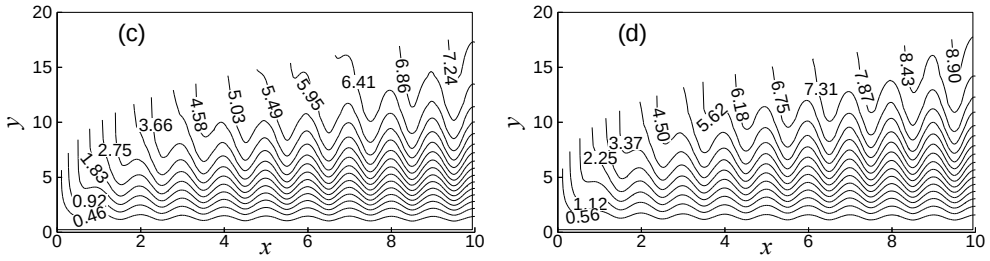

Fig. 6. Streamlines for (a) γ = 0.0 (b) γ = 2.0 (c) γ = 6.0 and (d) γ = 10.0 while α = 0.3, M = 0.5, Q = - 0.2 and Pr = 1.0.

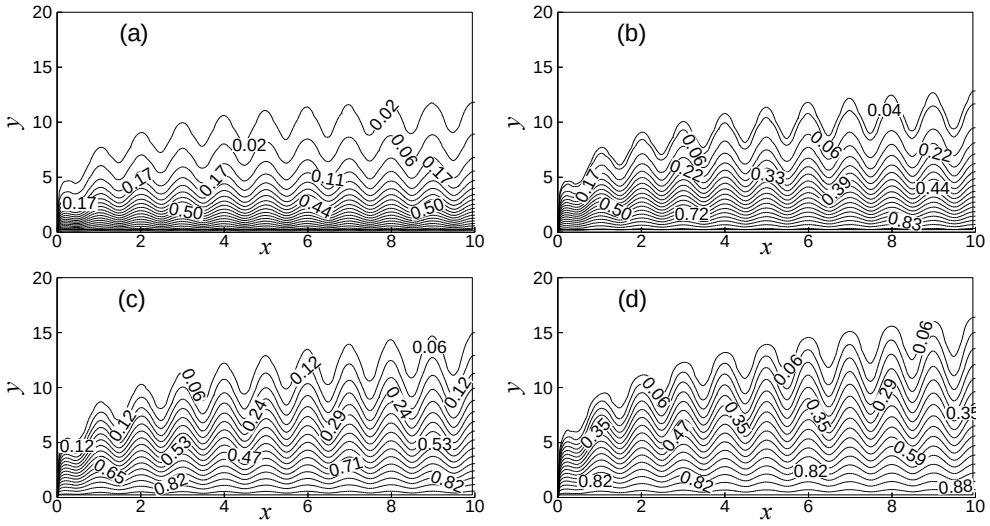

Fig. 7. Isotherms for (a) γ = 0.0 (b) γ = 2.0 (c) γ = 6.0 and (d) γ = 10.0 while α = 0.3, M = 0.5, Q = - 0.2 and Pr = 1.0.

5. Conclusion

The effect of heat absorption on MHD free convection flow with temperature dependent thermal conductivity along a vertical wavy surface has been studied numerically. The present investigation can be concluded as follows:

- The skin friction coefficient decreases and the rate of heat transfer increases in the presence of heat absorption. The velocity and thermal boundary layer becomes thinner for the effect of heat absorption.
- Increasing values of temperature dependent thermal conductivity variation parameter γ, the skin friction coefficient and the local rate of heat transfer significantly increase in the upstream region.
- The velocity of the fluid flow and the temperature distribution of the fluid within the boundary layer significantly increase for increasing values of γ.

References

[1] Yao L. S., 1983, Natural Convection along a Vertical Wavy Surface, ASME J. Heat Transfer 105, p. 465.
[2] Vejravelu K., Hadjinicolaou A., 1993, Heat Transfer in a Viscous Fluid over a Stretching Sheet with Viscous Dissipation and Internal Heat Generation, Int. comm. Heat Transfer 20, p. 417.
[3] Hossain M.A., Munir M. S., 2001, Natural Convection Flow of a Viscous Fluid about a Truncated Cone with Temperature Dependent Viscosity and Thermal Conductivity, Int. J. Nume. Met. for Heat Fluid Flow 11, p. 494.
[4] Molla M. M., Hossain M. M., Yao L. S., 2004, Natural Convection Flow along a Vertical Wavy Surface with uniform Surface Temperature in Presence of Heat Generation/Absorption, Int. J. Therm. Sci 43, p. 157.
[5] Parveen N., Alim M.A., 2012, MHD Free Convection Flow along a Vertical Wavy Surface with Temperature Dependent Thermal Conductivity in Presence of Heat Generation, Int. J. Energy Tech. 4, p. 1.
[6] Keller H.B., 1978, Numerical Methods in Boundary Layer Theory, Ann. Rev. Fluid Mech. 10, p. 417.

Available online at www.sciencedirect.com

SciVerse ScienceDirect

Procedia Engineering 00 (2012) 000–000

Procedia Engineering

www.elsevier.com/locate/procedia

5th BSME International Conference on Thermal Engineering

MHD natural convection in a rectangular cavity having internal energy sources with non-uniformly heated bottom wall

M. Obayedullah and M.M.K. Chowdhury
Department of Mathematics, Bangladesh University of Engineering and Technology
Dhaka-1000, Bangladesh, obayed@math.buet.ac.bd

Abstract

The present study deals with steady natural convection flow in a rectangular cavity containing internally heated and electrically conducting fluid. The bottom wall is non-uniformly heated while the upper wall of the cavity is well insulated. The left and right vertical walls are maintained at constant hot and cold temperature respectively. Numerical results have been obtained for the effect of various internal and external Rayleigh numbers and Hartmann numbers. Results are presented in the form of streamlines, isotherm contours. Average Nusselt numbers are expressed as a function of Rayleigh number. It is found that the temperature, fluid flow and heat transfer strongly depend on internal and external Rayleigh numbers and Hartmann numbers.

Keywords: natural convection; heat generation; non-uniform heating; rectangular cavity.

1. Introduction

Natural convection heat transfer induced by internal heat generation has received considerable attention because of its numerous application in geophysics and energy related engineering problems. Oreper and Szekely, 1983 [1] studied the effect of an externally imposed magnetic field on buoyancy driven flow in a rectangular cavity. Ozoe and Maruo, 1987 [2] investigated magnetic and gravitational natural convection of melted silicon and used two dimensional numerical computation for the rate of heat transfer. Garandet et al., 1992 [3] studied natural convection heat transfer in a rectangular enclosure with a transverse magnetic field. Rudraiah et al., 1995 [4] investigated the effect of surface tension on buoyancy driven flow of an electrically conducting fluid in a square cavity in the presence of a transverse magnetic field to see how this force damps hydrodynamic movements.

Gelfgat and Yoseph, 2001 [5] studied the effect of an externally imposed magnetic field on the linear stability of steady convection flow in a horizontally elongated rectangular cavity. Sarris et al., 2005 [6] presented a numerical study of two dimensional natural convection of an electrically conducting fluid in a laterally and volumetrically heated square cavity under the influence of a magnetic field. Mehmet and Elif, 2006 [7] studied the natural convection flow under a magnetic field in an inclined rectangular enclosure heated and cooled on adjacent walls. Kandaswamy et al., 2008 [8] studied MHD natural convection in an enclosure with partially active vertical walls. Nithyadevi et al., 2009 [9] studied magnetoconvection in a cavity with partially active vertical walls having time periodic boundary condition. Kahveci et al., 2009 [10] studied MHD natural convection flow and heat transfer in a laterally heated partitioned enclosure.

As per author's knowledge the literature review revealed that non-uniform temperature profile in the wall was not used in he magnetohydrodynamic natural convection flow in a rectangular cavity with heat generation. In this paper the investigation is carried out on the MHD natural convection flow in a rectangular cavity filled with heat generating fluid having parabolically heated bottom wall.

2. Formulation of the problem

A rectangular cavity filled with viscous incompressible fluid is shown in the Fig. 1. The cavity dimensions are defined by *L* for width .and H for height. The cavity is isothermally heated from the left vertical wall with a uniform constant temperature T_h and the right vertical with temperature $T_c (T_h > T_c)$. The bottom horizontal wall is heated with $T_h - (T_h - T_c)\frac{x}{L}(1-\frac{x}{L})$ while the remaining wall is considered perfectly insulated.

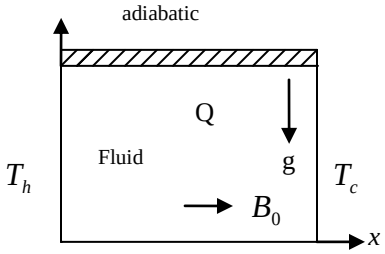

$$T_h - (T_h - T_c)\frac{x}{L}(1-\frac{x}{L})$$

Fig. 1 Physical model and coordinate system

Steady two-dimensional laminar magnetohdrodynamic free convective flow of viscous incompressible Boussinesq fluid such as water, air etc. with constant properties is assumed. Under these assumptions, equations of mass, momentum and energy are

$$\frac{\partial u}{\partial x} + \frac{\partial v}{\partial y} = 0 \tag{1}$$

$$u\frac{\partial u}{\partial x} + v\frac{\partial u}{\partial y} = -\frac{1}{\rho}\frac{\partial p}{\partial x} + \nu\left(\frac{\partial^2 u}{\partial x^2} + \frac{\partial^2 u}{\partial y^2}\right) \tag{2}$$

$$u\frac{\partial v}{\partial x} + v\frac{\partial v}{\partial y} = -\frac{1}{\rho}\frac{\partial p}{\partial y} + \nu\left(\frac{\partial^2 v}{\partial x^2} + \frac{\partial^2 v}{\partial y^2}\right) + g\beta(T - T_c) - \frac{\sigma {B_0}^2 v}{\rho} \tag{3}$$

$$u\frac{\partial T}{\partial x} + v\frac{\partial T}{\partial y} = \alpha\left(\frac{\partial^2 T}{\partial x^2} + \frac{\partial^2 T}{\partial y^2}\right) + \frac{Q}{\rho c_p} \tag{4}$$

The boundary conditions are:

$$u(x,0)=u(x,H)=u(0,y)=u(L,y)=0,$$

$$v(x,0)=v(x,H)=v(0,y)=v(L,y)=0.$$

$$T(x,0)= T_h - (T_h - T_c)\frac{x}{L}(1-\frac{x}{L}),\ T(0,y)= T_h,\ T(L,y)= T_c,\quad \frac{\partial T}{\partial y}(x,H) = 0.$$

where *u* and *v* are the velocity components in the *x* and *y* directions respectively; ρ is the fluid density, β is the coefficient of thermal expansion, c_p is the fluid specific heat, Q is the rate of internal heat generation per unit volume, B_0 is the magnetic induction, α is the thermal diffusivity and *v* kinematic viscosity of the fluid. To make the above equations dimensionless we introduce the following non-dimensional variables:

$$X = \frac{x}{L},\ Y = \frac{y}{L},\ U = \frac{uL}{\alpha},\ V = \frac{vL}{\alpha},\ P = \frac{pL^2}{\rho\alpha^2},\ \theta = \frac{T - T_c}{T_h - T_c}$$

where θ is the dimensionless temperature.

Substitution of the dimensionless variables into the Eqs.(1)-(4) leads to:

$$\frac{\partial U}{\partial X} + \frac{\partial V}{\partial Y} = 0 \qquad (5)$$

$$U\frac{\partial U}{\partial X} + V\frac{\partial U}{\partial Y} = -\frac{\partial P}{\partial X} + \Pr\left(\frac{\partial^2 U}{\partial X^2} + \frac{\partial^2 U}{\partial Y^2}\right) \qquad (6)$$

$$U\frac{\partial V}{\partial X} + V\frac{\partial V}{\partial Y} = -\frac{\partial P}{\partial Y} + \Pr\left(\frac{\partial^2 V}{\partial X^2} + \frac{\partial^2 V}{\partial Y^2}\right) + Ra_E \Pr\theta - Ha^2 \Pr V \qquad (7)$$

$$U\frac{\partial \theta}{\partial X} + V\frac{\partial \theta}{\partial Y} = -\frac{\partial P}{\partial X} + \left(\frac{\partial^2 \theta}{\partial X^2} + \frac{\partial^2 \theta}{\partial Y^2}\right) + \frac{Ra_E}{Ra_I} \qquad (8)$$

In the above equations Ra_E is the external Rayleigh number , Ra_I is the internal Rayleigh number , Pr is the Prandtl number and Ha is the Hartmann number defined respectively by the following equations.

$$Ra_E = \frac{g\beta(T_h - T_c)L^3}{\nu\alpha},\quad Ra_I = \frac{g\beta QL^5}{\nu\alpha k},\ \Pr = \frac{\nu}{\alpha} \text{ and } Ha^2 = \frac{\sigma {B_0}^2 L^2}{\mu}$$

The dimensionless boundary conditions are:

$$U(X,0)=U(X,A)=U(0,Y)=U(1,Y)=0,$$

$$V(X,0)=V(X,A)=V(0,Y)=V(1,Y)=0,$$

$$\theta(X.0)=1-X(1-X)\quad \theta(0,Y)=1,\ \theta(1,Y)=0\ ,\ \frac{\partial\theta}{\partial Y}(X,A)=0$$

where $A = H/L$ is the aspect ratio of the cavity which is taken as 0.75. The heat transfer coefficient in terms of local Nusselt number is defined by $Nu = -\frac{\partial\theta}{\partial n}$ where n denotes the normal direction on a plane.

The average Nusselt numbers at the bottom and side walls are computed as

$$\overline{Nu_b} = \int_0^1 Nu_b\, dX\ ,\qquad \overline{Nu_s} = \frac{1}{A}\int_0^A Nu_s\, dY$$

The discretization process involves a certain amount of error, which can be systematically reduced by a series of grid refinements. To this end, five types of grid densities have been chosen to check for the self-consistency of the present study. The grids chosen are: (a) 22342 nodes, 3453 elements, (b) 28455 nodes, 4421 elements (c) 35796 nodes, 5589 elements (d) 41124 nodes, 6424 elements (e) 47212 nodes, 7387 elements. Type (c) mesh density was found to give sufficient accuracy with modest computational time, and hence selected for the simulation study.

The governing Eqs.(5)-(8) along with the boundary conditions are solved numerically, employing finite element method based on Galerkin weighted residual formulation. To ensure convergence of solutions the following criteria is applied to all dependent variables over the solution domain

$$\Sigma\left|\Phi_{i,j}{}^{n} - \Phi_{i,j}{}^{n-1}\right| \le ERMAX$$

where Φ represents the dependent variables U, V, P and T ;the indexes i, j refers to space coordinates and the index n is the current iteration.. The value of ERMAX is chosen as 10^{-5}.

Table 1. Comparison of present numerical results with those obtained by Sathiyamoorty et al., 2007 [11]for the case Pr = 0.71 in the absence of magnetic field.

Ra_E	$\overline{Nu_b}$ (Present work)	$\overline{Nu_b}$ (Sathiyamoorty et al.)
10^3	3.7196	3.7294
10^4	4.7520	4.7753
10^5	6.8042	6.8272

3. Results and Discussions

Numerical results are presented to determine the effects of internal heat generation and magnetic field on the natural convection flow of an electrically conducting fluid in a rectangular cavity. The three governing parameters in this problem are the internal Rayleigh number Ra_I, the external Rayleigh number Ra_E and the Hartmann number Ha, Values of the internal Rayleigh number Ra_I range from 10^2 to 10^5 and the Hartmann number Ha from 00 to 50 while Pr=0.71 is kept fixed.

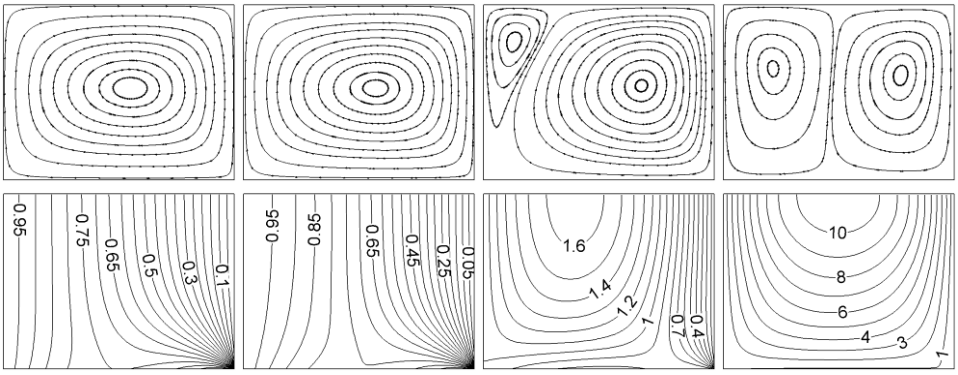

Fig. 2. Contour plots for $Ra_E=10^3$, $Ra_I=10^2$, Ha=20 streamline(top); isotherm(bottom)

Fig. 3. Contour plots for $Ra_E=10^3$ $Ra_I=10^3$, Ha=20 streamline(top); isotherm(bottom)

Fig. 4. Contour plots for $Ra_E=10^3$ $Ra_I=10^4$, Ha=20 streamline(top); isotherm(bottom)

Fig. 5. Contour plots for $Ra_E=10^3$ $Ra_I=10^5$, Ha=20 streamline(top); isotherm(bottom

The effects of internal Rayleigh number Ra_I has been considered first on the flow and temperature fields. The resulting flows of fluid and its temperature distributions have been shown in Figs. 2-5. where the top row gives the streamlines and the bottom row gives the isotherms for increasing values of internal Rayleigh number Ra_I=10^2, 10^3, 10^4 and 10^5 with Pr=0.71 , Ra_E=10^3 and Ha=20. Because of parabolic temperature profile in the bottom wall and uniformly heated left vertical wall fluid rises up along the left wall of the cavity and flow down along the right wall forming a single cell called primary cell as shown in the of Fig. 2(top). A single cell is formed because the internal Rayleigh number Ra_I is smaller than the external Rayleigh number Ra_E . With the increase of the internal Rayleigh number a secondary cell has been developed in top left corner of the cavity as shown in the Fig. 4(top). The increasing rate of heat within the cavity due to the increase of the internal Rayleigh Number leads to increase the flow rate in the secondary cell as well as increase in its size until it occupies half of the cavity. This effect of internal Rayleigh number on the flow field is reasonable since internal heat generation assists the buoyancy forces by accelerating the fluid flow. The left cell revolves anticlockwise because of greater internal Rayleigh number and the right cell revolves clockwise as expected. The fluid temperature increases significantly due to increase of the

internal Rayleigh number which is shown in the isotherms of Figs. 2-5 (bottom). It is clearly seen that owing to the increase of the internal Rayleigh Number the fluid temperature exceeds the surface temperature.

Figs. 6-9 depicts the effects of Hartmann number *Ha* on the flow and temperature fields. The flow and temperature distributions have been shown in these figures where the top row gives the streamlines and the bottom row gives the isotherms for increasing values of *Ha*= 00, 10, 20, 50 with the external Rayleigh number $Ra_E=10^3$, the internal Rayleigh number $Ra_I=10^4$ and $Pr=0.71$.

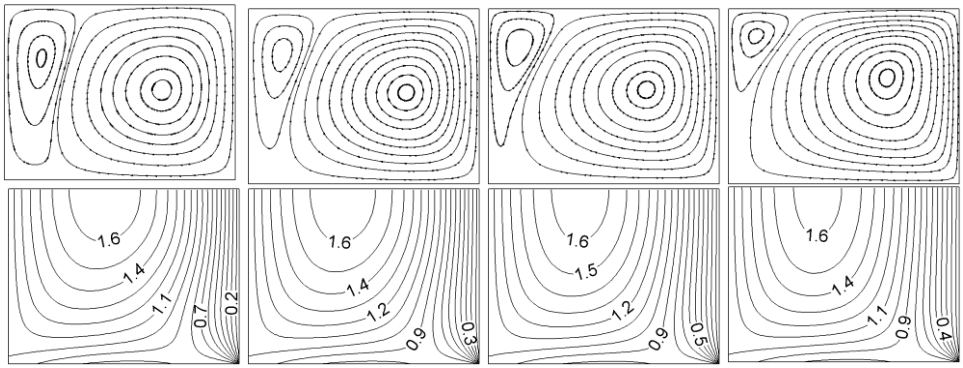

Fig. 6. Contour plots for $Ra_E=10^3$, $Ra_I=10^4$, *Ha*=00 streamline(top); isotherm(bottom)

Fig. 7. Contour plots for $Ra_E=10^3$ $Ra_I=10^4$, *Ha*=10 streamline(top); isotherm(bottom)

Fig. 8. Contour plots for $Ra_E=10^3$ $Ra_I=10^4$, *Ha*=20 streamline(top); isotherm(bottom)

Fig. 9. Contour plots for $Ra_E=10^3$ $Ra_I=10^4$, *Ha*=50 streamline(top); isotherm(bottom

Here two cells are formed as the internal Rayleigh number is greater than the external Rayleigh number. From the figures as shown in the top rows, it can be seen that intensities of the flow decrease owing to increase in the magnetic field. Because of the decrease of the intensity of the flow the left cell is becoming smaller. This is expected since presence of magnetic field usually retards the velocity field.

The corresponding effects of increasing Hartmann number on the isotherms may be viewed from the Figs. 6-9(bottom). It is seen that the isotherms become more curved due to the increase of the magnetic field strength, which is expected; since the magnetic field resists the flow.

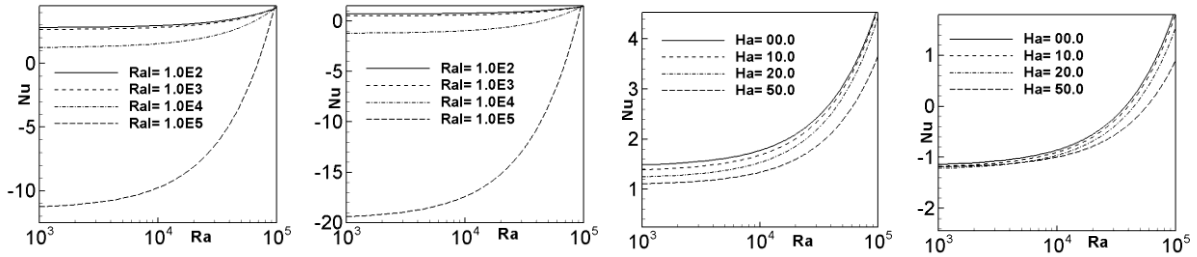

Fig. 10: Nusselt number as a function of external Rayleigh number for the (a) non-uniformly heated bottom wall and (b) heated left wall for varying Ra_I with *Ha*=20 (c) non-uniformly heated bottom wall and (d) heated left wall for varying *Ha* with $Ra_I= 10^4$, all with $Pr=0.71$.

The overall effects of internal Rayleigh number Ra_I on the average Nusselt number for non-uniformly heated bottom wall and heated left wall for $Pr=0.71$, and internal Rayleigh number $Ra_I= 10^2$, 10^3, 10^4 and 10^5 are displayed in Figs. 10(a) and (b) via average Nusselt number vs external Rayleigh number plot. It is seen that the average Nusselt Number is negative for both the non-uniformly heated bottom wall and heated

left wall. In both the cases heat transfer is very high for $Ra_I = 10^5$.

The effects of *Ha* on the average Nusselt number for bottom wall and left wall for Pr=0.71 and $Ra_I=10^4$ and. are shown in Figs. 10(c) and (d). Initially at $Ra_E = 10^3$ the heat transfer on the bottom wall is positive and left wall is negative. It is observed that the average Nusselt number smoothly increases as the external Rayleigh number increases. In both the cases average Nusselt numbers are reduced as the strengths of the applied magnetic field are increased.

4. Conclusion

Natural convection flow and heat transfer in a rectangular cavity in the presence of magnetic field is numerically investigated by using finite element method. The investigation is carried out to find the affect of the internal Rayleigh number Ra_I and Hartmann number *Ha*. Internal Rayleigh number Ra_I affects the flow structure and heat transfer inside the cavity. The heat transfer is enhanced with increasing internal Rayleigh number. The flow characteristics and heat transfer mechanisms inside the cavity also depend strongly upon the strength of the magnetic field. Strong suppression of the convective current can be obtained by applying strong magnetic field. This is why, reductions in the average Nusselt number *Nu* are produced as the strengths of the applied magnetic field are increased. Thus significant effect of the magnetic field is observed in the heat transfer mechanisms.

References:

[1] Oreper GM, Szekely J., 1983. The effect of externally imposed magnetic field on buoyancy driven flow in a rectangular cavity, J. of Crystal Growth 64, p. 505-515.

[2] Ozoe H, Maruo M., 1987. Magnetic and gravitational natural convection of melted silicon-two dimensional numerical computations for the rate of heat transfer, JSME 30, p. 774.

[3] Garandet JP, Alboussiere T, Moreau R., 1992.. Buoyancy driven convection in a rectangular enclosure with a transverse magnetic field, Int. J. of Heat and Mass Transfer 35, p. 741.

[4] Rudraiah N, Vankatachalappa M, Subraiah CK., 1995. Combined surface tension and buoyancy-driven convection in a rectangular open cavity in the presence of a magnetic field, Internal. J. Non-Linear Mech 30(5), p. 759.

[5] Gelfgat AY, Yoseph PZ., 2001. Effect of an external magnetic field on oscillatory instability of convective flows in rectangular cavity, Phys. Fluid 13, p. 2269.

[6] Sarris IE, Kakarantzas SC, Grecos AP, Vlachos NS., 2005. MHD natural convection in a laterally and volumetrically heated square cavity, Int. J. of Heat and Mass Transfer 48, p. 3443.

[7] Mehmet CE, Elif B., 2006. Natural convection flow under a magnetic field in an inclined rectangular enclosure heated and cooled on adjacent walls, Fluid Dynamics Research 38, p. 564.

[8] Kandaswamy P, Sundari SM, Nithyadevi N., 2008. Magneto convection in an enclosure with partially active vertical walls, Int. J. of Heat and Mass Transfer 51, p. 1946.

[9] Nithyadevi N, Kandaswamy P, Sundari SM., 2009. Magnetoconvection in a square cavity with partially active vertical walls: Time periodic boundary condition, Int. J. of Heat and Mass Transfer 52, p. 1945.

[10] Kahveci K, Oztuna S., 2009. MHD natural convection flow and heat transfer in a laterally heated partitioned enclosure, European Journal of Mechanics 28, p. 744.

[11] Sathiyamoorty M, Tanmay Basak Roy S, Pop I., 2007. Steady Natural convection flow in a square cavity with linearly heated side walls, International Journal of Heat and Mass Transfer 50, p.766.

Available online at www.sciencedirect.com

SciVerse ScienceDirect

Procedia Engineering 00 (2012) 000–000

Procedia Engineering

www.elsevier.com/locate/procedia

5th BSME International Conference on Thermal Engineering

Effect of inclination angles on heat transfer characteristics of a closed loop pulsating heat pipe (CLPHP)

Suchana Akter Jahan*, Mohammad Ali, Md.Quamrul Islam

Bangladesh University of Engineering & Technology, Dhaka-1000, Bangladesh

Abstract

At present Closed Loop Pulsating Heat Pipe (CLPHP) is a novel cooling strategy for successful thermal management though it is a complex heat transfer device having a strong thermo-hydrodynamic coupling to govern the thermal performance. This research is to study the effect of inclination angle and working fluid on the heat transfer characteristics and performance of CLPHP. The performance characterization has been done using two different working fluids of water and ethanol with inclination angle of 0˚ (vertical), 30˚, 45˚, 60˚, 75˚ and 90˚ (horizontal). The experiment is conducted on a CLPHP made of 148 cm long copper capillary tube of 3.0 mm outer diameter and 2.0 mm inner diameter creating a total of 13 turns. The total length of evaporator section is 39.5 cm and condenser section is 31.5 cm; while the rest is assumed to be adiabatic. The evaporator section is heated by electrical heat input, while the condenser section is cooled by atmospheric air flow. Since a PHP is recognized as a two phase heat transfer device, for comparative studies it is operated as a double-phase system by filling it 70% with the working fluid. The comparative study results in a better understanding of the underlying physics of the PHP operation. The experimental results indicate a strong influence of gravity and thermo physical properties of the working fluid on the performance of the CLPHP. The results demonstrate the effect of the input heat flux, inclination angle and physiochemical properties of the working fluid on the thermal performance of the device.

Keywords: Pulsating heat pipe; evaporation; condensation; inclination angle; water; ethanol

Nomenclature

R	thermal resistance, ˚C/W	T	temperature along the heat pipe, ˚C
ΔT	temperature drop along the device, ˚C	Q	heat input, W
L	length of heat pipe, cm	D	diameter of heat pipe, mm
IA	Inclination angle, ˚	FR	filling ratio, %
Subscripts			
th	thermal	*e*	evaporator section
a	adiabatic section	*c*	condenser section

* Corresponding author. Tel.: +880-1914-979498
E-mail address: suchana.mech@gmail.com

1. Introduction

Meandering tube pulsating heat pipes (PHPs) have already found some applications in micro and power electronics applications owing to favorable operational characteristics coupled with relatively cheaper costs. Although grouped as a subclass of the overall family of heat pipes, the subtle complexity of thermo-fluidic transport phenomena is quite unique justifying the need of a completely different research outlook. A closed loop pulsating or oscillating heat pipe consists of a metallic capillary tube wound in a serpentine manner and joined end to end as shown in Fig. 1. The empty capillary tube is filled partially or completely with the working fluids, which distributes itself naturally in the form of liquid–vapor slugs and bubbles inside the capillary tube.

A heat pipe is a heat transfer mechanism that combines the principles of both thermal conductivity and phase transition to efficiently manage the transfer of heat between two solid interfaces. This type of heat pipe is essentially a non-equilibrium heat transfer device. Groll [1], Nishio [2] and Shafii et al. [3] investigated that the sensible heat transfer was the major contributor in the overall heat exchange. Gaugler et al. [4] suggested the serpentine designs of heat pipes. However, it was not well appreciated until Grover et al. [5] invented its remarkable properties and began further development. Eastman et al. [6] first discussed applications of flexible, arterial, and flat plate heat pipes to areas outside of government concern. A heat transfer analysis of an inclined two-phase closed thermo siphon was developed by Zuo [7]. Amount of working fluid remained almost constant for a large range of inclination angles (0˚-70˚) and then significantly increased for further increase of inclination angle. At a certain inclination angle, the mean heat transfer co-efficient of the thermo siphon reached a maximum value.

2. Design and construction

The three basic components of a heat pipe are the container, working fluid and the wick or capillary structure. The function of the container is to isolate the working fluid from the outside environment. It has to therefore be leak-proof, maintain the pressure differential across its walls, and enable transfer of heat to take place from and into the working fluid. A first consideration in the identification of a suitable working fluid is the operating vapor temperature range. Within the approximate temperature band, several possible working fluids may exist, and a variety of characteristics must be examined in order to determine the most acceptable one. Prime requirements are compatibility with wick structure, thermal stability, high latent heat and thermal conductivity, low viscosity etc. The wick is a porous structure made of materials like steel, aluminum, nickel or copper in various ranges of pore sizes. The prime purpose of the wick is to generate capillary pressure to transport the working fluid from the condenser to the evaporator.

2.1. PHP design

The cooling device performance depends on its structure, shape, material and length. Thermal performance of any device vastly depends on a parameter known as thermal resistance.

Thermal resistance can be defined as:

$$R_{th} = \Delta T/Q \qquad (1)$$

The overall thermal resistance of a pulsating heat pipe composed of several components from evaporator to condenser. These are: two conductive thermal resistances in the wall R_{wall}, thermal resistance due to evaporation at evaporator R_{evap}, thermal resistance due to condensation at condenser R_{cond}, thermal resistance along the heat pipe length $R_{l\text{-}v}$, two contact resistances due to surface roughness R_{cont}. The conductive thermal resistance of the wall is negligible by using a wall material of high thermal conductivity. Resistance in the evaporator of heat pipe can be estimated to be between 0.001˚C/W and 1.180 x 10^{-4}˚C/W by using water or ethanol which has been widely approved to have better transport capabilities. Best evaporation resistance is achieved due to the best heat transfer in the case of square channel is due to the liquid film evaporation enhancement in the channel angles and best bubble rise in that case. For the same reason, a similar range for the heat transfer coefficient in the condensation region can be applied. Liquid vapor thermal resistance along the PHP, $R_{l\text{-}v}$, is the most important part of the thermal chain and is a function of the pressure and temperature state conditions from the evaporator to the condenser and this resistance determines the PHP heat transfer rate. This is influenced by number of turns, inclination angle, filling ratio, area of PHP etc. Generally PHPs should introduce small contact resistances. Usually in power electronics, contact thermal resistances appear between the power module and the cooling device, heat sink or heat exchanger due to the surface roughness.

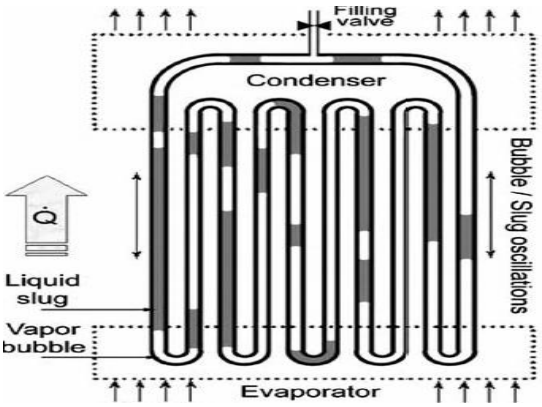

Fig. 1. Closed loop PHP

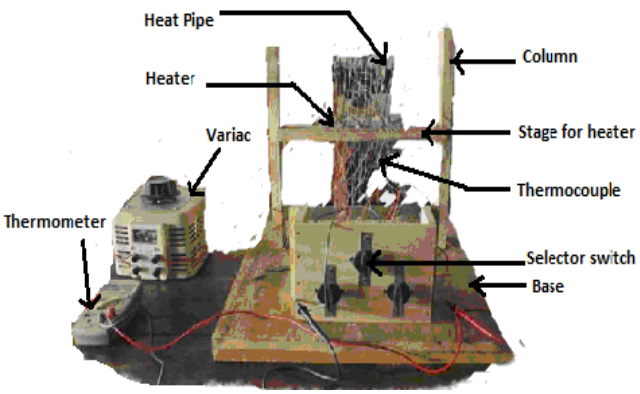

Fig. 2. Experimental setup

2.2. Heat transfer mechanism in heat pipes

Heat pipes rely on a temperature difference between the ends of the pipe, and cannot lower temperatures at either end beyond the ambient temperature. When one end of the heat pipe is heated the working fluid inside the pipe at that end evaporates and increases the vapor pressure inside the cavity of the heat pipe. The latent heat of evaporation absorbed by the vaporization of the working fluid reduces the temperature at the hot end of the pipe. The vapor pressure over the hot liquid working fluid at the hot end of the pipe is higher than the equilibrium vapor pressure over condensing working fluid at the cooler end of the pipe, and this pressure difference drives a rapid mass transfer to the condensing end where the excess vapor condenses, releases its latent heat, and warms the cool end of the pipe. Non-condensing gases in the vapor impede the gas flow and reduce the effectiveness of the heat pipe, particularly at low temperatures, where vapor pressures are low. In the case of vertically-oriented heat pipes the fluid may be moved by the force of gravity.

An interesting property of heat pipes is the temperature over which they are effective. Initially, it might be suspected that a water-charged heat pipe would only work when the hot end reached the boiling point (100°C) and steam was transferred to the cold end. However, the boiling point of water is dependent on absolute pressure inside the pipe. In an evacuated pipe, water will boil just slightly above its melting point (0°C). The heat pipe will operate, therefore, when the hot end is just slightly warmer than the melting point of the working fluid. Similarly, a heat pipe with water as a working fluid can work well above the boiling point (100°C), if the cold end is low enough in temperature to condense the fluid.

3. Experimental method

3.1. Experimental setup

The experimental setup is shown in Fig. 2. The setup consists of a meandering heat pipe (D_i: 2mm, D_o: 3mm, L: 148cm, material: copper), creating a total of 9 turns. The heat pipe is divided into 3 regions- the evaporator (39.5cm), adiabatic section (77cm) and the condenser (31.5cm).18 thermocouples (Type K **(**Chromel/Alumel); range: -200°C to +1200°C) are glued to the wall of heat pipe; 6 for each sections. These are compatible with the digital thermometer (Y type) used in temperature measurement. The evaporator section is inside an aluminum box, separated from outside using mica sheets, glass wool etc. with Nichrome wire (diameter = 0.25 mm, resistivity: 1.0×10^{-6} Ω-m, specific heat: 450 $Jkg^{-1}K^{-1}$) wounded inside, which is heated by a power supply unit (AC, 220V, 50Hz) via a variac (3ϕ, 300V,60 Hz). For cooling the working fluid, forced convection is used by a DC fan. The whole apparatus is set on a wooden test stand with provision of angular movement of the PHP. For avoiding complicacy, working fluids are incorporated in the heat pipe manually. The other accessories of the setup are adapter circuit, selector switches etc.

3.2. Experimental procedure

- After the construction of the whole setup the experiment is carried out.
- The experiment is performed for two different working fluids and six different angular orientations of the heat pipe.
- First the heat pipe is filled 100% by working fluid water (injecting by syringe) keeping the PHP in vertical (0˚) position.
- Different heat inputs were provided to the system and temperature reading of different sections were measured by digital thermometer.

- Then the position is changed to 30˚, 45˚, 60˚, 75˚, 90˚ positions and keeping the filling ratio the same, above procedure is repeated later on.
- The above three steps are carried out systematically for the working fluid ethanol.
- For cooling the condenser a cooling fan is used. It is connected to an adapter circuit.

4. Results and discussion

The experiments being carried out for water and ethanol and for 6 different angular orientations of the heat pipe, provide a similar trend of thermal characteristics. In this research, the value of thermal resistance is considered as an indication of efficiency, i.e. higher value of R_{th} refers to higher difference of temperature between evaporator and condenser section and eventually indicates a higher efficiency of the system.

4.1. Characteristics of temperature distribution

The Temperature vs. Heat input curves show a similar pattern for all the experimental conditions. So a typical curve is presented in Fig.3, which is taken for 60˚ inclination with water as working fluid. In fact, for all the experimental cases, the curves at first increase rapidly with heat input and then the rate of increase becomes slow to some extent. This is same for all the temperature data; i.e. for evaporator, condenser and adiabatic section. But, certainly, the rate of increase is different for different regions. After reaching the boiling point, the temperature increase in evaporator slows down due to the heat required in phase transfer. Slowing down of the temperature increase in the condenser section can be attributed to the fact that, at some point of time, it becomes close to the room temperature. So no further need of cooling is then necessary. Temperature in the evaporator rises higher in case of water compared with in that of ethanol. This is due to the difference in boiling temperature of them (water: 100˚C; ethanol: 78.1˚C). An adiabatic region was considered to be present in between the evaporator and the condenser, where temperature was expected to be constant throughout. But, in the assumed adiabatic region, temperature was not found to be constant; it increased at a small rate with input heat. Temperature distribution along the heat pipes can be summarized to be in somewhat exponential pattern for evaporator and condenser section.

4.2. Variation of thermal resistance

Thermal resistance is considered in this paper as an indicator of heat pipe effectiveness. It is defined as the ratio of difference in average temperature of evaporator section and average temperature of condenser section for any instance to the heat input at that time. It indicates how much resistance does heat experiences in the system; so that the condenser region temperature cannot rise very high, and the system thus seems to be effective in cooling purpose. The curves of thermal resistance are of similar pattern for all the cases. They are maximum at minimum heat input and minimum at maximum heat input; i.e. thermal resistance has an inverse relationship with heat input. These curves follow an exponential pattern, and a typical graph is shown in Fig.4, which is taken from the data set of 60˚ inclination with water. But, the fall of thermal resistance is not of the same rate for all cases, it varies up to some extent. The thermal resistance, R_{th} falls slowly in the inclined mode, in fact in the range of 30˚ to 75˚, so this working range is found to be more effective. As we have already mentioned that higher resistance means higher efficiency, so we can state that with highly heated appliances, heat pipe efficiency will fall down. But yet, this fall can be controlled with proper designing, which includes appropriate working fluid, filling ratio and inclination angle.

4.3. Effect of working fluid

By comparative analysis of experimental data, water is found to be a better working fluid than ethanol in the work endeavor. This is an expected behavior due to their thermo physical properties. Water boils at higher temperature (100˚C) than ethanol (78.1˚C). Moreover, water has a higher specific heat value (Cp= 4.187) than ethanol (Cp= 2.44). So heat is accumulated in water is higher in amount than ethanol; that allows it to keep the condenser region temperature low and resulting in better working efficiency. The optimum quantity of working fluid needed depends on various parameters and is still an area of research, as stated by Khandekar et al. [8] and Groll [1]. The curves show more or less an exponential pattern.

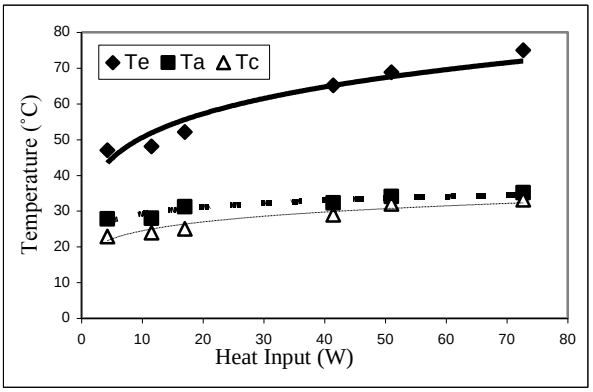

Fig. 3. Variation of temperature with heat input

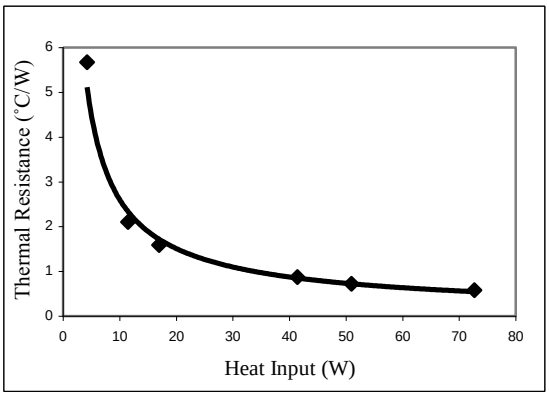

Fig.4. Variation of thermal resistance with heat input

Water shows higher thermal resistances than ethanol in subsequent cases, which is shown in Fig. 5.Thermal resistances drop with increase in heat input initially with higher slope in the curves. But, as heat input increases, the slope of the curves are smaller, indicating the smaller rate of decrease in thermal resistances.

4.4. Effect of inclination

The effect of heat flux in vertical orientation has been experimentally noted down by Tong et al. [9] and Khandekar et al. [10].In vertical mode the vapor bubbles which take up heat in the evaporator grow in size. Their own buoyancy helps them to rise up in the tube section. Simultaneously other bubbles, which are above in the tube, are also helped by their respective buoyant forces. These rising bubbles in the tube also carry the liquid slugs trapped in between them. In this mode of operation there is a natural tendency for the liquid slugs to travel downwards, helped by gravity force, toward the evaporator. In horizontal mode (90° inclination angle) of operation, there was hardly any macro movement of bubbles. This strongly suggests that gravity does play a role in the PHP. Since gravity force is ineffective, all the movement of bubbles and slugs has to be necessarily done by the pressure forces. These forces are created due to temperature difference, which exists between evaporator and condenser. At 60° to 75° inclination, closed loop PHP performs better than other position. Comparative analysis of inclination is shown in Fig.6. Effect of gravity, pressure differential in the system, temperature etc may have influence in this fact.

5. Summary and conclusions

Closed loop pulsating heat pipes are complex heat transfer systems with a very strong thermo- hydrodynamic coupling governing the thermal performance. The effect of pressure, bubble formation and phase transfer is very important in design of heat pipes. Different heat input to these devices give rise to different flow patterns inside the tubes. This in turn is responsible for various heat transfer characteristics. The study strongly indicates that design of these devices should aim at thermo-mechanical boundary conditions which resulting convective flow boiling conditions in the evaporator leading to higher local heat transfer co-efficient.

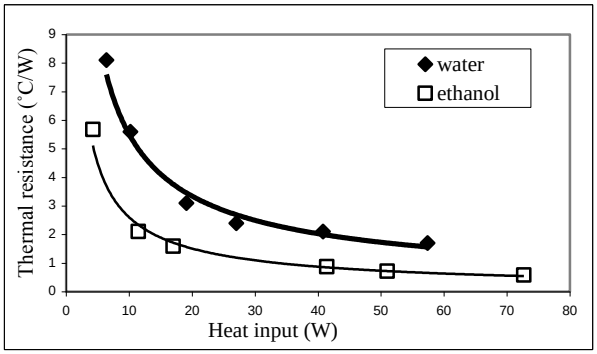

Fig. 5. Comparative study of working fluids

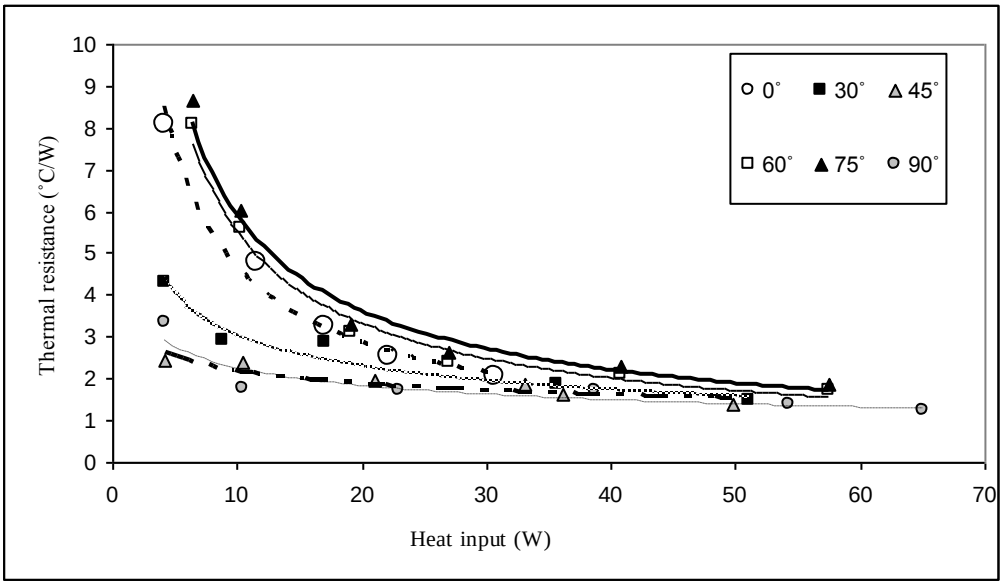

Fig. 6. Comparative thermal resistances with varying inclination

The inclination operating angle changes the internal flow patterns thereby resulting in different performance levels. In this research, best performance is obtained at 75˚ orientation. In all circumstances, water provided to be better performing than ethanol in the experiment. This can be well attributed to their thermo-physical properties. A close comprehensive look is required for designing heat pipes, as their performance is a function of orientation, filling ratios and working fluid. Most satisfactory pattern of design may vary up to some extent from case to case.

Acknowledgements

The authors feel greatly honored to be able to express their earnest gratitude to the Department of Mechanical Engineering, BUET for the accomplishment of this research.

References

[1] Groll, M., Khandekar, S.,2002. Pulsating heat pipes: a challenge and still unsolved problem in heat pipe science, Applied Thermal Engineering 23 (4), p. 17–28.
[2] Nishio, S., Nagata, S., Baba, S. and Shirakashi R., 2002. “Thermal performance of SEMOS heat pipes,” Proceedings of 12th International Heat Transfer Conference, Grenoble, France, pp. 477–482.
[3] Shafii, M., Faghri, A. and Zhang, Y., 2001. Thermal Modeling of Unlooped and Looped Pulsating Heat Pipes, ASME Journal on Heat Transfer 23, p. 1159–1172.
[4] Gaugler, Richard, 1944. Heat Transfer Devices, Dayton, Ohio.
[5] Grover, G.M., Cotter, T. P. and Erickson, G. F., 1964. Structures of Very High Thermal Conductance, Journal of Applied Physics 35 (6), p. 1990–1991.
[6] Eastman, G. Y., 1968. The Heat Pipe, Scientific American 218, p. 38-46.
[7] Zuo, Z. J. and Gunnerson, F. S., 1995. Heat Transfer Analysis of a Inclined Two-Phase Closed Thermosyphon, Journal of Heat Transfer 117, p. 1073-1075.
[8] Khandekar, S., Dollinger, N. and Groll, M., 2003. Understanding Operational Regimes of Pulsating Heat Pipes: An Experimental Study, Applied Thermal Engineering 23(6), p. 707–719.
[9] Tong, B., Wong, T. and Ooi, K., 2001. Closed-Loop Pulsating Heat Pipe, Applied Thermal Engineering 21(18), p. 1845–1862.
[10] Khandekar, S., Groll, M., Charoensawan, P. and Terdtoon, P., 2002. “Pulsating heat pipes: thermo-fluidic characteristics and comparative study with single phase thermosyphon,” Proceedings of the 12th International Heat Transfer Conference. Grenoble, France, p.459–464.

Available online at www.sciencedirect.com

SciVerse ScienceDirect

Procedia Engineering 00 (2012) 000–000

Procedia Engineering

www.elsevier.com/locate/procedia

5th BSME International Conference on Thermal Engineering

Effect of filling ratio on heat transfer characteristics and performance of a closed loop pulsating heat pipe

Himel Barua*, Mohammad Ali, Md. Nuruzzaman, M. Quamrul Islam, Chowdhury M. Feroz

Bangladesh University of Eengineering & Technology, Dhaka-1000, Bangladesh

Abstract

Thermal control is a generic need for any heat dissipation system. Heat pipes emerge as the most appropriate technology and most thermal effective solution due to their excellent heat transfer capability, heat transfer efficiency and structural simplicity. In many engineering applications higher heat flux is important. Two phase passive devices are proven solutions for modern microelectronics thermal management. This paper attempts to describe the heat transfer characteristics of closed loop pulsating heat pipe (CLPHP) which are new entrants in the family of closed passive two phase heat transfer system. It also shows the comparison of thermal efficiency of CLPHP for different filling ratios with two different working fluids, water and ethanol. This device is a combination of lot of events and mechanisms like bubble nucleation, collapse and agglomeration, bubble pumping action, pressure and temperature perturbations, flow regime changes, dynamic instabilities, meta-stable non equilibrium conditions, flooding, bridging etc. All contribute towards the thermal performance of a device. But, such a complex operating mechanism is not understood well yet and the present state of the art cannot predict the required design parameters for a given task. The aim of research work presented in this paper is to better understand the heat transfer characteristics of these mechanisms through experimental investigations. Experiments are conducted on a CLPHP made of capillary tube of 2.2mm inner diameter. The heat transfer characteristics and the performance of the CLPHP are investigated for filling ratios of 100 %, 82.5%, 63%, 41.3% and 28%. The results indicate that the performance of this device changes with the changing of working fluid, filling ratios and heat input.

Keywords: Electronic cooling, Closed Loop Pulsating Heat Pipe (CLPHP); Pressure pulsations; Bond Number; Thermal Resistance

Nomenclature

Eo	Eötvös number
Δρ	Density difference of two phases
G	Gravitational force
L	Characteristics length
OD	Outer diameter of tube
ID	Inner diameter of tube

Greek symbol

* Corresponding author. Tel.: +8801816805676;
E-mail address: himelbarua_me@yahoo.com

σ	Surface tension
ρ	Density
a	Acceleration associated with body force
r	Radius of capillary tube
γ	Surface tension of interface
Subscripts	
liq	Liquid
vap	Vapour
crit	Critical

1. Introduction

Heat pipe is device of very high thermal conductance. The idea of heat pipe was first suggested by Gaugler [1]. It was not, however, until its independent invention by Grover [2], Grover et al. [3] that the remarkable properties of the heat pipe became appreciated and serious development work took place. The main difference between the heat pipe and the thermo-siphon is orientation. In thermo-siphon, the evaporator has to be in lower side and the condenser is in upper side so that, after condensation the condensate will go downward due to the gravitational force, but in heat pipe the evaporator can be in any orientation. In this experiment, a thermo-siphon is used for observing its pulsating action under different heat input, filling ratio and different liquid. Here, condenser is placed in upper side, so the gravitational force will assist the liquid to move downward. There are different types of heat pipe. Pulsating or oscillating heat pipe is one of them. The general configuration of pulsating heat pipe is shown in Fig. 1. The pulsating heat pipe was first introduced by Akachi et al. [4]. Typically it comprises of a tube of capillary dimension, which has been evacuated and partially filled with the working fluid. Surface tension of liquid effects result in the formation of slugs of liquid interspersed with bubbles of vapour. The operation of pulsating heat pipes are outlined as, when one end of the of the capillary tube is heated (the evaporator), the working fluid evaporates and increases the vapour pressure, thus causing the bubbles in the evaporator zone to grow. This pushes the liquid towards the low temperature end (the condenser). Cooling of the condenser results in a reduction of vapour pressure and condensation of bubbles in that section of the heat pipe. The growth and collapse of bubbles in the evaporator and condenser sections, respectively, results in an oscillating motion within the tube. Heat is transferred through latent heat in the vapour and through sensible heat transported by the liquid slugs. The performance of a pulsating heat pipe depends on several parameters. They are (i) working fluid, (ii) internal diameter, (iii) total tube length, (iv) length of condenser, evaporator and adiabatic section, (v) number of turns and loops, and (vi) inclination angle.

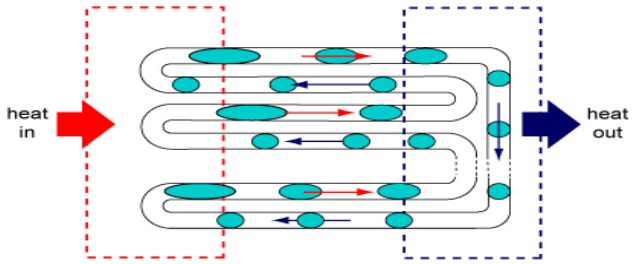

Fig 1: Pulsating heat pipe

The present experiment is done by two different working fluids. One is water and another is ethanol. The choice of working fluid depends on various properties. A first consideration in the identification of the working fluid is the operating vapour temperature and its inherent thermal conductivity. Within the acceptable temperature range several fluids can show the desired property and a variety of characteristics has to be examined in order to determine the most acceptable of these fluids for the application being considered. The prime requirements are as follows [5-10]: (i) good thermal stability, (ii) moderate vapours pressure on the operating temperature range, (iii) high latent heat, (iv) high thermal conductivity, (v) high surface tension, (vi) acceptable freezing or pour point, (vii) low liquid and vapour viscosity, and (viii) high $\frac{dP}{dT}$ that means the change of pressure is high with the change of temperature. Higher value of this parameter indicates high bubble formation and high heat transfer. The selection of the working fluid is also dependent on the base of thermodynamic consideration which is concerned with the various limitations of heat flow occurring within the heat pipe like viscous, sonic, capillary, entrainment and nucleates boiling limitation. In our experiment, water and ethanol are used as working fluid. At 21.5 ^{0}C, the surface tension force of water and ethanol is 72.75 cp and 21.25cp, respectively. As surface tension of water is

higher than ethanol, water will create good pumping action and bubble formation than ethanol which is essential for high heat transfer. Vapour pressure and merit number are two parameter used to screen potential working fluid. Merit number is a means of ranking the heat pipe fluids. The merit number of water and ethanol is 1.63×10^{11} and 1.61×10^{10} As, water has higher merit number than ethanol indicating higher surface tension and latent heat of vaporization which are the prior requirement for high heat transfer. According to merit number rating, water is more effective working fluid than ethanol in the basis of heat transfer.

2. Experimental setup

A circular heat pipe is built using capillary copper tubing with OD 2.3 mm and ID 2.2 mm. The total length of the pipe is 155 cm. The tubes are bent on U shape. Two of the bends, located at two extreme ends were kept longer on one side to complete the closed loop circuit through the T connector. The T connector is used for entering fluid in the pipe. Formation of slug in a capillary tube is attributed to the balance of gravity and surface tension forces, leading to the definition of Eötvös number or alternatively the Bond number. The theoretical maximum tolerable inner diameter of the PHP capillary tube is given by the following equation:

$$D_{crit} = 2[\sigma / g(\rho_{liq} - \rho_{vap})]^{1/2} \tag{1}$$

The Eötvös number is

$$Eo = (\Delta \rho g L^2) / \sigma \tag{2}$$

The relationship between Bond number and Eötvös number is

$$Eo = (Bo)^2 \tag{3}$$

where, Bond number is

$$Bo = \frac{\rho a L^2}{\gamma} \tag{4}$$

For successful pumping action inside the heat pipe the surface tension force has to be higher than the gravitational force. For this, the bond number value should be less than 2. The diameter of the tube should be lower of the critical diameter for the development of bubble pumping action. So, for the experiment the experimental diameter is chosen such that it coincides with the requirement. The whole experiment is done on vertical position which is denoted as 0^0 inclinations throughout the literature. The PHP is to be filled by different amount of working fluid. In this experiment, the filling ratios are 28%, 63%, 41.3%, 82.5%, and 100% for both working fluids. The filling procedure is done by a syringe injector. The filling is done thorough the T connector. After filling the tube on their desired filling ratios, the evaporator section has to be heated by the variac. By changing the variac voltage, different voltage and current are supplied to the evaporator. For heating the evaporator, nichrome wire is coiled in the evaporator and this wire is connected to the variac. For cooling the condenser a cooling fan is used. So the cooling is appeared to be done by forced convection. It is connected to an adapter circuit. The cooling fan is operated by DC current. So, the adapter circuit is used to convert the AC current to DC current. The air speed delivered by fan is around 3 m/s. The K type thermocouples are used to monitor the temperature of different position of the heat pipe. The temperature is recorded on a regular time interval. Generally, the time interval is 10 minutes. The temperature is recorded when the steady state condition is reached.

3. Results and Discussion

3.1. Effect of filling ratio on thermal resistance with different heat input

For both water and ethanol, the highest thermal resistance is obtained at lower heat input. Thermal resistance of ethanol is higher than water which indicates the low heat transfer through ethanol than water. With the increase of filling ratio, thermal resistance along with the rate of change of thermal resistance changes for both fluids. For water, at lower heat input and lower filling ratio, initially thermal resistance falls quickly. Figure 2 shows that at 45% filling ratio, the lowest thermal resistance is obtained for 5.3W and 11.5W heat input. Beyond that, it increases with filling ratio. At higher heat input as 21.1W, 29.75W, 47.6W and 57.8W and lower filling ratio, thermal resistance is lower because of the transformation of flow regime from slug flow to annular. So, heat transfer rate is higher. But, thermal resistance increases with the filling ratio and at nearly 50% -70% filling ratio, it remains constant indicating the presence of a vapour layer in the internal tube surface.

Heat transfer rate is nearly constant throughout that region. At higher filling ratio with the same heat input, the amount of evaporation decreases along with the temperature difference of evaporator and condenser which decreases the heat transfer. At lower heat input, with lower filling ratio, the heat transfer is dominated by conduction through the tube body and the liquid movement. For Ethanol, at 5.3W heat input and 28% filling ratio, thermal resistance is nearly 9.3, which is higher than water in same temperature and filling ratio. But, with the increment of filling ratio at same heat input, the thermal resistance falls drastically. So, the heat transfer rate increases quickly. In Fig. 3 it can be found that for lower heat inputs as 5.3W and 11.5W, the change rate of thermal resistance is higher. But, at higher heat inputs, between 21W to 57.8W, heat transfer is nearly constant throughout that region due to low thermal resistance change. The lowest thermal resistance is obtained at 68.9W heat input and beyond 60% filling ratio for all heat input.

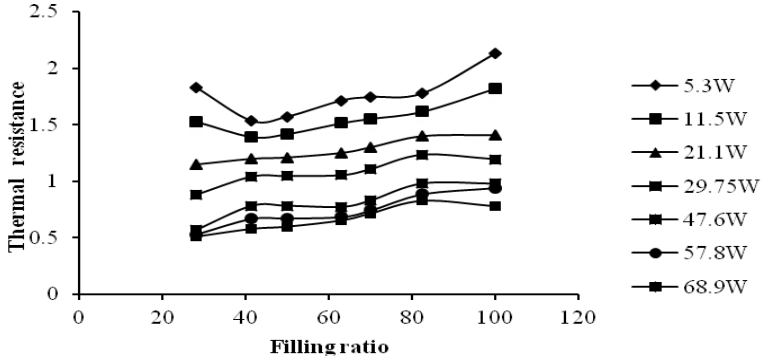

Fig 2: Variation of thermal resistance with filling ratio for water

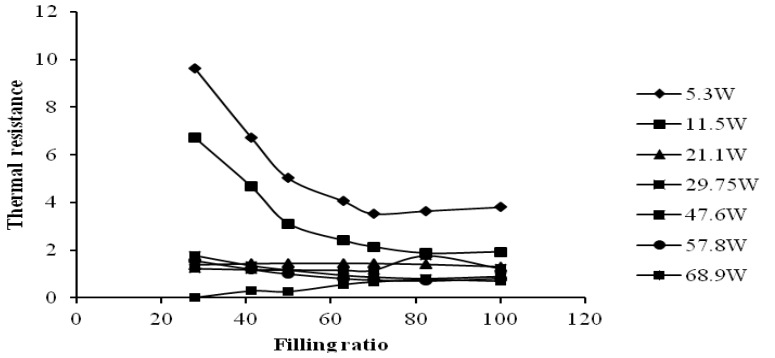

Fig 3: Variation of thermal resistance with filling ratio for ethanol

3.2. Effect of heat input on thermal resistance of water and ethanol with different filling ratio

Thermal resistance is reciprocal function of heat input and linear function of temperature difference of evaporator and condenser. With the increment of heat input, thermal resistance decreases. For water, at lower filling ratio and at lower heat input, thermal resistance is high because of the lack of internal energy in water. Figure 4 shows the variation of thermal resistance with heat input for water. For 28% filling ratio and at lower heat input, the thermal resistance is nearly 1.7 which is higher than ethanol in same heat input. With the increment of heat input for the same filling ratio, thermal resistance decreases quickly and heart transfer increases. But with the increase of filling ratio, the rate of decrement of thermal resistance goes down which indicates the slow increment of heat transfer rate. From Fig. 4, we can see that the highest thermal resistance for lower heat input is obtained at 100% filling ratio and the lowest is obtained for 28% at 70W heat input. Figure 5 shows that for ethanol at 28% filling ratio, thermal resistance is highest because of low specific heat of ethanol. For low heat input, temperature rise is low along with heat transfer. But, with the increment of heat input, thermal resistance changes drastically, specifically between 5W – 20W heat input. Beyond that region, the rate of change is lower and heat transfer seems nearly constant. With the increase of filling ratio, the thermal resistance at lower heat input decreases. As, the amount of working fluid is higher, the amount of evaporation is low, bubble formation is lower too. Heat transfer through advection dominates the system and heat transfer rate increases. But, for all the filling ratios, between 20W-

50W heat inputs, thermal resistance shows linear characteristics indicating the initialization of phase change. Beyond 60W heat input, for all filling ratios, turbulence of flow occurs due to high heat input and the flow rate increases, results increase of heat transfer and drop of thermal resistance.

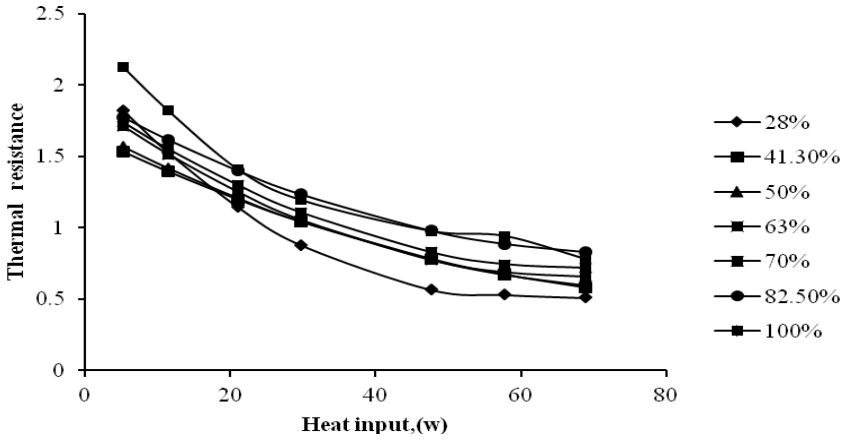

Fig 4: Variation of thermal resistance with heat input for water

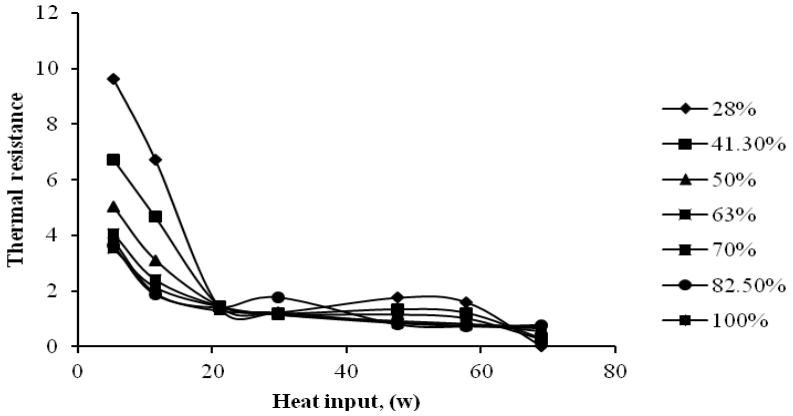

Fig 5: Variation of thermal resistance with heat input for ethanol

3.3. Effect of filling ratio on evaporation and condenser temperature for water and ethanol

Evaporation temperature increases with the increment of heat input. Maximum evaporation temperature will be obtained at the highest heat input. At 68.9 W heat input, the highest temperature is obtained and the minimum is at 5.3W for both water and ethanol. The evaporation temperature of water is higher than ethanol in same heat input. With the increment of heat input, the evaporation temperature rises. Figure 6 shows that for water, at same heat input, evaporator temperature decreases with the rise of filling ratio till 70%. Beyond 70% filling ratio, the evaporation temperature rises with the increment of filling ratio. From Fig.7 it can be found that for ethanol, the evaporation temperature remains constant throughout the filling ratio beyond 80%. Initially, the rate of increment of evaporation temperature is high, but, with increment of filling ratio, the rate mitigates. The change rate of evaporation temperature of water is higher than the ethanol. The lowest evaporation temperature is obtained at 70% filling ratio for water and at 100% for ethanol at different heat input. With the increment of heat input, condenser temperature increases for both water and ethanol. But, the condenser temperature profile with respect to change of filling ratio is different for water and ethanol. Figure 8 shows that for water at lower heat input, initially condenser temperature increases in slow rate with the increment of filling ratio. But, beyond 40%

filling ratio, the temperature reduces and reaches the lowest temperature at filling ratio nearly 60%. At that filling ratio thermal resistance is moderate. Beyond 60% filling ratio, condenser temperature increases slowly and the thermal resistance remains nearly same till 80%. After that, with the increment of filling ratio, condenser temperature remains nearly constant along with thermal resistance.

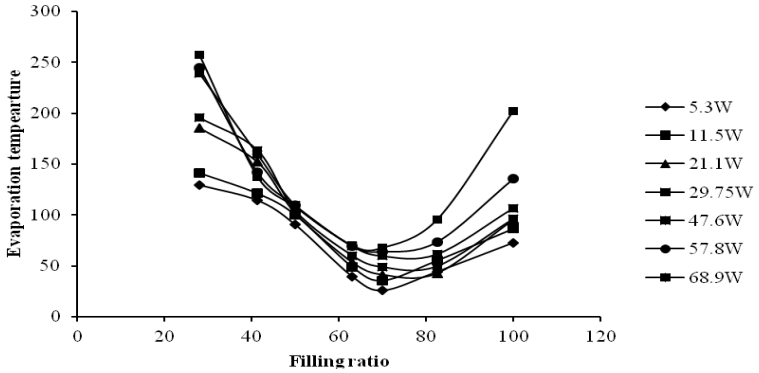

Fig 6: Variation of evaporation temperature with filling ratio for water

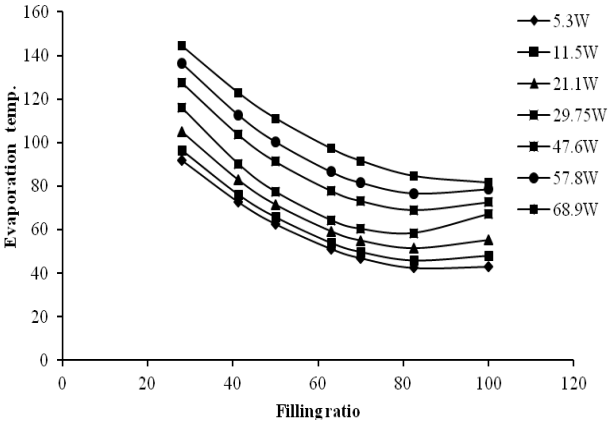

Fig 7: Variation of evaporation temperature with filling ratio for ethanol

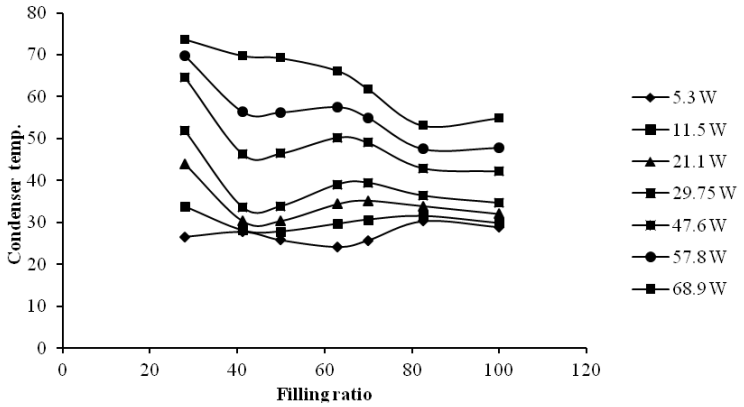

Fig 8: Variation of condenser temperature with filling ratio for water

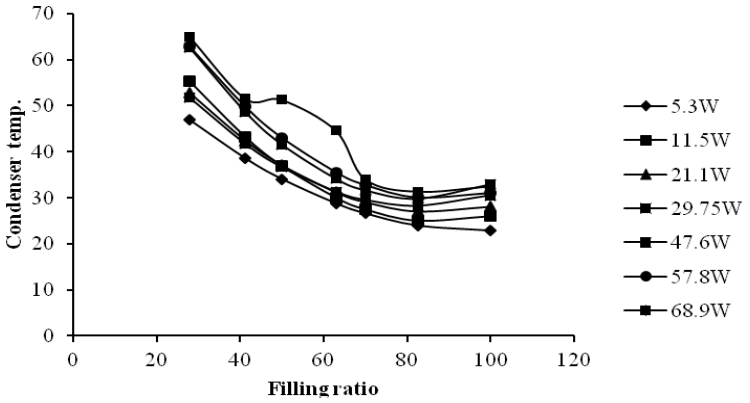

Fig 9: Variation of condenser temperature with filling ratio for Ethanol

The lowest condenser temperature of water is obtained near 40% filling ratio for all the high heat inputs beyond 29.75W. At that filling ratio, thermal resistance is lower for high heat inputs which have already been shown in Fig 2. For ethanol, the condenser profile is relatively smooth in comparison with the water. The lowest condenser temperature is found in the lowest heat input. And, with the increment of filling ratio, condenser temperature drops. Figure 9 shows that initially, the condenser temperature drops quickly but, with the increment of filling ratio the rate of change of condenser temperature becomes low. Near 60% filling ratio, the graph seems flat. At 80% filling ratio, the condenser temperature is the lowest along with thermal resistance for all heat input. Beyond that point, condenser temperature rises with the increment of filling ratio.

4. Conclusions

From the investigation of this heat pipe at different heat input, filling ratio and fluid, the following findings are obtained. For lower heat input, water is better working fluid than ethanol at wide range of filling ratio in the basis of heat transfer. But in higher heat input (more than 70W), both the working fluid shows nearly same thermal resistance. So, though in lower heat input, water transfers more heat than ethanol, in high heat input, both shows similar heat transfer rate. For water, both at lower and higher heat input, lower filling ratio shows less thermal resistance and most optimum heat transfer is obtained at nearly 30% filling ratio. For ethanol, at low heat input, the best performance is obtained at high filling ratio beyond 50% in the basis of heat transfer. For high heat input, it works as a effective working fluid at all filling ratio which indicates that, ethanol shows high heat transfer rate at high heat input for all filling ratio. For same filling ratio and heat input, water shows higher evaporation temperature than ethanol. For water, with the increase of filling ratio, evaporation temperature decreases and the lowest temperature is obtained at nearly 70% filling ratio. Beyond that filling ratio temperature increases again. In other case, for ethanol, evaporation temperature decreases with the filling ratio up to 80%. Beyond that, the temperature remains nearly constant. For water, initially condenser temperature decreases with the increment of filling ratio. Beyond a certain filling ratio it increases again. For ethanol, in all heat input, condenser temperature decreases with the rise of filling ratio up to 80% filling ratio. Beyond that, the temperature remains nearly constant.

Acknowledgements

The work was performed in heat transfer laboratory, fuel testing laboratory and instrumentation laboratory in Bangladesh University of Engineering and Technology (BUET), Dhaka-1000, Bangladesh. The authors are grateful to BUET, to provide laboratory facilities and other financial support for this research.

References

[1] Gaugler, R. S US patent 2350348.Appl. 21 Dec, 1972.Published 6 June 1944.
[2] Grover, G. M US patent 3229759.Filed 1963.
[3] Grover, G.M., Cotter, T.P. and Erickson, G.F. Structures of very high thermal conductance. J. App. Phys., Vol. 35, pp.1190-1191,1964.
[4] Akachi, H., Polaassek, F., SStulc, P., “Pulsating heat pipes”, Proceedings of the 5th International Heat Pipe Symposium, Melbourne, Australia, 1996, p. 208–217 (ISBN 0-08-042842-8).

[5] Wallis, G., “One Dimensional Two-Phase Flow”, McGraw Hill Inc., 1969 (ISBN 0-0706-794-28).
[6] Khandekar, S., Schneider, M., Groll, M., “Mathematical modeling of pulsating heat pipes: state-of-the-art and future challenges”, 5th ASME/ISHMT joint International Heat and Mass Transfer Conference, Kolkata, India, 2002, pp. 856–862 (ISBN 0-07-047443-5).
[7] Groll, M., Khandekar, S., “Pulsating heat pipes: a challenge and still unsolved problem in heat pipe science”, Proceedings of the 3rd International Conference on Transport Phenomena in Multiphase Systems, Kielce, Poland, 2002, pp. 35–44 (ISBN 83-88906-03-8).
[8] Duminy, S., “Experimental investigation of pulsating heat pipes”, Diploma thesis, Institute of Nuclear Engineering and Energy Systems (IKE), University of Stuttgart, Germany, 1998.
[9] Khandekar, S., Schneider, M., Schaafer, P., Kulenovic, R., Groll, M., “Thermofluid dynamic study of flat plate closed loop pulsating heat pipes”, Microsc. Thermophys. Eng. 6 (4) (2002) pp. 303–318 (ISSN 1089-3954).
[10] Shafii, M.B., Faghri, A., Zhang, Y., “Thermal modeling of unlooped and looped pulsating heat pipes”, ASME J. Heat Transfer 123 (2001) pp. 1159–1172.

.

Available online at www.sciencedirect.com

SciVerse ScienceDirect

Procedia Engineering 00 (2012) 000–000

Procedia Engineering

www.elsevier.com/locate/procedia

5th BSME International Conference on Thermal Engineering

Heat transfer enhancement in a tube using rectangular-cut twisted tape insert

Bodius Salam*, Sumana Biswas, Shuvra Saha, Muhammad Mostafa K Bhuiya

Department of Mechanical Engineering, Chittagong University of Engineering & Technology, Chittagong 4349, Bangladesh

Abstract

An experimental investigation was carried for measuring tube-side heat transfer coefficient, friction factor, heat transfer enhancement efficiency of water for turbulent flow in a circular tube fitted with rectangular-cut twisted tape insert. A copper tube of 26.6 mm internal diameter and 30 mm outer diameter and 900 mm test length was used. A stainless steel rectangular-cut twisted tape insert of 5.25 twist ratio was inserted into the smooth tube. The rectangular cut had 8 mm depth and 14 mm width. A uniform heat flux condition was created by wrapping nichrome wire around the test section and fiber glass over the wire. Outer surface temperatures of the tube were measured at 5 different points of the test section by T-type thermocouples. Two thermometers were used for measuring the bulk temperatures. At the outlet section the thermometer was placed in a mixing box. The Reynolds numbers were varied in the range 10000-19000 with heat flux variation 14 to 22 kW/m^2 for smooth tube, and 23 to 40 kW/m^2 for tube with insert. Nusselt numbers obtained from smooth tube were compared with Gnielinski [1] correlation and errors were found to be in the range of -6% to -25% with r.m.s. value of 20%. At comparable Reynolds number, Nusselt numbers in tube with rectangular-cut twisted tape insert were enhanced by 2.3 to 2.9 times at the cost of increase of friction factors by 1.4 to 1.8 times compared to that of smooth tube. Heat transfer enhancement efficiencies were found to be in the range of 1.9 to 2.3 and increased with the increase of Reynolds number.

Keywords: Heat transfer enhancement; rectangular–cut twisted tape insert; heat transfer enhancement efficiency.

1. Introduction

To improve the performance of heat exchanging devices for reducing material cost and surface area and decreasing the difference for heat transfer thereby for reducing external irreversibility, lot of techniques have been used. Among different passive means to increase heat transfer coefficient, twisted tape inserts are promising. The secondary flow (swirl flow) generated by twisted tape effects fluid flow across the tape-partitioned tube, promotes greater mixing and higher heat transfer coefficients. Experimental investigation of heat transfer and friction factor characteristics in a double pipe heat exchanger fitted with regularly spaced twisted tape elements were studied by Eiamsa-ard et al., 2006. Heat transfer, friction factor and heat transfer enhancement efficiency characteristics in a circular tube fitted with conical-ring turbulators and a twisted-tape swirl generator have been investigated experimentally by Promvonge and Eiamsa-ard, 2007. Influences of insertion of wire coils in conjunction with twisted tapes on heat transfer and friction characteristics in a circular tube using air as the test fluid were experimentally investigated by Promvonge, 2008. Eiamsa-ard et al., 2009, experimentally

* Corresponding author. Tel.: +880-31-714953; fax: +880-31-714910.
E-mail address: bsalam@cuet.ac.bd

Nomenclature

A	Area of the heated region of tube (m^2)
A_f	Flow area (m^2)
c_p	Specific heat of water at constant pressure (J/kg.K)
d_i	Tube inner diameter (m)
d_o	Tube outer diameter (m)
f	Friction factor (-)
h	Heat transfer coefficient ($W/m^2.K$)
k	Thermal conductivity of water (W/m.K)
k_w	Thermal conductivity of tube material (W/m.K)
L	Effective tube length for heat transfer (m)
L_t	Length between tappings (m)
m	Mass flow rate of water (kg/s)
Q	Heat transfer rate (W)
$\dot{Q}$	Volume flow rate (m^3/s)
q	Heat flux (W/m^2)
T	Temperature (^oC)
U_m	Mean velocity (m/s)
Nu	Nusselt number (-)
Nu_{th}	Nusselt number from Gnielinski, 1976 correlation (-)
Pr	Prandtl number (-)
Re	Reynolds number (-)
y	Tape pitch (m)
w	Tape width (m)
Δp	Pressure drop (N/m^2)

Greek symbols

δ	Tape thickness (m)
ρ	Density of water (kg/m^3)
μ	Dynamic viscosity of water (kg/m.s)
η	Heat transfer enhancement efficiency (-)

Subscripts

b	Bulk
e	With insert
i	Local value
in	Inlet
out	Outlet
pp	Constant pumping power
s	For smooth tube
wi	Inner surface
wo	Outer surface

investigated the influences of the tube with short-length twisted tape inserts on the heat transfer, friction factor, and heat transfer enhancement efficiency. Heat transfer, friction factor and heat transfer enhancement efficiency behaviors in a tube equipped with the combined devices between the twisted tape and constant/periodically varying wire coil pitch ratio were experimentally investigated by Eiamsa-ard et al., 2010a. Eiamsa-ard et al., 2010b experimentally determined the influences of twin-counter/co-twisted tapes on heat transfer rate, friction factor, and heat transfer enhancement efficiency. Heat transfer, flow friction and heat transfer enhancement efficiency characteristics in a tube fitted with delta-winglet twisted tape, using water as working fluid were investigated experimentally by Eiamsa-ard et al., 2010c. Murugesan et al., 2010, experimentally investigated heat transfer, friction factor, and heat transfer enhancement efficiency characteristics of a double pipe heat exchanger fitted with square-cut twisted tapes. Shabanian et al., 2011 reported the experimental and computational fluid dynamics modeling studies on heat transfer, friction factor and heat transfer enhancement efficiency of an air cooled heat exchanger equipped with classic and jagged twisted tape.

The scope of the present work is to experimentally investigate the tube side heat transfer and friction factor of a circular tube fitted with rectangular-cut twisted tape insert. Data are compared with smooth tube heat transfer and friction values and the values of heat transfer enhancement efficiency are reported.

2. Experimental

The schematic diagram of the experimental set up is shown in Fig 1. The test section was made from 914 mm of copper tube (26.6 mm ID and 30 mm OD), of which 900 mm was considered to be the test section. A stainless steel twisted tape was made by twisting 2 mm thick (δ) 20 mm width (w) straight strip. Tape pitch (y) of 105 mm was made which gave twist ratio (y/w) 5.25. The twisted tape was cut in the top region of 8 mm depth and 14 mm width rectangular cut to allow the flow from the both sides of the tape to mix at the cut regions. Figure 2 shows the twisted tape. The nichrome resistance wire was spirally wound uniformly on the outer surface of the test section to supply the heating power. Mica sheet was used between the tube and heating wire for electrical insulation. The heating wire was covered with mica sheet and fiber glass. The heating wire was connected to 220 Volt main. Five T-type (copper constantan) thermocouples were placed on five equally spaced points of the test section to measure the outer surface temperatures of the tube. Two thermometers were placed at the inlet and outlet of the tube to measure the inlet and outlet water temperatures respectively. To measure the outlet temperature, the thermometer was placed in a mixing chamber, which was thermally insulated to minimize the heat loss. A rotameter (Metric 24G, SS float) of 26 L/min capacity was provided to measure the water flow rate. A U-tube manometer was used to measure the pressure drop across the tube. The distance between two pressure tappings was 1180 mm.

Initially, water was taken in the tank and pumped to the test section through the rotameter. The flow rate of water was varied by the gate valve for different data and kept constant during the experiment. A minimum of 9.9 L/min was used and it was increased up to 18.9 L/min. After switching on the heating power the sufficient time was given to attain the steady state condition. In each run, data were taken for water flow rate, water inlet, outlet, tube outer surface temperatures and pressure drop readings.

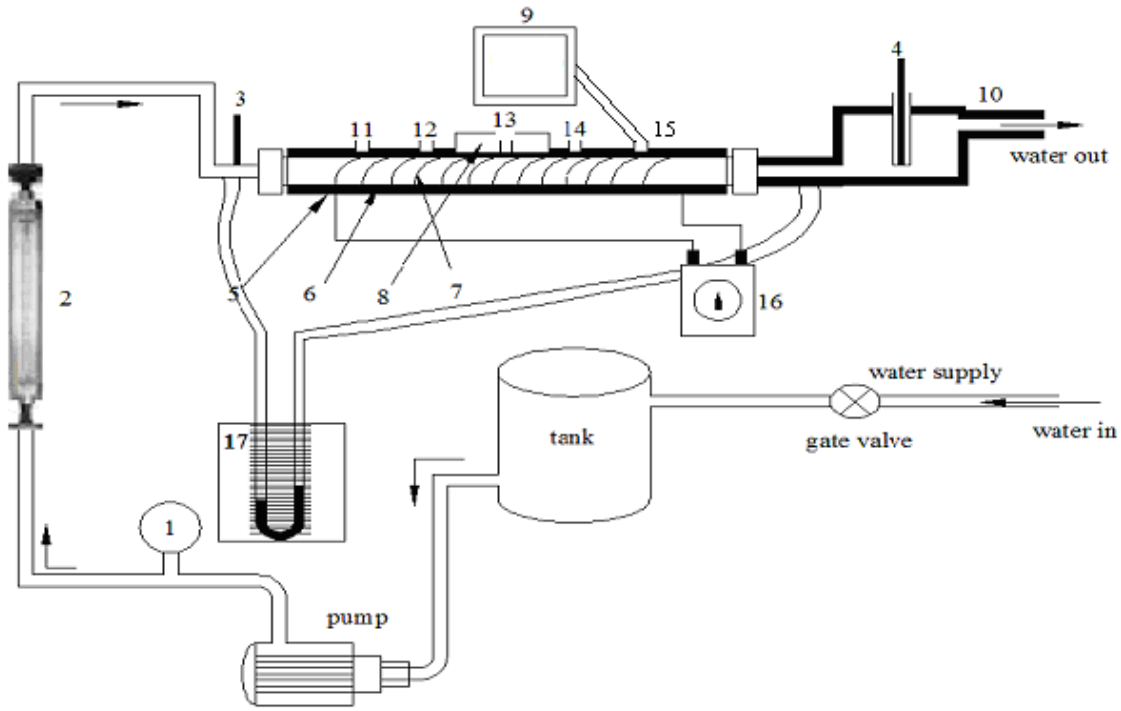

Fig. 1. Schematic diagram of experimental apparatus. 1. Pump 2. Rotameter 3.4. Thermometers 5. Insulation 6. Test section 7. Nichrome wire 8. AC source 9. Temperature reading device 10. Mixing chamber 11-15. Thermocouples 16. Voltage regulator 17. U-tube manometer.

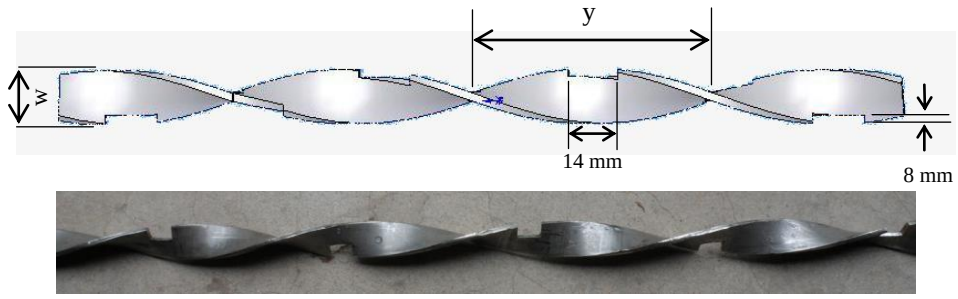

Fig. 2. Twisted tape insert.

3. Data reduction

Heat transfer rate by the heater to water was calculated by measuring heat added to the water. Heat added to water was calculated by,

$$Q = m\,c_p\left(T_{out} - T_{in}\right) \tag{1}$$

Heat transfer coefficient was calculated from,

$$h = \frac{q}{\left(T_{wi} - T_b\right)} \tag{2}$$

and heat flux was obtained from,

$$q = \frac{Q}{A} \tag{3}$$

where, $A = \pi d_i L$ (4)

The bulk temperature was obtained from the average of water inlet and outlet temperatures,

$$T_b = \frac{T_{in} + T_{out}}{2} \tag{5}$$

Tube inner surface temperature was calculated from one dimensional radial conduction equation,

$$T_{wi} = T_{wo} - Q \cdot \frac{\ln\left(d_o/d_i\right)}{2\pi k_w L} \tag{6}$$

Tube outer surface temperature was calculated from the average of five local tube outer surface temperatures,

$$T_{wo} = \sum_{i=1}^{5} T_{wo,i}/5 \tag{7}$$

Theoretical Nusselt number was calculated from Gnielinski, 1976, correlation,

$$Nu_{th} = \frac{\left(f/8\right)\left(Re - 1000\right)Pr}{1 + 12.7\left(f/8\right)^{1/2}\left(Pr^{2/3} - 1\right)} \tag{8}$$

where from Petukhov, 1970,

$$f = \left(0.79\ln Re - 1.64\right)^{-2} \tag{9}$$

$$Re = \frac{\rho U_m d_i}{\mu} \tag{10}$$

$$Pr = \frac{\mu C_p}{k} \tag{11}$$

$$Nu = \frac{h d_i}{k} \tag{12}$$

Mean water velocity was obtained from,

$$U_m = \frac{m}{A_f} \tag{13}$$

Flow area was obtained from,

$$A_f = \frac{\pi}{4} d_i^{\,2} \tag{14}$$

Friction factor, f can be calculated from

$$f = \frac{\Delta p}{\left(L_t/d_i\right)\left(\rho U_m^{\ 2}/2\right)} \tag{15}$$

Δp is the pressure drop across tappings. All the fluid properties were evaluated at bulk temperature.

4. Results and Discussions

Heat transfer and friction data for the smooth tube were collected first. These data were taken to check the validity of the set up and measurement techniques over the range of Reynolds number 10000 to 19070. Figure 3 shows the comparison of experimental Nusselt number for smooth tube with those calculated from Gnielinski, 1976 correlation. Data fall within -24.7% and -5.6% of the Gnielinski, 1976 values with r.m.s. value of error 20.3%. Salam et al., 2010 used the same set up and errors were found within -13% and +18% with r.m.s. value of error 12% when they compared the data with Dittus and Boelter, 1930 values. Nusselt numbers for the smooth tube and the tube with twisted tape insert are shown in Fig. 3. It is seen that, Nusselt numbers incresed with the increase of Reynolds number and twisted tape insert gave higher values of Nusselt number than those for smooth tube. For tube with twisted tape, Reynolds number was calculated based on inner diameter of the tube. For smoth tube Nusselt numbers, Nu_s, increased from 54 to 120 with the increase of Reynolds number from 10002 to 18811 respectively. For tube with rectangular-cut twisted tape insert for Re_e = 10116, Nusselt number, Nu_e, was found to be 125 and for Re = 19070, Nu_i was increased to 309. At comparable Reynolds numbers, Nusselt numbers in tube with rectangular-cut twisted tape insert were enhanced by 2.3 to 2.9 times compared to those of smooth tube with the average enhancement of 2.6 times. Swirl flow generated by twisted tape was responsible for thinning the thermal boundary layer and increasing the mixing between core and tube wall flows, Eiamsa-ard et al., 2009. Rectangular-cut in the twisted tape was responsible for additional disturbances which increased the tangential contact between secondary flow and the wall surface of the tube, Murugesan et al., 2010. This made heat transfer coefficient higher through the flow.

The variation of heat flux with Reynolds number for smooth tube and tube with rectangular-cut twisted tape insert is shown in Fig. 4. It is found that with the increase of Re heat fluxes increased and rectangular-cut twisted tape insert gave higher heat fluxes than those for smooth tube. Higher values of heat transfer coefficient was responsible for this enhancement, although temperature difference between wall and bulk fluid, $(T_{wi}-T_b)_e$ significantly decreased for tube with insert, Fig. 5. An average of 68% enhancement of heat flux was observed for tube with insert than that of smooth tube.

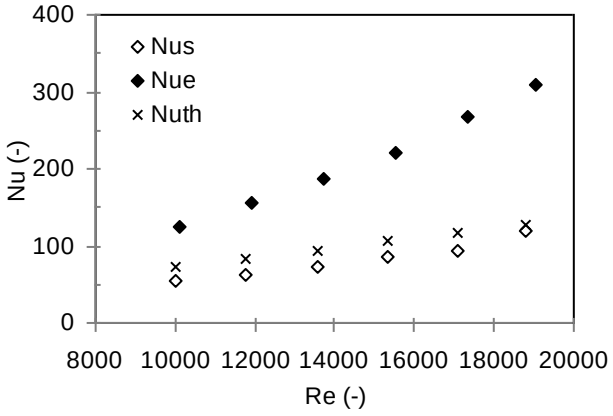

Fig. 3. The variation of Nusselt number with Reynolds number.

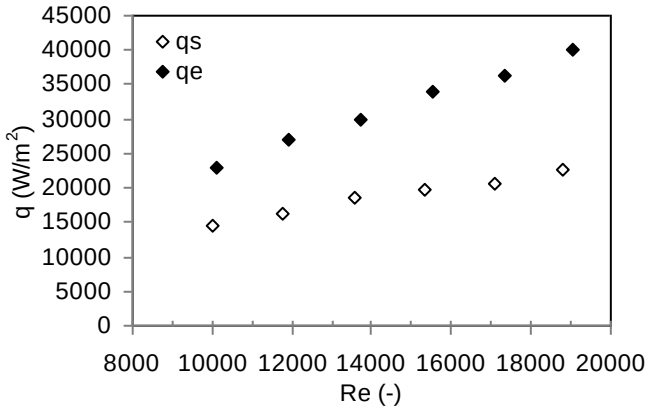

Fig. 4. The variation of heat flux with Reynolds number.

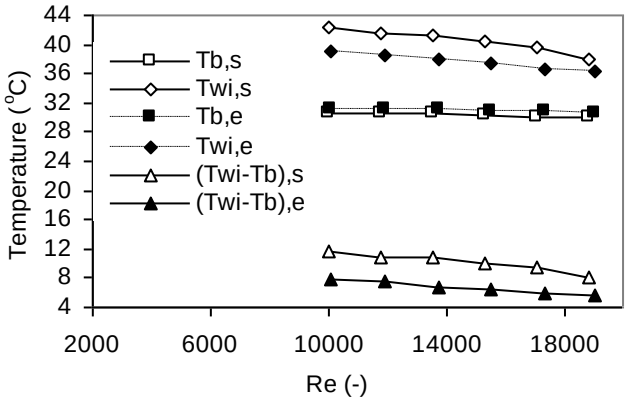

Fig. 5. The variation of temperature with Reynolds number.

Figure 6 shows the variations of friction factor with Reynolds number. Friction factors for both smooth tube, f_s and tube with insert, f_e decreased with the increase of Re. And f_e were found to be 39% to 80% higher than f_s. These higher values of f_e than f_s are due to the high viscous loss near the wall regions caused by swirl flow, Eiamsa-ard et al., 2010b. Figure 6 also shows the friction factor obtained from Petukhov relation, f_{th}. F_{th} were found to be significantly lower than f_s. Enterence effect could be the reason for this.

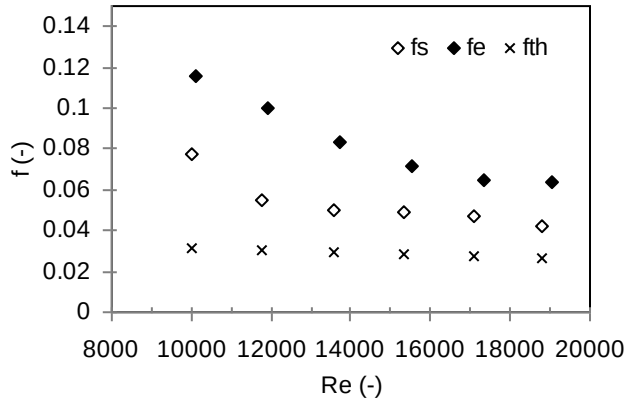

Fig. 6. The variation of friction factor with Reynolds number.

5. Heat transfer enhancement efficiency (η)

To assess the performance of heat exchanging devices with insert it is necessary to evaluate heat transfer enhancement efficiency (η). This efficiency is calculated using constant pumping power (Web and Kim, 2005; Murugresan et al., 2010). For constant pumping power,

$$\dot{Q}_e \times \Delta p_e = \dot{Q}_s \times \Delta p_s \quad (16)$$

Now considering the assumptions from Web and Kim, 2005 and from Eqs. (15) and (16)

$$f_e \cdot Re_e^3 = f_s \cdot Re_s^3 \quad (17)$$

The experimental values of Nusselt number and friction factor for smooth tube can be correlated as

$$Nu_s = 0.00053 Re_s^{1.1941} \cdot Pr^{0.3} \quad (18)$$

$$f_s = 147.2 Re_s^{-0.8305} \quad (19)$$

The errors between Nusselt numbers for experimental and predicted values for smooth tube were found to be in the range of -5.2% to 7% with r.m.s. value of 4.1%. For friction factor these errors were found to be from -9.5% to 10.3% with r.m.s. value 6.9%.

Similarly the experimental values of Nusselt number and friction factor for tube fitted with insert are correlated as

$$Nu_e = 0.00023 Re_e^{1.432} \cdot (y/w)^{-0.01} \quad (20)$$

$$f_e = 25.475 Re_e^{-1.0173} \cdot (y/w)^{2.4015} \quad (21)$$

The errors between Nusselt numbers for experimental and predicted values for tube with insert were found to be in the range of -2.2% to 1.4% with r.m.s. value of 1.5%. For friction factor these errors were found to be from -4.4% to 5.3% with r.m.s. value 3.3%.

From Eqns. (17), (19) and (21)

$$Re_s = 0.4455 Re_e^{0.9139} \cdot (y/w)^{1.107} \quad (22)$$

Heat transfer enhancement efficiency,

$$\eta = \left|\frac{h_e}{h_s}\right|_{PP} = \left|\frac{Nu_e}{Nu_s}\right|_{PP} \quad (23)$$

From Eqns. (18) and (22),

$$Nu_s = 0.0002 Re_e^{1.09} \cdot Pr^{0.3} \cdot (y/w)^{1.322} \quad (24)$$

From Eqns. (20), (23), and (24)

$$\eta = 1.2387 Re_e^{0.339} \cdot Pr^{-0.3} \cdot (y/w)^{-1.33} \quad (25)$$

Heat transfer enhancement efficiency, η, calculated using Eqn. (25) is shown in Fig. 7. It is quite obvious that with the increase of Reynolds number heat transfer enhancement efficiencies increased continuously. The value of η increased from 1.8 to 2.2 with the increase of Re from 10116 to 19070.

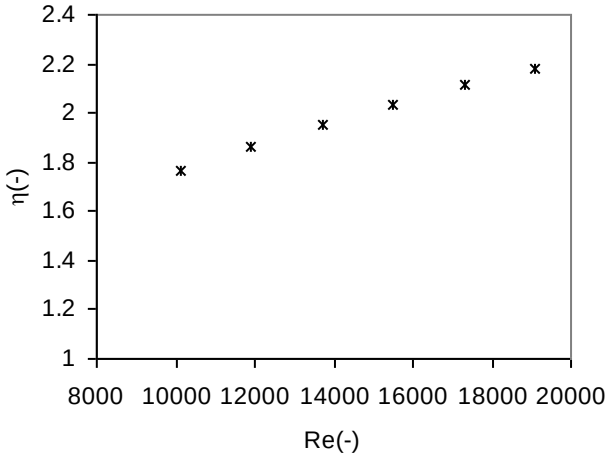

Fig. 7. The variation of heat transfer enhancement efficiency with Reynolds number.

6. Conclusions

An experimental investigation was carried out for measuring tube-side heat transfer coefficient, friction factor, heat transfer enhancement efficiency of water for turbulent flow in a circular tube fitted with rectangular-cut twisted tape insert. The results can be summarized as,

(a) The Nusselt number increased with the increase of Re. The experimental Nu_s values fall within -6% and -25% of the Gnielinski, 1976 value (Nu_{th}). The experimental values were enhanced by 2.3 to 2.9 times compared to Nu_s values.

(b) An average of 68% enhancement of heat flux was observed for tube with rectangular-cut twisted tape insert (q_e) than that of smooth tube (q_s).

(c) The experimental f_e values were found to be 39% to 80% higher than f_s values.

(d) The heat transfer enhancement efficiency (η) were found to be increased with Re, and η values ranged between 1.9

and 2.3.

References

[1] Dittus FW and Boelter LMK. Univ. Calif.(Berkely) Pub. Eng., Vol. 2, p. 443, 1930.
[2] Eiamsa-ard S, Nivesrangsan P, Chokphoemphun S and Promvonge P. Influence of combined non-uniform wire coil and twisted tape inserts on thermal performance characteristics. International Communications in Heat and Mass Transfer, 2010a; 37: 850-856.
[3] Eiamsa-ard S, Thianpong C and Eiamsa-ard P. Turbulent heat transfer enhancement by counter/co-swirling flow in a tube fitted with twin twisted tapes. Experimental Thermal and Fluid Science, 2010b; 34:53-62.
[4] Eiamsa-ard S, Thianpong C, Eiamsa-ard P and Promvonge P. Convective heat transfer in a circular tube with short-length twisted tape insert. International Communications in Heat and Mass Transfer, 2009; 36: 365-371.
[5] Eiamsa-ard S, Thianpong C and Promvonge P. Experimental investigation of heat transfer and flow friction in a circular tube fitted with regularly spaced twisted tape elements. International Communications in Heat and Mass Transfer, 2006; 33: 1225-1233.
[6] Eiamsa-ard S, Wongcharee K, Eiamsa-ard P and Thianpong C. Heat transfer enhancement in a tube using delta-winglet twisted tape inserts. Applied Thermal Engineering, 2010c; 30: 310-318.
[7] Gnielinski V. New equations for heat and mass transfer in turbulent pipe flow and channel flow. International Chemical Engineering, 1976; 16: 359-368.
[8] Murugesan P, Mayilsamy K and Suresh S. Turbulent heat transfer and pressure drop in tube fitted with square-cut twisted tape. Fluid Flow And Transport Phenomena, 2010; 18(4): 609-617.
[9] Petukhov BS. Heat transfer in turbulent pipe flow with variable physical properties in: J.P. Harnett (Ed.), Advances in Heat Transfer, vol. 6. Academic Press, New York; 1970.
[10] Promvonge P and Eiamsa-ard S. Heat transfer behaviors in a tube with combined conical-ring and twisted tape insert. International Communications in Heat and Mass Transfer, 2007; 34: 849-859.
[11] Salam B, Biswas S and Bhuiya MMK. Heat transfer enhancement in a tube using twisted tape insert. Proc. The 13th Asian Congress of Fluid Mechanics, 17-21 Dec. 2010, Dhaka, Bangladesh, 835-838.
[12] Shabanian SR, Rahimi M, Shahhosseini M and Alsairafi AA. CFD and experimental studies on heat transfer enhancement in an air cooler equipped with different tube inserts. International Communications in Heat and Mass Transfer, 2011; 38: 383-390.
[13] Webb RL and Kim NH. Principles of enhanced heat transfer. 2nd ed. Taylor & Francis, Boca Raton; 2005.

Available online at www.sciencedirect.com

SciVerse ScienceDirect

Procedia Engineering 00 (2012) 000–000

Procedia Engineering

www.elsevier.com/locate/procedia

5th BSME International Conference on Thermal Engineering

Buoyancy Driven Natural Convection Flow in an Enclosure with Two Discrete Heating from Below

Fahad Sadekin Zaman, Tanmoy Saha Turja, Md. Mamun Molla*

*Dept. of Electrical Engineering & Computer Science, North South University, Dhaka, 1229, Bangladesh,
E-mail: mmamun@northsouth.edu, mmamun@gmail.com

Abstract

Natural convection flow of air in a two-dimensional, rectangular enclosure with two discrete heating from below is studied numerically, using the stream function-vorticity formulation of the Navier-Stokes and energy equations. An implicit finite difference together with successive over relaxation (SOR) method is applied to solve the non-dimensional governing equations. Discrete heating is simulated by two heat sources on the bottom of the rectangular cavity and the different values of dimension less heat source height (H), is considered for this study. The Rayleigh number is varied from 10^3 to 10^7, based on the cavity height. The numerical results are presented in the form of streamline and isotherm as well as the physical quantities, such as, the local and average rate of heat transfer in terms of the local and average Nusselt number respectively. Businessman

Keywords: natural convection, rectangular cavity, discrete heating, finite difference, Nusselt number.

Nomenclature

g	Gravitational force
H	Height of the channel (m)
L	Length of the cavity (m)
P	pressure of the fluid (Pa.s)
Pr	Prandtl number
Ra	Rayleigh number
t	time (s)
T_H,T_c	Temperatures at different parts of the cavity
U,V	velocity components (m/s)
Greek symbols	
Ψ	Streamlines
Ω	Vorticity
α	Thermal diffusivity
ε	Heat source length
θ	Non-dimension temperature
ψ	Stream function
ρ	Density of the fluid
ν	Kinematic viscosity

* Corresponding author. Tel.: +88028852000, Ext 1519 (office)
E-mail address: mmamun@northsouth.edu, mmamun@gmail.com

1. Introduction

All electronic components generate heat when it's used. Surrounding temperature of the electronic components have a direct impact on the performance of the device. In order to achieve the optimal performance of the device, the temperature should be within the prescribed limit. Electronic components mounted on the vertical boards, these form channels or cavities and the heat generated by the components is removed by a naturally induced flow of air. Thermally induced buoyancy forces for the fluid motion and transport processes generated in an enclosure is getting much importance because of its practical significance in science and technology. The topic of natural convection in enclosures is one of the most active areas in heat transfer research today. The current study is the prototype of many industrial and engineering applications such as cooling of electronic equipments, meteorology, geophysics, operations and safety of nuclear reactors, energy storage, fire control, studies of air movement in attics and greenhouses, solar distillers, growth of crystals in liquids etc. Buoyancy driven flows are complex because of essential coupling between the flow and thermal fields.

In the literature, investigation on natural convection heat transfer reported that the heat transfer occurs in an enclosure due to the temperature differences across the walls, a benchmark solution to natural convection of air flow in a square cavity with differentially heated walls was given by *Davis et al.* [1] where $10^3 \leq Ra \leq 10^6$ was considered. A comparison exercise was also performed by *Davis and Jones* [2] to confirm the accuracy of the benchmark solution. Natural convection of air in enclosures heating from below and symmetrically cooling from the sides has been numerically investigated using stream function-vorticity formulation by *Ganzarolli and Milanez* [3]. Natural convection of air in enclosures heating from one side and cooling from the ceiling has been numerically investigated using stream function-vorticity formulation by *Aydin et al.* [4]. Natural convection of rectangular enclosures with localized heating from bottom and cooling from the sides has been numerically investigated in which air is used as a working fluid has been studied by *Aydin and Yang* [5]. The heat transfer of a rectangular cavity with adiabatic side walls and aspect ratios of 1, 2, 4 and 8 is considered, along with the inclination angle of the enclosure was varied from 0^o to 180^0 and the effect of inclination on flow field and heat transfer is studied in the paper by *Chang* [6]. Natural convection in enclosure with discrete isothermal heating from below is studied numerically using finite element method with aspect ratios of 0.5 to 1 and inclination angle of 0^o to 30^0 was considered, where the pressure-velocity form of the Navier–Stokes equations and energy equation are used to represent the mass, momentum, and energy conservations of the fluid medium in the enclosure by *Saha et al.* [7]. *Radhwan et al.* 8] have studied the natural convection in a square enclosure with discrete heating of one vertical wall with isothermal heating strip, the remainder of the wall and the opposing one are isothermally maintained at a lower temperature where they have found that the variation of the local Nusselt number is influenced by this flow pattern and the average Nusselt number is higher than that of a discrete heating strip mounted on an adiabatic wall. *Nasr et al.* [9] have studied the natural convection in an enclosed cavity heated from the lower corner and cooled from the ceiling using the control volume method and solved the full vorticity transport equation together with the stream function and energy equations. A laminar natural convection in an inclined complecated cavity with three flat and one wavy walls is numerically investigated by *Dalal et al.* [10] where they have used simple algorithm with deferred quick scheme in curvilinear coordinates and found that the angle of inclination affects the flow and heat transfer rate in the cavity. *Barletta et al.* [11] have studied the natural convection in a 2D cavity with two vertical isothermal walls and two adiabatic walls which are either straight and horizontal or elliptic and the dimensionless mass, momentum and energy balance equations are solved by means of two different software packages based on Galerkin finite element methods which provides a cross-validation of the results. Natural convection in differentially heated and partially divided square cavities with internal heat generation is studied by *Oztop and Bilgen* [12] where the vertical walls were isothermal, horizontal walls adiabatic and an isothermal partition at the reference temperature was attached to the bottom wall. They have obtained the result for various geometrical parameters specifying the height, thickness and position of the partition. *Wang and Hamed* [13] have studied the natural convection in inclined rectangular enclosures subjected to bidirectional temperature gradients where they have found that the thermal conditions of cavity end walls have a significant effect on mode-transition of thermal convection flows and hence, on heat transfer effectiveness inside the cavity, and on the Hysteresis phenomenon (multi-steady solutions) occurred as the cavity angle of inclination varied. *Jin et al.* [14] have studied the effects of rotation on natural convection cooling from three rows of heat sources in a rectangular cavity and found that the optimal distribution of heaters in rotating fluid is close to the results in the stationary situation if they have same dominated circulation direction. Numerical study of the natural convection flow resulting from the combined buoyancy effects of thermal and mass diffusion in a cavity with differentially heated side walls is studied by *Snoussi et al.* [15] using the Control-Volume based Finite Element Method (CVFEM) and solves the full vorticity transport equation together with the stream function, concentration and energy equations. *Ali and Hasanuzzaman* [16] did an experimental investigation natural convection heat transfer through a square enclosure of V-corrugated vertical plates. The result shows the increase of mass flow rate increases the heat transfer rate and the decrease of water inlet temperature increases the heat transfer rate. *Mohamed A. Teamah et al.* [17] investigated double diffusive convective flow in a square enclosure with segmented heat sources solved numerically. The numerical procedure adopted in this analysis yields consistent performance

over a wide range of parameters, Rayleigh number ($10^3 \leq Ra \leq 10^6$), dimensionless heater lengths ($0.2 \leq L/H \leq 1$), buoyancy ratio ($-10 \leq N \leq 10$) and Prandtl number ($0.01 \leq Pr \leq 100$). The results were compared with previous results and good agreements were found. *Dixit and Babu* [16] used lattice Boltzman method to stimulate high Rayleigh number in natural convection for a square cavity. The flow goes turbulent for $Ra \geq 10^8$, for $Ra \leq 10^6$ the flow is laminar. *Aswatha et al.* [17] have studied natural convection of air in a cavity subject to uniform, sinusoidal and linearly varying temperature at the bottom wall, symmetrically cooled side walls with uniform temperature and insulated top wall for the range of Ra from 10^3 to 10^7 and aspect ratios of 0.5 and 1.

The objective of the present work paper is to investigate the flow and heat transfer characteristics in a rectangular cavity using the stream function-vorticity formulation of the Navier-Stokes and energy equations subject to uniform temperature at an adiabatic bottom wall with two discrete heat sources. Side walls are symmetrically cooled with uniform temperature and top wall is adiabatic. The range of Ra varies from 10^3 to 10^7 based on the cavity height. An implicit finite difference together with successive over relaxation (SOR) method is applied to solve the non-dimensional governing equations. As it appears from the existing literature, this study is the first attempt at studying the natural convection phenomenon in an enclosure under the above mentioned thermal conditions. The partial heating from the bottom simulates the electronic components such as chips. As natural convection flow in enclosures arises in many engineering process, the results to be obtained here may be applicable to other fields as well. The effects of the Rayleigh number on the fluid flow and heat transfer is determined.

2. Formulation of the problem

A cavity as illustrated in Fig.1 is chosen for simulating natural convective flow and heat transfer characteristics. The cavity has the bottom wall with two heat sources which is assumed to be isothermally heated at constant temperature T_H, the side walls are isothermally cooled at a constant temperature T_C, while the bottom wall, except the heated part, and the top wall are considered to be adiabatic. The inertia force is negligible and the medium is considered to be isotropic. We consider the flow of air in the cavity where buoyant flow develops because of the thermal induced density gradient. Heat transfers from hot wall to cold walls. The governing equations for natural convection flow and conservation of mass, momentum and energy are written as:

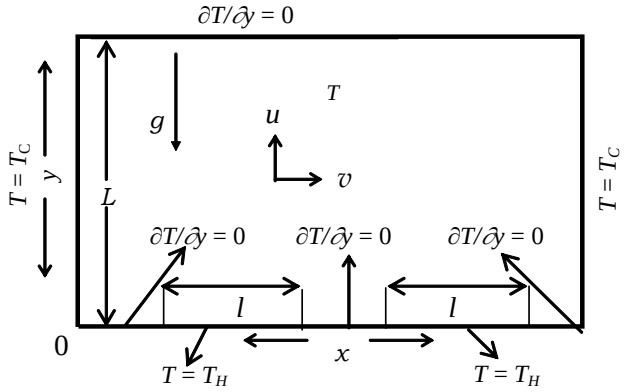

Fig.1: Schematic figure and coordinate systems

$$\frac{\partial u}{\partial x} + \frac{\partial v}{\partial y} = 0 \tag{1}$$

$$\frac{\partial u}{\partial t} + u\frac{\partial u}{\partial x} + v\frac{\partial u}{\partial y} = -\frac{1}{\rho}\frac{\partial p}{\partial x} + \upsilon\left(\frac{\partial^2 u}{\partial x^2} + \frac{\partial^2 u}{\partial y^2}\right) \tag{2}$$

$$\frac{\partial v}{\partial t} + u\frac{\partial v}{\partial x} + v\frac{\partial v}{\partial y} = -\frac{1}{\rho}\frac{\partial p}{\partial y} + \upsilon\left(\frac{\partial^2 v}{\partial x^2} + \frac{\partial^2 v}{\partial y^2}\right) + \rho g\beta(T - T_c) \tag{3}$$

$$\frac{\partial T}{\partial t} + u\frac{\partial T}{\partial x} + v\frac{\partial T}{\partial y} = \alpha\left(\frac{\partial^2 T}{\partial x^2} + \frac{\partial^2 T}{\partial y^2}\right) \tag{4}$$

Non- dimensional vorticity – velocity – temperature equations

$$\frac{\partial \Omega}{\partial \tau}+\frac{\partial (U\Omega)}{\partial X}+\frac{\partial (V\Omega)}{\partial Y}=\left(\frac{\partial^2}{\partial X^2}+\frac{\partial^2}{\partial Y^2}\right)\Omega+\frac{Ra}{Pr}\frac{\partial \theta}{\partial X} \tag{5}$$

$$\left(\frac{\partial^2}{\partial X^2}+\frac{\partial^2}{\partial Y^2}\right)\Psi=-\Omega \tag{6}$$

$$\frac{\partial \theta}{\partial \tau}+\frac{\partial (U\theta)}{\partial X}+\frac{\partial (V\theta)}{\partial Y}=\frac{1}{Pr}\left(\frac{\partial^2}{\partial X^2}+\frac{\partial^2}{\partial Y^2}\right)\theta \tag{7}$$

where the dimensionless variables are defined by

$$X=\frac{x}{L},\ Y=\frac{y}{L},\quad \tau=\frac{t}{L^2/\alpha},\quad U=\frac{u}{\alpha/L},$$
$$V=\frac{v}{\alpha/L},\quad \Psi=\frac{\psi}{\alpha},\quad \theta=\frac{T-T_C}{T_H-T_C},\quad Ra=\frac{g\beta\Delta TK}{\alpha\nu},\quad \overline{P}=\frac{\rho\alpha^2}{L^2}P \tag{8}$$

The non-dimensional stream function, ψ, satisfies the following equations

$$U=\frac{\partial \psi}{\partial Y},\quad V=-\frac{\partial \psi}{\partial X} \tag{9}$$

Boundary Conditions :

$$\psi=0,\quad \theta=0 \qquad \text{for } 0\le Y\le 1 \text{ at } X=0 \tag{10a}$$

$$\psi=0,\quad \theta=0 \qquad \text{for } 0\le Y\le 1 \text{ at } X=1 \tag{10b}$$

$$\psi=0,\quad \theta=1 \qquad \text{for } \frac{1}{4}-\varepsilon\le X\le\frac{1}{4}+\varepsilon \text{ and } \frac{3}{4}-\varepsilon\le X\le\frac{3}{4}+\varepsilon \text{ at } Y=0 \tag{10c}$$

$$\psi=0,\quad \frac{\partial\theta}{\partial Y}=0 \qquad \text{for } 0<X<\frac{1}{4}-\varepsilon,\ \frac{1}{4}+\varepsilon<X<\frac{3}{4}-\varepsilon \text{ and } \frac{3}{4}+\varepsilon<X<1, \text{ at } Y=0 \tag{10d}$$

$$\psi=0,\quad \frac{\partial\theta}{\partial Y}=0 \qquad \text{for } 0\le X\le 1 \text{ at } Y=1 \tag{10e}$$

where ε is the non-dimensional heat source length.

3. Numerical Procedures

The governing equations (5)-(7) along with the boundary conditions (10) are solved numerically, employing finite difference method. The convective and the diffusion terms are discretised by the central difference formula. The velocity-vorticity and the energy equations are solved using Alternating Direction Implicit (ADI) method and the stream function equation is solved by SOR (successive over relaxation) scheme where the relaxation parameter lies between 0 and 1. Here the grid is 100 ×100 and the time step dt = 10^{-3} is considered for the whole computations.

4. Results and Discussion:

The stream function-vorticity and energy equations (5)-(7) along with boundary conditions (10), are solved using an implicit finite difference together with successive over relaxation (SOR) method is applied to solve the non-dimensional governing equations. Figure 2 (a)-(b) describes the streamline and isotherms respectively for Ra = 10^3. In figure 2(c)-(d), we get similar patterns in the streamlines and isotherm while in this case we consider Ra = 10^4. In these cases, the flow is dominated the conduction effect. The streamlines form two symmetric cells with one is anti-clockwise (primary vortex) and the other one is clockwise (secondary vortex) rotating. However in case of Ra = 10^5, we get centrally located hot cell but the cool cell gets decentralized and corresponding isotherm illustrates a counter clockwise flow of fluid. As we can observe in figure 2c, the hot fluid is lifted up from the second heat source along the right cold wall of the cavity towards the adiabatic

ceiling and then flows down to the first heat source along the right cold wall of the cavity. In figure 2d, we notice that for Ra = 10^6 the result of interaction between warmer and colder fluid streams, the hot streamline cell grows wider and the shrinking cool streamline cell moves to top right corner of the cavity. Corresponding isotherm indicates an increase in the fluid flow inside the cavity. In the last figure 2e, that is for Ra = 10^7, the colder streamline cell disappears and the hot streamline cell fills up the hole cavity with the centre in the upper right quadrant of the cavity. The isotherms indicates a rapid cooling as the ascending warmer fluid lifted along the right conductive wall gets manoeuvred along adiabatic ceiling by a anti-clockwise circulation and gets cooled by the left conductive wall.

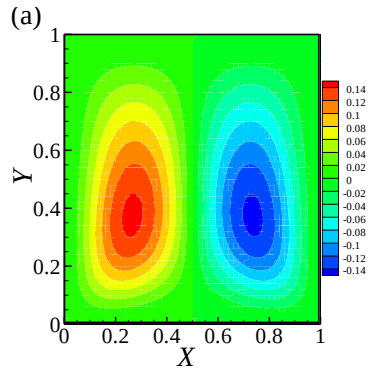

Ψ_{min} = -0.145679 and Ψ_{max} = 0.145891
Ra = 10^3

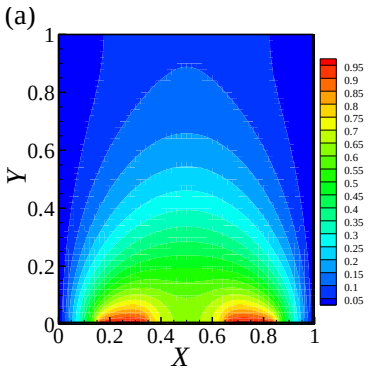

θ_{min} = 0.05 and θ_{max} = 0.95
Ra = 10^3

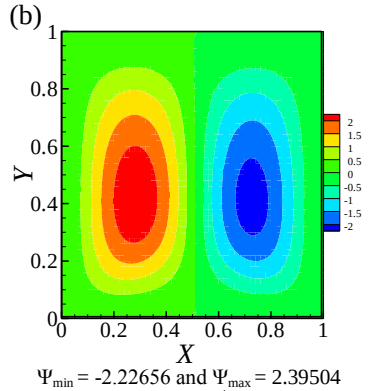

Ψ_{min} = -2.22656 and Ψ_{max} = 2.39504
Ra = 10^4

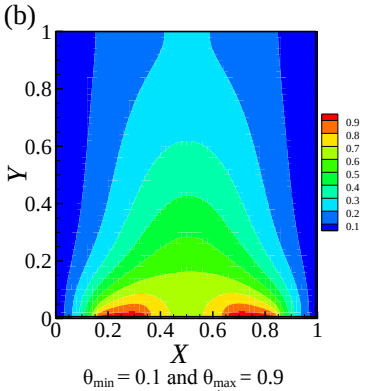

θ_{min} = 0.1 and θ_{max} = 0.9
Ra = 10^4

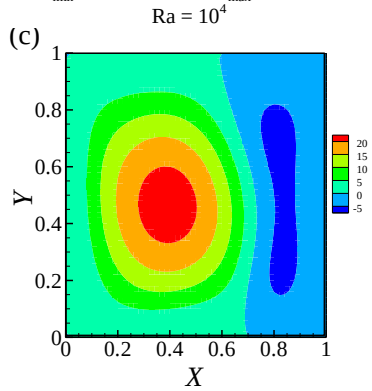

Ψ_{min} = -6.43348 and Ψ_{max} = 22.4412
Ra = 10^5

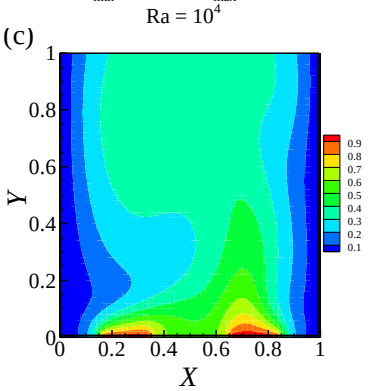

θ_{min} = 0.05 and θ_{max} = 0.95
Ra = 10^5

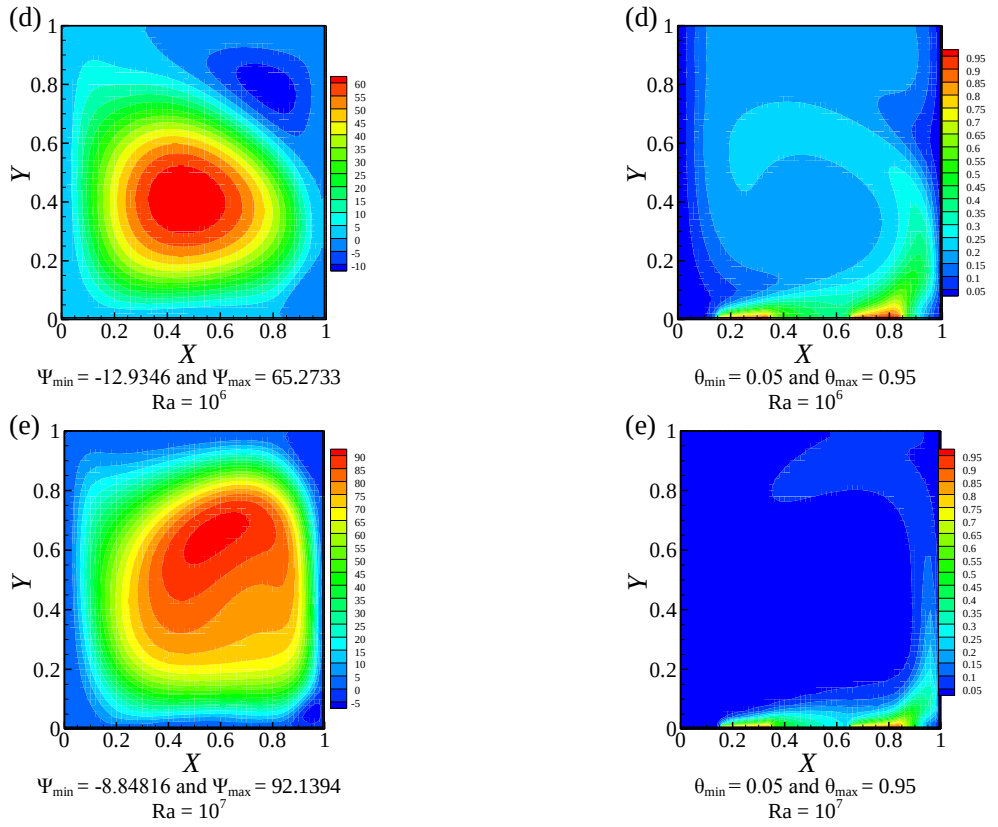

Fig. 2: Streamlines (left) and isotherms (right) for (a) $Ra = 10^3$; (b) $Ra = 10^4$; (c) $Ra = 10^5$; (d) $Ra = 10^6$; and (e) $Ra = 10^7$.

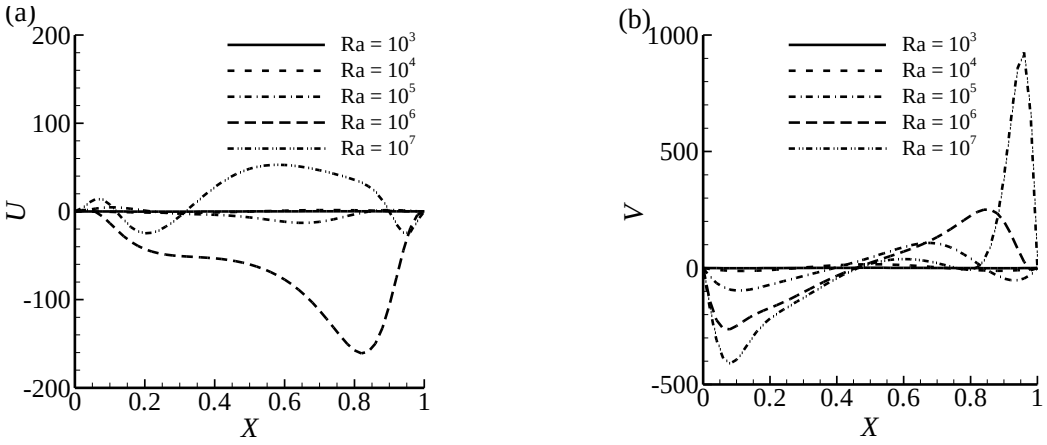

Fig. 3: Velocity distribution at $x/H = 0.5$ (a) horizontal velocity U (b) vertical velocity V

Figure 3, shows the U and V velocity distribution at the mid plane of x (x/H= 0.5) for Ra = 10^3, 10^4, 10^5, 10^6 and 10^7. Both U and V velocity for Ra = 10^3 and 10^4 is almost zero. However for U-velocity, as the Ra increases the values start to change. As we see little change for 10^5, there are sharp changes for 10^6 and 10^7. While we observe negative values for 10^6 with a peak of -160.9234, we get sort of a sinusoidal curve for 10^7 where peak positive value is 52.9224 and peak negative value is -24.8315. Meanwhile for V-velocity, we observe a sinusoid similar curve for Ra = 10^5 and 10^6. In case of 10^5 the negative peak is at -96.8676 and the positive peak is at 107.5218, while in case of 10^6 the negative peak is at -263.0850 and the positive peak is at 250.4922. However for Ra = 10^7 we observe a slightly different curve where there is a sharp positive peak with negative peak at -410.9853 and the positive peak at 925.7389.

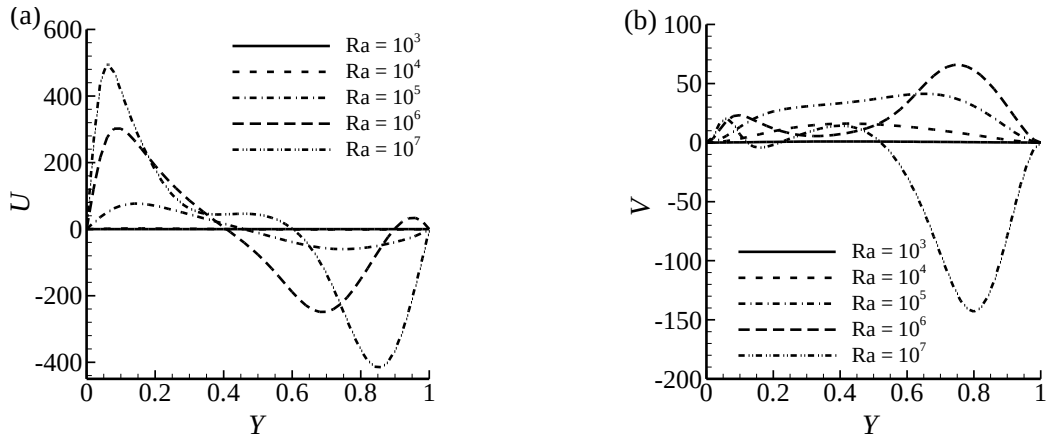

Fig. 4: Velocity distribution at $y/H = 0.5$ (a) horizontal velocity U (b) vertical velocity V.

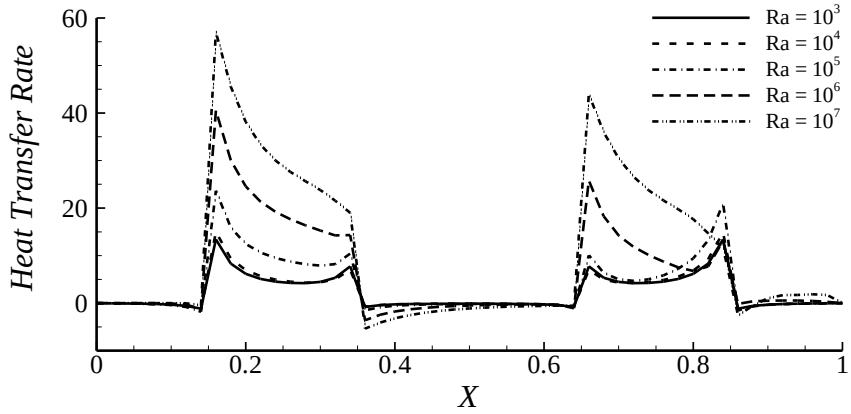

Fig. 5: Rate of heat transfer from the bottom wall for the different Rayleigh number, *Ra*.

The U and V velocity distribution at the mid plane of y (y/H =0.5) for Ra = 10^3, 10^4, 10^5, 10^6 and 10^7 are depicted in Figure 4. Both U and the V velocity for Ra = 10^3 is very slow. However for U velocity, as the Ra number increases to 10^4 the value remains almost same. A change is noticed for 10^5, while there are sharp changes for 10^6 and 10^7. While we observe a sinusoid similar curve for Ra = 10^5 and 10^6. For 10^5 we get the positive peak at 76.7706 and negative peak at -60.1649, where for 10^6 we get the positive peak at 302.2808 and negative peak at -249.0037. For 10^7 we get a sharp positive peak at 498.8073 and the negative peak at -415.0375. Meanwhile for V-Velocity, we observe a sort of elliptic curve for Ra = 10^4 with maximum value at 16.0494. In case of 10^5 the maximum value is 41.2675 while for 10^6 we get the maximum value at 65.7769. However for Ra = 10^7 we observe a slowly oscillating curve where there is a large negative peak at -140.8137and the positive peak is at 14.3060. These sorts of sharp changes occur because at the high Rayleigh number the fluid temperature is very high and both the velocities increases instantaneously.

Figure 5, describes the heat transfer characteristics of the cavity. As we can observe there is a sharp increase in the heat transfer rate at the edges of the heat sources while the heat transfer rate is almost zero at adiabatic parts of the bottom wall. It shows a slight negative value due to boundary conditions which can be considered as negligible. Now for the first heat source from the left we observe that, with increase in the Ra = 10^3, 10^4, 10^5, 10^6 and 10^7 the heat transfer rate increases significantly with sharp change at the edges. However in case of the second source while for Ra = 10^3, 10^4 and 10^5 the left edge of the source shows sharp increase in heat transfer rate, for Ra = 10^6 and 10^7 the sharp change occurs at the left edge of the source. Though, the heat sources show similar characteristics as we expected. In case of heat transfer it is also applicable that due to high Rayleigh number, we have an increase in the fluid temperature. As a result of which the heat transfer rate characteristics also changes and we observe an opposite graph for the second source compared with the first one.

5. Conclusion

In the present paper a problem on natural convection laminar flow from two discrete heating at the bottom wall has

been investigated numerically by employing an implicit finite difference method together with a Successive Over-Relaxation (SOR) technique. The results have been presented for the chosen fluid of Prandtl number Pr =0.71 and the Rayleigh number Ra (= 10^3, 10^4, 10^5, 10^6, 10^6). From the present investigation the following conclusion may be drawn:

- For increasing values of the Rayleigh number, the flow rate increases in both clock wise and anti-clockwise direction.
- The local rate of heat transfer from the heated parts increase owing to increase the Rayleigh number.
- Heat transfer rate at second source shows slightly different characteristic at higher Rayleigh numbers compared with the first source as it is observed.

References:

[1] G. De Vahl Davis, 'Natural Convection of air in a square cavity: A bench mark numerical solution', International Journal for numerical methods in fluids, vol. 3, 249- 264 (1983).

[2] G. De Vahl Davis, I. P. Jones, 'Natural convection in a square cavity: A comparison exercise', International Journal for numerical methods in fluids, vol. 3, 227- 248 (1983).

[3] M M. Ganzarolli, L. F. Milanez, 'Natural convection in rectangular enclosures heated from below and symmetrically cooled from the sides', Int. J. Heat Mass Transfer, Vol. 38, No. 6, pp. 1063-1073, 1995.

[4] O. Aydin, A. Unal, T. Ayhan, 'Natural convection in rectangular enclosures heated from one side and cooled from the ceiling', International Journal of Heat and Mass Transfer 42 (1999) 2345-2355.

[5] O. Aydin, W-J Yang, 'Natural convection in enclosures with localized heating from below and symmetrically cooling from sides', International Journal of Numerical Methods for Heat and Fluid Flow, Vol. 10 No. 5, 2000, pp. 518-529.

[6] Byong-Hoon CHANG, School of mechanical system engineering, Incheon, South Korea.

[7] Goutam Saha, Sumon Saha, M. Quamrul Islam and M. A. Razzaq Akhanda, 'Natural convection in enclosure with discreet isothermal heating from the below', Journal of Naval Architecture and Marine engineering, June 2007.

[8] Abdulhaiy M. Radhwan and Galal M. Zaki, 'Laminar natural convection in a square enclosure with discrete heating of vertical walls', JKAU Eng. Sci. Vol- 12 no.2, 2000, pp. 83-99.

[9] K. Ben Nasr, R. Chouikh, C. Kerkeni, and A. Guizani, 'Numerical study of natural convection in cavity heated from the lower corner and cooled from the ceiling', Applied Thermal engineering (2005).

[10] Amaresh Dalal and Manab Kumar Das, 'Laminar natural convection in an inclined complicated cavity with spatially variable wall temperature', International Journal of Heat and Mass Transfer 48 (2005) 3833-3854.

[11] A. Barletta, E. Nobile, F. Pinto, E. Rossi di Schio, and E. Zanchini, 'Natural convection in a 2D-cavity with vertical isothermal walls: cross validation of two numerical solutions', International journal ot thermal science, 2005.

[12] H. Wang, and M.S. Hamed, 'Flow mode transition of natural convection in inclined rectangular enclosures subjected to bidirectional temperature gradients', International journal of thermal science, 2005.

[13] H. Oztop and E. Bilgen, 'Natural convection in differentially heated and partially divided square cavities with internal heat generation', International journal of heat and fluid flow, 2005.

[14] L. F. Jin, K.W. Tou and C. P. Tso, 'Effects of rotation on natural convection cooling from three rows of heat sources in a rectangular cavity', International journal of heat and mass transfer 48 (2005) 3982-3994.

[15] L. Ben Snoussi, R. Chouikh, and A. Guizani, 'Numerical study of the natural convection flow resulting from the combined buyoncy effects of thermal and mass diffusion in a cavity with differentially heated side walls', Desalination 182 (2005) 143-150.

[16] Mohammad Ali and M. Hasanuzzaman, 'Heat transfer by natural convection through V-curved plates', Journal of mechanical engineering, vol-ME36, 2006

[17] Mohamed A. Teamah, Mohamed M. Khairat Dawood and Wael M. El-Maghlany, 'Double diffusive Natural convection in a square cavity with segmental heat sources', European journal of scientific research, vol-54. No.2, 2011,pp-287-301

[18] H.N. Dixit, V. Babu, 'Simulation of high Rayleigh number natural convection in a square cavity using the lattice Boltzmann method', International Journal of Heat and Mass Transfer 49 (2006) 727-739.

[19] C. J. Aswatha, G. Gowdha, S.N. Sridhara and K.N. Seetharamu, 'Buoyancy driven heat transfer in cavities subjected to thermal boundary conditions at bottom wall', Journal of Applied Fluid Mechanics, Vol.5, No.2, pp. 43-53, 2012

Available online at www.sciencedirect.com

SciVerse ScienceDirect

Procedia Engineering 00 (2012) 000–000

Procedia Engineering

www.elsevier.com/locate/procedia

5th BSME International Conference on Thermal Engineering

Study of Thermal Response of a Skin Stimulant Material with a Protective Fabric under a Hot Air Jet

AA Rezwan[a]*, S Hossain[a] and MA Islam[a]

[a]*Department of Mechanical Engineering, Bangladesh University of Engineering & Technology, Dhaka-1000, Bangladesh.*

Abstract

The present study focuses on the thermal response of a skin simulant material with a protective fabric (Kevlar 49) under a flame blast condition. This investigation has been conducted using a stream of hot air jet that has been impinged normally on the test surface with/without protective fabric to mimic the flame burst condition. The air jet temperature is 125°C and the jet velocity is 15 m/s and 19 m/s. The temperatures at various radial positions of the solid are measured using thermocouples and are used to calculate the surface heat flux to the skin simulant material. Subsequently, the local heat transfer coefficient and the local Nusselt Number for different radial positions of the base plate have been estimated, illustrated and analyzed for different longitudinal distance between nozzle and the test setup. The experimental results are then compared with Stoll Second Degree Burn Criterion of the ASTM Standard (F1060-01). The results show a significant reduction in heat transfer rate and exhibit an adequate protection due to the use of the protective fabric.

Keywords: Protective Fabric; Skin Simulant Material; Jet Impingement Cooling.

Nomenclature

T	Temperature (°C)	q	Heat Flux (W/m)
v	Velocity (m/s)	t	Time (s)
l	Nozzle to Plate Distance (mm)	d	Nozzle Diameter (mm)
r	Radial Distance (mm)	k	Thermal Conductivity (W/m.°C)
h	Heat Transfer Coefficient (W/m.°C)	c_p	Heat Capacity (kJ/kg.°C)
ρ	Density (kg/m3)	α	Thermal Diffusivity (m2/s)
Re	Reynolds Number	Nu	Nusselt Numeber

1. Introduction

The thermal performance of protective clothing has been a point of interest for several decades. The protection of firefighters and other employees working in many hazardous environments against high heat flux exposure is very crucial for their safe guard and for others' safety as well. So, the protective clothing is essential requirement in daily business for the staff of Fire Fighting Department, Policemen and Navy Military Staff and also for the workers in many chemical and bio-hazardous industries. Fire Resistive (FR) clothing has steadily improved over the years as new fabric materials and improved designs have reached the market. But their performance has not been studied in much detail for the safe keeping of their users yet. Many of these studies are based on fire services field experience.

* Corresponding author. Tel.: +8801552364999.
E-mail address: aashiquear@gmail.com

Most of this work dates back in 1960s' and 1970s' [1] when computers were significantly less advanced. Torvi [2] provides a review of work done on heat and mass transfer models applicable to fabrics in the high heat flux range that a firefighter may experience. The Government Industry Research Committee on Fabric Flammability considered mainly flammable fabrics used by the ordinary consumer [3-4]. Morse et al. [5] studied heat transfer and burn injury risk from exposure to jet fuel fires. Only three protective clothing materials were examined for use in US Air Force flight fabrics. Also, some model properties were determined by fitting the model results to experimental data. Stoll et al. [6-8] used a combination of analytical and experimental techniques to measure the thermal response of single fabric layers over skin. They developed diagnostics to rate the protection offered by a fabric with known properties. Their work eventually led to the thermal protective performance test. Many recent studies for the permeable protective fabric system have been conducted using air jet impingement. Many of these studies formulated a numerical model for comparing the thermal performance under various conditions [9]. Bamford and Boydell [10] developed a finite-difference-based burn injury evaluation code and Torvi [2] developed a finite element code to simulate the test. Very recently, Anguiano [11] performed an important study by using skin stimulant material to understand the extent of fire burn injury. In Bangladesh Islam et al [12] fabricated the thermal performance measuring system of the fire protecting fabric and performed a study on thermal protection system.

In the present study, jet impingement heat transfer has been experimented to simulate the flame impact to a solid surface covered with a FR fabric. Jet impingement has many practical applications due to its high heat and mass transfer. There are many factors affecting the heat transfer of jet impingement. These include the nozzle diameter (d), nozzle-to-plate distance (l), nozzle-exit velocity (vjet), thermophysical properties of the jet fluids. These factors are normally lumped into dimensionless groups: Nu, Re, Pr and l/d, which are then correlated.

2. Experimental Setup

The experimental study has been carried out by using a circular air jet facility as shown in Fig. 1. Detail explanation of different segment of the facility has been given in the previous studies [13]. The overall length of the flow facility is 9.0 m. It has axial flow fan unit, two settling chambers, two diffusers, a silencer and a flow nozzle. The fan unit consists of three Woods Aerofoil fans of the same series. The fan unit receives air through the butterfly valve and discharges it into the silencer of the flow duct. Flow from the silencer passes on to the settling chamber through a diffuser. At the discharge, side of this chamber there is a flow straighter and wire screen of 12 meshes to straighten the flow and to breakdown large eddies present in the air stream. Air from this chamber then flows to the second settling chamber through a nozzle and second diffuser. The flow straighter and wire screens are used here to ensure a uniform axial flow free of large eddies which may be present in the upstream side of the flow. The flow from the second settling chamber then enters the 100 mm long and 80 mm diameter circular nozzle. At the farthest end the diameter of the flow facility is reduced from 475 mm to 88.9 mm where the heating section is placed [13].

For producing hot air jet, an attachment shown in Fig. 2 has been installed. It includes a heating section of length 0.9 m consisting of 4 cartridge heaters of total power consumption of 3 kW. Five half circular baffles are placed in series in the heating section to enhance the heating capacity of the air. Air from the wind tunnel is passed through the entrance section, heating section and settling chamber, the finally through the nozzle to produce desired air jet. Swirling effect of the air due to the baffles ensures the uniform heating air from the heater surface. The heated air then passes through the long settling chamber to the nozzle having a diameter of 25.4 mm. This is to note that the settling chamber is insulated with asbestos cloth and heat tape to prevent the heat loss to the surrounding from the hot air. The air flow through the nozzle is set by operating required number of fans. The temperature of the air jet is set by controlling the supply voltage of the heater. The whole setup is mounted on rigid frames of M.S. pipes and plates and is securely fixed with the ground such that any unwanted vibration of the system is reduced to a minimum. To avoid the effect of ground shear, the setup is installed at an elevation of 1.4 m from the ground.

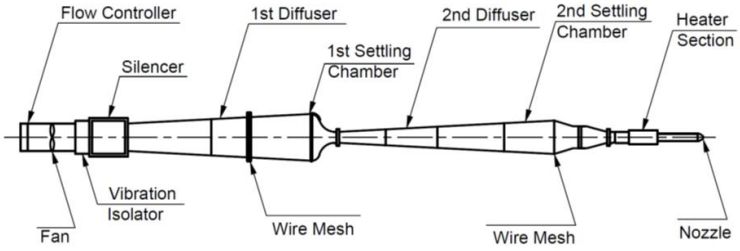

Fig. 1. Wind Tunnel for the Air Jet Facility [13]

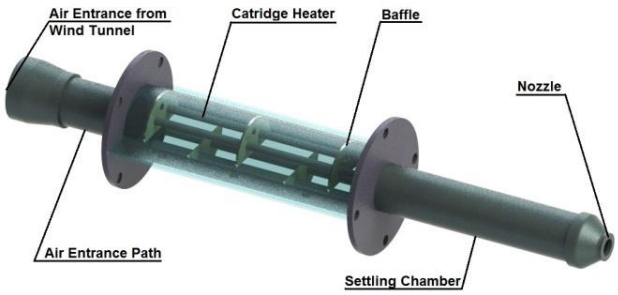

Fig. 2. Heater Section in Details [12]

For the present investigation, a nozzle diameter of 25.4 mm is used. The temperature of the jet impingement has kept within 125°C. The test has been performed for two jet velocity, 19 m/s and 15 m/s. For protective clothing, an Aluminized glass fiber with vapor absorbent stitched with Kevlar fiber has been used. The base plate is made of Masonite, which is used for making hard board. Seven K-Type (Ni-Cr/Ni-Al) thermocouple is installed in the base plate to measure the temperature.

One thermocouple is placed at the stagnation point, and 3 others in both top and bottom side from the centered thermocouple are placed on the Masonite plate (base plate) at a distance of 1.5 nozzle diameter from each. A wooden frame is used to hold the fabric and the base plate as per provisions outline in ASTM code [14]. The wooden frame can be displaced along longitudinal axis with the wind tunnel for different l/d locations from the nozzle. The data has been recorded using a data acquisition system (Picosoft).

Table 1. Experimental Condition

Parameters	Values
Jet Velocity (m/s)	19, 15
Temperature (°C)	125
Nozzle Dia (mm)	25.4
l/d	2, 4, 6
r/d	-4.5 ~ 4.5
Reynolds Number	3.17×104
Environmental Temperature (°C)	25 ~ 32

3. Experimental Procedure

The fan motors of the tunnel were first started for a particular air flow with the help of butterfly valve and run for about 15 minutes isolating the base plate. The isolating system comprised of an MS plate cooled by circulating water. The power to the heating section has been supplied for the desired air temperature and waited until the steady temperature of the air jet has been reached. At the same time picosoft system was made ready for data recording. Then the air jet was impinged on the base plate by removing the isolator quickly and the transient temperature response of the base plate was recorded for about three minutes. The same experiments were repeated for different conditions as given in Table–1. The collected data were used to estimate surface heat flux of the base plate, heat transfer co-efficient and Nusselt numbers by following the mathematical protocol given in Section 4.

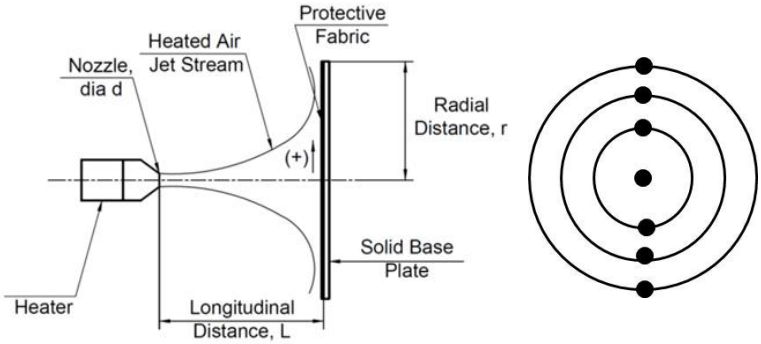

Fig. 3. Coordinate of the Setup (left), Thermocouple Position (right)

4. Mathematical Formulation

The base plate under jet impingement can be modeled as semi-infinite solid having a boundary of constant heat flux. Considering this, one can easily find the temperature distribution within the base plate as given in Eq. (1).

$$T(x,t) - T_i = \frac{2q\sqrt{\alpha t/\pi}}{k} e^{\left(\frac{-x^2}{4\alpha t}\right)} - \frac{qx}{k}\left(1 - \text{erf}\left(\frac{x}{2\sqrt{\alpha t}}\right)\right) \quad (1)$$

On the surface (x=0) this equation reduces Eq. (2) where T(t) are record during experiments and can be used to calculate the surface heat flux.

$$T(t) - T_i = \frac{2q\sqrt{\alpha t/\pi}}{k} \quad (2)$$

Given a heat flux at a particular location and time, Newton's law of cooling can be used to calculate the local heat transfer coefficient, h using Eq. (3).

$$q = h(T_{jet} - T_i) \quad (3)$$

The local Nusselt number as defined by Eq. (4) at any radial location, r/d, was derived from the surface heat flux history.

$$Nu = \frac{hd}{k} \quad (4)$$

Table 2. Thermal Properties of Masonite (base plate)

Parameters	Values
k	0.18 W/m.°C
ρ	1050 kg/m3
Cp	1.34 kJ/kg.°C

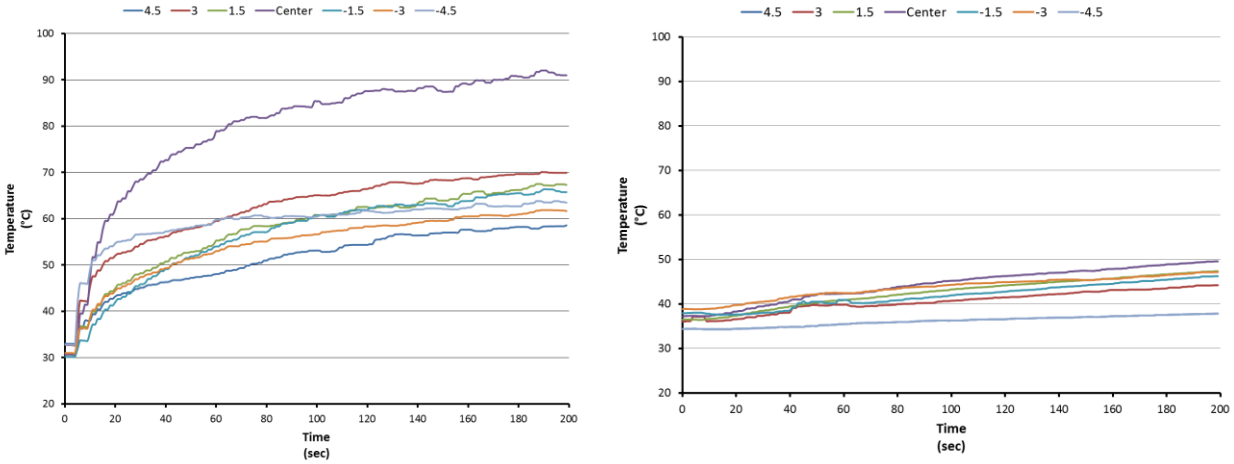

Fig. 4. Temperature rise before (left) and after (right) the fabric layer

5. Result and Discussion

A total of 12 experiments were performed yielding over 16,000 data points for different conditions as given in Table 1. The surface heat flux and Nusselt number variation for different experimental conditions are displayed and analyzed in this section.

Figures 4 show the PicoLog data attained for different experimental conditions. The data is presented for the entire 7 channel which represents the 7 thermocouple temperature readings. All readings are directly fed to the computer attached with the PicoLogger Data Acquisition System. The computer saves all the data in a table. Those are then used for calculation.

5.1. Heat Flux – Time Plot

Figures 5 show the surface heat flux variation of the base plate for both the conditions. In all of these figures the upper solid line represents the condition for base plate without fire retardant fabric system and the lower dashed line represents the condition with fire retardant fabric attached adjacent to the base plate. As shown in the Figure 5, the heat flux of the base plate without the fire retardant fabric rapidly increases and then slowly decreases with the increasing time. The maximum heat flux occurs within 20 second from the commencement of the jet impingement. The heat flux of the base plate with the fire retardant fabric system follows a different trend as shown. The heat flux in this case increases suddenly at the beginning and then decreases slowly having the values much lower than those without fabric conditions. As the space between nozzles to base plate increases, the maximum heat flux decreases for a particular experimental condition. This may be due to the effect of lower heat carrying capability of air and also for the entrainment occurs as the distance increases.

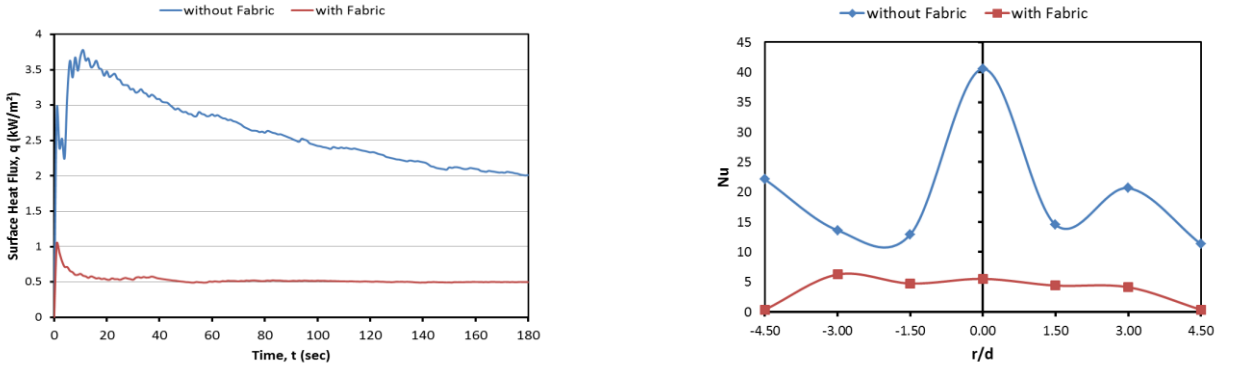

Fig. 5. Surface Heat Flux Variation with Time for l/d = 2 and v=19m/s (left), Nusselt Number Distribution for l/d = 2 at time t = 30s (right)

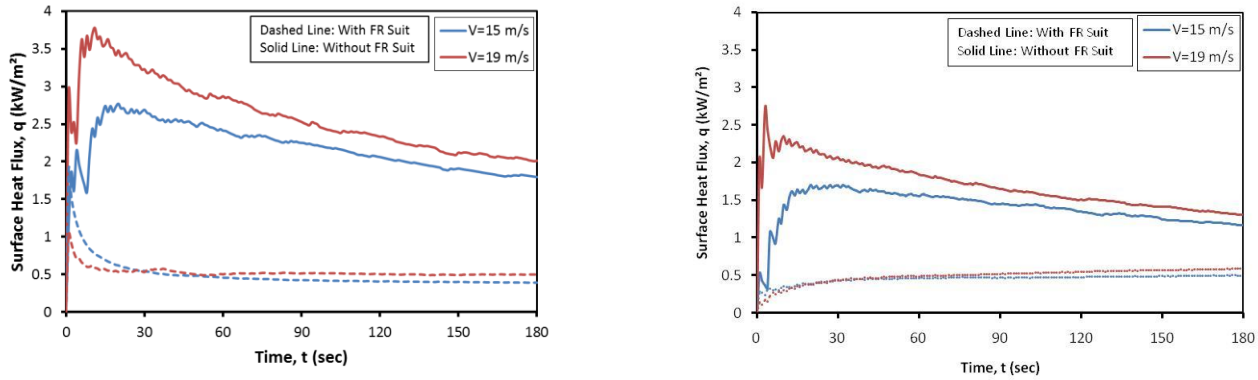

Fig. 6. Effect of Velocity on Surface Heat Flux for l/d = 2 (left) and l/d = 6 (right)

5.2. Effect of Velocity on Surface Heat Flux

The lower velocity of the impinging jet depicts a lower maximum heat flux for stagnation point and subsequent radial position than the higher velocity. But like the higher velocity air jet impingement, similar trends for the heat flux are observed for lower velocity.

In Figs. 11-13, the effects of velocity on surface heat flux have been shown. The surface heat flux of the base plate for velocity 19 m/s has been found higher than for 15 m/s with/without FR fabric. But with the FR fabric, the heat flux for velocity 15 m/s increase to a higher value suddenly after the start of jet impingement than for velocity 19 m/s for the position of l/d = 2 only. For other l/d position the heat flux for the earlier case has been found to be higher than the latter case.

5.3. Safety Comparison

The Stoll criterion [6-8] is a good approximation to compare the protective clothing / fire retardant clothing for their thermal response to the thermal injury. For this reason, present results are compared with the Stoll criterion to visualize the thermal effect.

Figure 7(a) shows the comparison for human tissue tolerance for pain sensation. In this figure, it can be seen that for both experimental and simulation result, the surface heat flux is well below the Stoll criterion, while the result for the condition of the base plate without fabric shows that it crosses the Stoll criterion curve. Thus it can be said that the Kevlar fabric, both alone and with other fabric, can resist the pain sensation.

Figure 7(b) shows the comparison for human tissue tolerance for the second degree burn. Here again the Kevlar fiber, both alone and with a system of fibers, can save the person who wear the protective suit made with Kevlar fiber.

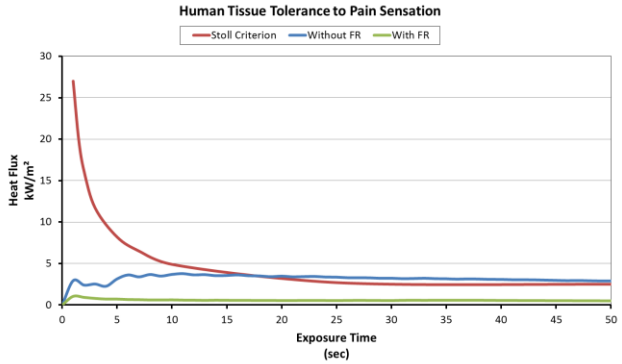

Fig. 7(a) Comparison with Stall Criterion for Human Tissue Tolerance to Pain Sensation

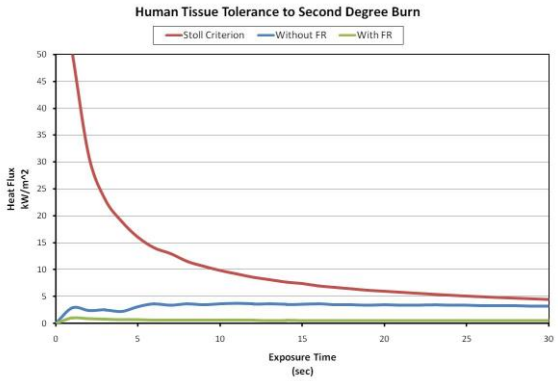

Fig. 7(b) Comparison with Stall Criterion for Human Tissue Tolerance to Second Degree Burn

6. Conclusion

Experiments are conducted using an air jet impinged on a base plate with/without the protective fabric system to mimic the flame blast condition for different experimental conditions. The measured temperatures are used to calculate the surface heat flux to the base plate. Moreover, the local heat transfer coefficient and the local Nusselt number for different radial positions of the base plate have been illustrated and analyzed in this study. The results have been compared with the Stoll criterion. The results show a significant decrease in heat transfer rate using the protective fabric and adequate protection to the pain sensation as well as to the second degree burn on human skin. The setup can be used for testing the heat transfer capability for any kind of fabric layer used for different purposes.

References

[1] Chen, N.Y., 1959, “Transient Heat and Moisture Transfer Through Thermally Irradiated Cloth.” Ph.D Thesis, Massachusetts Institute of Technology, Cambridge, Mass., USA.

[2] Torvi, D. A., 1997, “Heat Transfer in Thin Fibrous Materials Under High Heat Flux Conditions”, Ph.D Thesis, University of Alberta, Calgary, Alberta.

[3] Backer, S., Et al., 1976, *Textile Fabric Flammability*, The MIT Press, Cabridge, Mass., USA.

[4] Wulff, W., Zuber, N., et al., 1972, “Study of Hazards from Burning Apparel and the Relation of Hazards to Test Methods,” Second Final Report: Georgia Institute of Technology, NTIS: COM-73-10956

[5] Morse, H.L., Green, K. A., Thompson, J. G., Moyer, C. B., and Clark, K. J., 1972, “Analysis of the Thermal Response of Protective Fabrics,” Technical Report, Acurex Corp., Mountain View, Calif., USA

[6] Stoll, A. M., Chianta, M. A., and Munroe, L. R., 1964, “Flame-Contact Studies,” Transactions of the ASME, Journal of Heat Transfer, Vol. 86, pp 449-456

[7] Stoll, A. M. and Chianta, M. A., 1968, “Burn Protection and Prevention in Convective and Radiant Heat Transfer.” Aerospace Medicine, Vol. 39, pp. 1097-1100

[8] Stoll, A.M. and Chianta, M.A. “Method and Rating System for Evaluation of Thermal Protection,” Aerospace Medicine, Vol. 40, No. 11, pp. 1232-1238

[9] Lee, S., Park, C., Kulkarni, D., Tamanna, S., Knox, T., 2010, “Heat and Mass Transfer in a Permeable Fabric System under Hot Air Jet Impingement”, Proc. Int. Heat Transfer Conf. (IHTC14).

[10] Bamford, G. J. and Boydell, W., 1995, “ICARUS: A Code for Burn Injury Evaluation”, Fire Technology, Vol. 31, No. 4, pp. 307-335

[11] Anguiano, R. M., 2006, “Transient Heat Transfer through Thin Fibrous Layer”, M.Sc. Thesis, University of Alberta, Emonton, Albarta, Canada.

[12] Islam, M.A., Rezwan, A.A., Hossain, S, Islam, A.K.M.N., 2011, “Study of Transient Heat Transfer of A Solid With Protective Fabric Under Hot Air Jet Impingement”, *Proc. Int. Conf. on Mechanical Engineering (ICME2011)*

[13] Hasan, M. N., 2008, “Experimental Study of Flow Characteristics in the Near Field of a Thermally Stratified Co-axial Free Jet”, M.Sc. Thesis, Bangladesh University of Engineering & Technology, Dhaka, Bangladesh.

[14] ASTM F2703-08, “Standard Test Method for Unsteady-State Heat Transfer Evaluation of Flame Resistant Materials for Clothing with Burn Injury Prediction”

Available online at www.sciencedirect.com

SciVerse ScienceDirect

Procedia Engineering 00 (2012) 000–000

Procedia Engineering

www.elsevier.com/locate/procedia

5th BSME International Conference on Thermal Engineering

Heat of Adsorption and Adsorbed Phase Specific Heat Capacity of Methane/Activated Carbon System

Kazi Afzalur Rahman[a,*], Wai Soong Loh[b], Kim Choon Ng[b]

[a]*Department of Mechanical Engineering, Chittagong University of Enginnering & Technology, Chittagong 4349, Bangladesh*
[b]*Department of Mechanical Engineering, National University of Singapore, 9 Engineering Drive 1, Singapore 117576, Singapore*

Abstract

This study describes the thermodynamic formulations for the heat of adsorption and the adsorbed phase specific heat capacity from the rigor of classical thermodynamics with the involvement of adsorption parameters. The abovementioned thermodynamic quantities are evaluated from the equilibrium uptakes for adsorption of methane onto different types of activated carbon and found to be strongly dependent on the adsorption parameters along with the pressure and temperature. The adsorption uptake data of methane/Maxsorb III pair for temperatures both in sub- and supercritical regions are also used in the property evaluations and it is observed that the quantities vary with temperature and the trend is opposite between the sub- and supercritical regions.

Keywords: Heat of adsorption; Specific heat capacity; Adsorption parameters; Methane; Activated carbon.

Nomenclature

C	Adsorbate surface loading (g/g)
C_0	Maximum specific mass of adsorption (g/g)
c_p	Specific heat capacity (kJ/kg K)
E	Characteristics energy (J/mol)
H_{ads}	Heat of adsorption (kJ/kg)
h	Enthalpy (kJ/kg)
h_{fg}	Latent heat of evaporation (kJ/kg)
n	Heterogeneity parameter (-)
P	Pressure (bar)
P_{sat}	Saturation pressure (bar)
R	Gas constant (kJ/kg K)
s	Entropy (kJ/kg K)
T	Temperature (K)
T_b	Boiling temperature (K)
v_a	Adsorbate specific volume in adsorbed phase (cm^3/g)
v_b	Specific volume at the boiling point (cm^3/g)
W	Volumetric adsorbate uptake (cm^3/g)
W_0	Limiting volumetric adsorbate uptake (cm^3/g)

* Corresponding author. Tel.: +880 31 714953; fax: +880 31 714953.
E-mail address: afzalur99@yahoo.com

Greek symbols	
α	Thermal expansion coefficient of the adsorbed phase (K^{-1})
Subscripts	
a	Adsorbed phase
b	Boiling point
cri	Critical
g	Gaseous phase
sat	Saturation

1. Introduction

In adsorption process, the adsorbate molecules attract to the adsorbent surface with the existence of van der Waals forces and they accumulate in the pores of the adsorbent with phase transformation. The transformed phase of the adsorbate molecules is called as adsorbed phase which is treated as a distinguishable phase in thermodynamic viewpoint, even though the precise location of the phase boundary is uncertain [1]. The thermodynamic states of the adsorbed phase are not only function of pressure and temperature like gaseous phase but also depend on adsorbate surface loading or uptake [2,3]. Therefore, it is necessary to evaluate the thermodynamic quantities for the adsorbed phase and it is not reasonable to assume the adsorbed phase to be equal to the liquid phase or to the gaseous phase.

This article describes the theoretical framework of the heat of adsorption and the adsorbed phase specific heat capacity for an adsorbate-adsorbent pair. The thermodynamic formulations are performed from the rigor of classical thermodynamics by incorporating the adsorption equilibrium model that holds the relationship between the pressure, temperature, and the uptake for an adsorption system. The adsorbed phase specific volume is also taken into consideration in deriving the theoretical relations. The property values are derived qualitatively for adsorption of methane onto different types of activated carbon. Especially, the adsorption uptake data for the methane/Maxsorb III pair are available for a wide range of temperatures both in sub- and supercritical states and pressures up to 25 bar. These experimental uptake data are used in evaluating the abovementioned thermodynamic quantities for both the sub- and supercritical regions. The evaluated values show better estimation due to the involvement of the adsorption parameters in the theoretical formulations and also because of the consideration of adsorbed phase specific volume which was assumed to be same as the gaseous phase in a recent study by Chakraborty et al. [3].

2. Theory

2.1. Adsorption equilibrium model

The relationship between pressure, temperature and uptake of an adsorbate-adsorbent system is known as the adsorption equilibrium model. Among the adsorption equilibrium models available in the literature, the Dubinin-Astakhov (D-A) model is one of the popular isotherm model for adsorption of vapours and gases onto non-homogeneous carbonaceous solids [4]. The D-A isotherm model is used in this study to describe the adsorption equilibrium uptake for the methane/activated carbon system. The D-A model is expressed as

$$\frac{C}{\left(W_0/v_a\right)} = \exp\left[-\left\{\frac{RT}{E}\ln\left(\frac{P_s}{P}\right)\right\}^n\right] \tag{1}$$

where C is the amount of uptake in g/g, W_0 is the limiting uptake of adsorption space of the adsorbent in cm^3/g, E is the characteristic energy of the adsorption system, and n is the structural heterogeneity parameter. The adsorbed phase specific volume (v_a) can be estimated from the following empirical expression proposed by Ozawa et al. [5] for high pressure gas adsorption considering the thermal expansion of the adsorbate molecules.

$$v_a = v_b \exp\left[\alpha\left(T - T_b\right)\right] \tag{2}$$

where v_b is the specific volume of the liquid at the boiling point, T_b, and α is the thermal expansion coefficient of the adsorbed phase.

The saturation vapour pressure (P_{sat}) of the adsorbed phase depends on the adsorption temperature for the subcritical condition of the adsorbate and it can be determined from the following Dubinin's method, i.e. $P_{cri} = (T/T_{cri})^2 P_{cri}$, when the adsorption occurs above the critical point.

2.2. Heat of adsorption

The heat release during the adsorption process due to the change in energy level of the adsorbate molecules is known as the heat of adsorption and the Clausius-Clayperon equation has long been used for evaluation of heat of adsorption from the adsorption uptake data assuming ideal gas-phase behaviour of the adsorbate molecules in their gaseous phase [6,7].

$$H_{ads} = RT^2 \left[\left(\frac{\partial(\ln P)}{\partial T} \right)_C \right] \tag{3}$$

Now invoking the D-A isotherm model in Eq. (3), an explicit expression for the heat of adsorption can be obtained which is function of adsorbate surface loading (C), adsorbed phase specific volume (v_a), thermal expansion coefficient of the adsorbed phase (α), adsorption parameters (W_0, E, n) of the D-A isotherm model, saturation pressure (P_{sat}), and temperature.

$$H_{ads} = E \left[\left(\ln \frac{W_0}{C v_a} \right)^{1/n} + \frac{\alpha T}{n} \left(\ln \frac{W_0}{C v_a} \right)^{1-n/n} \right] + RT^2 \left(\frac{\partial \ln P_{sat}}{\partial T} \right) \tag{4}$$

Here, the second term of the right hand side is equal to ($2RT$) by using the proposed expression for saturation pressure (P_{sat}) in case of supercritical state. However, when the adsorption process occurs below the critical point, this term can be replaced with the heat of vaporization (h_{fg}) and the Eq. (4) becomes

$$H_{ads} = E \left[\left(\ln \frac{W_0}{C v_a} \right)^{1/n} + \frac{\alpha T}{n} \left(\ln \frac{W_0}{C v_a} \right)^{1-n/n} \right] + h_{fg} \tag{5}$$

2.3. Adsorbed phase specific heat capacity

Thermodynamically the adsorbed phase specific heat capacity ($c_{p,a}$) is defined by the temperature derivative of the differential adsorbed phase enthalpy (h_a) at constant surface loading (C) [2,3,6,8], i.e.,

$$c_{p,a} = \left(\frac{\partial h_a}{\partial T} \right)_C \tag{6}$$

The heat of adsorption (H_{ads}) can also be expressed as the difference between the gaseous phase enthalpy and the adsorbed phase enthalpy [6], i.e.,

$$H_{ads} = h_g - h_a \tag{7}$$

Thus, the adsorbed phase specific heat capacity can be re-written as

$$c_{p,a} = \left(\frac{\partial h_g}{\partial T} \right)_P - \left(\frac{\partial H_{ads}}{\partial T} \right)_C = c_{p,g} - \left(\frac{\partial H_{ads}}{\partial T} \right)_C \tag{8}$$

where $c_{p,g}$ is the specific heat capacity of the gaseous phase.

Invoking the expression for H_{ads} from Eq. (5) in the above Eq. (8), the $c_{p,a}$ becomes

$$c_{p,a} = c_{p,g} + \frac{\alpha^2(1-n)}{n^2} ET \ln\left(\frac{W_0}{Cv_a}\right)^{\frac{1-2n}{n}} - \left(\frac{\partial h_{fg}}{\partial T}\right)_P \tag{9}$$

The second term of the right-hand side can be determined from the adsorption parameters (W_0, E, n) of the D-A isotherm model, adsorbed phase specific volume (v_a), thermal expansion coefficient for the adsorbed phase (α), adsorbate surface loading (C), and temperature.

For sub-critical condition of the adsorbate, the partial term $\left(\partial h_{fg}/\partial T\right)_P$ can be expressed as $\left(c_{p,g} - c_{p,f}\right)$ and Eq. (9) eventually becomes

$$c_{p,a} = c_{p,f} + \frac{\alpha^2(1-n)}{n^2} ET \ln\left(\frac{W_0}{Cv_a}\right)^{\frac{1-2n}{n}} \tag{10}$$

For super-critical condition of the adsorbate, the partial term $\left(\partial h_{fg}/\partial T\right)_P$ reduces to $\left(2R\right)$in Eq. (9).

$$c_{p,a} = \left(\frac{\partial h_g}{\partial T}\right)_P - \left(\frac{\partial H_{ads}}{\partial T}\right)_C = c_{p,g} - \left(\frac{\partial H_{ads}}{\partial T}\right)_C \tag{11}$$

3. Results and Discussion

3.1. Adsorption Isotherms

The adsorption uptake data measured for methane/Maxsorb III pair using the volumetric technique are plotted Fig 1 for temperatures ranging from (120 to 350) K and pressures up to 25 bar. These experimental uptake data are reported by Loh et al. [9] for the temperatures in super-critical region from (278 to 350) K whilst Rahman et al. [10] has published the isotherm data for sub-cryogenic temperatures ranging from (120 to 220) K for the methane/Maxsorb III pair.

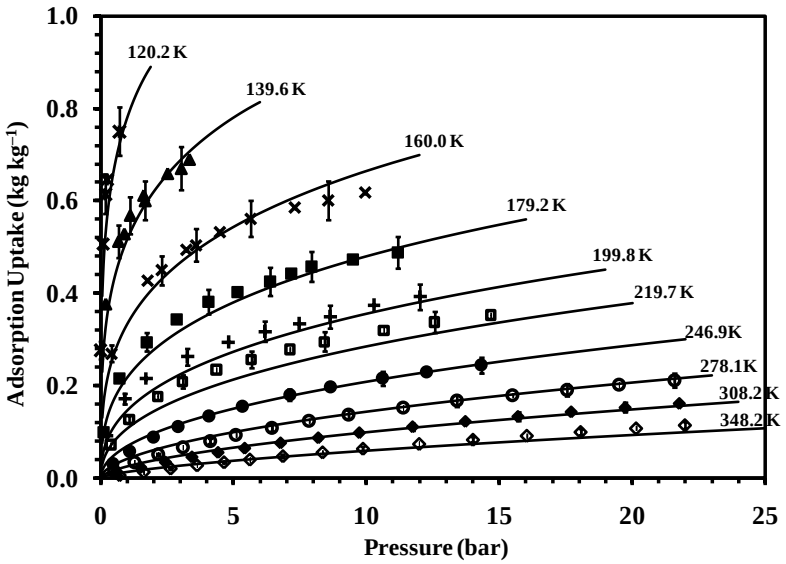

Fig. 1. Adsorption uptake data of methane/Maxsorb III pair for temperatures (120 to 350 K) with error bars of 7 %. Solid lines are predicted from the D-A isotherm model

To describe the experimental uptake data, the Dubinin-Astakhov isotherm model is used and it is found to be more appropriate for the present adsorbate-adsorbent pair due to (i) the accountability of the heterogeneity parameter and (ii) the consideration of the adsorbed phase volume correction. The expression for adsorbed phase specific volume (v_a) of Eq. (2) is incorporated with the D-A isotherm model and the thermal expansion coefficient (α) of the v_a expression has kept being float to regress well the isotherm data in sequence with the study by Rahman et al. [10]. The regressed adsorption parameters are 2.193 cm^3/g, 4757.3 J/mol, 1.05 and 0.0043 K^{-1} for W_0, E, n, and α, respectively. The heterogeneity parameter (n) is very close to unity which indicates the adsorbent surface to be highly heterogeneous and thus results a lower value of characteristics energy (E). An average regression error of about 7 % is found for this analysis. The solid lines in Fig 1 are predicted for the same temperatures from the D-A isotherm model using the regressed parameters. It can be seen that all the predicted isotherms are within 7 % of the experimental uptake data which is reasonable when a single isotherm model is employing to fit such a wide range of uptake data. The adsorption parameters found here are important in evaluating the heat of adsorption (H_{ads}) and the adsorbed phase specific heat capacity ($c_{p,a}$) as function of pressure (P), temperature (T) and amount of adsorption uptake (C).

3.2. Heat of Adsorption

The heat of adsorption (H_{ads}) values for methane/Maxsorb III pair are evaluated using Eq. (5) and plotted in Fig 2(a) and 2(b) against adsorbate surface loading (C/C_0) for sub- and supercritical temperatures, respectively. It can be seen that the heat of adsorption decreases with increasing temperature in the subcritical region and the trend is opposite in the supercritical states. Again, the heat of adsorption varies with adsorbate surface loading and approaches to a limiting value when adsorption process proceeds towards the saturation uptake limit. This variation of the heat of adsorption with the adsorbate surface loading is due to the surface heterogeneity of the adsorbent. These H_{ads} values are important for thermodynamic analysis of any adsorption system. For example, the effective thermal management of ANG storage system requires precise information of heat of adsorption that generates during the charge process of the system.

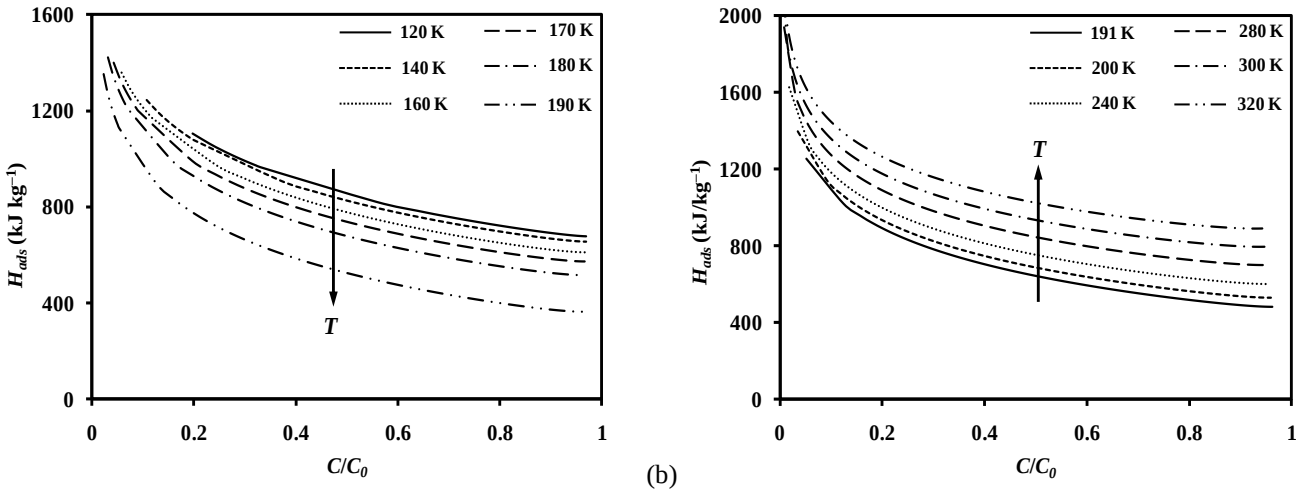

Fig. 2. Heat of adsorption (H_{ads}) for methane/Maxsorb III pair against adsorbate surface loading (C/C_0) at (a) Sub-critical and (b) Super-critical temperatures

The H_{ads} values are also evaluated for adsorption of methane onto different types of microporous activated carbons. Since the developed expression for H_{ads} requires the adsorption parameters (W_0, E, n, and α) for the adsorbate-adsorbent pair, a number of activated carbons are cited from the literature those conducted experiment for the adsorption isotherms of methane. All the cited samples are microporous in surface structure and the isotherm data are in the supercritical range. The adsorption uptake data of methane on these activated carbons are taken from the respective articles and regressed with the D-A isotherm model. The adsorbent characteristics of the carbon samples and the adsorption parameters of the D-A isotherm model are summarized in Table 1. The heat of adsorption (H_{ads}) values are plotted in Fig 3 against the adsorbate surface loading (C/C_0) at temperature of 298 K for adsorption of methane onto the activated carbon samples mentioned in Table 1. It is observed that the H_{ads} varies with adsorbate surface loading for all the samples and this variation is wider range in case of Maxsorb III than the other carbon samples.

Table 1. Parameters (W_0, E, n, α)* of the D-A isotherm model for adsorption of methane onto different types of activated carbon samples

Adsorbent Samples	**Temperature range of data measurement (K)**	**Limiting Uptake, W_0 (cm^3/g)**	**Characteristic Energy, E (J/mol)**	**Heterogeneity Parameter, n**	**Citation****
Maxsorb III	120 - 348	2.193	4757.3	1.05	a
AX21	233 - 333	1.08	5464.1	1.26	b
ACF (A-20)	278 - 348	0.717	6198.4	1.51	c
BPL	273 - 333	0.36	7040	1.54	d
Norit R1 Extra	273 - 323	0.43	7500	1.73	d
F30/470	303 - 343	0.389	7742.9	1.81	e
Chemviron	278 - 348	0.407	8684.1	1.86	f
Calgon AC	293 - 313	0.309	8955.1	2.41	g

*The value of α is 0.0025 K^{-1} for all pairs except methane/Maxsorb III.

**a. Present study; b. Zhou et al. [11]; c. Loh et al. [9] d. Himeno et al. [12]; e. Frère and De Weireld [13]; f. Author's unpublished data; g. Choi et al. [14].

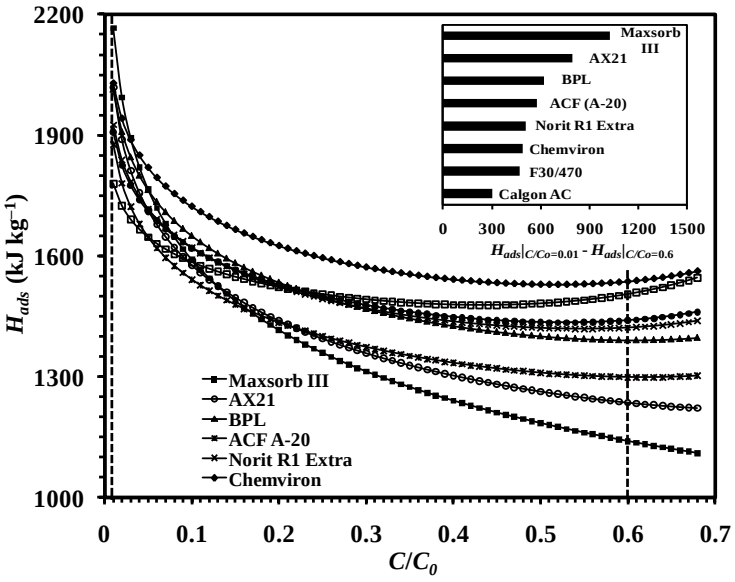

Fig. 3. Heat of adsorption (H_{ads}) for methane adsorption onto different types of activated carbon at temperature of 298 K

The difference of H_{ads} between surface loading of C/C_0=0.01 and C/C_0=0.6, i.e. $(H_{ads})_{C/Co=0.01} - (H_{ads})_{C/Co=0.01}$, is calculated for each sample and Maxsorb III gives considerably larger value as shown in the inset of Fig 3. Thus, it can be said that the degree of surface heterogeneity is higher for the Maxsorb III than the other activated carbon samples. This observation has also been confirmed by Loh et al. [9] from the pore size distribution of the Maxsorb III samples by the NLDFT method.

3.3. Adsorbed phase specific heat capacity ($c_{p,a}$)

The adsorbed phase specific heat capacity ($c_{p,a}$) is function of pressure, temperature and amount of adsorbate uptake whereas the bulk specific heat capacity (c_p) depends only on pressure and temperature. Therefore, it is necessary to evaluate the $c_{p,a}$ values for thermodynamic analysis of any adsorbate-adsorbent system and Eq. (9) is developed for this purpose. In Fig 4, the adsorbed phase specific heat capacity ($c_{p,a}$) values are plotted against temperatures for different constant pressures. The adsorbed phase c_p values are derived using Eq. (9) where the adsorption parameters (W_0, E, n, and α) evaluated for the methane/Maxsorb III pair are used in calculating the values. Due to the availability of adsorption uptake data of methane/Maxsorb III pair for a wide range of temperatures, it is reasonable to determine the $c_{p,a}$ values in both the sub- and supercritical regions. In Fig 4, it can also be observed that the isobaric $c_{p,a}$ values are decreasing except a slight increase in the supercritical region. At pressures below 10 bar, the $c_{p,a}$ values start to increase immediately after the critical point. These values are also important in the study of ANG storage system to analyze its cyclic processes.

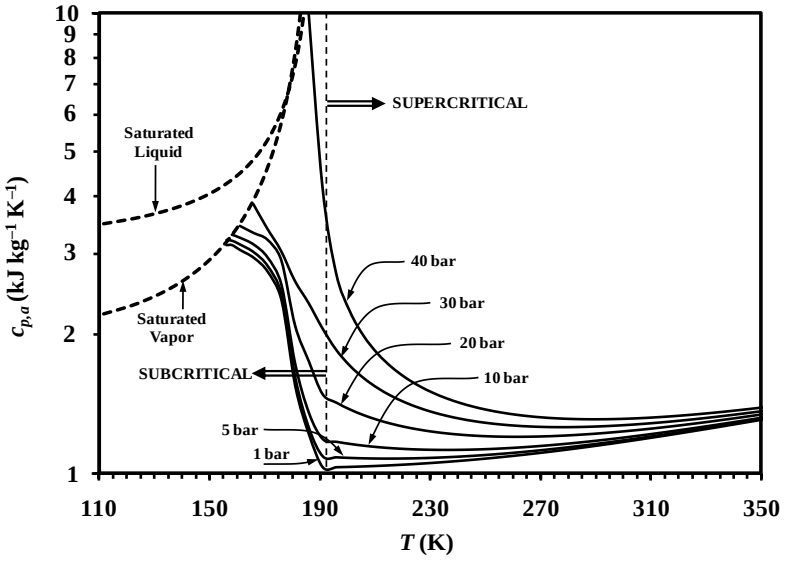

Fig. 4. Isobars for adsorbed phase specific heat capacity (c_p) of methane adsorption onto Maxsorb III

The $c_{p,a}$ values are evaluated for methane adsorption onto different activated carbon samples mentioned in Table 1 and plotted in Figs 5(a) and 5(b) for constant pressure, P = 5 bar and constant surface loading, C/C_0 = 0.5, respectively. It is observed that both the isobaric and isosteric $c_{p,a}$ values are increasing with temperatures and also in the similar trend in case of all the carbon samples. It is also observed that the $c_{p,a}$ values are dependent on the adsorption parameters and these two plots demonstrate the strong dependence on the characteristics energy (E) and the heterogeneity parameter (n). In general, the E and n values are larger in case of the adsorbent that have the lower degree of surface heterogeneity. Thus it can be said that the adsorbed specific heat capacity ($c_{p,a}$) of methane is relatively higher when adsorption occurs on adsorbents with heterogeneous surface.

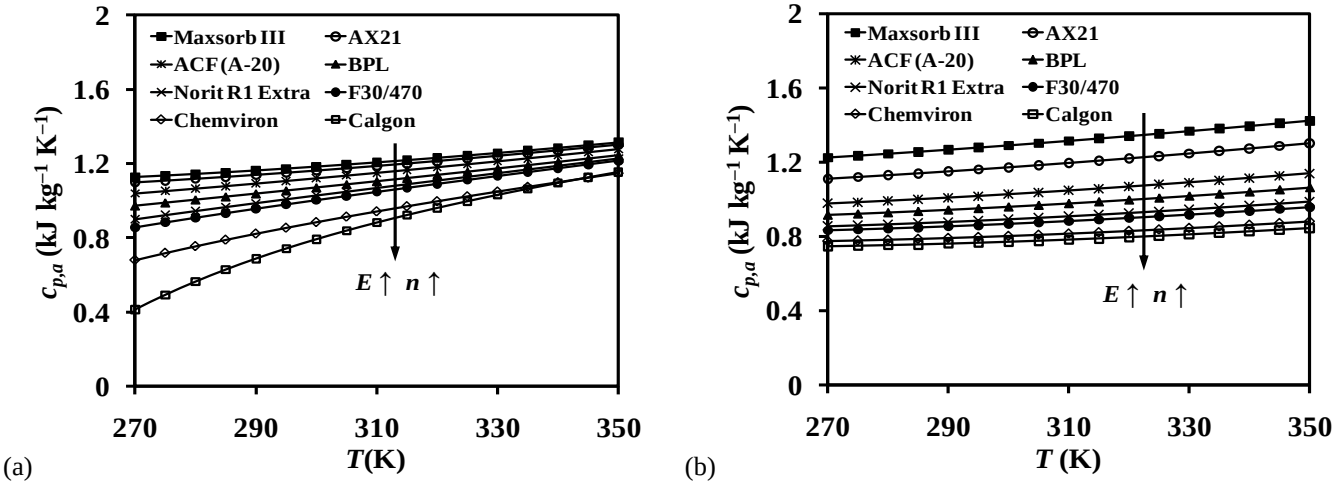

Fig. 5. Comparison of $c_{p,a}$ values evaluated for methane adsorption onto different activated carbons; (a) Isobars at P = 5 bar (b) Isosters at C/C_0 = 0.5

4. Conclusions

The thermodynamic frameworks of the heat of adsorption and the adsorbed phase specific heat capacity are described in this article. The evaluated property values are found to be strongly dependent on the adsorption parameters along with the pressure and temperature. It is observed that the heat of adsorption values are decreasing with temperature in the subcritical

region and the trend is opposite in the supercritical region for the methane/Maxsorb III pair. Similarly, the adsorbed phase specific heat capacity values are observed to decreasing with temperature in the subcritical region and there is a slight increase with temperature in the supercritical region. These evaluations are significant, as they directly affect the computation of the enthalpy and entropy balances of the adsorbed phase. Such key thermodynamic quantities are essential in designing and analyzing the ANG storage system.

Acknowledgements

The authors' gratefully acknowledge the financial support given by grants (R265-000-268-305) from A*STAR/MPA, Singapore and (R265-000-286-597) from King Abdullah University of Science and Technology (KAUST), KSA.

References

[1] Ruthven, D.M., 1984, Principles of Adsorption and Adsorption Processes, John Wiley and Sons, London.
[2] Chua, H.T., Ng, K.C., Chakraborty, A., Oo, N.M., 2003, Thermodynamic property fields of an adsorbate-adsorbent system, Langmuir 19, p.2254-2259.
[3] Chakraborty, A., Saha, B.B., Ng, K.C., Koyama, S., Srinivasan, K., 2009, Theoretical insight of physical adsorption for a single-component adsorbent + adsorbate system: I. Thermodynamic property surfaces, Langmuir 25(4), p.2204-2211.
[4] Do, D.D., 1998, Adsorption Analysis: Equilibria and Kinetics, Imperial College Press, Singapore.
[5] Ozawa, S., Kusumi, S., Ogino, Y., 1976, Physical adsorption of gases at high pressure. IV. An improvement of the Dubinin-Astakhov adsorption equation, J. Col. Inter. Sci. 56, p. 83-91.
[6] Al-Muhtaseb, S.A., Ritter, J.A., 1999, Roles of surface heterogeneity and lateral interactions on the isosteric heat of adsorption and adsorbed phase heat capacity, J. Phys. Chem. B 103, p.2467-2479.
[7] Myers, A.L., 2002, Thermodynamics of adsorption in porous materials, AIChE J. 48, p.145-160.
[8] Chakraborty, A., Saha, B.B., Koyama, S., Ng, K.C., 2007, Specific heat capacity of a single component adsorbent-adsorbate system, Appl. Phys. Lett. 90, p.171902.
[9] Loh, W.S., Rahman, K.A., Chakraborty, A., Saha, B.B., Choo, Y.S., Khoo, B.C., Ng, K.C., 2010, Improved Isotherm data for Adsorption of Methane on Activated Carbons, J. Chem. Eng. Data 55, p.2840–2847.
[10] Rahman, K.A., Loh, W.S., Yanagi, H., Chakraborty, A., Saha B.B., Chun, W.G., Ng, K.C., 2010, Experimental adsorption isotherm of methane onto activated carbon at sub- and supercritical temperatures, J. Chem. Eng. Data 55, p.4961–4967.
[11] Zhou, L., Zhou, Y., Li, M., Chen, P., Wang, Y., 2000, Experimental and modeling study of the adsorption of supercritical methane on a high surface activated carbon, Langmuir 16, p.5955-5959.
[12] Himeno, S., Komatsu, T., Fujita, S., 2005, High pressure adsorption equilibria of methane and carbon dioxide on several activated carbons, J. Chem. Eng. Data 50, p.369-376.
[13] Frère, M.G., De Weireld, G.F., 2002, High-pressure and high-temperature excess adsorption isotherms of N_2, CH_4, and C_3H_8 on Activated Carbon, J. Chem. Eng. Data 47, p.823-829.
[14] Choi, B.U., Choi, D.K., Lee, Y.W., Lee, B.K., 2003, Adsorption equilibria of Methane, Ethane, Ethylene, Nitrogen, and Hydrogen onto activated carbon, J. Chem. Eng. Data 48, p.603-607.

Available online at www.sciencedirect.com

SciVerse ScienceDirect

Procedia Engineering 00 (2012) 000–000

Procedia Engineering

www.elsevier.com/locate/procedia

5th BSME International Conference on Thermal Engineering

Mixed convection along a vertical flat plate in a non-absorbing medium

Sadia Siddiqa[a,*] , M. A. Hossain[b], S. C. Saha[c]

[a]*COMSATS Intitute of Information Technology, Chak Shahzad, Islamabd, Pakistan*
[b]*Rtd. Professor, University of Dhaka, Dhaka, Bangladesh*
[c]*School of Chemistry, Physics & Mechanical Engineerin,Queensland University of Technology, GPO Box 2434, Brisbane Queensland 4001, Australia*

Abstract

Here mixed convection boundary layer flow of a viscous fluid along a heated vertical semi-infinite plate is investigated in a non-absorbing medium. The relationship between convection and thermal radiation is established via boundary condition of second kind on the thermally radiating vertical surface. The governing boundary layer equations are transformed into dimensionless parabolic partial differential equations with the help of appropriate transformations and the resultant system is solved numerically by applying straightforward finite difference method along with Gaussian elimination technique. It is worthy to note that Prandlt number, Pr, is taken to be small (<< 1) which is appropriate for liquid metals. Moreover, the numerical results are demonstrated graphically by showing the effects of important physical parameters, namely, the modified Richardson number (or mixed convection parameter), *Ri**, and surface radiation parameter, *R*, in terms of local skin friction and local Nusselt number coefficients.

Keywords: Mixed convection; boundary layer; non absorbing medium.

1. Introduction

Mixed convection is one of the transport phenomena in which both free and forced convection occurs together. The study of mixed convection along with thermal radiation has greatly been increased due to its importance in many practical applications. For instance, important engineering application where mixed convection occurs are cooling of electronic systems, chemical processing equipments, crystal growing, nuclear reactors, food processing and several other industrial processes. In the literature Sparrow *et al.* [1], Merkin [2], Lloyd and Sparrow [3], Tingwei *et al.* [4] and Raju *et al.* [5] studied the simplest physical model of such a flow by considering 2D laminar mixed convective flow along a vertical flat plate.

Heat transfer for sufficiently high temperature surfaces needs a simultaneous analysis of the influence of several kinds of heat transfer mechanisms. One such mechanism through which heat can be transferred more rapidly is by the absorption, emission and scattering of radiation by the fluid. Initially, Ozisik [6], Sparrow and Cess [7] and Arpaci [8] investigated the influence of thermal radiation and natural convection over the semi-infinite vertical plate. Further, considering the Rosseland diffusion approximation, investigations on the natural convection flow as well as on the mixed convection flow of an optically dense gray fluid have been accomplished by Hossain *et al.* [9], Hossain and Rees [10], Molla and Hossain [11], Siddiqa *et al.* [12] and Siddiqa *et al.* [13]. Besides this, heat transfer can also be determined for a non-absorbing medium in which absorption, emission and scattering processes are neglected and the surface of the object uniformly emits into the surrounding medium a constant thermal flux. Considering this, Martynenko *et al.* [14], Salomatov and Puzyrev [15] and Sokovishin and Shapiro [16] investigated the influence of thermal radiation in a non-absorbing medium under different circumstances.

In the present analysis, mixed convection boundary layer flow is considered along a semi-infinite vertical plate in a non-absorbing medium. It is futhre assumed that the processes of radiation absorption, emission and scattering are ignored and

the relationship between convection (mixed) and thermal radiation is established through a boundary condition of second kind on the thermally radiating vertical surface. The governing boundary layer equations are reduced to the convenient form with the help of appropriate formulation. The transformed system of equations is numerically integrated by employing finite difference method in conection with Gaussian elimination method. Numerical results thus obtained are expressed graphically in terms of local skin friction and local Nusselt number coefficients with effect of physical parameters that controls the flow field.

2. Mathematical Formulation

Consider the 2D steady state mixed convection boundary layer flow of a viscous incompressible fluid along a semi-infinite vertical heated surface in a non-absorbing medium. It is assumed that the processes of radiation absorption, emission and scattering are neglected. It is also supposed that the surface temperature of the flat plate, T_w, is sufficiently higher than the ambient fluid temperature, T_∞. Therefore under the usual Boussinesq approximation the governing boundary layer equations can be written as

$$\frac{\partial u}{\partial x}+\frac{\partial v}{\partial y}=0 \tag{1}$$

$$u\frac{\partial u}{\partial x}+v\frac{\partial u}{\partial y}=\nu\frac{\partial^2 u}{\partial y^2}+g\beta\left(T-T_\infty\right) \tag{2}$$

$$u\frac{\partial T}{\partial x}+v\frac{\partial T}{\partial y}=\alpha\frac{\partial^2 T}{\partial y^2} \tag{3}$$

where u, v are the velocity components in the x and y directions respectively, ν the kinematic coefficient of viscosity, g identifies the gravitational force, β the coefficient of thermal expansion, α the thermal diffusivity and T the temperature of the fluid in the thermal boundary layer. The coordinate system and the flow configuration of the problem are shown in Fig. 1.

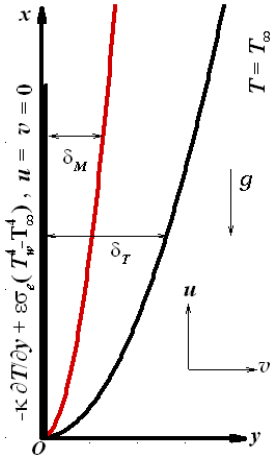

Fig. 1: Physical model and coordinate axis

The relationship between convection and thermal radiation is developed with the help of a boundary condition of second kind on the vertical surface which is supposed to be a gray diffusion radiator with emissivity ε. Therefore the boundary conditions can be written as (see [14]).

$$u(x,0)=v(x,0)=0,\ \kappa\left(\frac{\partial T}{\partial y}\right)_{y=0}=-q_w+\varepsilon\sigma_e\left(T_w^4-T_\infty^4\right) \tag{4}$$

$$u(x,\infty)=u_\infty,\ T(x,\infty)=T_\infty$$

where σ_e is the Stefan-Boltzmann constant and κ the thermal conductivity of the fluid.

We now introduce the following dimensionless parameters

$$\bar{u}=\frac{u}{u_\infty},\quad \bar{v}=\frac{L}{\nu Re_L^{1/2}}v,\quad \bar{x}=\frac{x}{L},\quad \bar{y}=\frac{Re_L^{1/2}}{L}y,\quad T-T_\infty=\frac{q_w L}{\kappa}Re_L^{-1/2}\theta \tag{5}$$

where $Re_L=u_\infty L/\nu$ is the dimensionless Reynolds number and L the characteristic length of the vertical surface.

Substituting (5) into the Eqs. (1)-(4), the following set of dimensionless governing equations (dropping bars) are obtained

$$\frac{\partial u}{\partial x}+\frac{\partial v}{\partial y}=0 \tag{6}$$

$$u\frac{\partial u}{\partial x}+v\frac{\partial u}{\partial y}=\frac{\partial^2 u}{\partial y^2}+Ri\,\theta \tag{7}$$

$$u\frac{\partial \theta}{\partial x}+v\frac{\partial \theta}{\partial y}=\frac{1}{\Pr}\frac{\partial^2 \theta}{\partial y^2} \tag{8}$$

The boundary conditions to be satisfied are

$$u(x,0)=v(x,0)=0,\ \left(\frac{\partial\theta}{\partial y}\right)_{y=0}=-1+\xi\theta(2+R\xi\theta)(2+2R\xi\theta+R^2\xi^2\theta^2) \tag{9}$$
$$u(x,\infty)=1,\ \theta(x,\infty)=0$$

where

$$Ri=\frac{Gr_L}{Re_L^{5/2}},\quad Gr_L=\frac{g\beta q_W L^4}{\kappa\nu^2},\quad R=\frac{q_W}{\sigma_e\varepsilon T_\infty^4},\quad \xi=\frac{R_L}{Re_L^{1/2}},\quad R_L=\frac{\sigma_e\varepsilon T_\infty^3 L}{\kappa},\quad \Pr=\frac{\nu}{\alpha} \tag{10}$$

In Equation (10) *Ri* is the mixed convection parameter or sometimes called buoyancy parameter, *R* the surface radiation parameter that measures the ratio of total heat flux transported from the surface of the wall to the radiative component and ξ the radiative length parameter that measures the degree of intensity of the ratio of radiative component and Reynolds number. It should be noted that for $\xi = 0$ the surface becomes non-radiating. Moreover, Prandtl number, Pr, calculates the strength of momentum diffusivity to the thermal diffusivity.

The method of solution of the present problem posed through the set of equations (6)-(9) follows after adopting the following transformations:

$$u=U,\quad v=x^{-1/2}V,\quad Y=x^{-1/2}y,\quad \theta=x^{1/2}\Theta,\quad \chi=x^{1/2}\xi \tag{11}$$

Substituting (11) in Equations (6)-(9) one obtains

$$\frac{1}{2}\chi\frac{\partial U}{\partial\chi}-\frac{Y}{2}\frac{\partial U}{\partial Y}+\frac{\partial V}{\partial Y}=0 \tag{12}$$

$$\frac{1}{2}\chi U\frac{\partial U}{\partial\chi}+\left(V-\frac{1}{2}YU\right)\frac{\partial U}{\partial Y}=\frac{\partial^2 U}{\partial Y^2}+Ri^*\chi^3\Theta \tag{13}$$

$$\frac{1}{2}\chi U\frac{\partial \Theta}{\partial\chi}+\left(V-\frac{1}{2}YU\right)\frac{\partial \Theta}{\partial Y}+\frac{1}{2}U\Theta=\frac{1}{\Pr}\frac{\partial^2 \Theta}{\partial Y^2} \tag{14}$$

The corresponding boundary conditions are

$$U(\chi,0)=V(\chi,0)=0,\ \left(\frac{\partial\Theta}{\partial Y}\right)_{Y=0}=-1+\chi\Theta(2+R\chi\Theta)(2+2R\chi\Theta+R^2\chi^2\Theta^2) \tag{15}$$
$$U(\chi,\infty)=1,\ \Theta(\chi,\infty)=0$$

where Ri^* ($=Ri/\xi^3$, the modified Richardson number).

Once the quantities *U* and Θ and their derivatives are evaluated, one can calculate local skin friction coefficient, $CfRe_\chi^{1/2}$ and local Nusselt number coefficient $NuRe_\chi^{-1/2}$ which are significant from engineering point of view. Below are the expressions for these physical quantities, respectively.

$$CfRe_\chi^{1/2}=\left(\frac{\partial U}{\partial Y}\right)_{Y=0}$$
$$NuRe_\chi^{-1/2}=\left[\frac{1}{\Theta}\left(1-\chi\Theta(2+R\chi\Theta)(2+2R\chi\Theta+R^2\chi^2\Theta^2)\right)\right]_{Y=0} \tag{16}$$

The system of equations (12)-(15) are solved numerically by employing finite difference method. For this, discretization process is initiated and central-difference quotients are used for diffusion terms whilst backward difference quotients are employed for the convection terms. Finally a system of algebraic equations is obtained which is solved with through Gaussain elimination method. The system of equations (12)-(15) is solved numerically by employing finite difference method. For this, discretization process is initiated and central-difference quotients are used for diffusion terms whilst backward difference quotients are employed for the convection terms. Finally a system of algebraic equations is obtained

which is solved with through Gaussain elimination method.

3. Results and Discussion

In the present paper, the effect of mixed convection flow along a semi-infinite vertical plate is analyzed in the nonabsorbing medium. The surface rediation effects are considered in the present model and particularly the processes of radiation absorption, emission and scattering are neglected. However, the relationship between convection and thermal radiation is established with the help of second kind of boundary condition on the thermally radiating vertical surface. The dimensionless boundary layer equations are transformed into parabolic partial differential equations and the solutions are then obtained numerically through finite difference method along with Gaussian elimination method. The resultant numerical solutions are discussed graphically in terms of local skin friction coefficient and local Nusselt number coefficient in the light of several physical parameters, such as, mixed convection parameter, Ri^*, and surface radiation parameter, R. Its worthy to note that these results are obtained for flulids having Prandtl number very small (<<1).

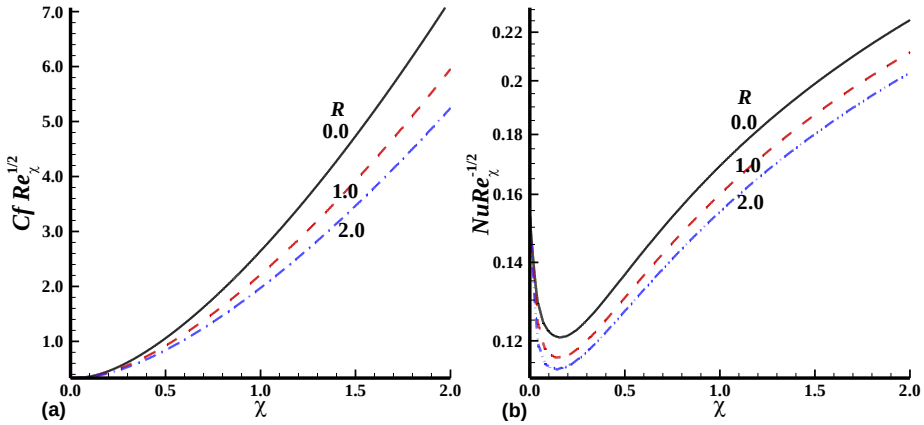

Fig. 2: (a) Variation of local skin friction and (b) Local Nusselt number with χ for R = 0.0, 1.0, 2.0 while Pr = 0.05 and Ri^* = 10.0

The influence of surface radiation parameter, R is discussed initially on local skin friction coefficient, $CfRe_\chi^{1/2}$, and local Nusselt number coefficient, $NuRe_\chi^{-1/2}$, in Fig. 2 for R = 0.0, 1.0, 2.0 while other parameters are Pr = 0.05 and Ri^*= 10.0. In can be seen from these figures that coefficient of local skin friction and coefficient of local Nusselt number decreases considerably owing to the increase in the surface radiation parameter, R. Physically it happens due to the reason that R is acting as source term which increses energy at the vicinity of the fluid and as a result coefficients of local skin friction and local Nusselt number enhances. In addition, Figs. 2(a)-2(b) show that momentum as well as thermal boundary layer thicknesses decreases slightly as R enhances.

Further, the variation of local skin friction coefficient, $CfRe_\chi^{1/2}$, and local Nusselt number coefficient, $NuRe_\chi^{-1/2}$, is inspected for Ri^* = 10.0, 50.0, 100.0 whereas Pr = 0.05 and R = 2.0 in Fig. 3. One can observe that wall shear stress and rate of heat transfer increases substantially as buoyancy force is intensified. Physically it happens due to the reason that $Ri^* > 0$ acts like supportive driving force which accelerates the fluid flow with in the boundary layer and consequently skin friction enhances and heat transfer rate reduces significantly.

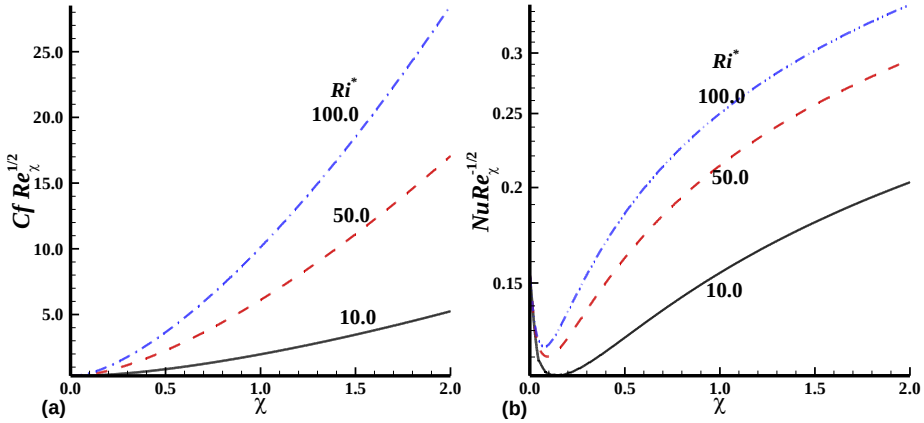

Fig. 3: (a) Variation of local skin friction and (b) Local Nusselt number with χ for Ri^* = 10.0, 50.0, 100.0 while Pr = 0.05 and R = 2.0.

4. Conclusions

In the present work, mixed convection flow along a semi-infinite vertical surface is considered in the non-absorbing medium. The relationship between convection and thermal radiation is set up through the second kind of boundary condition on the thermally radiating vertical surface. The governing equations are reduced to suitable form by using approptirate transformations. The reduced equations are integrated numerically with finite difference method in connection with Gaussian elimination technique. The numerical results are abtained in terms of $CfRe_{\chi}^{1/2}$ and $NuRe_{\chi}^{-1/2}$, for different values of the parameters, such as, surface radiation parameter, R, Richardson number, Ri^{*}, and locally varying parameter, χ, for fluids having Pr = 0.05. From the present analysis it is concluded that (i) coefficient of local skin friction and coefficient of local Nusselt number diminishes owing to the increase in the surface radiation parameter, R.

References

[1] Sparrow, E. M., Eichorn, R., Gregg., J. L., 1959. Combined Forced and Free Convection in Boundary Layer Flow, Phys. Fluids 2, p. 319-328.

[2] Merkin, J. H., 1969. The Effects of Buoyancy Forces on the Boundary Layer Flow Over Semi-Infinite Vertical Flat Plate in a Uniform Free Stream, J. Fluid Mech. 35, p. 4398-4450.

[3] Lloyd, J. R., Sparrow, E. M., 1970. Combined Forced and Free Convection Flow on Vertical Surfaces, Int. J. Heat Mass Transfer 13, p. 434-438.

[4] Tingwei, G., Bachrum, R., Dagguent, M., 1982. Influence de la Cconvective Natural le sur la Cconvection Fforce Andessus D‘une Ssurface Plane Vertical Voumise a un Flux de Rayonnement, Int. J. Heat Mass Transfer 25, p. 1061-1065.

[5] Raju, M. S., Liu, X. R., Law, C. K., 1984. A Formulation of Combined Forced and Free Convection Past Horizontal and Vertical Surfaces, Int. J. Heat Mass Transfer 27, p. 2215-2224.

[6] Ozisik, M. N., 1973. Thermal Radiation Transfer and Interactions with Conduction and Convection, John Wiley & Sons: New York.

[7] Sparrow, E. M., Cess, R. D., 1962. Radiation Heat Transfer, Augmented Edition. Hemishpere Media. Int. J. Heat Mass Transfer 5, p. 179-806.

[8] Arpaci, V. S., 1968. Effect of Thermal Radiation on the Laminar Free Convection From a Heated Vertical Plate, Int. J. Heat Mass Transfer 11, p. 871-881.

[9] Hossain, M. A., Kutubuddin, M., Pop, I., 1999. Effect of Conduction-Radiation Interaction on the Mixed Convection Flow from a Horizaontal Cylinder, Heat Mass Transfer 35, p. 307-314.

[10] Hossain, M. A., Rees, D. A. S., 1998. Radiation Conduction Interaction on Mixed Convection Flow Along a Slender Vertical Cylinder, AIAA J. Thermophys. Heat Transfer 12, p. 611-614.

[11] Molla, M. M., Hossain, M. A., 2007.S Radiation Effect on Mixed Convection Laminar Flow Along a Vertical Wavy Surface, Int. J. Therm. Sci. 46, p. 926-935.

[12] Siddiqa, S., Asghar, S., Hossain, M. A., 2011. Radiation Effects on Natural Convection Flow Over an Inclined Flat Plate with Temperature-Dependent Viscosity, Proc. IMechE Part C: J. Mechanical Engineering Science 225, p. 407-419.

[13] Siddiqa, S., Asghar, S., Hossain, M. A., 2012. Radiation Effect on Mixed Convection Flow of Viscous Fluid Having Temperature Dependent Density Along Permeable Vertical Plate, J. Eng. Phys. Thermophys. 85, p. 339-348.

[14] Martynenko, O. G., Sokovishin, Y. A., Shapiro, M. V., 1977. Free-Convection and Radiative Heat Transfer on a Vertical Plane Surface. Inzhenerno-Fizicheskii Zhurnal. 32, p. 1071-1079.

[15] Salomatov, V. V., Puzyrev, E. M., 1971. Influence of Thermal Radiation on the Laminar Boundary Layer of a Non-Absorbing Fluid, Inzhenerno-Fizicheskii Zhurnal. 20, p. 1008-1014.

[16] Sokovishin, Y. A., Shapiro, M. V., 1977. Heat Transfer of a Vertical Cylinder by Free Convection and Radiation, Inzhenerno-Fizicheskii Zhurnal. 33, p. 694-699.

Available online at www.sciencedirect.com

SciVerse ScienceDirect

Procedia Engineering 00 (2012) 000–000

Procedia Engineering

www.elsevier.com/locate/procedia

5th BSME International Conference on Thermal Engineering

Simulation of two-phase natural circulation cooling using air water system

S.T.Revankar[a,b,*], K.W. Song[a], S.F. Huang[a], B.W Rhee[c], R.J. Park[c], K.S. Ha[c], J.H. Song[c]

[a]*Division of Advanced Nuclear Engineering, POSTECH Pohang, Gyungbuk, Republic of Korea*
[b]*School of Nuclear Engineering, Purdue University, West Lafayette, IN 47906, USA*
[c]*Korean Atomic Energy Research Institute, Daejeon, Republic of Korea*

Abstract

A closed loop natural circulation system employs thermally induced density gradients in single phase or two-phase liquid form to induce circulation of the working fluid thereby obviating the need for any mechanical moving parts such as pumps and pump controls. Due to its passive nature the reliability of these systems is very high. That is the reason natural circulation cooling has been considered in advanced reactor core cooling and in engineered safety systems. Natural circulation cooling has been proposed to remove reactor decay heat by external vessel cooling for in-vessel core retention and for external core catcher cooling during sever accident scenario. First a scaling analysis was carried out for natural circulation flow in a closed loop. Based on the scaling analyses simulation of steam-water natural circulation is carried out with air-water flow in an inclined rectangular channel. The heat flux corresponding to the decay heat is simulated with air flux to the test section to produce equivalent flow quality. Design calculations were carried out for typical core catcher design to estimate the expected natural circulation rates. The natural circulation flow rate of the water and two-phase pressure drop were obtained for different air injection rate expressed as void fraction for a select downcomer pipe size. These results can be scaled to steam water system using scaling consideration presented.

Keywords: two-phase natural circulation; scaling; core-catcher cooling system; simulation; severe accident.

Nomenclature

A	flow area [m^2]
a	cross-sectional area [m^2]
c_p	specific heat [j/kg·C]
D	diameter [m]
d	conduction depth
f	friction factor
g	gravitational acceleration [m/s^2]
H	height [m]
i	Enthalpy [J/kg]
i_{fg}	latent heat of vaporization [J/kg]
j	superficial velocity [m/s]

* Corresponding author. Tel.: +82-54-279-9560; fax: +82-54-279-9559.
E-mail address: shripad@postech.ac.kr

K	minor loss coefficient
L	two-phase axial length (m)
l	length [m]
$\dot{m}$	mass flow rate [kg/s]
N	non-dimensional number
N_d	drift flux number
N_{Fr}	Froud number
N_f	friction number
N_o	orifice number Eq
N_{pch}	phase change number (= Zuber number)
N_{sub}	subcooling number
N_{th}	thermal inertia ratio number
N_{Zu}	Zuber number
p,P	Pressure [Pa]
Q	heat or power [W]
R	ratio of fluid density to gas density
T^*	time ratio number
u	velocity [m/s]
V_{gj}	drift velocity [m/s]
x	Quality
Greek Symbols	
α	void fraction
α_s	thermal diffusivity [m^2/s]
δ	conduction depth [m]
μ	dynamic viscosity [kg/m·s]
ρ	density [kg/m^3]
	Surface tension [N/m]
Subscripts	
e	exit
f	liquid
g	gas
i	ith component
lp	liquid phase
o	reference point/component
s	surface
sp	single phase
sub	subcooling
two	two-phase
th	thermal
Superscripts	
*	dimensionless quantity

1. Introduction

Natural circulation flow has been used in number of thermal transport systems. Such systems employ thermally induced density gradients in single phase fluid or two-phase gas-liquid mixture to induce circulation of the working fluids without need for any external power or mechanical moving parts such as pumps and pump controls. This increases the reliability and safety of the cooling system and reduces installation, operation and maintenance costs. Therefore natural circulation based cooling methods have been considered in advanced reactor core cooling and in engineered safety systems. Recently natural circulation cooling has been proposed to remove reactor decay heat during severe accident scenario where the reactor core might experience high temperature leading core melt. Designs for external vessel cooling for in-vessel core retention using natural circulation have been studied [1, 2].Similarly if the corium is discharged from the reactor vessel the ex-vessel corium containment and cooling have been considered where a core catcher plate is cooled by natural circulation. The natural circulation flow is similar to external vessel cooling where water flows through an inclined narrow gap below hot surface and is heated to produce boiling. The two-phase natural circulation enables cooling of the corium pool collected on core catcher.

Recently Song et al., [3] have developed a core catcher concept, which can be adapted for both existing reactors and the advanced light water reactors. This core catcher is a passively actuating device, which can arrest, stabilize and cool the molten core material inside the reactor cavity and thus reduce its impact on containment pressurization. Primary goal of the proposed ex-vessel core catcher is to reliably accommodate and rapidly stabilize the corium, including the entire core inventory and reactor internals that is injected into the cavity following a postulate severe accident. The ability of natural circulation cooling of the core catcher plate dictates its effectiveness in retaining the corium. The core catcher system has a large water supply that circulates through an inclined channel where the upper core catcher plate is cooled by the water flow in the channel. The two-phase natural circulation is driven by steam-water boiling process at inclined region. The geometry of cooling channel is rectangular with an inclined channel section (inclination angle of ~10 degree) followed by a vertical section. The flow starts from a single phase liquid and with boiling processes bubbles are generated in the flow. Hence various flow regimes are possible as void fraction increases along the cooling channel. The flow in the channel hence is continuously developing as the steam quality is increasing. The flow rate is function of the heat flux and flow loop losses.

2. Scaling Considerations

The scaling of the two-phase flow is carried out using the transient form of governing equations, mass, momentum and energy balances based on one-dimensional drift flux model [4]. For a two-phase natural circulation system, similarity groups have been developed from a perturbation analysis to these governing equations. The set of mass, momentum and energy equations are integrated along the loop, and the transfer functions between the inlet perturbation and various variables are obtained. The four equation drift flux model consisting of the mixture mass, momentum and energy equations and vapour continuity equation is analytically integrated along the flow path. From this, the integral response functions between various variables such as the velocity, density, void fraction, enthalpy and pressure drop are obtained. The non-dimensionalization of these response functions yields the key integral scaling parameters. From these, the scaling criteria for dynamic simulation can be obtained [4]. The important dimensionless groups that characterize the kinematic, dynamic and energy similarities are for two-phase are given in Table 1.

Table 1. Two-Phase Similarity Parameters

Phase Change No. $N_{pch} \equiv \left(\frac{4q'''\delta l_o}{Du_o\rho_f i_{fg}}\right)\left(\frac{\Delta\rho}{\rho_g}\right) = N_{Zu}$	Subcooling No. $N_{sub} \equiv \left(\frac{i_{sub}}{i_{fg}}\right)\left(\frac{\Delta\rho}{\rho_g}\right)$
Froud No. $N_{Fr} \equiv \left(\frac{u_o^2}{gl_o\alpha_o}\right)\left(\frac{\rho_f}{\Delta\rho}\right)$	Drift-flux No. $N_{di} \equiv \left(\frac{V_{gj}}{u_o}\right)_i$ (Void-Quality Relation)
Time Ratio No. $T_i^* \equiv \left(\frac{l_o/u_o}{\delta^2/\alpha_s}\right)_i$	Thermal Inertia Ratio, $N_{thi} \equiv \left(\frac{\rho_s c_{ps}\delta}{\rho_f c_{pf} d}\right)_i$
Friction No. $N_{fi} \equiv \left(\frac{f\,l}{D}\right)_i \left[\frac{1+x\left(\Delta\rho/\rho_g\right)}{\left(1+x\Delta\mu/\mu_g\right)^{0.25}}\right]\left(\frac{a_o}{a_i}\right)^2$	Orifice No. $N_{oi} \equiv K_i\left[1+x^{3/2}\left(\Delta\rho/\rho_g\right)\right]\left(\frac{a_o}{a_i}\right)^2$
where $\alpha_o = \left(\frac{\rho_f}{\Delta\rho}\right)\left(\frac{1}{1+(N_d+1)/(N_{Zu}-N_{sub})}\right)$.	

The scaling of the natural circulation with air air-water system requires fluid-fluid scaling consideration for flow dynamic similarity. The void fraction is related to quality through void quality relation. The drift velocity between gas liquid phase The x_e the vapour quality at the exit of the heated section in prototype from the similarity of the Zuber and subcooling numbers yields:

$$\left(x_e\right)_R\left(\frac{\Delta\rho}{\rho_g}\right)_R = 1. \tag{1}$$

.This indicates that the vapour quality should be scaled by the density ratio. If this condition is satisfied, the friction similarity in terms of N_{fi} and N_{oi} can be approximated by dropping the terms related to the two-phase friction multiplier. Furthermore, by definition it can be shown that

$$N_d = \left(\frac{\Delta\rho}{\rho_g} x_e\right)\left(\frac{\rho_f}{\Delta\rho\alpha_o} - 1\right) - 1 \tag{2}$$

Therefore, similarity of the drift flux number requires void fraction similarity.

$$(\alpha_e)_R \left(\frac{\Delta\rho}{\rho_f}\right)_R = 1 \; or \; (\alpha_e)_R \approx 1. \tag{3}$$

Also, since V_{gj} depends on the flow regime, this group parameter also characterizes the flow pattern. The density ratio group, given by the $(\Delta\rho/\rho_g)$ term, scales the fluids. This also appears in the groups N_{sub}, N_{pch}, N_f, and N_o. The representative constitutive equation for the relative motion based on the drift velocity correlation is given by:

$$V_{gj} = 0.2\left(1 - \sqrt{\frac{\rho_g}{\rho_f}}\right) j + 1.4\left(\frac{\sigma g \Delta\rho}{\rho_f^2}\right)^{\frac{1}{4}}. \tag{4}$$

where the volumetric flux, j, in the heated section is given by:

$$j = \left(1 + x\left(\frac{\Delta\rho}{\rho_g}\right)\right) u_o. \tag{5}$$

The classical void-quality correlation is:

$$\alpha = \alpha\left(x, \left(\frac{\rho_g}{\rho_f}\right), \left(\frac{\mu_g}{\mu_f}\right), etc.\right). \tag{6}$$

The relative motion similarity based on the drift velocity correlation becomes,

$$N_d = 0.2\left(1 - \sqrt{\frac{\rho_g}{\rho_f}}\right)\left[1 + x\left(\frac{\Delta\rho}{\rho_g}\right)\right] + \frac{1.4}{u_o}\left(\frac{\sigma g \Delta\rho}{\rho_f^2}\right)^{\frac{1}{4}}. \tag{7}$$

3. Scaled System Design

First a design of the scaled facility is carried out using set of geometrical parameters corresponding to a core catcher design by Song et al. [3]. Table 2 lists the prototype core catcher key geometric parameters. For this design the following parameters were matched between the prototype and the scaled facility: heat flux, mass flux, exit void fraction, total pressure drop and friction coefficient. The scaled facility has same channel height and length along the flow direction as the prototype but with scaled down channel width. The width of the scaled facility is 0.3 m instead of 16 m as in prototype. The system scales for components in the scaled model are shown in Table 2. Instead of heated section and steam generated due to boiling, air is used to simulate the two-phase flow in the coolant channel. The heat flux corresponding to the decay heat is simulated with air flux to the test section to produce equivalent flow quality. The upper tank is also simplified with single tank where two phase separation occurs and downcomer line is connected. A schematic of the test geometry is shown in Figure 1, where the steam generated is replaced by air injection rate.

Table 2. Scales for model and prototype system

Component	Prototype	Air-water modeling
Downcomer	6.6mxΦ0.15m, N=13	6.6mxΦ0.1m, N=1
Horizontal part	0.3mx0.1mx16m	0.3mx0.1mx0.3m
Inclined part	2.74mx0.1mx16m, 10°	2.74mx0.1mx0.3m, 10°
Vertical part	1mx0.1mx16m	1mx0.1mx0.3m
Heating power	10MW, 0.5%-100%	187.5kW, 0.5%-100%

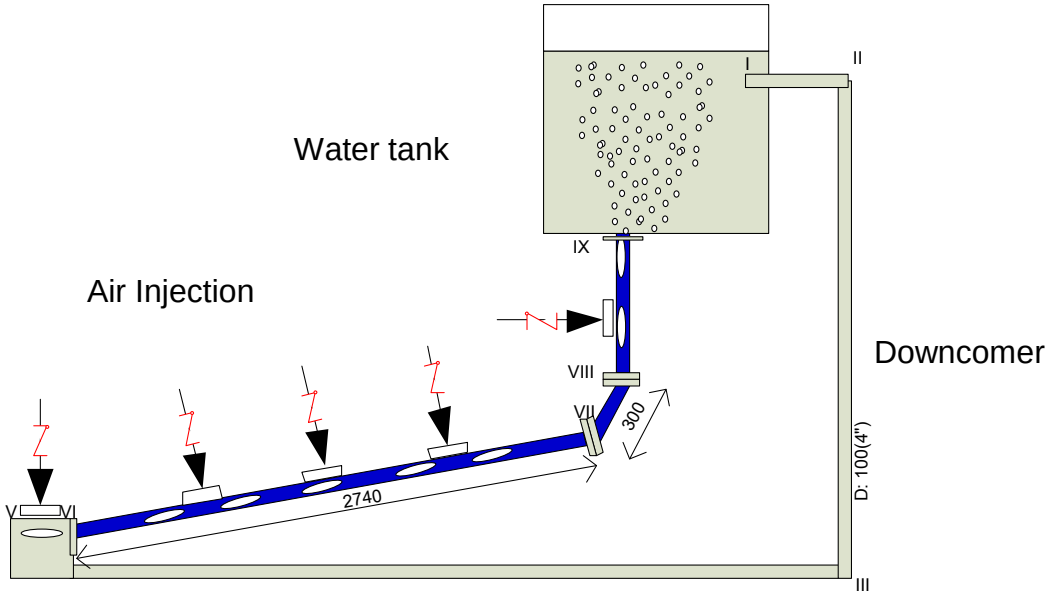

Figure 1. Schematic of air-water simulation loop

4. Natural Circulation Flow Rate and Pressure Drop

Design calculations were carried out for typical core catcher design to estimate the expected natural circulation rates. The loop mass flow rate in the coolant channel is determined by a balance between the pressure drop and hydrostatic head difference. The basic governing equations involved matching total buoyancy pressure drop due to the present of gas phase with the total pressure loss in the flow loop. For the pressure drop in the loop, we assume that the major pressure drop occurs in the two-phase part of the loop, where the pressure drop is expressed as below

$$\Delta p_{two} = \frac{1}{2}\frac{1}{\rho_f A^2}\dot{m}_{lp}^2\left(\frac{fL_{two}}{D}+K_{two}\right)\left(1+(R-1)\frac{x_e}{2}\right)+\frac{1}{2}\frac{1}{\rho_f A^2}\dot{m}_{lp}^2\left(\frac{fL_{sp}}{D}+K_{sp}\right) \tag{8}$$

It consists of skin friction and geometric loss. As there will be a flow blockage in the coolant channel we included the geometric loss K factor. Here R is density ratio, which is defined as ρ_f/ρ_g. L_{two} is the length of two phase region, L_{sp} is the length of single phase region, K_{two} is the geometric K factor in the two phase region, and K_{sp} is the geometric K factor in the single phase region. A is the flow area. Here, x_e is the flow quality at the exit.

As the density ratio R is in the order of 1000, we can neglect the second term in eqn. (1). And let's assume that the length of two phase region is close to L. Then the pressure drop can be approximated as

$$\Delta p_{two} = \frac{1}{2}\frac{1}{\rho_f A^2}\left(\frac{Q}{x_e i_{fg}}\right)^2\left(\frac{fL}{D}+K\right)\left(1+(R-1)\frac{x_e}{2}\right) \tag{9}$$

We will assume that the inlet flow is saturated for simplicity in the analysis. The energy balance in the heating section determines the exit flow quality

$$Q = \dot{m}_{lp} i_{fg} x_e \tag{10}$$

The driving head, which is difference between the cold water column and two phase column in the coolant channel, is as below

$$\Delta p_{dr} = \Delta\rho\alpha Hg = \frac{x_e R}{x_e(R-1)+2}\Delta\rho Hg \tag{11}$$

where the relation between the void fraction and flow quality is used by assuming that the liquid velocity and vapor velocity are the same,

$$\alpha = \frac{1}{1+\frac{1-x}{x}\frac{u_g}{Ru_f}} \tag{12}$$

For assumed downcomer pipe size and given air flow rate corresponding to the heat flux, the void fraction and the mass flow rates were calculated. Both homogenous two-phase flow and a drift flux model were assumed for the two phase system. Typical drift flux velocity in the inclined section was about ≤ 2 m/s.

In Figure 2 the mass flux is shown as function of heat load where qmax corresponds to the reference heating power given in Table 1. For model facility the downcomer pipe sizes of 10cm (4 inch)) and 7.5cm) (3 inch) were used in the calculations. From figure it seen that the 7.5 cm downcomer pipe gives slightly lower mass flux as compared to the prototype. The 10 cm diameter downcomer pipe given high mass flux in the model facility. So for the design 10 cm pipe seems as appropriate sized pipe since one can easily introduce additional losses with valve or orifice to match the prototype mass flux with the scaled model mass flux.

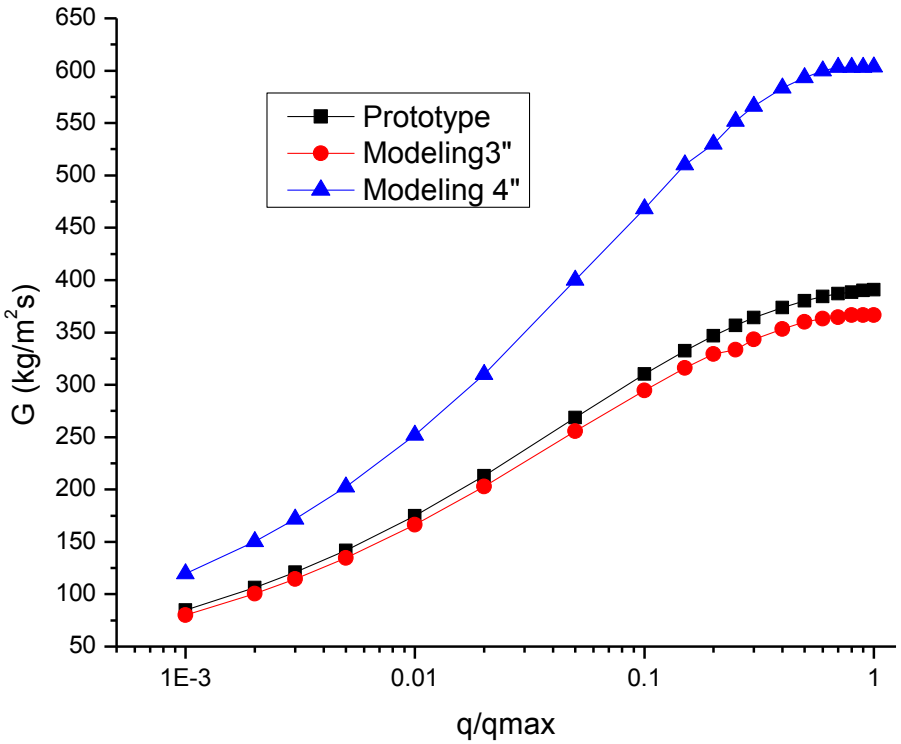

Figure 2. The natural circulation mass flux as function of heat load in the prototype and air-water model loop

In figure 3, exit void fraction is shown for different heat loads. Again here the values of exit void fraction for the prototype fall between the values of the exit void fraction calculated for 7.5 cm and 10cm downcomer pipes in the scaled facility.

The total two phase pressure drop in the heated section is shown in Figure 4(a) as function of heat load for different additional minor loss in the 10 cm downcomer pipe defined with minor loss coefficient K. The two phase pressure drop increases with K. However it is mainly depends on the void fraction which is function of heat load. In Figure 4(b), the total downcomer single phase pressure drop is shown as function of K for different heat load.

In Figure 5(a) and 5(b) the gas and liquid superficial liquid velocities and the single phase and two phase pressure drop in the model core catcher cooling channel are plotted as function of void fraction. The pressure drop and the superficial velocities of gas and liquid increase non-linearly with increase in void fraction.

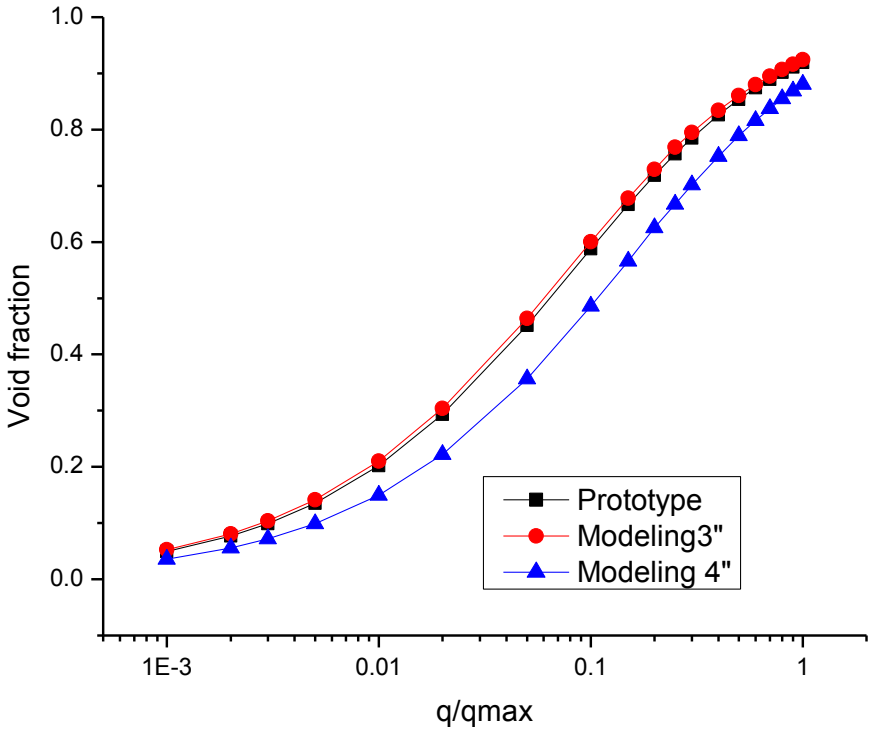

Figure 3. The exit void fraction as function of heat load in the prototype and air-water model loop

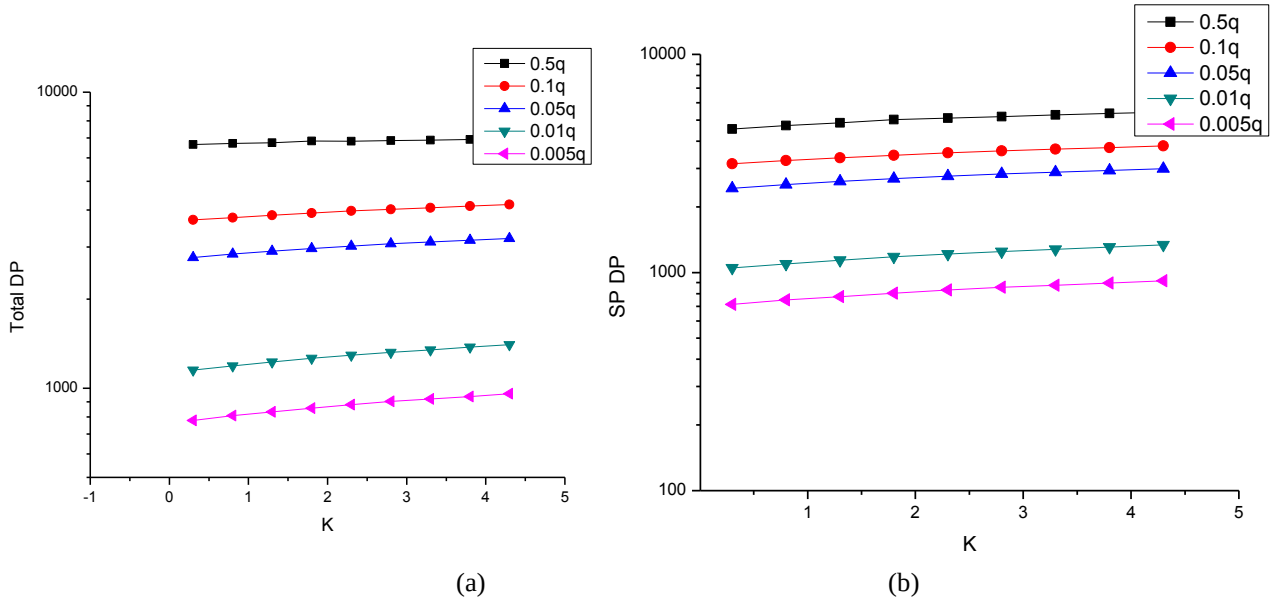

(a) (b)

Figure 4. (a) Total two phase pressure drop and (b) total single phase as function of minor loss coefficient K at different heat load.

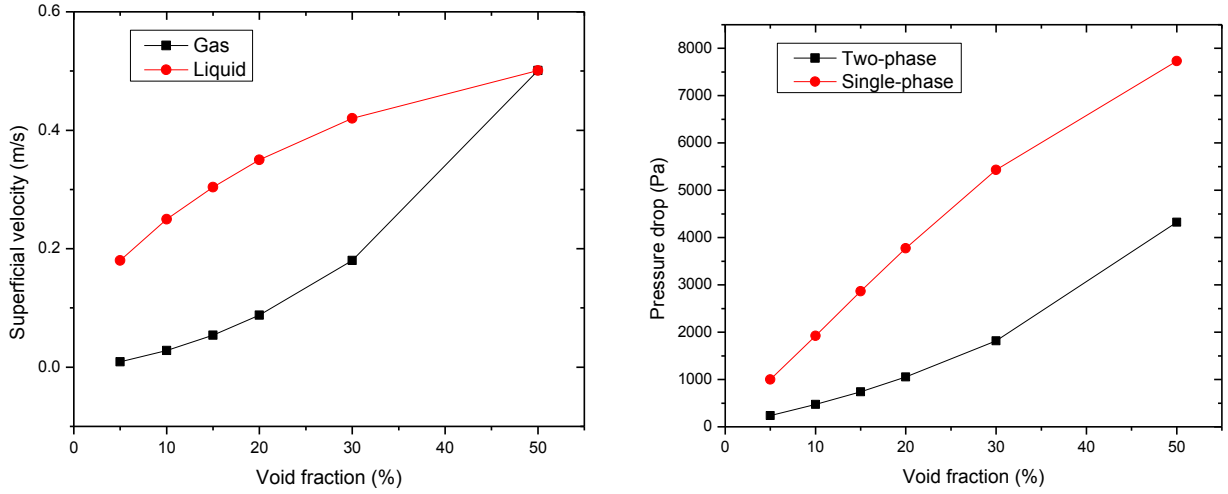

(a) (b)

Figure 5 (a) Gas and liquid superficial velocities and (b) total single phase and two phase pressure drop as function of exit void fraction with 10 cm diameter downcomer

5. Conclusions

Passive cooling based on natural circulation is utilized in core catcher system of advanced reactors to handle severe accident scenarios. A scaling analysis was performed to simulate a prototype core catcher cooling system with air-water two phase natural circulation loop. Key similarity parameters were identified for simulation of the two-phase natural circulation. A scaled down test facility design was conceived based on the scaling analysis. The natural circulation mass flux, system pressure drop were calculated for both prototype and the scaled model facility. Based on the calculation results a proper sized downcomer pipe for the model facility was obtained. Various pare metric results are presented that characterise the natural circulation phenomena in the core catcher cooling systems. Using the scaling parameters one can easily related results obtained from the scaled facility to the prototype condition.

Acknowledgements

This work was supported by KAERI and by World Class University program through the National Research Foundation of Korea funded by the Ministry of Education, Science and Technology (R31-30005).

References

[1] Song, J.H., Kim, S.B., and Kim, H.D., 2002, Analysis of External Cooling of the Reactor Vessel during Severe Accidents, Nuclear Technology, 138, p. 79.

[2] Ha, K.S., Park, R.J., et al., 2004, “A Non-Heating Experimental Study on the Two-Phase Natural Circulation through the Annular Gap between Reactor Vessel and Insulation under External Vessel Cooling,” ICAPP'04, Pittsburgh, PA USA. June 13-17, pp.1721-1728,

[3] Song, J. H., Ha, K. S., Park, R. J., Kim, J. T., and Cheung, F. B., 2011 “A Core Catcher Design for the Advanced Light Water Reactor,” Proceedings of International Conference on Advanced Nuclear Power Plants (ICAPP), Nice, France, May 2011.

[4] Ishii M., Revankar, S.T., et al. 1998, The three-level scaling approach with application to the Purdue University Multi-Dimensional Integral Test Assembly (PUMA), Nuclear Engineering and Design, 186, pp. 177.

Available online at www.sciencedirect.com

SciVerse ScienceDirect

Procedia Engineering 00 (2012) 000–000

Procedia Engineering

www.elsevier.com/locate/procedia

5th BSME International Conference on Thermal Engineering

Similarity solution of unsteady combined free and force convective laminar boundary layer flow about a vertical porous surface with suction and blowing

M. M. Touhid Hossain[a, *], Bichakshan Mandal[b] and Mohammad Arif Hoossain[a]

[a]*Department of Mathematics, Khulna University of Engineering & Technology, Khulna- 9203, Bangladesh*
[b]*Department of Mathematics, Govt. Mojid Memorial City College, Khulna- 9000, Bangladesh*

Abstract

In this paper the unsteady laminar combined free and forced convective boundary layer flow about a vertical porous plate in viscous incompressible fluid with suction and blowing is considered. The governing non-dimensional boundary layer partial differential equations are simplified first by using Boussinesq approximation. Secondly, similarity transformations are introduced on the basis of detailed analysis in order to transform the simplified coupled partial differential equations into a set of ordinary differential equations. The transformed complete similarity equations are then solved numerically by using Nachtsheim-Swigert shooting iteration technique along with sixth order Runga-Kutta method. The flow phenomenon has been characterized with the help of obtained flow controlling parameters such as suction parameter, buoyancy parameter, Prandtl number and the other driving parameter. The effects of the involved parameters on the velocity and temperature fields across the boundary layer are investigated. Numerical results for the velocity and temperature distributions are presented graphically. It is found that a small suction or blowing can play a significant role on the patterns of flow and temperature fields.

Keywords: Similarity solutions; comined convection; porous surface; suction and blowing.

1. Introduction

Mixed convection flows, or combined forced and free convection flows, arise in many transport processes in engineering devices and in nature. These flows are characterized by the buoyancy parameter (measure of the influence of the free convection in comparison with that of forced convection on the fluid flow) which depends on the flow configuration and the surface heating conditions. The problem of free, mixed and forced convection over a horizontal porous plate has been attracted the interest of many investigators (Viz. Clark and Riley [1], Schneider [2] and Merkin and Ingham [3] among several others) in view of its applications in many engineering and geophysical problems. Ramanaiah *et al.* [4] considered the problem of mixed convection over a horizontal plate subjected to a temperature or surface heat flux varying as a power of x.

The problem of mixed convection due to a heated or cooled vertical flat plate provides one of the most basic scenarios for heat transfer theory and thus is of considerable theoretical and practical interest and has been extensively studied by Sparrow *et al.* [5], Wilks [6], Afzal & Banthiya [7], Hunt & Wilks [8], Lin & Chen [9], Hussain & Afzal [10], Merkin *et al.* [11] etc. However, the problem of forced, free and mixed convection flows past a heated or cooled body with porous wall is of interest in relation to the boundary layer control on airfoil, lubrication of ceramic machine parts and food processing. Watanabe [12] has considered the mixed convection boundary layer flow past an isothermal vertical porous flat plate with uniform suction or injection. Sattar [13] made analytical studies on the combined forced and free convection flow in a porous medium. Further, a vast literature of similarity solution has appeared in the area of fluid mechanics, heat transfer,

* Corresponding author. Tel.: +88-041-813-508; fax: +88-041-774-403.
E-mail address: mthosain@yahoo.co.in

and mass transfer, etc. as it is one of the important means for the reduction of a number of independent variables with simplifying assumptions. It is revealed that the similarity solution, which being attained for some suitable values of different parameters, might be thought of being the solution of the convective boundary-layer context either near the leading edge or far away in the downstream. Deswita *et al.* [14] obtained a similarity solution for the steady laminar free convection boundary layer flow on a horizontal plate with variable wall temperature. Hossain and Mojumder [15] presented the similarity solution for the steady laminar free convection boundary layer flow generated above a heated horizontal rectangular surface. Furthermore, the study of complete similarity solutions of the unsteady laminar natural convection boundary layer flow above a heated horizontal semi-infinite porous plate have been considered by Hossain *et al.* [16, 17].

The similarity solutions in the context of mixed convection boundary layer flow of steady viscous incompressible fluid over an impermeable vertical flat plate were discussed by Ishak *et al.* [18]. Ramanaiah *et al.* [19] studied the similarity solutions of free, mixed and forced convection problems in a saturated porous media. The aim of the present paper is, therefore, to obtain a complete similarity solution of the unsteady laminar combined free and forced convection boundary layer flow about a heated vertical porous plate in viscous incompressible fluid and be attempted to investigate the effects of several involved parameters on the velocity and temperature fields and other flow parameters like skin friction, heat transfer coefficients across the boundary layer. We are also tried to predict the role of small suction or blowing velocity on these parameters as well.

2. Basic equations of the flow and mathematical analysis

A semi- infinite porous plate extending vertically upwards and which is fixed with its leading edge horizontal is placed in an unsteady free stream. The plate is heated to a certain unsteady temperature above the ambient temperature T_e. Heat is supplied by diffusion from the plate. The density of the fluid near the plate is reduced so that the fluid near the plate is buoyant compared with the fluid in the free stream at a large distance from the plate. Consequently layers of the fluid close to the plate begin to rise. It is supposed that the maximum velocity created in this buoyant layer at a distance L from the bottom of the plate is U. If the Reynolds number based on this velocity U is sufficiently large, buoyant flow is amenable to Prandtl's boundary layer analysis.

Consider that the flow direction is along the x-axis. Then the simplified form of the basic boundary layer equations of mass, momentum and energy for a laminar two-dimensional unsteady viscous and heat conducting fluid of variable properties above a semi-infinite heated vertical porous surface in dimensionless form subject to a body force are as follows:

$$\frac{D\rho}{Dt}+\rho\left(\frac{\partial u}{\partial x}+\frac{\partial v}{\partial y}\right)=0 \tag{1}$$

$$\rho\frac{Du}{Dt}=\left(\rho-\rho_e\right)g_x+\rho_e\left(\frac{\partial u_e}{\partial t}+u_e\frac{\partial u_e}{\partial x}\right)+\frac{\partial}{\partial y}\left(\mu\frac{\partial u}{\partial y}\right) \tag{2}$$

$$\rho c_p\left[\frac{D\theta}{Dt}+\theta\left\{\frac{\partial}{\partial t}\left(\ln\Delta T\right)+u\frac{\partial}{\partial x}\left(\ln\Delta T\right)\right\}\right]=\frac{\partial}{\partial y}\left(k\frac{\partial\theta}{\partial y}\right)-\frac{\rho c_p}{\Delta T}\left(u-u_e\right)\frac{\partial T_e}{\partial x} \tag{3}$$

Since at a particular station (x, t) the pressure p does not very with y through the boundary layer, we have written $p = p_e$,

$u\to u_e$, $\rho\to\rho_e$, $T\to T_e$ and $\frac{\partial}{\partial y}\to 0$. Also we have written $\frac{T-T_e}{T_w-T_e}=\theta$, $\Delta T=T_w-T_e$ (4)

where ΔT and T_e are functions of x and t. $T_e = T_0$ (= constant) is one of the solutions of (4).

3. Similar solutions for the Boussinesq approximation

In this step we will simplify the above boundary layer equations (1)-(3) using the usual Boussinesq approximation. Thus the elimination of the first term ($D\rho/Dt$) in the continuity equation (1) will be found to be lead to great simplification in the boundary layer equations. Since the fluid property variations other than density variation in the buoyancy term of the momentum equation are ignored completely in this approximation, it is also assumed here that the fluid temperature outside the boundary layer T_e is constant. Hence we get

$$\frac{\partial u}{\partial x}+\frac{\partial v}{\partial y}=0 \tag{5}$$

$$\frac{Du}{Dt}=-g_x\beta_T\Delta T\theta+\frac{\partial u_e}{\partial t}+u_e\frac{\partial u_e}{\partial x}+\upsilon\frac{\partial^2 u}{\partial y^2} \tag{6}$$

$$\frac{D\theta}{Dt}+\theta\left\{\frac{\partial}{\partial t}\left(\ln\Delta T\right)+u\frac{\partial}{\partial x}\left(\ln\Delta T\right)\right\}=\frac{\upsilon}{\mathrm{Pr}}\frac{\partial^2\theta}{\partial y^2} \tag{7}$$

where $\rho\approx\rho_r$, $\mu\approx\mu_r$, $k\approx k_r$, $c_p\approx c_{pr}$ and $\upsilon\left(=\frac{\mu_r}{\rho_r}\right)$ and $\mathrm{Pr}\left(=\frac{\mu_r c_{p_r}}{k_r}\right)$ are the kinematic viscosity and the Prandtl number of the fluid, respectively.

4. Equations governing similar solutions

To reduce the above system of equations (5)-(7) into suitable forms we adopt the method of similarity solutions. Hence the following substitutions are introduced–

$\xi=x,\ \phi=\frac{y}{\gamma\left(x,t\right)},\ \tau=t\quad u=UF_{\xi}\quad -v=\left(\gamma UF\right)_{\xi}-\phi U\gamma_{\xi}-v_w$

The equation of continuity (5) permits us to write $u=\frac{\partial\psi}{\partial y}$, $v=-\frac{\partial\psi}{\partial x}$, where $\psi\left(x,y,t\right)$ is the stream function at any point (x, y, t).

With the traditional substitution $\int_0^{\phi}\frac{u}{U\left(x,t\right)}d\phi_1=F\left(\xi,\phi,\tau\right)$, we have $\psi\left(\xi,\phi,\tau\right)=\gamma\left(\xi,\tau\right)U\left(\xi,\tau\right)F\left(\xi,\phi,\tau\right)-\psi\left(\xi,0,\tau\right)$, where the velocity components u and v are found to be $u=UF_{\xi}$, $v_w=-\frac{\partial\psi\left(\tau,\xi,0\right)}{\partial\xi}$ and $-v=\left(\gamma UF\right)_{\xi}-\phi U\gamma_{\xi}-v_w$.

Here $v_w=-\frac{\partial\psi\left(\tau,\xi,0\right)}{\partial\xi}$ represents the non-zero wall velocity called the suction or blowing velocity normal to the porous surface, so that fluid can either be sucked or blown through it. Physically, $v_w<0$ and $v_w>0$ represent the suction and blowing velocity through the porous surface, respectively. For uniform suction (or blowing) $v_w=\text{constant}$. However, $v_w=0$ implies that the surface is impermeable to the fluid. In view of above transformation, equations (5) to (7) become

$$\upsilon F_{\phi\phi\phi}+\left(a_0\phi+a_3\right)F_{\phi\phi}+\frac{1}{2}\left(a_1+a_2\right)FF_{\phi\phi}-a_2F_{\phi}^{\,2}-a_4F_{\phi}\vartheta+a_6=0 \tag{8}$$

$$\frac{\upsilon}{\mathrm{Pr}}\vartheta_{\phi\phi}+\left(a_0\phi+a_3\right)\vartheta_{\phi}+\frac{1}{2}(a_1+a_2)F\vartheta_{\phi}-(a_7+a_8F_{\phi})\vartheta=0 \tag{9}$$

where $F(\xi,\phi,\tau)$ and $\vartheta(\xi,\phi,\tau)$ are assumed at this stage to be function of ϕ alone and the *a*'s are given by

(*i*) $a_0=\gamma\gamma_{\tau}$, (*ii*) $a_1=(\gamma^2u_e)_{\xi}$, (*iii*) $a_2=\gamma^2\left(u_e\right)_{\xi}$, (*iv*) $a_3=-\gamma v_w$, (*v*) $a_4=\frac{\gamma^2\left(u_e\right)_{\tau}}{u_e}$, (*vi*) $a_5=-\frac{\gamma^2\beta_T g_x\Delta T}{u_e}$,

vii) $a_6=\frac{\gamma^2}{u_e}\left\{\left(u_e\right)_{\tau}+u_e\left(u_e\right)_{\xi}\right\}$, (*viii*) $a_7=\gamma^2\left(\ln\Delta T\right)_{\tau}$ and (*ix*) $a_8=\gamma^2u_e(\ln\Delta T)_{\xi}$ (10)

The boundary conditions which are imposed in order to determine the solutions of the transformed boundary layer equations (8)-(19) are given by: $F\left(0\right)=F_{\phi}\left(0\right)=0,\ F_{\phi}\left(\infty\right)=1;\ \theta\left(0\right)=1,\ \theta\left(\infty\right)=0$ (11)

The relations in equation (10) furnish us with the conditions under which similarity solutions are obtained provided that all *a*'s must be constants and thus the equations (8)-(9) will become non-linear ordinary differential equations.

In view of conditions (*ii*) and (*i*) stated in equation (10), we have $\gamma^2u_e=a_1\xi+A\left(\tau\right)$ and $\gamma^2=2a_0\tau+B\left(\xi\right)$, where $A\left(\tau\right)$ is either a function of τ or constant and $B\left(\xi\right)$ is either a function of ξ or constant. The above two relations yield

$$\frac{dA}{d\tau}.\frac{dB}{d\xi}=\left(2a_0+a_4\right)\left(a_1-a_2\right) \tag{12}$$

Therefore, the forms of the similarity equations, the scale factors $u_e\left(\tau,\xi\right)$ and $\gamma\left(\tau,\xi\right)$ entirely depend on the equation (12) which yields possibilities of four similarity cases, namely

(A) both $\frac{dA}{d\tau}$ and $\frac{dB}{d\xi}$ are finite constants, (B) both $\frac{dA}{d\tau}$ and $\frac{dB}{d\xi}$ are zero, (C) $\frac{dA}{d\tau}\neq0$, but $\frac{dB}{d\xi}=0$ and

(D) $\frac{dA}{d\tau}=0$, but $\frac{dB}{d\xi}\neq 0$. both $\frac{dA}{d\tau}$ and $\frac{dB}{d\xi}$ are finite constants.

4.1. Similarity case to be considered

Of these four similarity cases, only the Case (A) for which both ($dA/d\tau$) and ($dB/d\xi$) are finite constants has been studied here for the sake of brevity. Thus, we have $u_e = u_0$ (constant) and $\gamma^2 = 2a_0\tau + \frac{a_1}{u_0}\xi + \frac{C}{u_0}$ where C is any arbitrary constant. Substituting these in the conditions (i) to (ix) of equation (10) yields the relations between the constants as follows: a_0, a_1 are arbitrary and $a_2 = a_4 = 0$ $a_6 = 0$, $a_7 = -2a_0$, $a_8 = -a_1$, $a_3 = -\sqrt{2a_0\tau + \frac{a_1}{u_0}\xi + \frac{C}{u_0}}\,v_w$ and $a_5 = -\beta_T g_x \Delta T\left(\frac{2a_0\tau}{u_0} + \frac{a_1\xi + C}{u_0^{\,2}}\right)$. Substituting the constants and choosing $F = \alpha_1 f$ and $\phi = \alpha_2\eta$ the above equations (8) to (9) reduce to:

$$f_{\eta\eta\eta} + (\eta + \beta f + f_w)\, f_{\eta\eta} + \left(\frac{U_F}{u_0}\right)^2 \vartheta = 0 \tag{13}$$

$$\mathrm{P_r}^{-1}\vartheta_{\eta\eta} + (\eta + \beta f + f_w)\vartheta_\eta + 2(1+\beta f_\eta)\vartheta = 0 \tag{14}$$

subject to the transformed boundary conditions: $f(0) = f_\eta(0) = 0,\ f_\eta(\infty) = 1;\ \vartheta(0) = 1,\ \vartheta(\infty) = 0$ (15)

where it is also chosen that $\alpha_1 = \alpha_2$, $\frac{a_0\alpha^2{}_1}{\upsilon} = 1$, $\frac{a_1}{2a_0} = \beta$, $\frac{a_5}{a_0} = \left(\frac{U_F}{u_0}\right)^2$, $-\frac{L_c v_w R_e^{-\frac{1}{2}}}{\upsilon} = f_w$ with $U_F{}^2 = -g_x\beta_T\Delta T L_c$ and $L_c = 2\{u_0(\tau+\tau_0) + \beta(\xi+\xi_0)\}$ is the local characteristic length. The terms $\frac{a_5}{a_0}\vartheta = \left(\frac{U_F}{u_0}\right)^2\vartheta$ in the momentum equation indicates how important buoyancy effects are compared with the forced flow effects. The flow is said to be aided when $U_F{}^2/u_0{}^2$ is greater than zero and called an opposing flow when this parameter is less than zero. When $U_F{}^2 << u_0{}^2$ the flow becomes a forced flow, whereas for $u_0{}^2 << U_F{}^2$ the flow becomes a free convection flow. The skin friction and heat transfer coefficients τ_w and q_w associated with the equations (13) and (14) are: $\tau_w = \frac{\mu u_0}{L_c}\mathrm{Re}^{\frac{1}{2}} f_{\eta\eta}(0)$ and $q_w = -\frac{k\Delta T}{L_c}R_F{}^{\frac{1}{2}}\theta_\eta(0)$.

The $\Delta T-$variation for this case is $\Delta T \propto \frac{1}{L_c}$.

5. Numerical solution and discussions

To obtain the solution of the differential equations (13) – (14) with the boundary conditions (15), a numerical procedure based on Nachtsheim-Swigert shooting iteration technique (guessing the missing value) (Nachtsheim & Swigert (1965)) together with Runge-Kutta sixth order integration scheme is implemented. The effects of various parameters on the flow and temperature fields have been determined for different values of the suction/blowing parameter f_w, the driving parameter β (the ratio between the changes of local boundary-layer thickness with regard to position and time), the buoyancy parameter $U_F{}^2/u_0{}^2$ (the square of the ratio between the fluid velocity caused by buoyancy effects and external velocity for the forced flow) and the Prandtl number Pr. Since there are four parameters of interest in the present problem which can be varied, to observe the effect of one, the other three parameters are kept as constants. Under these conditions the solutions to the problem thus obtained finally by employing the above mentioned numerical technique are plotted and tabulated in terms of the similarity variables.

The effects of f_w on the velocity and temperature profiles are plotted in Fig. 1 (a) and (b), respectively. From Fig. 1 (a) we see that, for the case of suction ($f_w > 0$), the velocity profiles increase with the increase of η near the surface, become maximum and then decrease and finally become zero asymptotically but for the case of blowing ($f_w < 0$), velocity decreases near the surface and then increases with increasing η and finally leads to zero asymptotically. Further, velocity profiles decrease with increasing f_w for the suction case but for blowing, the magnitude of the velocity increase with the increase of f_w. The usual stabilizing effect of the suction parameter on the boundary layer growth is also evident from this figure. From Fig. 1 (b), we see that the temperature profiles increase close to the plate surface and away from the surface they decrease asymptotically and finally become zero with the increase of η, for the case of suction ($f_w > 0$). A reverse situation is found for the case of blowing ($f_w < 0$), that is, temperature profiles decrease first close to the plate surface and away from the

surface they increases asymptotically and finally become zero with the increase of η. It is also observed that temperature decreases with increasing suction but increases with the increase of blowing.

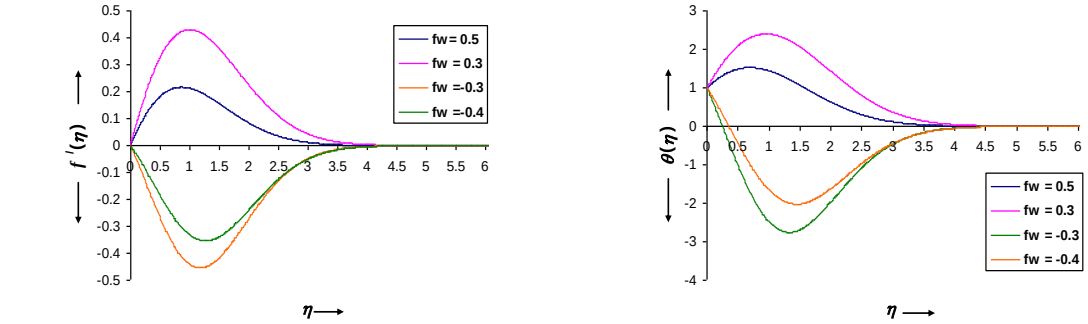

(a) (b)

Fig. 1 (a) Velocity profiles and (b) Temperature profiles for different values of f_w (with fixed values of $U_F^2/u_0^2 = 0.3$, β = -0.5 and $P_r = 0.72$).

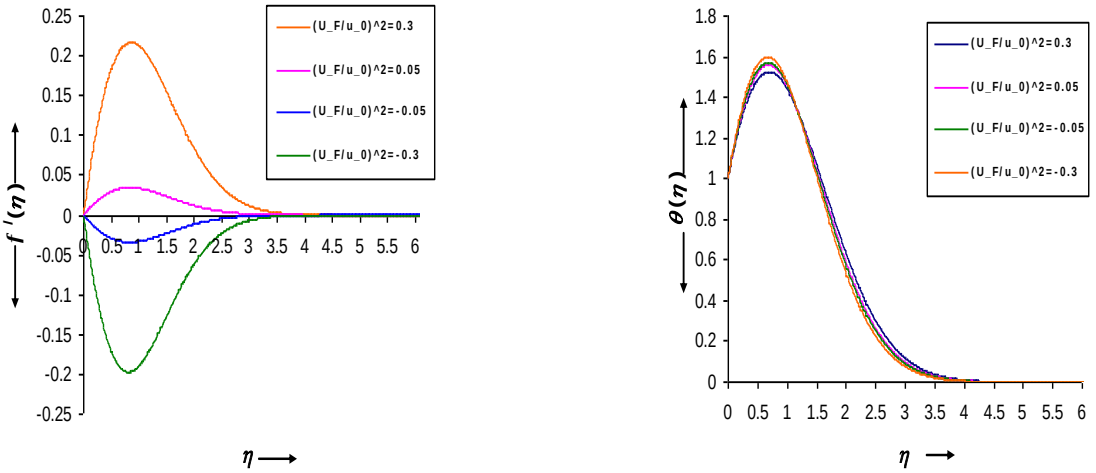

(a) (b)

Fig. 2 (a) Velocity profiles and (b) Temperature profiles for different values of U_F^2/u_0^2 (with fixed values of f_w= 0.5, β = -0.5 and $P_r = 0.72$).

Fig. 2 (a) and (b) show the effect of buoyancy parameter on the velocity and temperature profiles. We see from Fig. 2 (a) that, with the decreases in U_F^2/u_0^2 the maximum velocity reduces and thus the velocity became zero within short range for smaller values of $U_F^2/u_0^2 > 0$. Further, for $U_F^2/u_0^2 < 0$, the magnitudes of the velocity profiles increase with the increase of the magnitude of U_F^2/u_0^2. The unusual shape of temperature profiles in Fig. 2 (b) indicates that the wall receives more and more heat from the fluid as the buoyancy parameter U_F^2/u_0^2 decreases. This is due to the plate possessing an infinite source of heat at the leading edge, that is, $\Delta T \propto 1/t$ at $x = 0$, hence $T_w \to \infty$ as $t \to 0$.

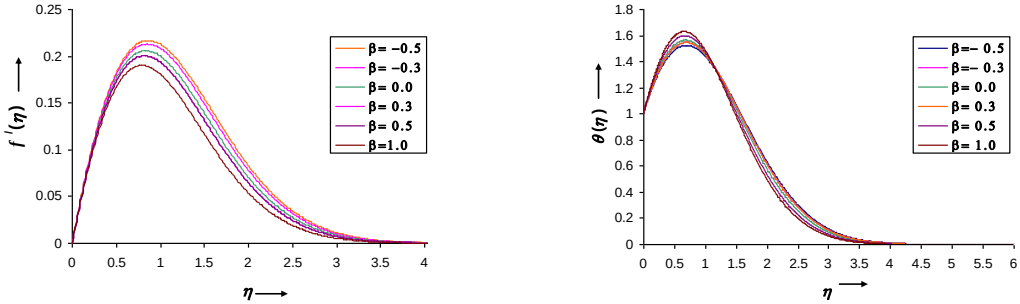

(a) (b)

Fig. 3 (a) Velocity profiles and (b) Temperature profiles for different values of β (with fixed values of f_w= 0.5, $U_F^2/u_0^2 = 0.3$ and $P_r = 0.72$).

From Fig. 3 (a) we observe that, velocity profiles became maximum at about $\eta = 0.8$ and they became zero at about $\eta = 3.25$ for all the values of β. Here the maximum velocity also decreases with the increase of β. Fig. 3 (b) exhibits the effect of β on the temperature profiles. Temperature first increases with increasing η and then decreases again and reduces to zero asymptotically as $\eta = 3.55$. In the range of $\eta = 1.2$, temperature increases with the increase in β and after that it decreases with increasing β.

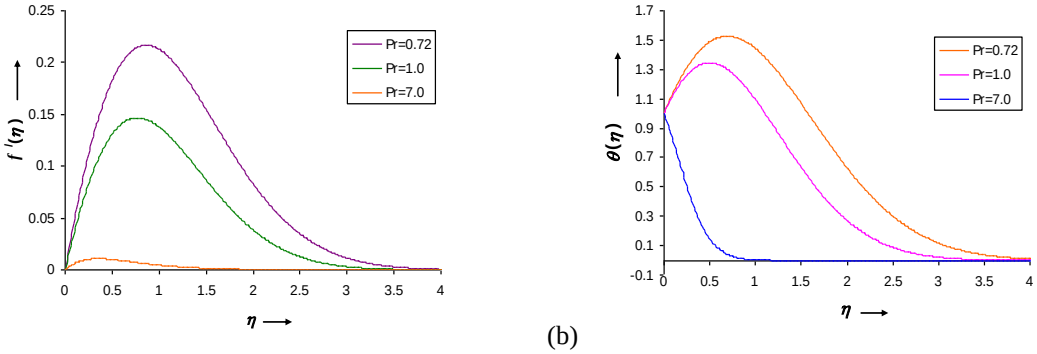

(a) (b)

Fig. 4 (a) Velocity profiles and (b) Temperature profiles for different values of P_r (with fixed values of $f_w = 0.5$, $(U_F/u_o)^2 = 0.3$ and $\beta = -0.5$).

The velocity and temperature profiles exhibit remarkable changes with the variation of *Pr* as observed from Fig. 4 (a) and (b). It is observed from Fig. 4 (a) that with the increase in η for different values of *Pr*, the pick values of velocity shift a little but they decrease rapidly with the increase in *Pr*. Like before, temperature decreases faster with increasing *Pr* as is seen in Fig. 4 (b).

The values proportional to the coefficients of skin friction ($f''(0)$) and heat transfer ($\theta'(0)$) are tabulated in Table 1. From the table it is seen that with the increase in f_w, both the coefficients of skin friction and heat transfer decrease for $f_w > 0$ but increases when $f_w < 0$. Whereas, the coefficient of skin friction increases but the coefficient of heat transfer decreases with increasing U_F^2/u_0^2. The reverse condition is observed for β variation. Here $f''(0)$ reduces with the increasing β but $\theta'(0)$ raises with increase in β. Again both $f''(0)$ and $\theta'(0)$ reduces with the increase in *Pr*. Unfortunately, no experimental data is available to us to compare our numerical results.

Table 1: Variation of the coefficients of skin friction and heat transfer with f_w , U_F^2/u_0^2, β and Pr.

Values Proportional to the coefficients of skin-friction ($f''(0)$) and heat transfer ($\theta'(0)$) with the variation of			
suction parameter *fw* for fixed $U_F^2/u_0^2 = 0.3$, $\beta = -0.5$ and $P_r = 0.72$:	*fw*	$f''(0)$	$\theta'(0)$
	0.50	0.52320	1.526461
	0.30	0.84130	2.840729
	-0.30	-0.49521	-3.80264
	-0.40	-0.31224	-2.56273
buoyancy parameter $(U_F/u_o)^2$ for fixed $f_w = 0.5$, $\beta = -0.5$ and $P_r = 0.72$:	U_F^2/u_0^2	$f''(0)$	$\theta'(0)$
	0.30	0.52320	1.526461
	0.05	0.085305	1.623241
	0.00	0.000218	1.636134
	-0.05	-0.08467	1.657115
	-0.30	-0.49989	1.743277
driving parameter β for fixed $f_w = 0.5$, $(U_F/u_o)^2 = 0.3$ and $P_r = 0.72$:	β	$f''(0)$	$\theta'(0)$
	-0.50	0.5232	1.526461
	-0.30	0.519727	1.583731
	0.00	0.51023	1.639961
	0.30	0.503857	1.703614
	0.50	0.500048	1.744627
	1.00	0.491727	1.842658
Prandtl's Number *Pr* for fixed $f_w = 0.5$, $(U_F/u_o)^2 = 0.3$ and $\beta = -0.5$:	*Pr*	$f''(0)$	$\theta'(0)$
	0.72	0.52320	1.526461
	1.0	0.399249	1.402178
	7.0	0.075811	-1.50982

6. Conclusions

Similarity solution for the two-dimensional unsteady laminar combined free and forced convection boundary layer flow over a semi-infinite heated vertical porous plate with the similarity case $(dA/d\tau)$ and $(dB/d\xi)$ = *finite constants* has been

studied in this paper. On the basis of the findings the following conclusions can be drawn:

a) with the increase in the magnitude of suction/blowing the magnitude of the velocity increases, where as with the increase of the suction and blowing the maximum values of the temperature decreases. Also suction decreases both the coefficients of skin friction and heat transfer while blowing increases those.

b) with the increase in the buoyancy parameter the velocity increases (when buoyancy is negative velocity also remain negative). Up to a certain region (very close to the plate) with the increase in the buoyancy, temperature decreases but there after the relationship is reversed.

c) with the increase in the control parameter the velocity decreases, but always remain positive. Up to a certain region (very close to the plate) with the increase in control parameter temperature increases and there after the relationship is reversed.

d) with the increase in *Pr* both the velocity and temperature decrease. Also both the values proportional to the coefficients of skin-friction and heat transfer decrease with the increase in the Prandtl's number.

References

[1] Clarke JF, Riley N. Natural convection induced in a gas by the presence of a hot porous horizontal surface. Q. J1. Mech., Appl. Math. 1975; 28, 373–396.

[2] Schneider W. A similarity solution for combined forced and free convection flow over a horizontal plate. Int. J. Heat Mass Transf. 1979; 22, 1401–1406.

[3] Merkin JH, Ingham DB. Mixed convection similarity solutions on a horizontal surface. ZAMP 1987; 38, 102–116.

[4] Ramanaiah G, Malarvizhi G and Merkin JH. A unified treatment of mixed convection on a permeable horizontal plate. Wäfirme-und Stoffübertragung 1991; 26, 187–192.

[5] Sparrow EM, Eichorn E and Gregg JL. Combined forced and free convection in boundary layer flow. Phys. Fluids 1959; 2, 319–328.

[6] Wilks G. Combined forced and free convection flow on vertical surfaces. Int. J. Heat Mass Transf. 1973; 16, 1958–1963.

[7] Afzal N and Banthiya NK. Mixed convection over a semi-infinite vertical flat plate. J. Appl. Math. Phys. 1977; 28, 993–1004.

[8] Hunt R and Wilks G. On the behaviour of laminar boundary-layer equations of mixed convection near a point of zero skin friction. J. Fluid Mech. 1980; 101, 377–391.

[9] Lin HT and Chen CC. Mixed convection from a vertical plate with uniform heat flux to fluids of any Prandtl number. J. Chin. Inst. Chem. Eng. 1987; 18, 209–220.

[10] Hussain T and Afzal N. Computer extension of perturbation series for mixed convection on a vertical plate: favourable and adverse flows. Fluid Dyn. Res. 1988; 4, 107–121.

[11] Merkin JH, Pop I and Mahmood T. Mixed convection on a vertical surface with a prescribed heat flux: the solution for small and large Prandtl numbers. J. Eng. Math. 1991; 25, 165–190.

[12] Watanabe T. Forced and free mixed convection boundary layer flow with uniform suction or injection on a vertical flat plate. Acta Mech. 1991; 89, 123–132.

[13] Sattar MA. Free and forced convection boundary layer flow through a porous medium with large suction. International Journal of Energy Research 1993; 17, 1–7.

[14] Deswita L, Nazar R, Ahmad R, Ishak A and Pop I. Similarity Solutions of Free Convection Boundary Layer Flow on a Horizontal Plate with Variable Wall Temperature. European Journal of Scientific Research 2009; Vol. 27(2), 188–198.

[15] Hossain MMT and Mojumder R. Similarity solution for the steady natural convection boundary layer flow and heat transfer above a heated horizontal surface with transpiration. Int. J. of Appl. Math. and Mech. 2010; 6(4), 1–16.

[16] Hossain MMT, Mojumder R and Hossain MA. Solution of natural convection boundary layer flow above a semi-infinite porous horizontal plate under similarity transformations with suction and blowing. Daffodil International University Journal of Science and Technology 2011; 6(1), 43–51.

[17] Hossain MMT, Hossain MA and Mojumder R. A study of similarity solutions for the unsteady natural convection flow above a semi-infinite heated horizontal porous plate with transpiration. Proceedings of the 13th Asian Congress of Fluid Mechanics (ACFM) 17–21 December, 2010, Dhaka, Bangladesh; 1462–1465.

[18] Ishak A, Nazar R and Pop I. Dual solutions in mixed convection boundary-layer flow with suction or injection. IMA Journal of Applied Mathematics 2007; 1−13.

[19] Ramanaiah G and Malarvizhi G. Unified treatment of similarity solutions of free, mixed and forced convection problems in saturated porous media. Proc. of Sixth Int. Conf. on Numerical Method in Thermal Problems, Swansea, U.K. 1989; 431−439.

Available online at www.sciencedirect.com

SciVerse ScienceDirect

Procedia Engineering 00 (2012) 000–000

Procedia Engineering

www.elsevier.com/locate/procedia

5th BSME International Conference on Thermal Engineering

Unsteady Solutions with Convective Heat Transfer through a Curved Duct Flow

Rabindra Nath Mondal[a]* Md. Saidul Islam[b] and Md. Kutub Uddin[c]

[a]*Department. of Mathematics, Faculty of Science, Jagannath University, Dhaka-1000, Bangladesh*
[b]*Mathematics Discipline; Science, Engineering and Technology School, Khulna University, Khulna-9208, Bangladesh*
[c]*Department of Mathematics, University of Dhaka, Dhaka-1000, Bangladesh*
Email: rnmondal71@yahoo.com

Abstract

Unsteady solutions with convective heat transfer through a curved duct flow has been studied numerically by using a spectral method, and covering a wide range of the temperature difference between the vertical sidewalls for the Grashof number, $100 \le Gr \le 2000$, where the outer wall is heated and the inner wall cooled. In this paper, unsteady solutions are obtained by the time evolution calculations for two cases of the Dean numbers, Case I: Dn = 100 and Case II: Dn = 500 for the aspect ratio $1 \le l \le 3$. It is found that, at Dn = 100 there appears a steady-state solution for small or large Gr. For moderate Gr, however, the steady-state solution turns into periodic solution, if the aspect ratio is increased. For Dn = 500, on the other hand, it is found that the steady-state solution turns into chaotic solution for small and large Gr for any aspect ratio lying in the range. For moderate Gr, however, the steady-state solution turns into chaotic solution through periodic solutions in the scenario "*steady* $\rightarrow$ *periodic* $\rightarrow$ *chaotic*", if the aspect ratio is increased. Effects of secondary flow on convective heat transfer are also investigated.

Keywords: Curved duct, secondary flow, aspect ratio, time evolution, chaos, heat transfer

Nomenclature

Dn	: Dean number	T	: Temperature		
g	: Gravitational acceleration	u	: Velocity components in the $x-$direction		
Gr	: Grashof number	v	: Velocity components in the $y-$direction		
h	: Half height of the cross section	w	: Velocity components in the $z-$direction		
d	: Half width of the cross section	x	: Horizontal axis		
L	: Radius of the curvature	y	: Vertical axis		
P_r	: Prandtl number	z	: Axis in the direction of the main flow		
t	: Time	λ	: Resistance coefficient		
Greek letters					
δ	: Curvature of the duct	μ	: Viscosity	υ	: Kinematic viscosity
ρ	: Density	κ	: Thermal diffusivity	ψ	: Sectional stream function

* Corresponding author. Tel.: +88-01710851580; Fax: +88-02-7113752.
E-mail address: rnmondal71@yahoo.com

1. Introduction

The study of flow and heat transfer in curved ducts and channels has been and continues to be an area of paramount interest of many researchers because of the diversity of their practical applications in fluids engineering, such as in fluid transportation, refrigeration, air conditioning systems, heat exchangers and blade-to-blade passages in modern gas turbines. One of the interesting phenomena of the flow through a curved duct is the bifurcation of the flow because generally there exist many steady solutions due to channel curvature. Studies of the flow through a curved duct have been made, experimentally or numerically, for various shapes of the cross section by many authors. However, an extensive treatment of the bifurcation structure of the flow through a curved duct of rectangular cross section was presented by Winters [1] and Mondal [2].

The time-dependent behavior of the flow in a curved rectangular duct of large aspect ratio was investigated, in detail, by Yanase et al. [3] numerically. They performed numerical investigation of isothermal flows through a curved rectangular duct and addressed the time-dependent behavior of the unsteady solutions. Chandratilleke and Nursubyakto [4] presented numerical calculations to describe the secondary flow characteristics in the flow through curved ducts of aspect ratios ranging from 1 to 8 that were heated on the outer wall, where they studied for small Dean numbers and compared the numerical results with their experimental data. Wang and Yang [5] performed numerical as well as experimental investigations of periodic oscillations for the fully developed flow in a curved square duct. However, unsteady flow characteristics through a curved duct with rectangular cross section of aspect ratio 2 were investigated in detail by Yanase *et al*. [6]. Mondal et al [7] investigated time-dependent behaviour of flows with convective heat transfer in a curved square duct. Recently, Mondal *et al.* ([8], [9]) performed numerical prediction of the unsteady solutions by time-evolution calculations for the flow through a curved square duct and discussed the transitional behavior of the unsteady solutions. To the best of the authors' knowledge, however, there has not yet been done any substantial work studying the effects of aspect ratios on the unsteady flow characteristics for the non-isothermal flows through a curved rectangular duct. But from the scientific as well as engineering point of view it is quite interesting to study the unsteady flow behavior in the presence of buoyancy forces by varying aspect ratios, because this type of flow is often encountered in engineering applications. The present paper is, therefore, an attempt to fill up this gap with the study of the flow characteristics through a curved rectangular duct for various aspect ratios.

2. Mathematical Formulations

Consider an incompressible viscous fluid streaming through a curved duct with rectangular cross section whose width and height are 2*d* and 2*h*, respectively. The coordinate system with the relevant notations are shown in Fig. 1. It is assumed that the outer wall of the duct is heated while the inner one is cooled. The temperature of the outer wall is $T_0 + \Delta T$ and that of the inner wall is $T_0 - \Delta T$, where $\Delta T > 0$. The x, y, and z axes are taken to be in the horizontal, vertical, and axial directions, respectively. It is assumed that the flow is uniform in the axial direction, and that it is driven by a constant pressure gradient *G* along the center-line of the duct, i.e. the main flow in the axial direction as shown in Fig. 1.The variables are non-dimensionalized by using the representative length *d* and the representative velocity $U_0 = \nu/d$ .We introduce the non-dimensional variables defined as

$$u = \frac{u'}{U_0}, \qquad v = \frac{v'}{U_0}, \quad w = \frac{\sqrt{2\delta}}{U_0} w', \quad x = \frac{x'}{d}, \quad \bar{y} = \frac{y'}{d}, \quad z = \frac{z'}{d}$$

$$T = \frac{T'}{\Delta T}, \quad t = \frac{U_0}{d} t', \quad \delta = \frac{d}{L}, \quad P = \frac{P'}{\rho U_0^2}, G = \frac{\partial P'}{\partial z'} \frac{d}{\rho U_o{}^2}$$

where u, v, and w are the non-dimensional velocity components in the x, y, and z directions, respectively; t is the non-dimensional time, P the non-dimensional pressure, δ the non-dimensional curvature, and temperature is non-dimensionalized by ΔT. Henceforth, all the variables are nondimensionalized if not specified.

The sectional stream function ψ is introduced in the *x*- and *y*- directions as

$$u = \frac{1}{1+\delta x} \frac{\partial \psi}{\partial \bar{y}}, v = -\frac{1}{1+\delta x} \frac{\partial \psi}{\partial x}. \tag{1}$$

A new coordinate variable y' is introduced in the y direction as $y = ly'$, where $l = h/d$ is the aspect ratio of the duct cross section. From now on y denotes y' for the sake of simplicity. Then the basic equations for w, ψ and T are derived from the Navier-Stokes equations and the energy equation under the *Boussinesq approximation* as,

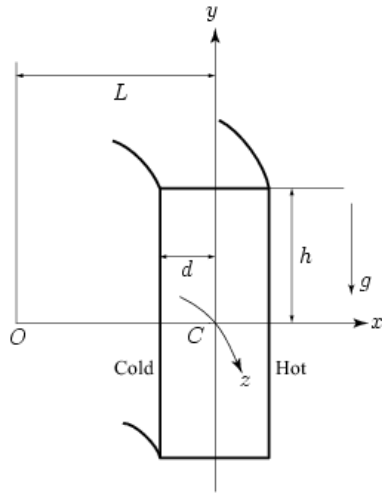

Figure 1. Coordinate system of the curved rectangular duct

$$(1+\delta x)\frac{\partial w}{\partial t}+\frac{1}{l}\frac{\partial(w,\psi)}{\partial(x,y)}-D_n+\frac{\delta^2 w}{1+\delta x}=(1+\delta x)\Delta_2 w-\frac{\delta}{l(1+\delta x)}\frac{\partial\psi}{\partial y}w+\delta\frac{\partial w}{\partial x} \tag{2}$$

$$\left(\Delta_2-\frac{\delta}{1+\delta x}\frac{\partial}{\partial x}\right)\frac{\partial\psi}{\partial t}=-\frac{1}{l(1+\delta x)}\frac{\partial(\Delta_2\psi,\psi)}{\partial(x,y)}+\frac{\delta}{l\left(1+\delta x\right)^2}\times\left[\frac{\partial\psi}{\partial y}\left(2\Delta_2\psi-\frac{3\delta}{1+\delta x}\frac{\partial\psi}{\partial x}+\frac{\partial^2\psi}{\partial x^2}\right)-\frac{\partial\psi}{\partial x}\frac{\partial^2\psi}{\partial x\partial y}\right]+\frac{\delta}{\left(1+\delta x\right)^2}$$
$$\times\left[3\delta\frac{\delta^2\psi}{\partial x^2}-\frac{3\delta^2}{1+\delta x}\frac{\partial\psi}{\partial x}\right]-\frac{2\delta}{1+\delta x}\frac{\partial}{\partial x}\Delta_2\psi+\frac{1}{l}w\frac{\partial w}{\partial y}\times\Delta_2^2\psi-Gr(1+\delta x)\frac{\partial T}{\partial x}, \tag{3}$$

$$\frac{\partial T}{\partial t}+\frac{1}{l(1+\delta x)}\frac{\partial(T,\psi)}{\partial(x,y)}=\frac{1}{\mathrm{Pr}}\left(\Delta_2 T+\frac{\delta}{1+\delta x}\frac{\partial T}{\partial x}\right). \tag{4}$$

where

$$\Delta_2\equiv\frac{\partial^2}{\partial x^2}+\frac{1}{l^2}\frac{\partial^2}{\partial y^2},\quad \frac{\partial(f,g)}{\partial(x,y)}\equiv\frac{\partial f}{\partial x}\frac{\partial g}{\partial y}-\frac{\partial f}{\partial y}\frac{\partial g}{\partial x}. \tag{5}$$

The Dean number D_n, the Grashof number G_r, and the Prandtl number P_r, which appear in Eqs. (2) to (4) are defined as

$$D_n=\frac{Gd^3}{\mu\nu}\sqrt{\frac{2d}{L}},\quad G_r=\frac{\beta g\Delta T d^3}{\nu^2},\quad P_r=\frac{\nu}{k} \tag{6}$$

where μ,ν,k and g are the viscosity, the coefficient of thermal expansion, the coefficient of thermal diffusivity and the gravitational acceleration respectively.

The rigid boundary conditions for w and ψ are used as

$$w(\pm1,y)=w(x,\pm1)=\psi(\pm1,y)=\psi(x,\pm1)=\frac{\partial\psi}{\partial x}(\pm1,y)=\frac{\partial\psi}{\partial y}(x,\pm1)=0 \tag{7}$$

and the temperature T is assumed to be constant on the walls as

$$T(1,y)=1,\ T(-1,y)=-1,\ T(x,\pm1)=x. \tag{8}$$

The upper and lower walls are adiabatic. In the present study, *Dn* and *Gr* are varied while δ and *Pr* are fixed as δ = 0.1 and *Pr* = 7.0 (water).

3. Method of numerical calculation

In order to obtain the numerical solutions, spectral method is used. The main objective of the method is to use the expansion of the polynomial functions that is the variables are expanded in the series of functions consisting of Chebyshev polynomials. The expansion function $\phi_n(x)$ and $\psi_n(x)$ are expressed as

$$\Phi_n(x)=\left(1-x^2\right)C_n(x),\ \Psi_n(x)=\left(1-x^2\right)^2C_n(x), \tag{9}$$

where $C_n(x)=\cos(n\cos^{-1}(x))$ is the n^{th} order Chebyshev polynomial. $w(x,y,z)$, $\psi(x,y,t)$ and $T(x,y,t)$ are expanded in terms of $\Phi_n(x)$ and $\Psi_n(x)$ as

$$\left.\begin{aligned} w(x,y,z) &= \sum_{m=0}^{M}\sum_{n=0}^{N} w_{mn}(t)\Phi_m(x)\Phi_n(y), \\ \psi(x,y,t) &= \sum_{m=0}^{M}\sum_{n=0}^{N} \psi_{mn}(t)\Psi_m(x)\Psi_n(y), \\ T(x,y,t) &= \sum_{m=0}^{M}\sum_{n=0}^{N} T_{mn}(t)\Phi_m(x)\Phi_n(y)+x, \end{aligned}\right\} \tag{10}$$

where M and N are the truncation numbers in the x and y directions respectively. The expansion coefficients w_{mn}, ψ_{mn} and T_{mn} are then substituted into the basic Eqs. (2), (3) and (4) and the collocation method is applied. As a result, the nonlinear algebraic equations for w_{mn}, ψ_{mn} and T_{mn} are obtained. The collocation points are taken to be

$$\left.\begin{aligned} x_i &= \cos\left[\pi\left(1-\frac{i}{M+2}\right)\right], \quad i=1,...,M+1, \\ y_i &= \cos\left[\pi\left(1-\frac{i}{N+2}\right)\right], \quad j=1,...,N+1. \end{aligned}\right\} \tag{11}$$

where $i=1,...,M+1$ and $j=1,...,N+1$. In the present study, numerical calculations are carried out over a wide range of the Grashof number $100 \le Gr \le 2000$ for two cases of the Dean numbers, Dn = 100 and Dn = 500 for the aspect ratio $1 \le l \le 3$. Steady solutions are obtained by the Newton-Raphson iteration method. Finally, to calculate the unsteady solutions, Crank-Nicolson and Adams-Bashforth methods together with the function expansion and collocation methods are applied to the equations (2) to (4).

4. Resistance coefficient

We use the resistance coefficient λ as one of the representative quantities of the flow state. It is also called the *hydraulic resistance coefficient*, and is generally used in fluids engineering, defined as

$$\frac{P_1^* - P_2^*}{\Delta z^*} = \frac{\lambda}{dh^*}\frac{1}{2}\rho\left\langle w^*\right\rangle^2, \tag{12}$$

where quantities with an asterisk denote the dimensional ones, $\langle\,\rangle$ stands for the mean over the cross section of the rectangular duct, and $d_h^* = 4(2d\times 2dh)/(4d+4dh)$. The main axial velocity $\langle \omega^* \rangle$ is calculated by

$$\langle \omega^* \rangle = \frac{\nu}{4\sqrt{2\delta d}}\int_{-1}^{1} dx \int_{-1}^{1} \omega(x,y,t)dy \tag{13}$$

Since $\left(P_1^* - P_2^*\right)/\Delta z^* = G$, λ is related to the mean non-dimensional axial velocity $\langle w\rangle$ as

$$\lambda = \frac{16\sqrt{2\delta}Dn}{3\langle w\rangle^2}, \tag{14}$$

where $\langle w\rangle = \sqrt{2\delta}d/\nu\left\langle w^*\right\rangle$. . For the unsteady solutions, the Nusselt number, *Nu*, is defined as

$$Nu_{\tau_c} = \frac{1}{2}\int_{-1}^{1} \langle\langle \left.\frac{\delta T}{\delta x}\right|_{x=-1} \rangle\rangle dy, \quad Nu_{\tau_h} = \frac{1}{2}\int_{-1}^{1} \langle\langle \left.\frac{\delta T}{\delta x}\right|_{x=1} \rangle\rangle dy \tag{15}$$

where $\langle\langle\rangle\rangle$ denotes an average over a time interval τ . Equation (14) will be used to find the resistance coefficient of the flow evolution by numerical computations.

5. Results and Discussion

5.1 *Steady solutions*

We obtained two branches of steady solutions for the non-isothermal flow through a curved square duct for the Grashof number $100 \le Gr \le 2000$. A solution structure of the steady solutions, for example, is shown in Fig. 2(a) for Gr = 500 and $100 \le Dn \le 4000$. Then we draw typical contours of secondary flow patterns and temperature profiles at Dn= 100, 500, 1000 and 2000 as shown in Fig. 2(b), where we see that the steady flow consists of asymmetric two- and four-vortex solutions. It is found that the first branch consists of asymmetric two-vortex solution while the second branch is composed of asymmetric two- and four-vortex solution. It is also found that at the same value of Dn dual solutions exist. Then we investigated solution structure of the steady solutions for the non-isothermal flow through a curved rectangular duct of aspect ratio 2, and we obtained five branches of steady solutions for $100 \le Gr \le 2000$. A solution structure of the steady solutions, for example, is shown in Fig. 3(a) for Gr = 500 and $100 \le Dn \le 1000$. Typical contours of secondary flow patterns and temperature profiles are obtained at Dn = 300, 500, 800 and 1000 on various branches as shown in Fig. 3(b), where we see that the steady flow consists of asymmetric two-, four-, six-, eight- and ten-vortex solutions. It is found that at Dn = 1000, we obtained two- and multi-vortex solutions.

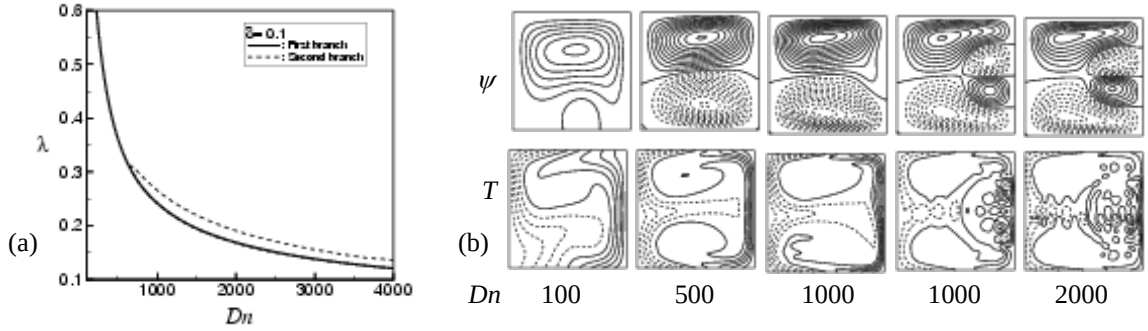

Figure 2: (a) Solution structure of the steady solution branches for the curved square duct flow for Gr = 500. (b) Secondary flow patterns (top) and temperature distributions (bottom) at some values of the Dean number.

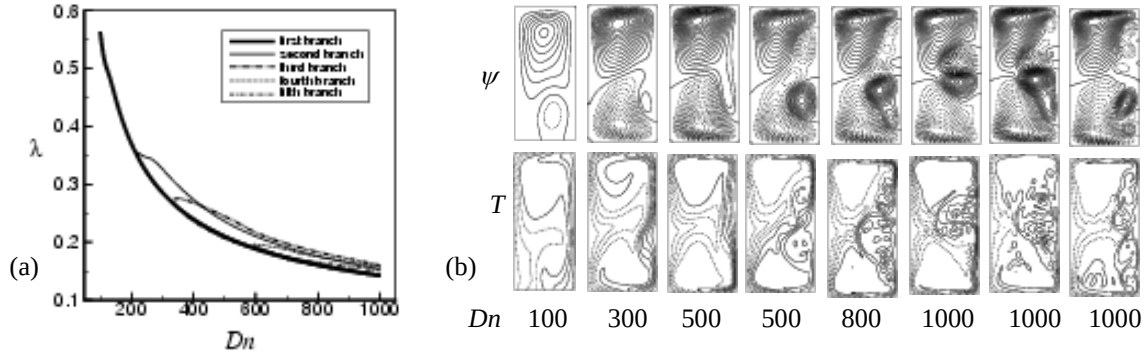

Figure 3: (a) Solution structure of the steady solution branches for the curved rectangular duct flow for Gr = 500. (b) Secondary flow patterns (top) and temperature distribution (bottom) at Dn = 300, 500, 800 and 1000 on various branches.

5.2 *Unsteady solutions*

In order to study the nonlinear behaviour of the unsteady solutions, time evolution calculations of the Nusselt numbers (Nu) are performed. In the present study, we perform time evolutions of Nu for the aspect ratios l = 1, 2 and 3 over a wide range of the Grashof number $100 \le Gr \le 2000$ for two cases of the Dean numbers, *Case I:* Dn =100 and *Case II*: Dn = 500. Since we are considering temperature difference between the vertical sidewalls for the large Grashof numbers, time-evolution of Nu is more significant than that of the resistance coefficient.

5.2.1 *Case I*: *Dn* =100

Time evolutions of Nu for Dn =100 and l = 1(square duct) are shown in Fig. 4(a) for Gr =100, 500, 1000 and 2000. It is found that the unsteady flow is a steady-state solution for any Gr lying in the range. Then we draw contours of secondary flow patterns and temperature profiles at time t = 10 in Fig. 4(b). As seen in Fig. 4(b), the unsteady solution is an

asymmetric two-vortex solution for *Gr* =100 and 500, but a single-vortex solution for *Gr* = 1000 and 2000. Then, we perform time evolution calculations of *Nu* for *Dn* = 100 and *l* = 2 as shown in Fig. 5(a). It is found that the unsteady flow is a steady-state solution for *Gr* = 100, 500 and 2000, but periodic oscillating solution for *Gr* =1000. Contours of secondary flow and temperature profile are shown in Fig. 5(b) for *Gr* =100, 500, 1000 and 2000 at time *t* =15. It is found that secondary flow is a two-vortex solution for *Gr* =100, 500 and 1000 but a single-vortex solution for *Gr* = 2000. It is found that as the Grashof number increases, the asymmetricity disappears; this is because the buoyancy force becomes strong at large Grashof number while the centrifugal force becomes weak at small Dean numbers.

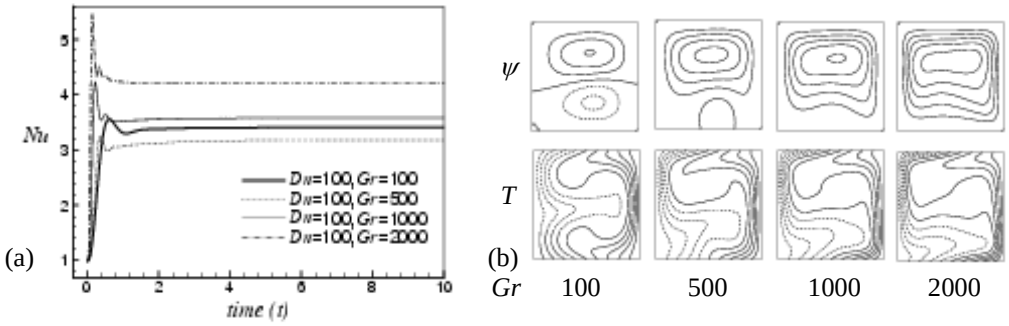

Figure 4: (a) Time evolution of *Nu* for *Dn* = 100 and *l* =1 (square duct). (b) Contours of secondary flow patterns (top) and temperature profiles (bottom) at time *t* = 10.

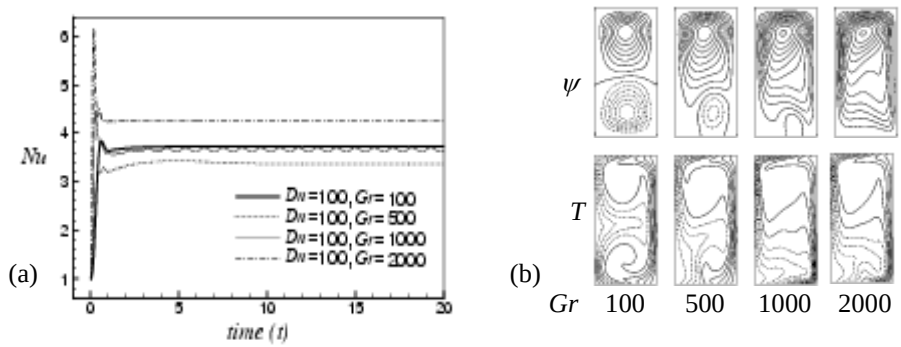

Figure 5: (a) Time evolution of *Nu* for *Dn* = 100 and *l* = 2 (rectangular duct). (b) Contours of secondary flow patterns (top) and temperature profiles (bottom) for *Gr* = 100, 500, 1000 and 2000 at time *t* = 15.

Next, we show time evolution results of *Nu* for *Dn* = 100 and *l* = 3 in Fig. 6(a). As seen in Fig. 6(a), the time-dependent solution is a steady-state solution for *Gr* = 100, but periodic for *Gr* = 500 and 1000. If the Grashof number is increased further (*Gr* = 2000), the flow then becomes steady-state again. Contours of secondary flow pattern and temperature profile are shown in Fig. 6(b) for *Gr* = 100 to 2000 at time *t* = 30, where it is seen that the unsteady flow at *Dn* = 100 and *l* = 3 is a two- and single-vortex solution at various *Gr*.

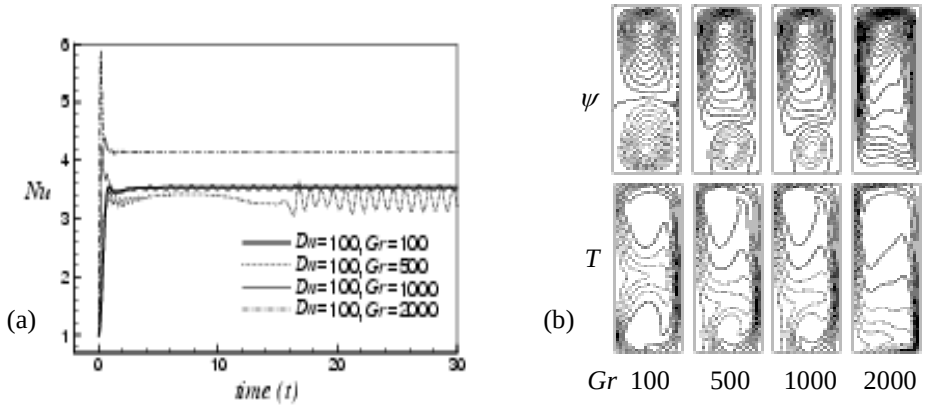

Figure 6: (a) Time evolution of *Nu* for *Dn* = 100 and *l* = 3 (rectangular duct). (b) Contours of secondary flow (top) and temperature profile (bottom) for *Gr* = 100, 500, 1000 and 2000 at time *t* = 30.

5.2.2 *Case II*: *Dn* = 500

We perform time evolution calculations of *Nu* for *Dn* = 500 and *l* = 1 at *Gr* =100, 500, 1000 and 2000 and it is found that the unsteady flow is a steady-state solution for any *Gr* lying in the range considered in this study. We draw the contours of secondary flow patterns and temperature profiles and it is found that the unsteady solution is a two-vortex solution for any *Gr* lying in the stated range. Then, we perform time evolution calculations of *Nu* for *Dn* =500 and *l* = 2 as shown in Fig. 7(a). It is found that the flow oscillates irregularly with the large windows of quasi-periodic oscillations for *Gr* =100 and 500, which suggests that the flow is chaotic. However, the flow becomes periodic at *Gr* = 1000. If *Gr* is increased further (*Gr* = 2000, for example), the flow becomes chaotic again. To observe the periodic change of the secondary flow patterns and temperature distributions, contours of secondary flow and temperature profiles are shown in Fig. 7(b) for *Gr* = 1000, where it is seen that the unsteady flow at *Gr* = 1000 is a two-vortex solution.

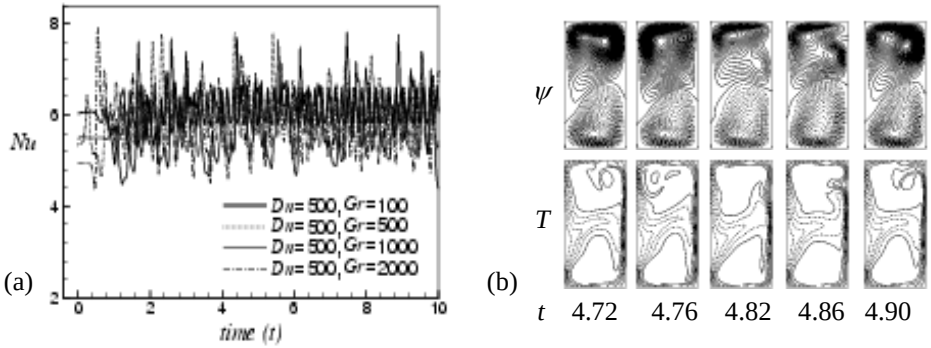

Figure 7: (a) Time evolution of *Nu* for *Dn* = 500 and *l* = 2. (b) Contours of secondary flow (top) and temperature profile (bottom) for *Gr* = 1000 at time $4.72 \le t \le 4.90$.

Next, time evolutions of *Nu* for *Dn* = 500 and *l* = 3 are shown in Fig. 8(a), where it is found that the flow is chaotic for any value of *Gr* and the chaotic solution takes place nearly at the same value of *Nu* whatever the value of *Gr* is. It is found that as the aspect ratio is increased, the steady-state solution turns into a chaotic solution through periodic solution; this is because as the aspect ratio increased the centrifugal force becomes stronger than at small value of the Dean number. In order to observe the change of the flow patterns and temperature distributions, contours of typical secondary flow patterns and temperature profiles are shown in Fig. 8(b) for *Gr* = 1000. As seen in the secondary flow patterns, the chaotic solution at *Gr* = 1000 is composed of four- and six-vortex solutions, though we obtained only two-vortex solutions for *Gr* = 1000 at *l* = 2. The temperature distribution is consistent with the secondary vortices. It is found the secondary flow enhances heat transfer in the flow.

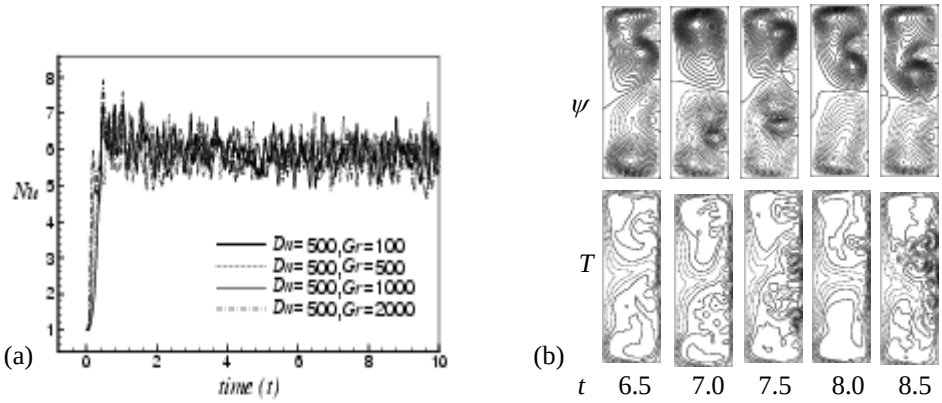

Figure 8: (a) Time evolution of *Nu* for *Dn* = 500 and *l* = 3. (b) Contours of secondary flow (top) and temperature profile (bottom) for *Gr* = 1000 at time $6.5 \le t \le 8.5$.

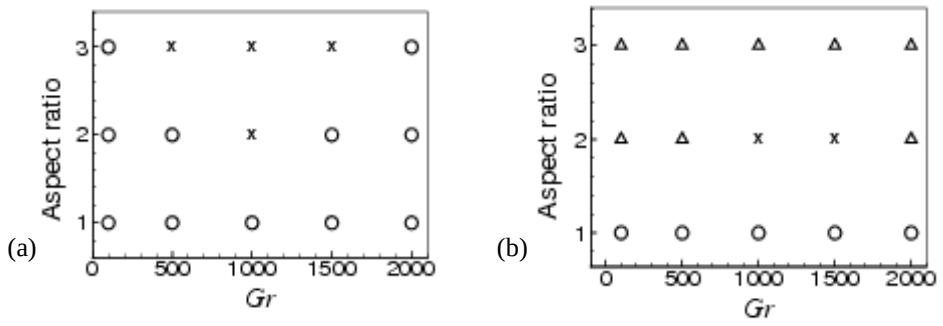

Figure 9: Time-dependent solutions in the Grashof number vs. aspect ratio (*Gr* - *l*) plane. (a) for *Dn* = 100, (b) for *Dn* = 500.(O: steady-state solution, $\times$: periodic solution and Δ: chaotic solution).

Finally, the complete unsteady solutions, obtained by the time evolution computations in the present study, are shown by two phase diagrams in Fig. 9(a) for *Dn* = 100 and in Fig. 9(b) for *Dn* = 500 in the Grashof number vs. aspect ratio plane for $100 \le Gr \le 2000$ and $1 \le l \le 3$. In this figure, the circles indicate steady-state solutions, crosses periodic solutions and triangles chaotic solutions. From Fig. 9, we can easily get to know about the unsteady flow characteristics for various *Gr* and *l*.

6. Conclusions

We obtained two branches of steady solutions for the curved square duct flow while five branches of asymmetric steady solutions for curved rectangular duct flow. Time evolution calculations of the Nusselt number for *Dn* = 100 show that there appears a steady-state solution for any *Gr* lying in the range of $100 \le Gr \le 2000$ for small aspect ratio; for large aspect ratio, however, the flow becomes periodic at moderate *Gr* (*Gr* = 1000 for *l* = 2 and *Gr* = 500 and 1000 for *l* = 3), and the flow undergoes in the scenario ``$steady \rightarrow periodic \rightarrow steady$", if *Gr* is increased. On the contrary, for small and large *Gr* (*Gr* = 100 and 2000), we always get steady-state solution whatever the aspect ratio is. For the moderate *Gr*, however, the steady flow turns into periodic solution, if *l* is increased. Time evolution calculations for *Dn* = 500 and *l* = 1 show that we again get a steady-state solution for any *Gr* lying in the range considered in this study. For *l* = 2, however, the flow becomes chaotic at small and large *Gr* (*Gr* =100, 500 and 2000) but periodic for *Gr* =1000. For large aspect ratio (*l* = 3), on the other hand, we always get chaotic solution whatever *Gr* is. It is observed that the steady-state solution turns into chaotic solution through periodic or multi-periodic oscillation for small and large *Gr* (*Gr* =100, 500 and 2000) for any *l* in the range in the scenario ``$steady \rightarrow periodic \rightarrow chaotic$", if the aspect ratio is increased.

References

[1] Winters, K. H., 1987. A bifurcation study of laminar flow in a curved tube of rectangular cross-section, *J. Fluid Mech.* Vol. **180**, pp. 343--369.

[2] Mondal, R. N. (2006). Isothermal and Non-isothermal Flows Through Curved ducts with Square and Rectangular Cross Sections, *Ph.D. Thesis*, Department of Mechanical Engineering, Okayama University, Japan.

[3] Yanase, S., Kaga, Y. and Daikai, R., 2002. Laminar flows through a curved rectangular duct over a wide range of the aspect ratio, *Fluid Dyn. Res*., Vol. **31**, pp. 151--183.

[4] Chandratilleke, T. T. and Nursubyakto. 2003. Numerical prediction of secondary flow and convective heat transfer in externally heated curved rectangular ducts. *International Journal of Thermal Sciences*, Vol. **42**, pp. 187-198.

[5] Wang, L. and Yang, T., 2005. Periodic oscillation in curved duct flows, *Physica D*, Vol. **200**, pp. 296—302.

[6] Yanase, S, Mondal, R. N. and Kaga, Y. (2005). Numerical study of non-isothermal flow with convective heat transfer in a curved rectangular duct, *International Journal of Thermal Sciences*, Vol. **44** (11), pp. 1047-1060.

[7] Mondal, R. N., Kaga, Y., Hyakutake, T. and Yanase, S. (2006). Effects of curvature and convective heat transfer in curved square duct flows, ASME *Journal of Fluids Engineering*, Vol. **128**, pp. 1013-1022.

[8] Mondal, R. N., Kaga, Y., Hyakutake, T. and Yanase, S. (2007). Bifurcation diagram for two dimensional steady flow and unsteady solutions in a curved square duct, *Fluid Dynamics Research*, Vol. **39,** pp. 413-446.

[9] Mondal, R. N., Uddin, M. S., Ali, M. A. and Datta, A. K. (2009). Time-dependent solutions of the flow through a curved duct for large Dean numbers, *Journal of Mathematics*, Vol. **2**(1), pp.91-104.

Available online at www.sciencedirect.com

SciVerse ScienceDirect

Procedia Engineering 00 (2012) 000–000

Procedia Engineering

www.elsevier.com/locate/procedia

5th BSME International Conference on Thermal Engineering

Finite Difference Solution of MHD Mixed Convection Flow with Heat Generation and Chemical Reaction

Tanvir Ahmed and Md. Mahmud Alam*

Mathematics Discipline, Khulna University, Khulna-9208, Bangladesh

Abstract

Unsteady MHD mixed convection flow from a vertical plate in porous media in the presence of internal heat generation with chemical reaction, Hall current and thermal radiation has been studied. To obtain the non-similar momentum, energy and concentration equations, usual non-dimensional variables have been used. A finite difference technique with stability and convergence analysis is used to solve the obtained non-similar, coupled, non linear partial differential non-dimensional equations. The obtained solutions are shown graphically. Finally, a qualitative comparison with previous work is shown in tabular form.

Keywords: Hall current; MHD; Soret, Dufour; Chemical reaction; Finite Difference

1. Introduction

The effect of chemical reaction and thermal radiation on MHD boundary layer flow has become important in several industrial, scientific and engineering fields. The growing need for chemical reactions in chemical and hydrometallurgical industries requires the study of heat and mass transfer with chemical reaction. There are many transport processes that are governed by the combined action of buoyancy forces due to both thermal and mass diffusion in the presence of the chemical reaction. These processes are observed in nuclear reactor safety and combustion systems, solar collectors. From the point of applications, Das et al. [1] investigated the effect of the first-order homogeneous chemical reaction of an unsteady flow past a vertical plate with the constant heat and mass transfer. For industrial applications such as glass production, furnace design, space technology applications, cosmical flight aerodynamics rockets, and spacecraft re-entry aerothermodynamics which are operated under the higher temperature with radiation effects are significant. In view of this, Sattar and Kalim [2] studied the unsteady free convection interaction with thermal radiation in a boundary layer flow past a vertical porous plate. Aydin and Kaya [3] investigated the effect of radiation on MHD mixed convection flow about a permeable vertical plate. The Soret and Dufour effects have been found to influence the flow field in mixed convection boundary layer over a vertical surface embedded in a porous medium. Stanford et al. [4] has studied the effect of thermal radiation, Hall currents, Soret and Dufour on MHD flow by mixed convection over a vertical surface in porous media. Recently, Aurangzaib and Shafie [5] investigated the effects of Soret and Dufour on unsteady MHD flow by mixed convection over a vertical surface in porous media with internal heat generation, chemical reaction and Hall current.

* Corresponding author. Tel.: +88-041-725741; Cell: +8801912982811; fax: +88-041-731244.
E-mail address: alam_mahmud2000@yahoo.com

Hence our aim of this research is to extend the work of Aurangzaib and Shafie [5] to solve the problem by implicit finite difference scheme. The proposed model has been transformed into non-similar coupled partial differential equation by usual transformations. Finally, the comparison of the present results with the results of Aurangzaib and Shafie [5] has been shown. The obtained results are shown graphically as well as tabular form.

2. Mathematical Formulation

Consider MHD mixed convective heat and mass transfer flow of a viscous incompressible fluid over an isothermal semi-infinite vertical flat plate through a porous medium. The flow is also subjected to a constant suction velocity. The positive x coordinate is measured along the plate in the direction of fluid motion and the positive y coordinate is measured normal to the plate. The leading edge of the plate is taken as coincident with $z-$axis. A uniform magnetic field B_0 is applied normal to the flow region. The imposed magnetic field vector B_0 can be taken as $\mathbf{B}=(0,B_0,0)$. The magnetic Reynolds number of the flow is taken to be small enough field and the magnetic field is negligible in comparison with applied magnetic field and the magnetic lines are fixed relative to the fluid. Initially, it is considered that the plate as well as the fluid is at the same temperature $T(=T_\infty)$ and concentration level $C(=C_\infty)$. Also it is assumed that the fluid and the plate is at rest after that the plate is to be moving with a constant velocity U_∞ in its own plane. Instantaneously at time $t>0$, the temperature of the plate and spices concentration are raised to $T_w(>T_\infty)$ and $C_w(>C_\infty)$ respectively, which is there after maintained constant, where T_w, C_w are temperature and spices concentration at the wall and T_∞, C_∞ are the temperature and concentration of the species outside the plate respectively. The physical configuration of the problem is furnished in Fig. 1.

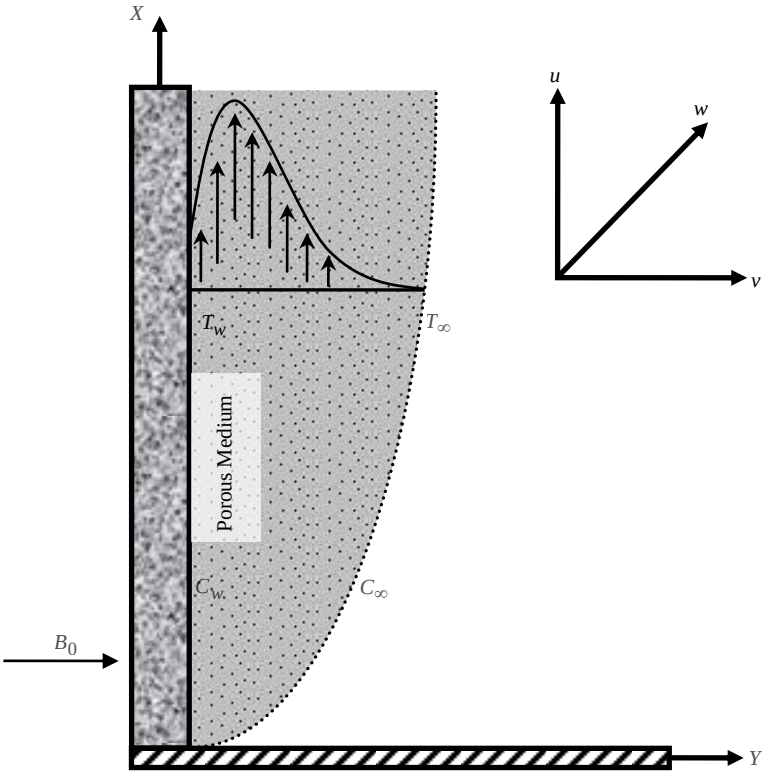

Fig. 1. Physical configuration and coordinate system.

Under the electromagnetic Boussinesq approximations, the MHD unsteady flow and heat and mass transfer with heat generation and chemical reaction are governed by the following equations are given by:

Momentum equation in $x-\text{axis}$:

$$\frac{\partial u}{\partial t}-v_0\frac{\partial u}{\partial y}=\upsilon\frac{\partial^2 u}{\partial y^2}+gB_T\left(T-T_\infty\right)+gB_C\left(C-C_\infty\right)-\frac{\sigma B_0^2}{\rho\left(1+m^2\right)}\left(u+mw\right)-\frac{\mu}{\rho k_1}u \tag{1}$$

Momentum equation in $x-\text{axis}$:

$$\frac{\partial w}{\partial t}-v_0\frac{\partial w}{\partial y}=\upsilon\frac{\partial^2 w}{\partial y^2}+\frac{\sigma B_0^2}{\rho\left(1+m^2\right)}\left(mu-w\right)-\frac{\mu}{\rho k_1}w \tag{2}$$

Energy equation:

$$\frac{\partial T}{\partial t}-v_0\frac{\partial T}{\partial y}=\frac{\kappa}{\rho c_p}\frac{\partial^2 T}{\partial y^2}+\frac{Dk_t}{c_s c_p}\frac{\partial^2 C}{\partial y^2}+\frac{\sigma B_0^2}{\rho C_p\left(1+m^2\right)}\left(u^2+w^2\right)-\frac{1}{\rho C_p}\frac{\partial q_r}{\partial y}+\frac{Q}{\rho c_p}\left(T-T_\infty\right)^p \tag{3}$$

Concentration equation:

$$\frac{\partial C}{\partial t}-v_0\frac{\partial C}{\partial y}=D\frac{\partial^2 C}{\partial y^2}+\frac{Dk_t}{T_m}\frac{\partial^2 T}{\partial y^2}-k_0\left(C-C_\infty\right)^q \tag{4}$$

with the corresponding boundary conditions are

$$u=U_\infty,\ w=0,\ T=T_w,\ C=C_w \quad \text{at } y=0 \tag{5}$$

$$u=0,\ w=0,\ T\to T_\infty,\ C\to C_\infty \quad \text{as } y\to\infty \tag{6}$$

where u, v and w are the x, y and z components of velocity vector, $m=\omega_e t_e$ is the Hall parameter, where ω_e is the electron frequency, υ is the kinematic coefficient viscosity, μ is the fluid viscosity, ρ is the density of the fluid, κ is the thermal conductivity, c_p is the specific heat at the constant pressure , k_0 is the rate of chemical reaction and D is the coefficient of mass diffusivity, k_t is the thermal diffusion ratio, c_s is the concentration susceptibility, respectively. Here p and q are considered as positive constant. The radiative heat flux q_r is described by the Rosseland approximation such that $q_r=-\frac{4\sigma^*}{3k^*}\frac{\partial T^4}{\partial y}$, where σ^* and k^* are the Stefan-Boltzman constant and the mean absorption coefficient, respectively. We assume that the temperature difference within the flow are sufficiently small so that the T^4 can be expressed as a linear function after using Taylor series to expand T^4 about the free stream temperature T_∞ and neglecting higher-order terms. This result in the following approximation: $T^4\approx 4T_\infty^3 T-3T_\infty^4$.

To obtain the governing equations and the boundary condition in dimension less form, the following non-dimensional quantities are introduced as;

$$Y=\frac{yU_\infty}{\upsilon},\ U=\frac{u}{U_\infty},\ W=\frac{w}{U_\infty},\ \tau=\frac{tU_\infty^2}{\upsilon},\ \overline{T}=\frac{T-T_\infty}{T_w-T_\infty}\ \text{and}\ \overline{C}=\frac{C-C_\infty}{C_w-C_\infty}$$

Substituting the above relations in equations (1)-(4) and corresponding boundary conditions (5) and (6) are;

$$\frac{\partial U}{\partial \tau}-S\frac{\partial U}{\partial Y}=\frac{\partial^2 U}{\partial Y^2}+G_r\overline{T}+G_m\overline{C}-\frac{M}{\left(1+m^2\right)}\left(U+mW\right)-KU \tag{7}$$

$$\frac{\partial W}{\partial \tau}-S\frac{\partial W}{\partial Y}=\frac{\partial^2 W}{\partial Y^2}+\frac{M}{\left(1+m^2\right)}\left(mU-W\right)-KW \tag{8}$$

$$\frac{\partial \overline{T}}{\partial \tau}-S\frac{\partial \overline{T}}{\partial Y}=\left(\frac{1+R}{P_r}\right)\frac{\partial^2 \overline{T}}{\partial Y^2}+D_u\frac{\partial^2 \overline{C}}{\partial Y^2}+\frac{ME_c}{\left(1+m^2\right)}\left(U^2+W^2\right)+\beta\overline{T}^{\,p} \tag{9}$$

$$\frac{\partial \overline{C}}{\partial \tau}-S\frac{\partial \overline{C}}{\partial Y}=\frac{1}{S_c}\frac{\partial^2 \overline{C}}{\partial Y^2}+S_r\frac{\partial^2 \overline{T}}{\partial Y^2}-\gamma\overline{C}^{\,q} \tag{10}$$

boundary conditions are;

$$U=1,\ W=0,\ \overline{T}=1,\ \overline{C}=1 \text{ at } Y=0 \tag{11}$$

$$U=0,\ W=0,\ \overline{T}=0,\ \overline{C}=0 \text{ as } Y\to\infty, \tag{12}$$

where τ represents the dimensionless time, Y is the dimensionless Cartesian coordinate, U and W are the dimensionless velocity component in X and Z direction, $\overline{T}$ is the dimensionless temperature, $\overline{C}$ is the dimensionless concentration, $S=\frac{v_0}{U_\infty}$ (Suction Parameter), $G_r=\frac{gB_T(T_w-T_\infty)\upsilon}{U_\infty^3}$ (Grashoff Number), $G_m=\frac{gB_C(C_w-C_\infty)\upsilon}{U_\infty^3}$ (Modified Grashoff Number), $K=\frac{\mu\upsilon}{\rho k_1 U_\infty^2}$ (Permeability of the porous medium), $M=\frac{\sigma B_0^2\upsilon}{\rho U_\infty^2}$ (Magnetic Parameter), $R=\frac{16\sigma^* T_\infty^3}{3k^*\kappa}$ (Radiation Parameter), $P_r=\frac{\rho c_p\upsilon}{\kappa}$ (Prandlt Number), $D_u=\frac{Dk_t}{\upsilon c_s c_p}\frac{(C_w-C_\infty)}{(T_w-T_\infty)}$ (Dufour Number), $E_c=\frac{U_\infty^2}{c_p(T_w-T_\infty)}$ (Eckert Number), $\beta=\frac{Q_0\upsilon(T_w-T_\infty)^{p-1}}{\rho c_p U_\infty^2}$ (Heat Generation or Absorption Parameter), $S_c=\frac{\upsilon}{D}$ (Schimidt Number), $S_r=\frac{Dk_T}{\upsilon T_m}\frac{(T_w-T_\infty)}{(C_w-C_\infty)}$ (Soret Number) and $\gamma=\frac{k_0\upsilon(C_w-C_\infty)^{q-1}}{U_\infty^2}$ (Chemical Reaction Parameter).

3. Shear Stress, Nusselt and Sherwood Number

From the velocity field, the effects of various parameters on the shear stress have been calculated. Shear stress in x-direction, $\tau_x=\mu_0\left(\frac{\partial U}{\partial Y}\right)_{Y=0}$ which is proportional to $\left(\frac{\partial U}{\partial Y}\right)_{Y=0}$. Shear stress in z-direction, $\tau_z=\mu_0\left(\frac{\partial W}{\partial Y}\right)_{Y=0}$ which is proportional to $\left(\frac{\partial W}{\partial Y}\right)_{Y=0}$. From the temperature field, the effects of various parameters on Nusselt number have been investigated. Nusselt number, $Nu=-\mu_0\left(\frac{\partial \overline{T}}{\partial Y}\right)_{Y=0}$ which is proportional to $-\left(\frac{\partial \overline{T}}{\partial Y}\right)_{Y=0}$. And from the concentration field, the effects of various parameters on Sherwood number have been analyzed and the Sherwood number, $Sh=-\mu_0\left(\frac{\partial \overline{C}}{\partial Y}\right)_{Y=0}$ is proportional to $-\left(\frac{\partial \overline{C}}{\partial Y}\right)_{Y=0}$.

4. Numerical Solutions

In order to solve the non-dimensional system by the implicit finite difference technique, it is required a set of finite difference equations. In this case, the region within the boundary layer is divided by some perpendicular lines of Y-axis,

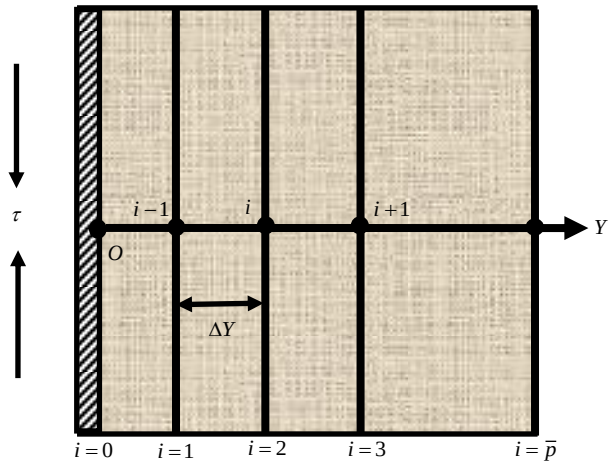

Fig. 2. Finite difference system grid.

where Y-axis is normal to the medium as shown in Fig. 2. It is assumed that the maximum length of boundary layer is $Y_{\max}=(25)$ as corresponds to $Y\to\infty$ i.e. Y varies from 0 to 25 and the number of grid spacing in Y directions is $\bar{p}(=400)$, hence the constant mesh size along Y axis becomes $\Delta Y=0.0625(0\le Y\le 25)$ with a smaller time-step $\Delta t=0.001$.

Let $U', W', \bar{T}'$ and $\bar{C}'$ denote the values of $U, W, \bar{T}$ and $\bar{C}$ at the end of a time-step respectively. Using the implicit finite difference approximation, the following appropriate set of finite difference equations are obtained as;

$$\frac{U_i^{n+1}-U_i^n}{\Delta\tau}-S\frac{U_{i+1}^n-U_i^n}{\Delta Y}=\frac{U_{i+1}^n-2U_i^n+U_{i-1}^n}{(\Delta Y)^2}+G_r\bar{T}_i^n+G_m\bar{C}_i^n-\frac{M}{(1+m^2)}\left(mW_i^n+U_i^n\right)-KU_i^n \tag{13}$$

$$\frac{W_i^{n+1}-W_i^n}{\Delta\tau}-S\frac{W_{i+1}^n-W_i^n}{\Delta Y}=\frac{W_{i+1}^n-2W_i^n+W_{i-1}^n}{(\Delta Y)^2}+\frac{M}{(1+m^2)}\left(mU_i^n-W_i^n\right)-KW_i^n \tag{14}$$

$$\frac{\bar{T}_i^{n+1}-\bar{T}_i^n}{\Delta\tau}-S\frac{\bar{T}_{i+1}^n-\bar{T}_i^n}{\Delta Y}=\left(\frac{1+R}{P_r}\right)\frac{\bar{T}_{i+1}^n-2\bar{T}_i^n+\bar{T}_{i-1}^n}{(\Delta Y)^2}+D_u\frac{\bar{C}_{i+1}^n-2\bar{C}_i^n+\bar{C}_{i-1}^n}{(\Delta Y)^2}$$
$$+\frac{ME_c}{(1+m^2)}\left\{\left(U_i^n\right)^2+\left(W_i^n\right)^2\right\}+\beta\left(\bar{T}_i^n\right)^p \tag{15}$$

$$\frac{\bar{C}_i^{n+1}-\bar{C}_i^n}{\Delta\tau}-S\frac{\bar{C}_{i+1}^n-\bar{C}_i^n}{\Delta Y}=\frac{1}{S_c}\frac{\bar{C}_{i+1}^n-2\bar{C}_i^n+\bar{C}_{i-1}^n}{(\Delta Y)^2}+S_r\frac{\bar{T}_{i+1}^n-2\bar{T}_i^n+\bar{T}_{i-1}^n}{(\Delta Y)^2}-\gamma\left(\bar{C}_i^n\right)^q \tag{16}$$

with the finite difference boundary conditions,

$$U_0^n=1, W_0^n=0, \bar{T}_0^n=1, \bar{C}_0^n=1 \tag{17}$$

$$U_L^n=0, W_L^n=0, \bar{T}_L^n=0, \bar{C}_L^n=0 \text{ where } L\to\infty \tag{18}$$

Here the subscript i designates the grid points with Y coordinate and the superscript n represents a value of time, $\tau=n\Delta\tau$ where $n=0,1,2,\ldots\ldots$. The primary velocity (U), secondary velocity (W), temperature $(\bar{T})$ and concentration $(\bar{C})$ distributions at all interior nodal points may be computed by successive applications of the above finite difference equations. The numerical values of the local shear stresses, local Nusselt number and local Sherwood are evaluated by **Five-point** approximate formula and the average shear stresses, average Nusselt number and average Sherwood number are calculated by the **Simpson's** $\frac{1}{3}$ integration rule. The stability conditions of the method are;

$$-\beta\Delta\tau+2\left\{S\frac{\Delta\tau}{\Delta Y}+\left(\frac{1+R}{Pr}\right)\frac{2\Delta\tau}{(\Delta Y)^2}\right\}\le 2,\ \gamma\Delta\tau+2\left\{S\frac{\Delta\tau}{\Delta Y}+\frac{2\Delta\tau}{Sc(\Delta Y)^2}\right\}\le 2, \text{ and } \left(K+\frac{M}{1+m^2}\right)\Delta\tau+2\left\{S\frac{\Delta\tau}{\Delta Y}+\frac{2\Delta\tau}{(\Delta Y)^2}\right\}\le 2 \text{ and}$$

convergence criteria of the problem are $m\ll 1$, $D_u\ll 1$ or $S_r\ll 1$, $K\le 911$, $\beta\ge -1760$, and $\gamma\le 846$ when $S=2.00$, $R=0.20$, $P_r=7.00$, $S_c=0.94$.

5. Results and Discussion

To observe the physical situation of the problem, the steady-state solutions have been illustrated in Figs. 3-7 when $p=2$ and $q=2$. The primary velocity, secondary velocity and temperature distributions are displayed for various values of Dufour number D_u respectively illustrated in Figs. 3(a), 3(b) and 4(a). These results show that the primary velocity, secondary velocity and temperature distributions increase with the increase of D_u. The effect of Soret number S_r on the primary velocity, secondary velocity and concentration distributions are respectively illustrated in Figs. 4(b), 5(a) and 5(b). These results show that the primary velocity, secondary velocity and concentration distributions increase with the increase of S_r. The concentration distribution is shown in Fig. 6(a) for various values of chemical reaction parameter γ with two values of Schimdt number $S_c=0.60$ (water vapor) and $S_c=0.94$ (carbon dioxide) respectively. It is noted that the concentration decreases with the increase of γ, where $\gamma<0$ and $\gamma>0$ are treated as genarative and destructive chemical reaction respectively. The concentration also decreases with the increase of S_c leads to thining of the concentration boundary layers. Fig. 6(b) displays the temperature distribution for several values of heat generation or absorption parameter β and Prandlt number P_r. It is noted that the temperature increases with increase of β, where $\beta<0$ and $\beta>0$ are treated as heat absorption and genaration respectively. The temperautre increases with the increase Prandlt number P_r. This is consistent with the well known fact that the thermal boundary layer thickness increasing with the increase P_r. The Nusselt

number for different values of heat genaration or absorption parameter β and Prandlt number P_r are displayed graphically in Fig. 7(a). The Nusselt number decreases with the rise of β and increases with the rise of P_r. The Sherwood number for different values of chemical reaction parameter γ and Schimdt number S_c are displayed graphically in Fig. 7(b). The Sherwood number increases with the increase of γ and S_c.

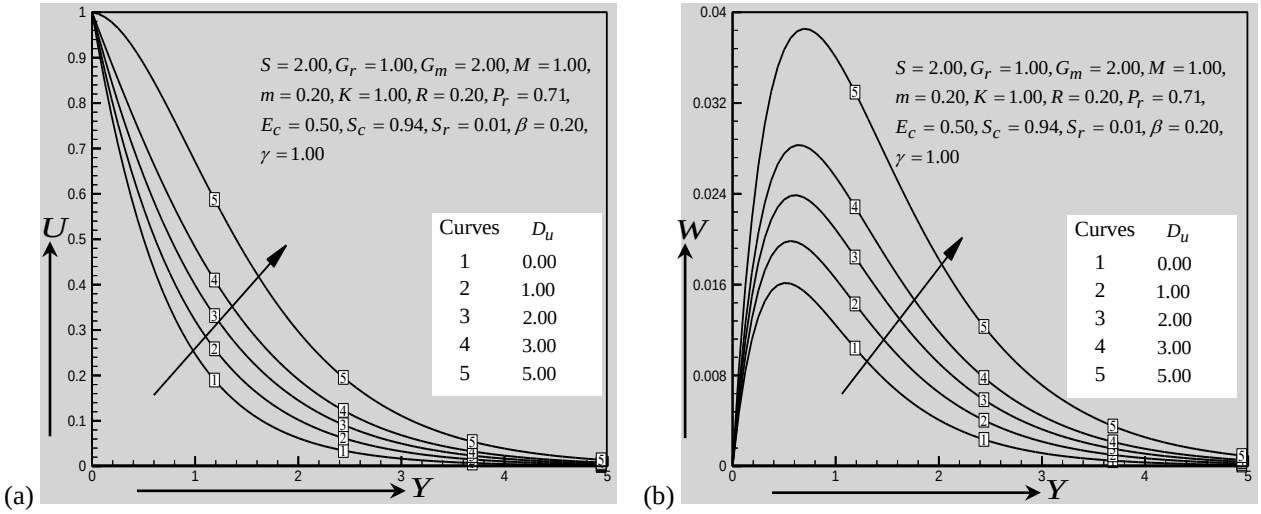

Fig. 3. Illustration of (a) Primary velocity profiles and (b) Secondary velocity profiles for various values of D_u when $p = 2$ and $q = 2$.

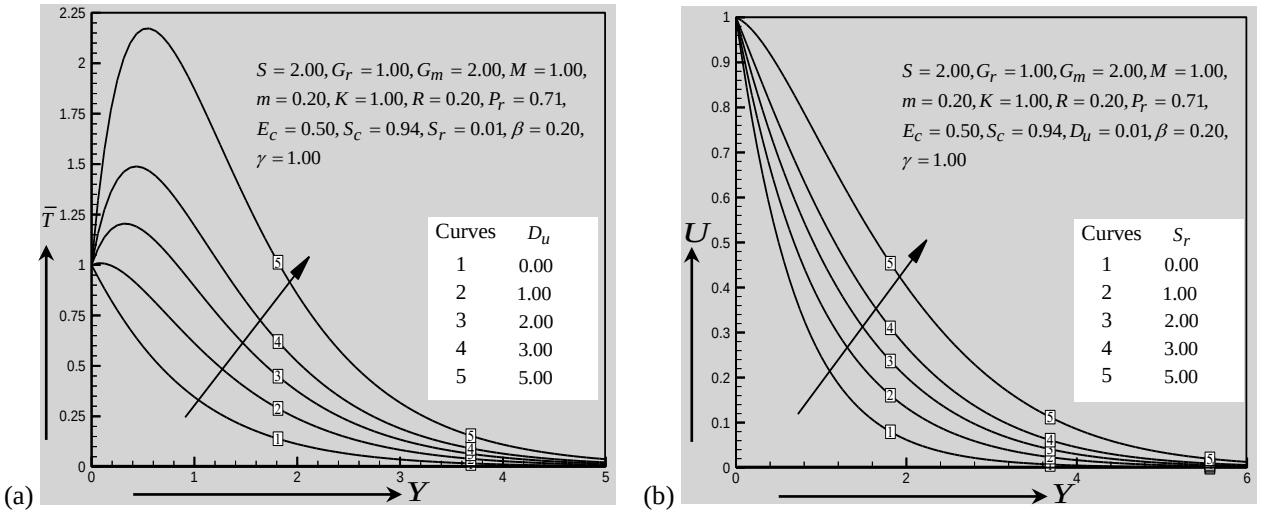

Fig. 4. Illustration of (a) Temperature profiles for varios values of D_u and (b) Primary velocity profiles for various values of S_r when $p = 2$ and $q = 2$.

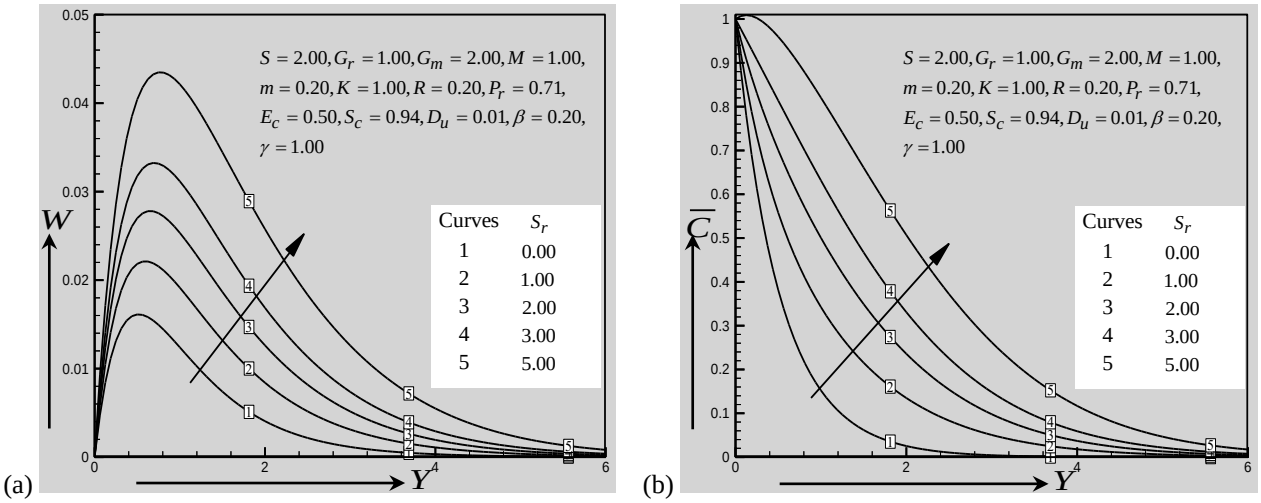

Fig. 5. Illustration of (a) Secondary velocity profiles and (b) Concentration profiles for various values of S_r when $p = 2$ and $q = 2$.

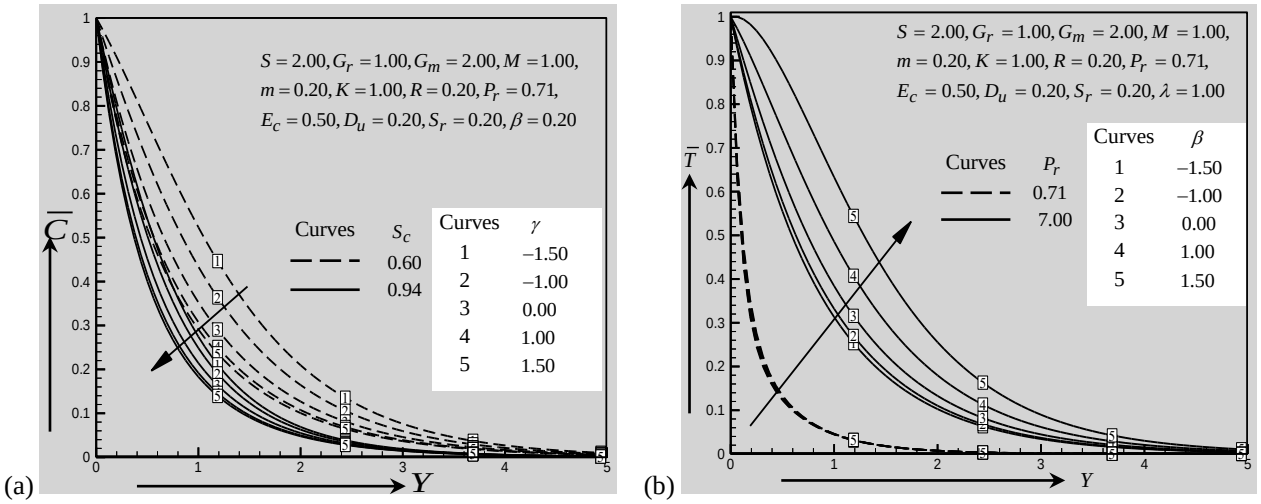

Fig. 6. Illustration of (a) Concentration profiles for various values of γ and (b) Temperature profiles for various values of β when $p = 2$ and $q = 2$.

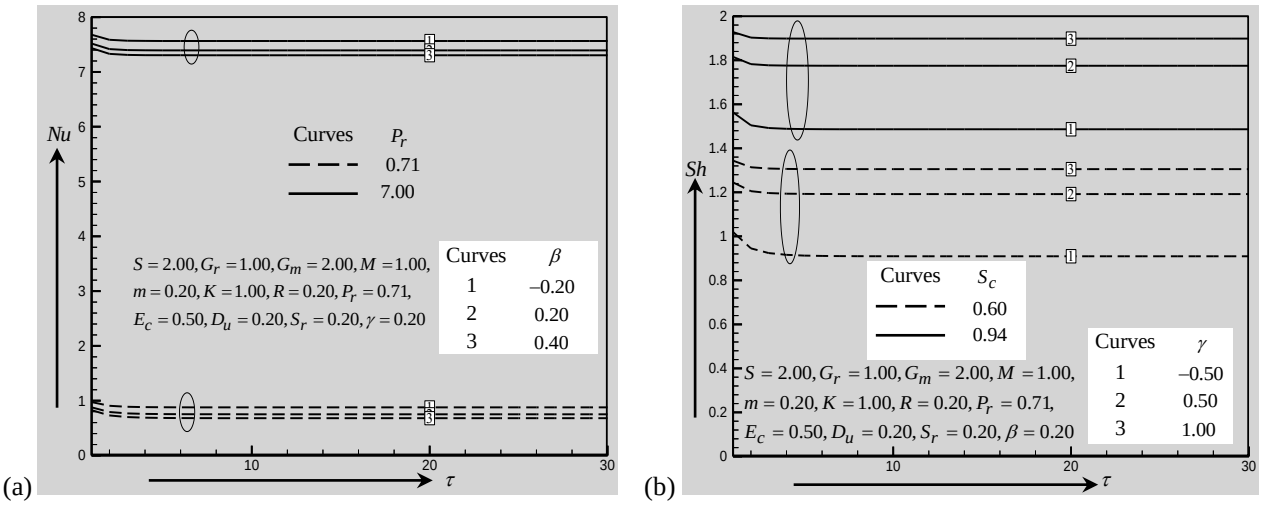

Fig. 7. Illustration of (a) Nusselt number for various values of β and P_r and (b) Sherwood number for various values of γ and S_c when $p = 2$ and $q = 2$.

Finally, a qualitative comparison of the present steady-state results with the published results (Aurangzaib and Shafie **[5]**) is presented in table 1. The accuracy of the present results is qualitatively as well as quantitatively good in case of all the flow parameters.

Table 1. Qualitative comparison of the present results with the previous results

Increased Parameter	Previous results given by Aurangzaib and Shafie **[5]**						Present results					
	$f'(\eta)$	$h(\eta)$	$\theta(\eta)$	$\phi(\eta)$	Rate of H. T.	Rate of C.	U	V	T	C	Nu	Sh
Du	Inc.	Inc.	Inc.				Inc.	Inc.	Inc.			
Sr	Inc.	Inc.		Inc.			Inc.	Inc.		Inc.		
γ				Dec.		Inc.				Dec		Inc.
Sc				Dec.		Inc.				Dec.		Inc.
β			Inc.		Dec.				Inc.		Dec.	
Pr			Dec.		Inc.				Inc.		Inc.	
R			Inc.						Inc.			

6. Conclusions

In this study, In this study, the finite difference solution of unsteady MHD mixed convection heat and mass transfer over a permeable vertical plate in the presence of heat generation, chemical reaction, thermal radiation and Hall current for $p \le 2$ and $q \le 2$ is investigeted. In present investigation, the primary velocity, secondary velocity and temperature distributions increase with the increase of Dufour number. The primary velocity, secondary velocity and concentration distributions increase with the increase of Soret number. The concentration decreases with the increase of chemical reaction parameter and Schimidt number. It is also seen that temperature increases for the increase of heat genaration or absorption parameter and Prandlt number. The Nusselt number decreases with the increase of heat genaration or absorption parameter and increases with the and Prandlt number. The Sherwood number increases with the increase of chemical reaction parameter and Schimdt number.

References

[1] Das, U. N., Dekha, R., Soungalgekar, V. M., 1994. Effects on m ass transfer on flow past an impulsively started infinite vertical plate with constant heat flux and chemical reaction, Forschungim Ingenieurwesen 60, pp. 284-287.

[2] Satter, M. A., Kalim, H., 1996. Unsteady free-convection interaction with thermal radiation in a boundary layer flow past a vertical porous plate, J. Math. Phys. Sci. 30(1). Pp. 25- 37.

[3] Aydin, O., Kaya, A., 2008. Radiation effect on MHD mixed convection flow about a permeable vertical plate, Heat Mass Transfer 45, pp.239-246.

[4] Stanford Shateyi, Sandile Sydney Mosta and Precious Sibanda, 2010. The effects of thermal radiation, Hall currents, Soret and Dufour on MHD flow by mixed convection over a vertical surface in porous media, Mathematical Problems in Engineering, Article ID 627475.

[5] Aurangzaib, Sharidan Shafie, 2011. Effects of Soret and Dufour on unsteady MHD flow by mixed convection over a vertical surface in porous media with internal heat generation, chemical reaction and Hall current, Canadian Journal on Science and Engineering Mathematics 2(4), pp-153-162.

Available online at www.sciencedirect.com

SciVerse ScienceDirect

Procedia Engineering 00 (2012) 000–000

Procedia Engineering

www.elsevier.com/locate/procedia

5th BSME International Conference on Thermal Engineering

Double Diffusive Mixed Convection in a Channel with a Circular Heater

A.K. Azad[a], M.J.H. Munshi[b], M.M. Rahman[c]*

[a]*Department of Business Administration, International Islamic University, Chittagong, Bangladesh*
[b]*Department of Mathematics, Hamdard University Bangladesh, Gozaria, Munshiganj, Bangladesh*
[c]*Department of Mathematics, Bangladesh University of Engineering and Technology, Dhaka-1000, Bangladesh*

Abstract

Double diffusive mixed convection in an open channel with a circular heater on the bottom wall has been investigated in this paper. Constant temperatures and concentrations are considered along the semi-circle and the lateral walls of the channel are adiabatic. Galerkin weighted residual finite element method have been used to solve the governing equations. Calculations were performed for Rayleigh numbers and Lewis number. Reynolds and Prandtl numbers are fixed as 100 and 0.7 for whole study, respectively. Various characteristics such as streamlines, isotherms, isoconcentration and heat and mass transfer rate in terms of the average Nusselt number and Sherwood numbers are presented for the aforesaid parameters. It is found that, average Nusselt number at the heat source decreases and overall mass transfer rate in terms of average Sherwood number increases with the rising of Lewis number. In addition, Rayleigh numbers have also significant effect on the heat and mass transfer process.

Keywords: Channel flow, finite element method, circular cavity, double diffusive mixed convection.

Nomenclature

Br	buoyancy ratio	T_i	inlet flow temperature
c	mass concentration (kg m^{-3})	(u, v)	velocity components (ms^{-1})
c_h	high mass concentration	(U, V)	dimensionless velocity component
c_i	Inlet mass flow concentration	w	height of the channel
C	dimensionless mass concentration	(x, y)	dimensional coordinates (m)
D	mass diffusivity (m^{2}s^{-1})	(X, Y)	dimensionless coordinates
g	gravitational acceleration (ms^{-2})	*Greek symbols*	
k	fluid conductivity (Wm^{-1}K^{-1})	α	thermal diffusivity (m^{2}s^{-1})
L	length of cavity (m)	β_T	coefficient of thermal expansion (K^{-1})
Le	Lewis number	β_c	coefficient of mass expansion (m^{3}kg^{-1})
Nu	average Nusselt number	μ	dynamic viscosity (kg m^{-1}s^{-1})
p	dimensional pressure (Nm^{-2})	ν	kinematic viscosity (m^{2}s^{-1})
P	non-dimensional pressure	θ	non-dimensional temperature
Pr	Prandtl number	ρ	Density (kgm^{-3})
Re	Reynolds number	ρ*	dimensionless density
Ri	Richardson number	ψ	streamfunction
Sh	average Sherwood number	*subscripts*	
T	temperature (K)	i	inlet state
T_h	hot wall temperature		

* Corresponding author. Tel.: +8801552556549; fax: +880-2-8613046.
E-mail address: m71ramath@gmail.com

1. Introduction

Mixed convection is that type of heat transfer in which there is a noteworthy interaction between free and forced convection. Mixed convective heat transfer in open cavities has long been studied and received increases attention due to its application of practical interest, such as nuclear reactors, solar receiver, thermal storage and open cavity packaging of semiconductors. Studies associated with mixed convection in open cavities have received increasing consideration. Pavlovic and Penot, 1991, performed an experimental investigation of the mixed convection heat transfer in an open isothermal cubic cavity. They concluded that the convective heat loss for the central solar receiver. A numerical analysis of laminar mixed convection in a channel with an open cavity and a heated wall bounded by a horizontally insulated plate was presented by Manca et al., 2003, where the authors considered three heating modes: assisting flow, opposing flow and heating from below. Later, a similar problem for the case of assisting forced flow configuration was tested experimentally by Manca et al., 2006.

The double-diffusive mixed convection in a channel with an open enclosure has also found wide applications in engineering, such as cooling of electronic components, finned heat exchangers, cavity of solar central receivers, chemical processing, thermal and pollution control, evaporative cooling and fire control in buildings. There are several studies related to mixed convection for combined heat, and mass transfer. Deng et al., 2004, made a numerical study for a laminar double diffusive mixed convection in a two-dimensional ventilated enclosure with discrete heat and contaminant sources. They investigated the characteristics of the airflow and heat/contaminant transport structures in the indoor air environment by means of a convection transport visualization technique. At the same time, Costa, 2004, carried out a numerical study for double-diffusive natural convection in parallelogrammic enclosures filled with moist air. Chamkha and Naser, 2001, studied the problem of unsteady, laminar double-diffusive convective flow of a binary gas mixture in an inclined rectangular enclosure filled with a uniform porous medium. A numerical simulation of double diffusive natural convection in rectangular enclosure in the presence of magnetic field and heat source was performed by Teamah, 2008. Teamah and El-Maghlany, 2010, numerically simulated double-diffusive mixed convective flow in a rectangular enclosure with insulated moving lid. Brown and Lai 2005 numerically investigated a horizontal channel with an open cavity and obtained correlations for combined heat and mass transfer which covered the entire convection regime from natural, mixed to forced convection.

In view of the aforesaid statements, it is seemed that the double diffusive mixed convection in a channel with a circular cavity has not been addressed yet. In the present study, we undertake this task varying the Lewis number Le ($0.1 \leq Le \leq 10$) and Rayleigh number Ra ($10^3 \leq Ra \leq 10^5$) .A comprehensive study of the flow field, temperature and concentration distribution with detailed analysis on heat and mass transfer evaluation will be done.

2. Physical Model

The physical system under study with the system of coordinates is sketched in Fig. 1. The problem deals with a two-dimensional open channel of length L with semi-circular heater of diameter $0.5L$. The flat walls are adiabatic and semi-circular wall is under the boundary conditions with a high temperature T_h and high concentration C_h. It is assumed that the height of the channel $w = 0\ 25L$. The forced flow of fresh air, imposed at the inlet, has a temperature T_i, a concentration c_i and a horizontal velocity, u_i. Gravity acts in the vertical direction.

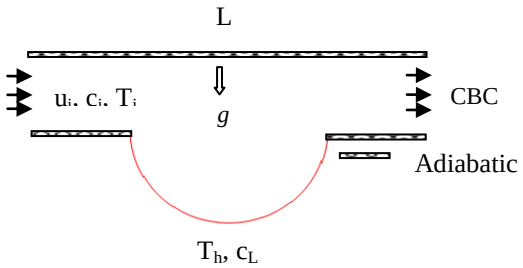

Fig.1. Physical configuration for the problem with boundary conditions

3. Mathematical Formulation

The flow is considered steady, laminar, incompressible and two-dimensional. The field equations governing the heat transfer and fluid flow include the continuity equation, the Navier–Stokes equations and the energy equation, which can be expressed in non-dimensional form as:

$$\frac{\partial U}{\partial X}+\frac{\partial V}{\partial Y}=0 \tag{1}$$

$$U\frac{\partial U}{\partial X}+V\frac{\partial U}{\partial Y}=-\frac{\partial P}{\partial X}+\frac{1}{\mathrm{Re}}\left(\frac{\partial^2 U}{\partial X^2}+\frac{\partial^2 U}{\partial Y^2}\right) \tag{2}$$

$$U\frac{\partial V}{\partial X}+V\frac{\partial V}{\partial Y}=-\frac{\partial P}{\partial Y}+\frac{1}{\mathrm{Re}}\left(\frac{\partial^2 U}{\partial X^2}+\frac{\partial^2 U}{\partial Y^2}\right)+\frac{Ra}{\mathrm{Re}^2\,\mathrm{Pr}}\left(\theta+BrC\right) \tag{3}$$

$$U\frac{\partial \theta}{\partial X}+V\frac{\partial \theta}{\partial Y}=\frac{1}{\mathrm{Re}\,\mathrm{Pr}}\left(\frac{\partial^2 \theta}{\partial X^2}+\frac{\partial^2 \theta}{\partial Y^2}\right) \tag{4}$$

$$U\frac{\partial C}{\partial X}+V\frac{\partial C}{\partial Y}=\frac{1}{\mathrm{Re}\,\mathrm{Pr}\,Le}\left(\frac{\partial^2 C}{\partial X^2}+\frac{\partial^2 C}{\partial Y^2}\right) \tag{5}$$

where the dimensionless variables are introduced as:

$$X=\frac{x}{L},Y=\frac{Y}{L},U=\frac{u}{u_i},V=\frac{v}{u_i},P=\frac{p}{\rho u_i^2},\theta=\frac{T-T_i}{T_h-T_i}\ \text{ and }\ C=\frac{c-c_i}{c_h-c_i}$$

As can be seen from the Eqs. (1)-(5), five parameters that preside over this problem are the Reynolds number (*Re*), Prandtl number (*Pr*), Rayleigh number (*Ra*), Lewis number (*Le*) and buoyancy ratio (*Br*), which are defined respectively as

$$\mathrm{Re}=\frac{u_i L}{\nu},\ \mathrm{Pr}=\frac{\nu}{\alpha},\ Ra=\frac{g\beta\left(T_h-T_i\right)L^3}{\nu\alpha},\ Le=\frac{\alpha}{D},\text{and }Br=\frac{\beta_c\left(c_h-c_i\right)}{\beta_T\left(T_h-T_i\right)}$$

The dimensionless boundary conditions corresponding to the considered problem are as follows

at inlet: $U=1,\ V=0,\ \theta=0, C=0$

at outlet: $\frac{\partial U}{\partial X}=0, V=0, \frac{\partial \theta}{\partial X}=0, \frac{\partial C}{\partial X}=0$

at all solid boundaries other than semi-circle: $U,V=0,\ \frac{\partial \theta}{\partial N}=\frac{\partial C}{\partial N}=0$

on semi-circle: $U=V=0, \theta=C=1$

where *N* is the non-dimensional distances either *X* or *Y* direction acting normal to the surface.

The average heat and mass transfer rates on the surface of heat and contaminant sources can be evaluated by the average Nusselt and Sherwood numbers, which are defined respectively as

$$Nu=-\int_0^1\frac{\partial \theta}{\partial Y}dX\ \text{ and }\ Sh=-\int_0^1\frac{\partial C}{\partial Y}dX$$

4. Solution Scheme

The Galerkin weighted residual method of finite element formulation has been used as a numerical procedure. The finite element method begins by the partition of the continuum area of interest into a number of simply shaped regions called elements. These elements may be different shapes and sizes. Within each element, the dependent variables are approximated using interpolation functions. In the current study erratic grid size system is considered especially near the walls to capture the rapid changes in the dependent variables. The coupled governing equations (2)-(5) are transformed into sets of algebraic equations using finite element method to reduce the continuum domain into discrete triangular domains.

The system of algebraic equations is solved by iteration technique. The solution process is iterated until the subsequent convergence condition is satisfied:
$\left|\Gamma^{m+1}-\Gamma^{m}\right| \le 10^{-6}$ where m is number of iteration and Γ is the general dependent variable.

5. Results and Discussion

A numerical study has been performed to determine the effects of the double-diffusive mixed convection flow in a horizontal channel with an open cavity. For the intention of discussing the results, the numerical calculations are presented in the form of streamlines, isotherms, and concentration. With this aim, different parameters such as, Lewis number (*Le*) and Rayleigh number (*Ra)* are considered. In addition, the Lewis number *Le*, characterizes the mass transfer exchange between the two different concentration zones Moreover, Reynolds number (*Re*), Prandtl number (*Pr*), and buoyancy ratio (*Br*) are held fixed at 100, 0.7, and 1, respectively.

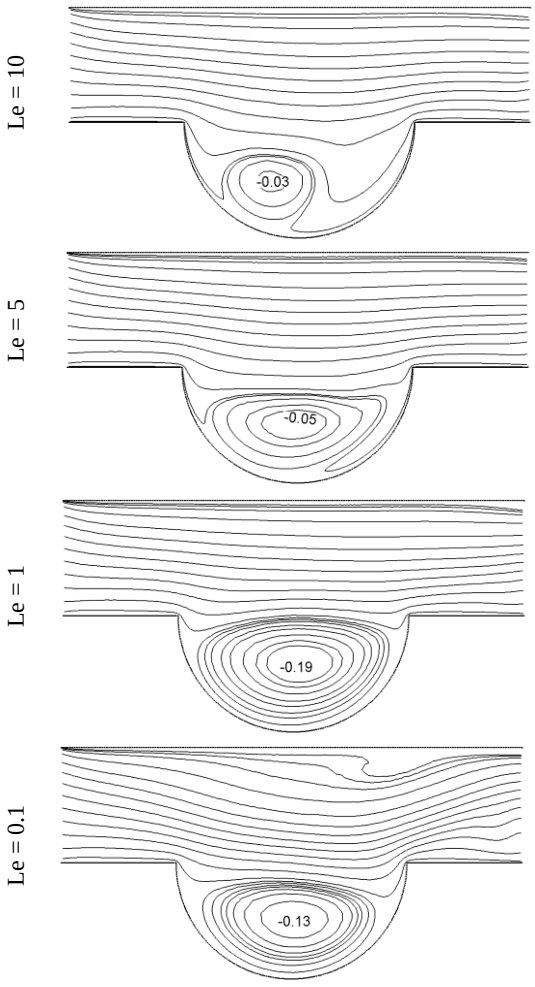

Fig. 2. Streamlines for selected values of Lewis number, *Le* at Ra = 1.E+5.

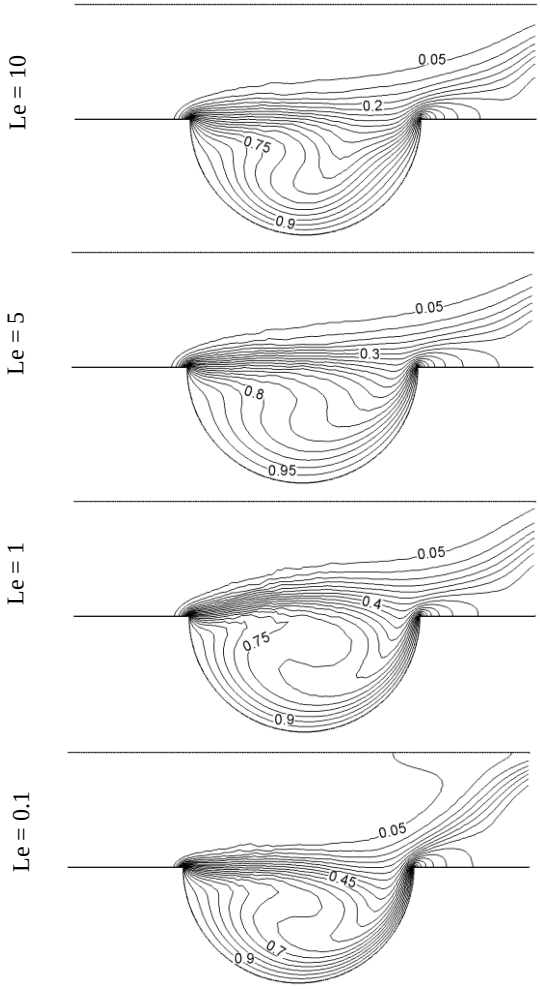

Fig. 3. Isotherms for selected values of Lewis number, *Le* at Ra = 1.E+5.

The influence of Lewis number, *Le* on streamlines and isotherms are demonstrated in Figs. 2-3. The Lewis number *Le* varied from 0.1 to 10 while keeping *Br* = 1 fixed. In Fig. 2, the streamlines in the through flow sprint almost analogous, apart from for those near the opening to the cavity, which twist near the cavity inside. Besides, the flow inside the lower part of the cavity is seen as a large rotating cell in a clockwise direction. Shape change was detected in the rotating cell due to the variation of *Le* inside the cavity. On the other hand, Lewis number has a visible significant effect on the strength of the rotating cell inside the cavity.

The corresponding isotherms are clustered deeply near the bottom surface of the cavity which indicates steep temperature gradients at the vertical direction in this cavity as shown in Fig. 3. In the residual region of the cavity, the temperature gradients are feeble and this implies that the temperature differences are very minute in the interior region of the cavity due to the strong effects of the mechanically-driven circulations.

Fig. 4 illustrates a concentration for different Lewis number at *Br* = 1. From this figure, it is seen that for *Le* = 0.1, the concentration contours in the cavity align almost parallel to the horizontal wall, which is evocative of the supremacy of high mass transfer. Moreover, a significant change in the concentration contours is noticeable for the higher values of Lewis number.

The effect of Lewis number on the average value of Nusselt and Sherwood numbers at $Ra = 10^3, 10^4, 10^5$ is illustrated in Fig. 5. For lower values of Ra ($= 10^3, 10^4$), the average Nusselt number decreases very slowly as the Lewis number is increased. But the average Sherwood number increases swiftly with the increasing of Lewis number for lower Ra. On the other hand, for $Ra = 10^5$, the average Nusselt number decreases constantly with the increasing *Le* up to 5, later it increases. It is also observed that the average Sherwood number with the increasing *Sh* up to 1 then it decreases for $Ra = 10^5$.

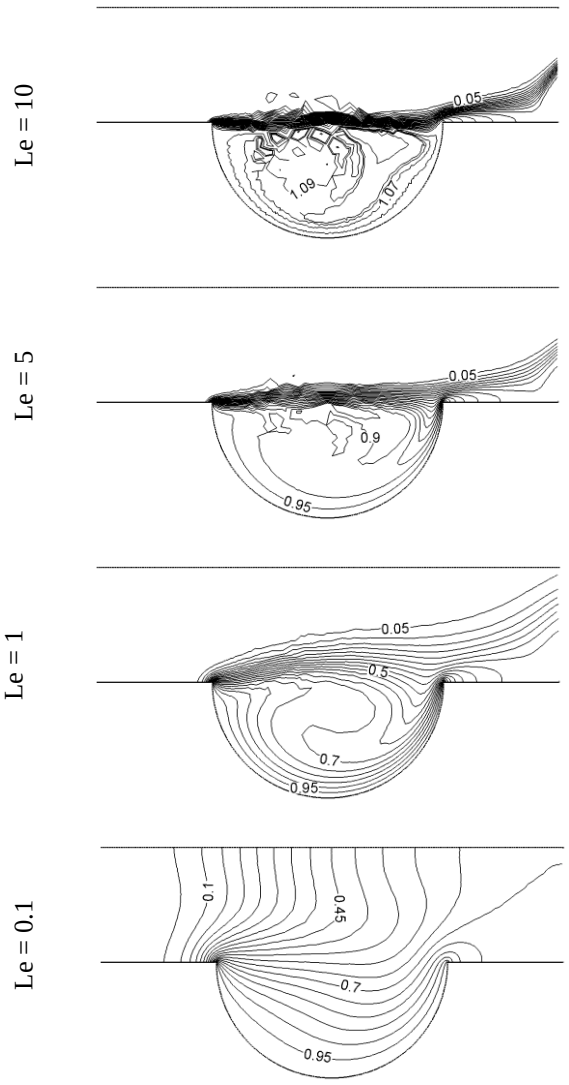

Fig. 4. Isoconcentration for selected values of Lewis number, Le at Ra = 1.E+5.

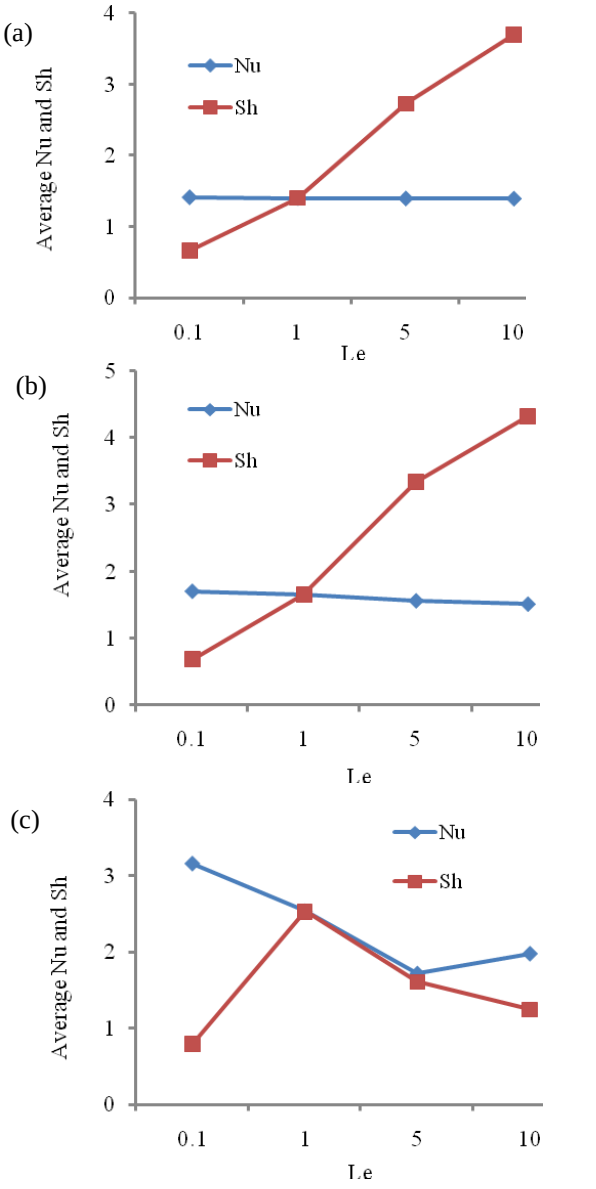

Fig. 5. Average Nusselt and Sherwood numbers for (a) Ra = 1.E+3, (b) Ra = 1.E+4 and (c) Ra = 1.E+5 versus Lewis number

6. Concluding Remarks

This work deals with the effect of double-diffusive mixed convection in a horizontal channel along with an open semi circular cavity. The finite element method is engaged for numerical simulation. Graphical results of the flow structure, temperature, and concentration for Lewis number *Le* is presented and discussed. The following conclusions may be drawn from the above mentioned study:

- The control of the Lewis number on the isotherms is noteworthy. Moreover, strength of buoyancy-induced vortex decreases with the increase of the Lewis number in the streamlines.
- Overall mass transfer rate in terms of average Sherwood number increases with the augmented of Lewis number *Le*.

The results of this study suggest several guidelines for the thermal design of cooling of electronic components, finned heat exchangers, cavity of solar central receivers, etc.

Acknowledgements

The authors like to express their gratitude to the Department of Mathematics, Bangladesh University of Engineering and Technology (BUET), Dhaka, Bangladesh.

References

[1] Pavlovic MD, Penot F. Experiments in the mixed convection regime in an isothermal open cubic cavity. Exp Therm Fluid Sci 1991; 4 **:** 648–55.
[2] Manca O, Nardini S., Khanafer K, Vafai K. Effect of heated wall position on mixed convection in a channel with an open cavity. J Numer Heat Transfer 2003; 43 (3); 259-82.
[3] Manca O, Nardini S, Vafai K. Experimental investigation mixed convection in a channel with an open cavity. Exp Heat Transfer 2006; 19 (1): 53–68.
[4] Deng QH, Zhou J, Mei C, Shen YM. Fluid, heat and contaminant transport structures of laminar double-diffusive mixed convection in a two-dimensional ventilated enclosure. Int J Heat Mass Transfer 2004; 47**:** 5257–69.
[5] Costa VAF. Double-diffusive natural convection in parallelogrammic enclosures. Int J Heat Mass Transfer 2004; 47: 2913–26.
[6] Chamkha AJ, Naser HA. Double-diffusive convection in an inclined porous enclosure with opposing temperature and concentration gradients. Int J Therm Sci 2001; 40: 227-44.
[7] Teamah MA. Numerical simulation of double diffusive natural convection in rectangular enclosure in the presences of magnetic field and heat source. Int J Therm Sci 2008; 47: 237-48.
[8] Teamah MA, El-Maghlany WM. Numerical simulation of double-diffusive mixed convective flow in a rectangular enclosure with insulated moving lid. Int J Therm Sci 2010; 49: 1625–38.
[9] Brown NM, Lai FC. Correlations for combined heat and mass transfer from an open cavity in a horizontal channel. Int Commun Heat Mass Transfer 2005; 32(8): 1000-8.

Available online at www.sciencedirect.com

SciVerse ScienceDirect

Procedia Engineering 00 (2012) 000–000

Procedia Engineering

www.elsevier.com/locate/procedia

5th BSME International Conference on Thermal Engineering

Some studies on wall-to-bed heat transfer in a pressurized circulating fluidized bed unit

Pankaj Kalita[a]*, Pinakeswar Mahanta[b], Ujjwal K. Saha[b]

[a]*Centre for Energy, Indian Institute of Technology Guwahati, Guwahati – 781039, India*
[b]*Department of Mechanical Engineering, Indian Institute of Technology Guwahati, Guwahati – 781039, India*

Abstract

In the present work, a pressurized circulating fluidized bed (PCFB) unit of 54 mm inner diameter and riser height of 2000 mm has been fabricated to investigate the effect of pressure on suspension density and heat transfer. The effects of blending of biomass in sand, and superficial velocity on bed hydrodynamics and heat transfer has also been studied. Experiments have been conducted at four different percentage blending of biomass such as 2.5 %, 7.5 %, 15 % and 20 % in sand with two different weight composition ratios and at a superficial velocity of 5 m/s. Operating pressure is varied from 1 to 5 bar in a step of 2 bar. Results show that, the axial heat transfer coefficient increases from the bottom to the top of heat transfer probe with the increase in operating pressure. The radial variation of heat transfer coefficient decreases from the wall to the core of the heat transfer probe. The heat transfer coefficient is also found to be higher in between the 7.5 to 15 % biomass blending in sand. The overall uncertainty in calculating heat transfer coefficient is found to be 3.90 %.

Keywords: Circulating fluidized bed; heat transfer coefficient; operating pressure; bed voidage; suspension density.

Nomenclature

A_B	Cross sectional area of the bed in m^2
A_D	Cross sectional area of downcomer in m^2
A_{htp}	Surface area of heat transfer probe in m^2
G_s	Solid circulation rate in kg $m^{-2}s^{-1}$
h	Heat transfer coefficient
Δh	difference of height in manometric fluid measured in cm of water column
I	Supply current
L_a	Solid accumulation height in m
L_m	Difference between two consecutive pressure taps
q	Heat flux
t	Time to accumulate particular height after closing ball valve in sec
T_{bi}	Bed temperature in K

* Corresponding author. Tel.: +91-361-2583127; fax: +91-361-2690762.
E-mail address: pankajk@iitg.ernet.in

T_{bs}	Bulk surface temperature in K
U_{sup}	Superficial velocity in m/s
B/S	Biomass (sawdust) to sand ratio
V	Supply Voltage
Greek symbols	
ρ_g	Gas density in kg/m^3
ρ_s	Solid density in kg/m^3
ρ_{sus}	Suspension density in kg/m^3
ε	Bed voidage
ε_{mf}	Bed voidage at minimum fluidization

1. Introduction

Circulating fluidized bed (CFB) has emerged as an environmentally acceptable technology for burning wide range of solid fuels to generate steam and electricity with improved plant efficiency. Pressurized circulating fluidized bed (PCFB) is the second generation technology which is still in the pilot scale level. Extensive research on the design and various parameters influencing the performance of a PCFB is in progress, both in industrial and academic level because of its unique advantages such as compactness, fuel flexibility and higher efficiency apart from in-situ capture of SO_2 and NOx [1-3]. As compactness is an important feature of PCFB boiler, the heat transfer plays an important role in design and operation of a PCFB boiler. The performance of a PCFB unit is influenced by a number of factors, including superficial velocity, solid circulation rate, solid inventory, and particle size distribution. The effect of these operating parameters was studied by various researchers [1-3]. Change of any of these parameters changes the bed hydrodynamics such as bed voidage, suspension density etc. and this causes a change in the heat transfer along the bed height. The knowledge of bed hydrodynamics at varied pressure condition is very essential in designing and optimization of PCFB components. Many researchers have reviewed the bed hydrodynamics and heat transfer at atmospheric conditions [3-6]. At present, not much information is reported on PCFB riser hydrodynamics and on cluster characteristics length and residence time. Some of the reported literature related to bed hydrodynamics and its effect on heat transfer is discussed in the following subsections.

The effect of hydrodynamic parameters, pressure and temperature on bed-to-wall heat transfer coefficient was studied by Reddy and Basu [7]. Gungor and Eskin [8], developed a two dimensional model considering the hydrodynamic behavior of CFB to investigate the effect of superficial velocity on bed hydrodynamics. Gupta and Nag [1], reported that, with the increase in superficial velocity, the bed voidage increases in the bottom portion and decreases in the top region as more solids are lifted up due to more drag force in a PCFB. The concentration of sand particles is more in the riser column for higher bed inventory, and hence, the bed voidage is lower. Reddy and Knowlton [9], investigated the effect of operating pressure on CFB riser hydrodynamics in a 300 mm diameter tube. The result obtained was contradictory to those obtained by Plasynski *et al.*,[10]. The difference was attributed to higher gas pressure drop in the smaller tube compared to the larger diameter tube. It is also observed that the pressure drop due to gas density is inversely proportional to diameter raised to the power of 1.25. Richgerg *et al.* [11], conducted some experimental investigations in a 0.19 m diameter and 9 m high pilot scale PCFB unit in order to characterize the flow patterns in a PCFB. The obtained information is used to develop an easy correlation for the prediction of internal solids reflux in a riser reactor as a function of solids/gas density ratios and the dimensionless superficial gas velocity. It is reported that, the local voidage, and the gas and solid velocities change continuously from the axis to the wall [12-15]. The voidage is highest along the axis of the riser column and lowest in the wall which is observed by various researchers [3, 14, 16]. The radial voidage distribution is much flatter in the upper section of the bed, as well as at lower circulation rates. In case of fast fluidized beds, there is a gas-solid boundary layer, where the solid generally moves downward. This is investigated that for both in large commercial boilers as well as in laboratory units [16-17]. Yue *et al.*, [18] suggested that by changing the bed inventory, one can influence the suspension density. As commented by Li and Kwauk [19], and Kunii and Levenspiel [20], the suspension density along the height of a CFB boiler varies exponentially as it does in the freeboard region of a bubbling fluidized bed. However, Andersson and Leckner [21], and Brereton and Stromberg [22] found that, the profile to be better represented by a power-law equation. Yates [23] reviewed the effect of pressure and temperature on fluidized bed and emphasized that more effort needs to be devoted to CFB's as there are many gaps in understanding the flow regime that exist in these system. Wu *et al.* [24] and Ebert *et al.* [25] suggested that, except for a very dilute bed, the superficial gas velocity does not have any great influence on the heat transfer coefficient. It is a result of a relatively low contribution of the gas convection component. In some situations, the

heat transfer coefficient at constant circulation rate even decreases with the increase of superficial velocity due to the resulting decrease in the suspension density [25-27]. Divillo and Boyd [28], show a major effect of superficial velocity but a minor effect of suspension density on the heat flux. Various researchers [1, 3-6] suggested that, the heat-transfer coefficient in a CFB riser increases from the bottom to the top and is influenced by a number of factors, including air flow, solid circulation rate, solid inventory, and particle size distribution. Basu [3] emphasized that, the major effect of these parameters on the heat transfer is due to their influence on the suspension density. Glicksman [29] studied the effect of heat transfer coefficient and its dependency on suspension density. It is concluded that, the heat transfer coefficient is found to vary as square root of the cross-section average suspension density. Divilio and Boyd [28], presented an overview of the effect of suspension density on the heat transfer using the data from the laboratory, pilot plants, and operating plants. They observed that, the suspension density varies with the height of the riser. As the combustor gets taller, the solid suspension density decreases further, resulting in lower heat transfer coefficients. Gupta and Nag [1], studied the bed to wall heat transfer behavior in a 37.5 mm ID and 1940 mm height PCFB riser where the heat transfer coefficient was found increasing with an increasing operating pressure as well as with an increase in gas superficial velocity. It was also observed that, with the increase in pressure, the bed voidage increased in the bottom zone of the riser and decreased in the top zone, thereby increasing the suspension density at the top zone. Recently, similar observations have been made by Kalita *et al.* [30]. In the book written by Oka and Oka [31], it is reported that 12 % biomass blending in sand in the case of bubbling fluidized bed found to be optimum for maximum heat transfer and proper gasification. Although much work has been done on the effect of various operating parameters on heat transfer associated with the CFB, it is very essential to study the operating parameters on the PCFB. Besides, study related to the blending of biomass in sand at varied proportions is a challenge for optrimization of a gasification and combustion process. In the present investigation, the effects of blending of biomass in sand on bed hydrodynamics and heat transfer at varied operating pressures in a pressurized circulating fluidized bed has been studied.

2.0 Materials and Method

2.1 Setup description

The schematic diagram of the pressurized circulating fluidized bed (PCFB) setup is shown in Fig.1. A photograph of the setup is shown in the Fig.2. The PCFB unit comprises of a riser, a transparent downcomer, and a cyclone separator. The riser is made of stainless steel of ID 54 mm and height of 2000 mm. Air is supplied to the CFB unit through the bottom of the riser by a high pressure centrifugal blower and a compressor. The air flow rate is measured by a standard orifice meter and is regulated by an air control valve and a bypass arrangement. The air passes through a porous distributor plate (straight hole) of 16.8 % opening area which is fixed at the bottom of the riser column. The entrained solids goes out of the riser are recovered in a cyclone separator and are then sent to the bottom of the riser column through a transparent return leg of ID 24.5 mm. Static pressures and hence voidage were measured along the riser height at 6 (six) different locations such as 120 mm, 192.5 mm, 370 mm, 495 mm, 970 mm and 1570 mm above the distributor plate. Suspension densities at those points were also calculated. Fine wire mesh (200 μm) and cigarette filters are used at the pressure taping ends to minimize the pressure fluctuations and to avoid the escape of sand particles from the column. Pressure drops are measured with U-tube water filled manometer fabricated for this purpose. The heat transfer probe of height 500 mm is located at a height of 1300 mm above the distributor plate i.e. at the upper splace region of the riser. Necessary thermocouples are facilitated to measure the surface and bed temperatures. The locations of the thermocouples from the distributor plate are 1400, 1500, 1600, 1700 and 1800 mm. Besides, thermocouples are also installed to measure the radial temperature variations in the bed at d/D of 0.2, 0.3, 0.4, 0.6 and 0.8. A heater coil (rated 1000 Watt and resistance 46 Ohms) of the required length is wrapped uniformly around the probe. Adequate electrical and thermal insulation are provided. Mica sheet of 1 mm thickness is used as electrical insulation over which heater coil is warped. For thermal insulation, ceramic wool and ceramic rope is used around the probe. The axial heat loss by conduction is also prevented by providing ceramic wool insulation in between the joints. Both surface and bed temperatures are measured with chromal-alumal thermocouples and these have been calibrated before use. Agilent 34972 LXI data acquisition/ switch unit is used for measurement and record of temperature.

2.2 Experimental procedure

A measured quantity of inventory is fed into the unit through the top of the cyclone separator and rests on the ball valve of the transparent return leg (downcomer) till the valve open. The heat transfer probe is heated by providing a known heat flux before the start of experiment. High precision pressure gauge (Swegelock make) is used for the measurement of the compressor delivery pressure. Blower delivery air flow is controlled by a gate valve installed along the flow, and the flow rate is calculated by measuring the orifice pressure drop (D and D/2 tapings) in the U-tube water manometer. Finally, the superficial velocity is calculated by using the measured orifice pressure drop. In each experiment, controlled amount of air is supplied from the blower at a required superficial velocity to the CFB loop. Compressed air is supplied from the

compressor at a required pressure to the riser bottom. For each operating conditions, about 60 minutes time is required to attain the thermal and hydrodynamic equilibrium. For thermal equilibrium, temperature rise is monitored, and for hydrodynamic equilibrium, circulation rate is monitored. Once the equilibrium condition is reached, experimental data such as temperature, pressure drop and circulation rate are recorded in a data sheet for further analysis. Same procedure is followed with every change in operating parameters. Experiments were performed at a constant heat flux of 830 W/m^2 and at a superficial velocity of 5 m/s. The axial and radial variation of heat transfer coefficient with four proportions blending of sawdust in sand such as 2.5 %, 7.5 %, 15 % and 20 % have been studied and compared. Comparisons were also made at two different sets of weight composition ratios one of which is weight composition of sawdust with 400 gm sand and the other is weight composition of sawdust with 600 gm of sand. The percentage blending of sawdust is kept constant irrespective of weight compositions. All the experiments were conducted at three different system pressures of 1, 3 and 5 bar. Average particle size of sawdust and sand used for the experiment is calculated to be 407 μm and 309 respectively. Finally, bed hydrodynamics (bed voidage, suspension density and solid circulation rate) and heat transfer characteristics (axial and radial) were investigated. All the experiments were repeated thrice in order to establish the repeatability.

*2.3 **Working formula***

For the axial probe, the wall-to-bed heat transfer coefficient is estimated from the measured local surface to bed temperatures as given below

$$h_{\mathrm{i}} = \frac{q}{A_{\mathrm{htp}}\left(T_{\mathrm{bs}} - T_{\mathrm{bi}}\right)} = \frac{V \times I}{A_{\mathrm{htp}}\left(T_{\mathrm{bs}} - T_{\mathrm{bi}}\right)} \tag{1}$$

where i, represents any location along the riser height and A_{htp}, is the heat transfer probe surface area. T_{bs} and T_{bi} are bulk surface temperatures and bed temperatures ,respectively.

The ***suspension density*** of the bed (ρ_{sus}) can be evaluated by the equation (Kunni and Levenspiel [20])

$$\rho_{\mathrm{sus}} = \rho_{\mathrm{s}}\left(1-\varepsilon\right) + \varepsilon\rho_{\mathrm{g}} \tag{2}$$

where voidage (ε) is defined as the volume fraction of the bed occupied by air bubbles, and ρ_{g} is the density of air in kg/m^3.

Voidage (ε) may be calculated by using the following expression,

$$\varepsilon = 1 - \frac{10 \times \Delta h}{\rho_{\mathrm{s}} \times L_{\mathrm{m}}} \tag{3}$$

where Δh is the difference of height in manometric fluid measured in cm of water column, L_{m} is the difference between two consecutive pressure taps across which pressure drops, and ρ_{s} is the density of sand in kg/m^3.

Solid circulation rate or solid mass flux (G_s) is given by,

$$G_{\mathrm{s}} = \frac{\rho_{\mathrm{s}} \times L_{\mathrm{a}} \times A_{\mathrm{D}} \times \left(1-\varepsilon_{\mathrm{mf}}\right)}{A_{\mathrm{B}} t} \tag{4}$$

3.0 Results and discussion

Figures 3 through 5 present the variation and comparison of bed voidage at operating pressures of 1, 3 and 5 bar. The comparisons were made at two different weight composition ratios and at a superficial velocity of 5 m/s. In these conditions percentage blending of biomass is maintained at 15%. As observed, the bed voidage is first decreases and then increases, before it decreases at the exit of the riser which may be better represented by S-shaped bed voidage profile. With the increase of pressure, the bed voidage decreases at the exit of the riser, this may be due to the increase in concentration of particles at the riser exit. This is observed to be more in the case of weight composition ratio of 90:600.

The variation of heat transfer coefficient at a height of 1.6 m from the distributor plate at 2.5 %, 7.5 %, 15 % and 20 % blending is shown in the Figs.6 through 9. The comparisons were made at two different weight composition ratios and at a superficial velocity of 5 m/s. From these figures it has been observed that, the heat transfer coefficient increases with the increase in operating pressures. The heat transfer coefficient is found to be higher (120-135 W/m^2-K) at 7.5 % blending (Fig.7) with weight composition ratio of 30 gm: 400 gm as compared to the other three percentage blending. The heat

transfer coefficient is found to be lowest (90-105 W/m^2-K) at 20 % biomass blending (Fig.9) in comparison to the other blending at the superficial velocity of 5 m/s. This may be due to the lowest solid circulation rate observed in both the cases as compared to the other percentage blending. The values of the solid circulation rate at three different operating pressures and at four different % blending of sawdust at the superficial velocity of 5 m/s is shown in the table-1.

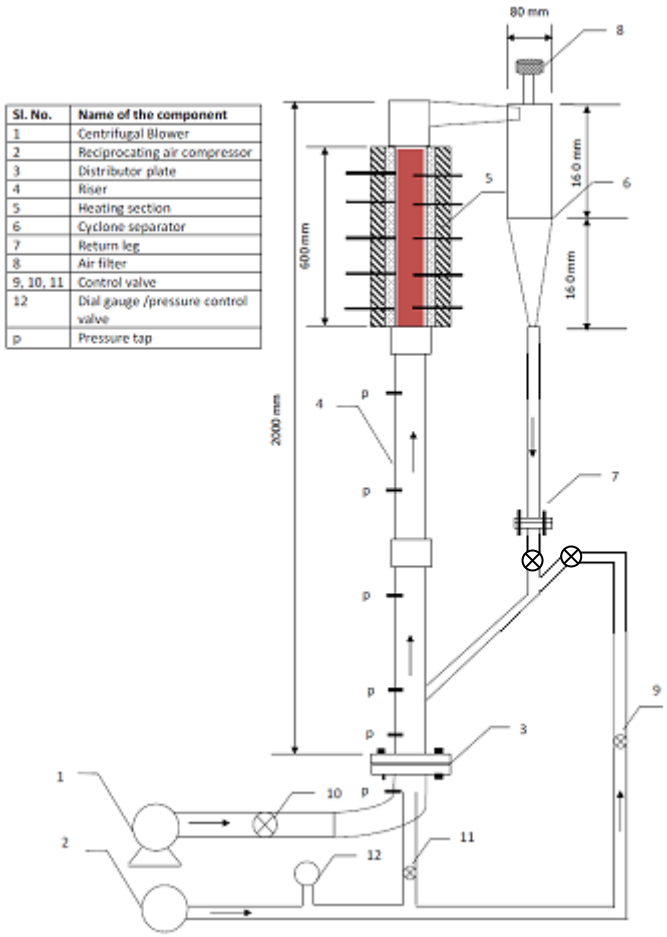

Sl. No.	Name of the component
1	Centrifugal Blower
2	Reciprocating air compressor
3	Distributor plate
4	Riser
5	Heating section
6	Cyclone separator
7	Return leg
8	Air filter
9, 10, 11	Control valve
12	Dial gauge /pressure control valve
p	Pressure tap

Fig.1 Schematic of experimental setup

Fig.2 Photograph of the experimental setup

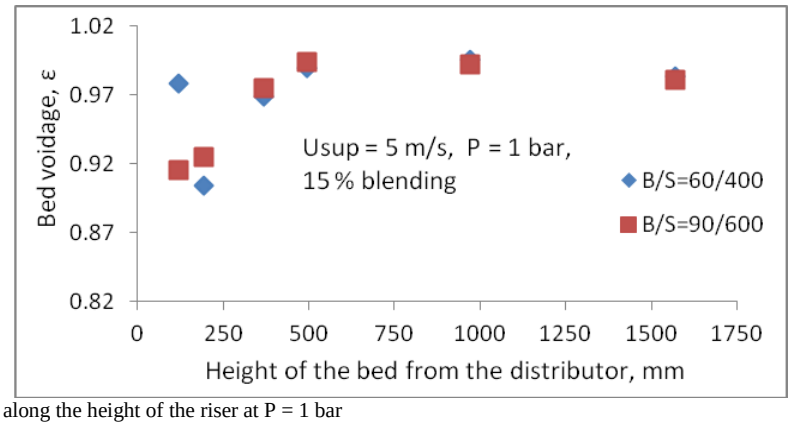

Fig.3 Variation of bed voidage along the height of the riser at P = 1 bar

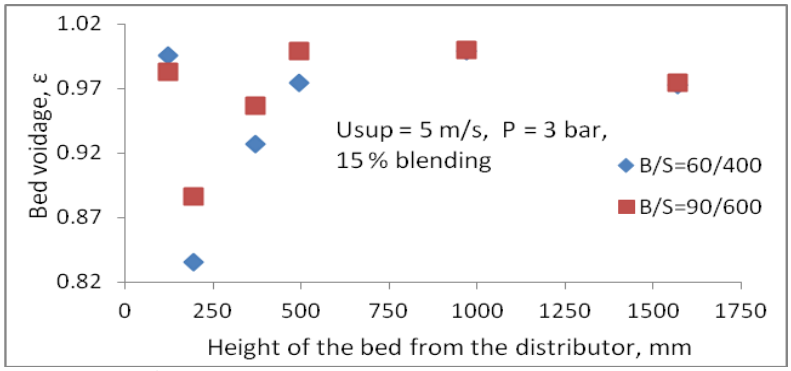

Fig.4 Variation of bed voidage along the height of the riser at P = 3 bar

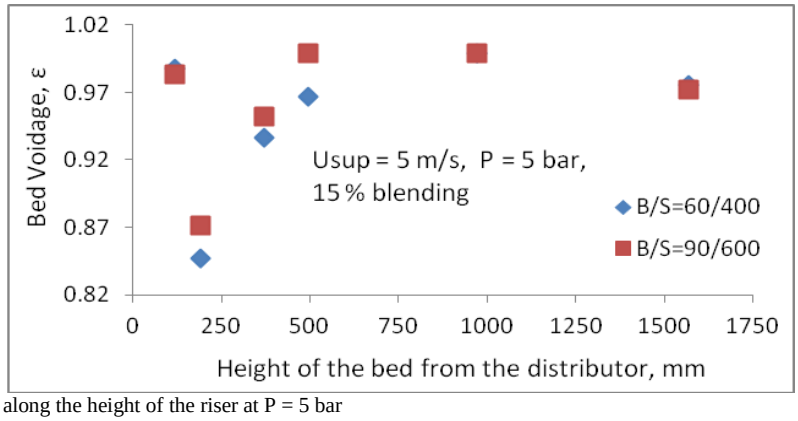

Fig.5 Variation of bed voidage along the height of the riser at P = 5 bar

Figure 10 show the variation of heat transfer coefficient along the heat transfer probe at the operating pressure of 5 bar and at the superficial velocity of 5 m/s. It is observed that, the heat transfer coefficient increases from the bottom to the top of the heat transfer probe. This is a representative figure for percentage blending of biomass in sand at varied pressure conditions. The similar variation of heat transfer coefficient without blending of biomass is demonstrated by Gupta and Nag [1]. The suspension density variation at a height of 1.57 m from the distributor with operating pressures at the superficial velocities of 5 m/s is shown in the Fig.11. The comparison is made at a percentage blending of 15 % and at two different weight composition ratios. It has been observed that, the suspension density increases with the increase in operating pressure in both the weight composition ratios. However, the higher values of suspension density have been observed at the weight composition ratio of 90 gm: 600 gm.

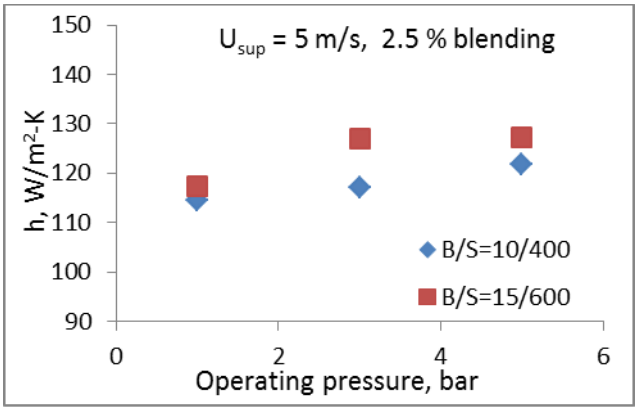

Fig.6 Variation of heat transfer coefficient at 2.5 % blending

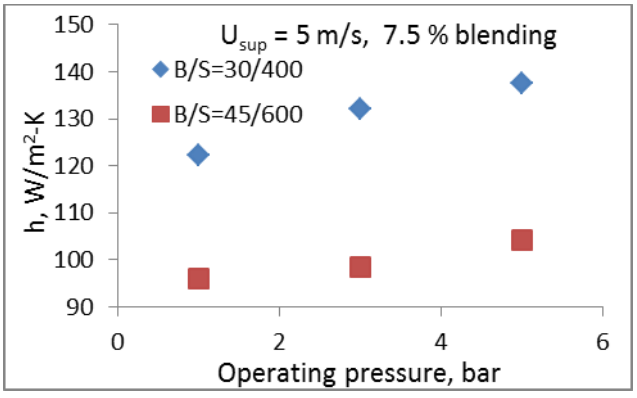

Fig.7 Variation of heat transfer coefficient at 5 % blending

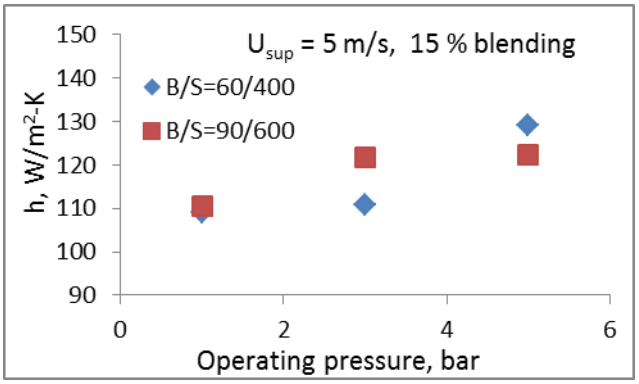

Fig.8 Variation of heat transfer coefficient at 15 % blending

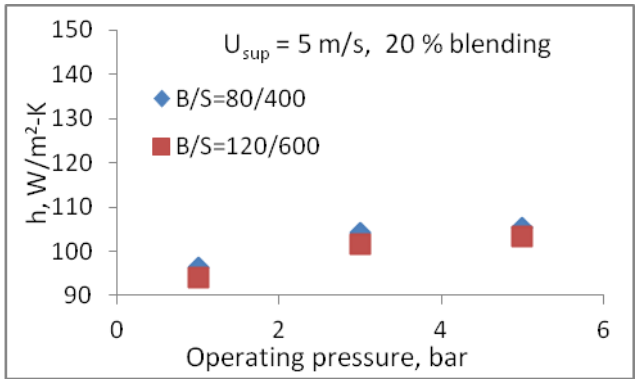

Fig.9 Variation of heat transfer coefficient at 20 % blending

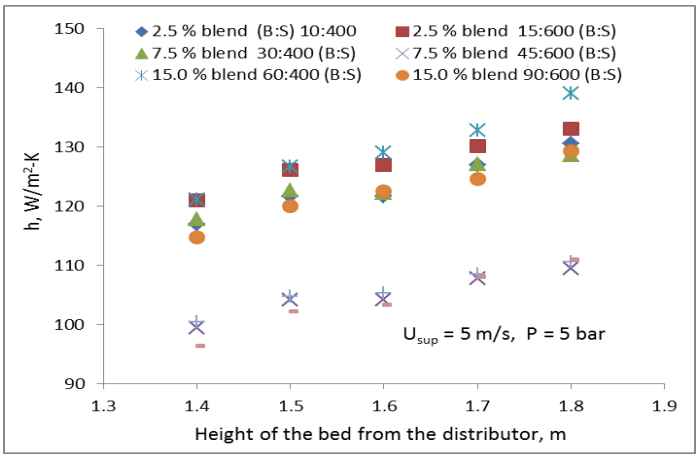

Fig.10 Comparison of variation of heat transfer coefficient along the heat transfer probe

Table 1. Solid circulation rate, G_s (kg $m^{-2}s^{-1}$) data with pressure

Pressure in bar	2.5 % blend		7.5 % blend		15.0 % blend		20.0 % blend	
	(B/S) 10:400	(B/S) 15:600	(B/S) 30:400	(B/S) 45:600	(B/S) 60:400	(B/S) 90:600	(B/S) 80:400	(B/S) 120: 600
				U_{sup} = 5 m/s				
1	0.816	1.381	0.946	1.072	0.773	0.912	0.205	0.0817
3	1.164	1.086	1.623	0.753	1.094	1.762	0.926	0.1388
5	0.9517	1.455	1.798	1.350	1.637	1.327	0.989	0.3033

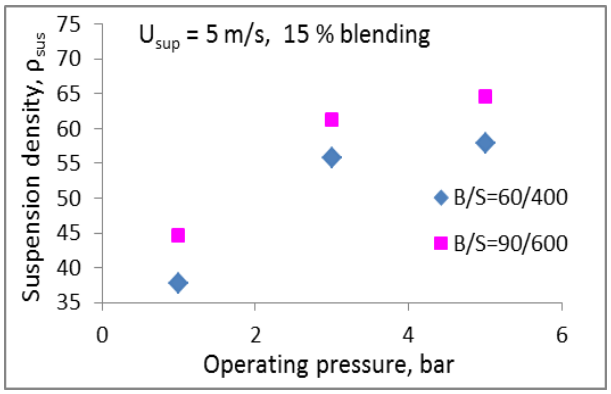

Fig.11 Variation of suspension density at U_{sup} = 5 m/s

The comparison of radial variation of heat transfer coefficient at two different % blending of sawdust such as 2.5 % and 15 % is shown in the Figs.12 and 13. These plots have been made at a distance of 1.6 m from the height of the distributor. From these figures it has been observed that, the heat transfer coefficient decreases from the wall to the core of the riser. This may be due to decrease in particle concentration from the wall to the core of the riser. It is also observed that with the increase in pressure, heat transfer coefficient increases. This may be due to the increase in particle concentration with increase in pressure. At 20 % biomass blending heat transfer coefficient near to the wall of the riser is found be highest and at the core it is found to be lowest. This is probably due to the diffusion of particles from the core to the wall of the riser.

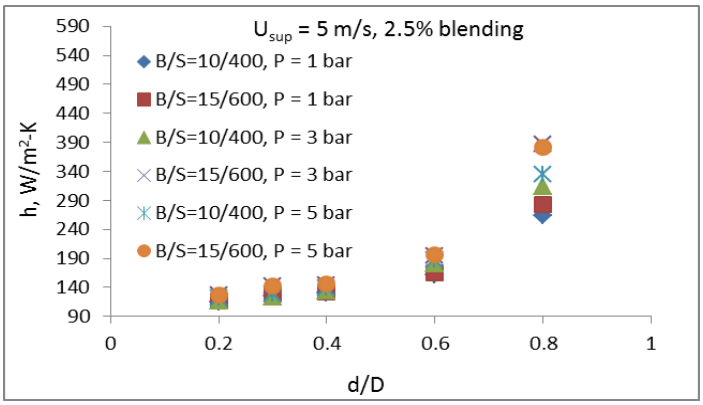

Fig.12 Comparison of radial heat transfer coefficient at 2.5 % blending

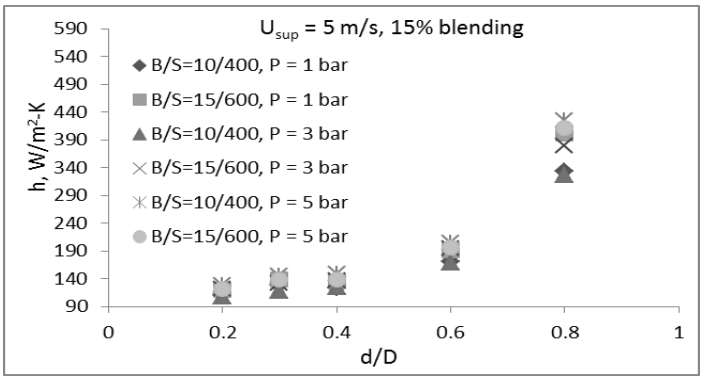

Fig.13 Comparison of radial heat transfer coefficient at 15 % blending

4.0 Conclusions

In the present investigation, the experiments have been conducted at four different percentage blending of biomass such as 2.5 %, 7.5 %, 15 % and 20 % in sand with two different weight composition ratios and at a superficial velocity of 5 m/s. Operating pressure is varied from 1 to 5 bar in a step of 2 bar. The summary of the experimental observations are as follows

- The suspension density increases with the increases in operating pressures.
- The axial heat transfer coefficient increases with an increase in operating pressure at all the % blending
- The radial heat transfer coefficient decreases from the wall (about 480 W/m^2-K) to the core (93 W/m^2-K) of the riser in all the operating conditions.
- The solid circulation rate increases with an increase in operating pressures, and it decreases with the increase in % blending of sawdust.
- More homogenous fluidization and uniform heat transfer coefficient has been observed with the increase in operating pressure. 7.5 - 15 % sawdust blend in sand is observed to be optimum for obtaining higher heat transfer coefficient at both the sets of weight compositions.

References

[1] Gupta, A.V.S.S.K.S., Nag, P.K., 2002. Bed-to-Wall Heat Transfer Behavior in a Pressurized Circulating Fluidized Bed, International Journal of Heat and Mass Transfer 45, pp.3429-3436.
[2] Basu, P., Cheng, L., 1996. Heat transfer in a pressurized circulating fluidized bed, International Journal of Heat and Mass Transfer 39(13), pp.2711-2722.
[3] Basu, P., 2006. Combustion and Gasification in Fluidized Beds, Taylor & Francis Group (CRC Press), New York.
[4] Basu, P., Nag, P.K., 1996. Heat Transfer to Walls of a Circulating Fluidized Bed Furnace, Chemical Engineering Science 51(1), pp.1-26.
[5] Basu, P., Nag, P.K., 1987. An investigation into heat transfer in circulating fluidized beds, International Journal of Heat and Mass Transfer 30(11), pp.2399-2409.
[6] Grace, J.R., 1986. Heat Transfer in Circulating Fluidized Beds, in:P.Basu (Ed.), Circulating Fluidized Bed Technology, Pergamon, Canada, pp.63-81.
[7] Reddy, B.V., Basu, P., 2002. Estimation of the Effect of System Pressure and CO_2 Concentration on Radiation Heat Transfer in a Pressurized Circulating Fluidized Bed Combustor, Institution of Chemical Engineers Trans IChemE, 80 (Part A).
[8] Gungor, A., Eskin N., 2007. Hydrodynamic Modeling of a Circulating Fluidized Bed, Powder Technology 172, pp.1-13.
[9] Reddy, S.B.K., Knowlton, T.M., 1996. "The effect of pressure on CFB riser hydrodynamics", Proceedings of the 5th International Conference on CFB, Beijing, DB15 (CFB V preprints).
[10] Plasynski, S., Klinzing, G., Mathur, M., 1994. High Pressure Vertical Pneumatic Transport Investigation, Powder Technology 79, pp.95–109.
[11] Richtberg, M., Richter, R., Wirth, K.-E., 2005. Characterization of the Flow Patterns in a Pressurized Circulating Fluidized Bed, Powder Technology 155, pp.145-152.
[12] Hartge, E.U., Rensner, D., Werther J., 1988. Solid Concentration and Velocity Patterns in Circulating Fluidized Beds, in *Circulating Fluidized Bed Technology II* (Edited by P. Basu and J. F. Large), Pergamon Press, Oxford, pp.165-180.
[13] Horio, M., Morishita, K., Tachibana, O., Murata, N., 1988. Solid Distribution and Movement in Circulating Fuidized Beds, in *Circulating Fluidized Bed Technology II* (Edited by P. Basu and J. F. Large), Pergamon Press, Oxford, pp.147-154.
[14] Li, J.J., Zhang, H., Yang, H.R., Wu, Y.X., Lu, J.F., Yue, G.X., Zhang, 2009. "Hydrodynamic model with binary particle diameter to predict axial voidage profile in a CFB combustor", Proceedings of the 20th International Conference on Fluidized bed Combustion, pp.768-773.
[15] Yates, J.G., 1997. Experimental Observations of Voidage in Gas Fluidized Beds, in: J. Chaouki, F. Larachi, M.P. Duducovic (Eds.), Non-Invasive Monitoring of Multiphase Flows, Elsevier, Amsterdam, pp.141-160.
[16] Tang, J.T., Engstrom, F., 1987, "Technical assessment on the Ahlstrom pyroflow circulating and conventional bubbling tluidized bed combustion systems", Proceedings of the 9th International Conference on Fluidized Bed Combustion (Edited by J. P. Mustonen), ASME, New York, pp.38-54.
[17] Schaub, G., Reimert, R., Albrecht, J., 1989. "Investigation of mission rates from large scale CFB combustion plants" Proceedings of the l0th International Conference on Fluidized Bed Combustion (Edited by A. Manaker), ASME, New York, pp.685-691.
[18] Yue, G., Lu, J., Zhang, H., Yong, H., Zhang, J., Liu, Q., 2005. "Design theory of circulating fluidized boilers", Proceedings of the 18th International Conference on Fluidized Bed Combustion, Jia, L., Ed., ASME, New York, paper: FBC 78134.
[19] Li, Y., Kwauk, M., 1980. "The dynamics of fast fluidization", Proceedings of the 3rd International Conference on Fluidized Bed Combustion (Edited by J. R. Grace and J. M. Matsen), Henniker, New Hampshire, August 3-8, pp.539-544.
[20] Kunii, D., Levenspiel, O., 1991. Fluidization Engineering, Butterworth-Heinemann, USA, 1991.
[21] Andersson, B.A., Leckner, B., 1992. Experimental methods of estimating heat transfer in circulating fluidized bed. International Journal of Heat and Mass Transfer 35, pp.3353-3362.
[22] Brereton, C.M.H., Stromberg, L., 1986. Some Aspects of Fluid Dynamic Behavior of Fast Fluidized Beds, in *Circulating Fluidized Bed Technology* (Edited by P. Basu), Pergamon Press, Toronto, pp.133-144.
[23] Yates, J.G., 1996. Effects of Temperature and Pressure on Gas-Solid Fluidization, Chemical Engineering Science 51(2), pp.167-205.
[24] Wu, R., Lim, C.J., Chauki, J., Grace, J.R., 1987. Heat Transfer from a Circulating Fluidized Bed to Membrane Water Wall Cooling Surfaces, A.I.Ch.E.J. 33, pp.1888-1893.
[25] Ebert, T.A., Glicksman, L.R., Lints, M., 1993. Determination of Particle and Gas Convective Heat Transfer Component in Circulating Fluidized Bed, Chemical Engineering Science 48, pp.2179-2188.
[26] Nag, P.K., Ali, Moral, M.N., 1990. Effect of Probe Size on Heat Transfer at the Wall in Circulating Fluidized Beds, International Journal of Energy Research 14, pp. 965-974.
[27] Mahalingam, M., Kolar, A.K., 1991.Heat Transfer Model for the Membrane Wall of a High Temperature Circulating Fluidized Bed, in *Circulating Fluidized Bed Technology Ill* (Edited by P. Basu, M. Horio, and M. Hasatani), Pergamon Press, Oxford, pp.239-246.
[28] Divilio, R.J., Boyd, T.J., 1994. Practical Implications of the Effect of Solids Suspension Density on Heat Transfer in Large Scale CFB Boilers, in *Circulating Fluidized Bed Technology IV* (Edited by A. Avidan), AIChE, New York, pp.334-339.
[29] Glicksman, L., 1988. Circulating Fluidized Bed Heat Transfer, in *Circulating Fluidized Bed Technology II* (Edited by P. Basu and J. F. Large), Pergamon Press, Oxford, pp. 13 29.
[30] Kalita P., Saha U. K., and Mahanta P., 2012. Parametric study on the hydrodynamics and heat transfer along the riser of a pressurized circulating fluidized bed unit, Experimental Thermal and Fluid Science, doi: http://dx.doi.org/10.1016/j.expthermflusci.2012.09.001.
[31] Oka, N., Simeon, Anthony, E.J., Oka, S., 2004. Fluidized Bed Combustion, Marcel Dekker Inc (CRC Press), New York.